LEARNING CENTRE
CITY CAMPUS, HOWARD STREET
SHEFFIELD S1 1WB

REFERENCE

ProQuest LLC.
789 East Eisenhower Parkway
P.O. Box 1346
Ann Arbor, MI 48106 – 1346

Surface Layer Evolution in Glow Discharge Optical Emission Spectroscopy

Linghao Chen

A thesis submitted in partial fulfilment of the requirements
of Sheffield Hallam University
for the degree of Doctor of Philosophy

May 2005

Abstract

Glow discharge optical emission spectroscopy (GDOES) is a modern analytical technique for the analysis of the chemical composition of bulk materials and the depth profiling of multi-layer structures. Most research in the use of GDOES has concentrated on developing accurate methodologies for quantitative analysis and depth profiling. However, this thesis presents a study on various aspects of surface layer evolution under argon ion etching in GDOES.

The GDOES technique relies on the ion bombardment of sample surfaces which removes material from the surface, layer by layer, on the atomic scale. During the surface layer evolution, the ion bombardment causes different surface micro-textures and preferential sputtering in individual crystallites, which can cause degradation of depth resolution in GDOES depth profiling. Experimental results using pure iron specimens in this study show a correlation between textures induced by GDOES sputtering and the sputtering rate, and a difference in the sputtering rate for crystallites with different crystal orientations.

In studying ion bombardment by GDOES in semiconductors, a novel pitting morphology on the surface of a carbon-coated silicon wafer was observed and characterised in detail. This may have a potential application in the fabrication of micro-lens arrays. The generation and development of the pits were investigated, which are believed to be dependent upon the different sputtering rates between the film and the substrate. Geometric features of the pits were obtained using atomic force microscope (AFM) and the sphere-like surface of the pit was confirmed. The experimental work in this study also shows that the Grimm source in GDOES is a powerful etching tool. Eroded surfaces of metal specimens with little damage to the crystallites and phase structures were obtained by GDOES etching. The method was found to be an ideal process for specimen preparation for electron back-scattered diffraction (EBSD). The GDOES-etched surface of single crystal copper showed that the damaged layer formed by mechanical polishing using 6 micron diamond paste was about 1–2 μm and was removed after only a few tens of seconds of GDOES etching. GDOES etching was also applied to an investigation of internal oxides in carburised steels. The eroded surfaces provided plan views of the morphologies of internal oxides of carburised steels by scanning electron microscopy (SEM) images. Results of energy dispersive spectrometer (EDS)/SEM elemental mappings of different layers of the steels were in good agreement with GDOES depth profiles, which revealed that the elements Cr, Mn and Si were involved in the oxides.

The last section of the thesis is about hydrogen detection in GDOES. The study includes a detailed analysis of: hydrogen contamination in GDOES, the hydrogen detection status of GDOES, the sample matrix effects on hydrogen detection and hydrogen effects on elemental concentrations in GDOES measurements. The experiments have confirmed that water vapour is the main source of the hydrogen contamination. When the GDOES system has stabilised, GDOES could be employed to differentiate specimens containing different concentrations of hydrogen. The experiments also showed that different hydrogen intensities could have resulted from different matrices even when the specimens were believed to contain no hydrogen. A possible explanation could be that variations of the γ-electron ejection from different matrices and different sputtered atoms in the glow discharge, which altered the plasma and the energy distribution in the glow region, resulted in the variation of the excitation of the hydrogen atoms in the source. However, there are still some results in the matrix effects which could not be explained. The experiments concerning the consequence of hydrogen effects on apparent elemental concentrations in GDOES measurements were also undertaken using two steel standards. The results indicated that the hydrogen in the source has a negative effect on the signal from most of the metal elements in the specimens, and a positive effect on the non-metal and semiconductor elements.

Acknowledgements

I would first like to thank Prof. John M. Rodenburg, the direct of study, and Dr. Mike C. Simmonds, the supervisor of the study, for providing me this opportunity to be involved in this research project at the Materials Research Institute of Sheffield Hallam University, for the supervision given throughout the study, and for help in this thesis.

I would also like to thank Dr. Xiaoxue An and Dr. Hanchang Xu for supplying me with the carburised steels and plating samples described in Chapter 5 and Chapter 6 and helpful discussions about the relevant sections.

Thanks are given to Dr. Hywel Jones and Dr. Cornelia Schönjahn for their help in pointing out errors in English in this thesis. Thanks are also given to Prof. Keith Berrington for his helpful comments on this thesis.

I am very grateful towards all the technical supports and help given to me from staffs in the Materials Research Institute.

I would like to acknowledge Sheffield Hallam University for their financial support of this study.

And of course, to my family for giving me much needed encouragement and all time supports.

Contents

Chapter 1 Introduction

Glow Discharge Optical Emission Spectroscopy (GDOES) is a modern analytical instrument for analysis of the chemical composition of bulk materials and depth profiling of multi-layer structures. Sputtering and atomic optical emission are combined in the Grimm source (Grimm, 1968) in GDOES, providing an extremely rapid, accurate and reliable technique with the advantages of simple specimen preparation, relatively deep analytical depth and good reproducible measurements compared to other quantitative techniques. GDOES is now routinely used to analyse industrial and research materials (Payling, 1997a).

The motivation for this work was to examine the special considerations which must be taken into account when GDOES is used to do analyses of quantitative depth profiling. Most research in the use of GDOES has concentrated on developing accurate methodologies for quantitative depth profiling. However, the study on GDOES in the Materials Research Institute of Sheffield Hallam University, where this project was undertaken, has presented some results and novel applications, which have not been found in the literature. This thesis presents a study on various aspects of surface layer evolution under argon ion etching in GDOES. The GDOES technique relies on ion bombardment of the specimen surface which removes material from the surface layer by layer, on the atomic scale. During the surface layer evolution, the ion bombardment can cause different surface micro-textures and preferential sputtering in individual crystallites, which can cause degradation of depth resolution in GDOES depth profiling (Chapter 3). On the other hand, the ion bombardment can induce a new morphology on a surface with previously coated material of a low sputtering rate, for example the pitting phenomenon (Chapter 4), which may have a potential application in the manufacture of micro-lens arrays, such as for new unique-marker technology. The

Grimm source in GDOES is also a powerful etching tool. The eroded surface has little damage in the underlying crystallites and so it can be used as a method for preparing a surface for electron back-scattered diffraction (EBSD), which is a powerful method for measuring crystallite orientation in microcrystalline materials. The etching method can also be used to obtain a plan view of internal oxides of steels using scanning electron microscopy (SEM) (Chapter 5). In Chapter 6, the study is focused on various issues which impact upon hydrogen measurement in the glow discharge source of the GDOES instrument.

In GDOES depth profile analysis, the elemental intensities after a particular sputtering time can be converted into an elemental concentration and sputtered depth. Therefore, the best depth resolution would be obtained when the sample surface is eroded layer-by-layer uniformly. However, the specimen is often eroded non-uniformly to a greater or lesser degree. On a gross level, the depth resolution is affected by the shape of the sputtered crater and roughness of the bottom surface of the crater (Quentmeier, 1997). The best crater shape can be obtained by choosing optimum discharge conditions, i.e. the voltage, the current and the argon pressure (Angeli *et al.*, 1993; Quentmeier 1994 and Bengtson, 1996). The roughness of the bottom surface is believed to be due to differential sputtering of the sample material depending on size and orientation of the crystal structures (Quentmeier, 1997 and Angeli, 1997). Until now there have been no detailed reports in the literature of the orientation effects on the sputtering rate in GDOES. In this study, the effect of crystal orientation on the sputtering rate of different crystals and the effect on depth resolution have been investigated for the first time in detail (Chapter 3). Pure iron was chosen as the test specimen because of its metallurgical significance and its moderate sputtering rate relative to other elements commonly analysed in GDOES. With its high purity, the influence of non-uniformly distributed elements in the specimen on sputtering can also be eliminated. The specimens were sputtered in the GDOES with a dc source for different sputtering times under the condition of optimal parameters for best sputtered crater shape. SEM was used to observe the micro-textures on the bottom of sputtered craters. The orientations

of the selected 'micro' areas with typical surface textures were obtained by EBSD. The sputtered depth corresponding to the selected areas were measured based on the correlation between the SEM images and profiles of craters recorded by a profilometer. Different sputtering rates between the [001] and [111] poles have been observed and there is also a correlation between the eroded crystal surface textures and crystal orientation. The results imply that samples with small grain size will have the best possible depth resolution in GDOES.

Until now, all applications of GDOES have focused on chemical composition analysis and depth profiling of materials. However, the Grimm source is also in itself a powerful tool to ion-etch the surface. In Chapter 4, it is demonstrated that GDOES etching can introduce novel surface phenomena on silicon wafers. Although the analytical capability of the GDOES is not part of the etching process, it is required in this particular study in order to estimate when a surface layer (which is crucial for the pitting process that is being characterised) has been partially or completely removed. By stopping the etching process at well-defined points during the removal of the surface layer, the GDOES can be used to examine the effects of sudden changes in the sputtering rate at surface layer interfaces. This study is therefore facilitated by the GDOES's analytical capability. It is known that surface topography can be developed under extended high energetic ion bombardment from existence of small pits to a characteristic shape (Carter *et al.*, 1983). In the present work, a silicon surface with carbon coating was eroded in the GDOES. Immediately after the carbon layer was completely removed (as measured by the loss of the carbon signal in the analytical part of the GDOES), uniformly distributed micron-size pits were left on the surface of the silicon. The mechanism of pit generation appears to be due to a large difference in the sputtering rate between the coating and the substrate. The geometry of the pits was measured using atomic force microscopy (AFM), which further revealed the pit has a spherical surface. These pits have potential application as micro-lens arrays.

In the first part of Chapter 5, the results of the EBSD patterns collected from the surfaces of the pure iron and the copper after GDOES etching have shown that a high-power Grimm source, as generally employed in GDOES, is an excellent tool for removing surface damage in iron specimens prior to study using EBSD. The technique is extremely fast and can in principle be applied to any sample, without the use of any chemicals. The Grimm source itself is a simple system (e.g. as compared to an ion beam thinner), and so could represent a very cheap and fast specimen preparation route.

GDOES was also used successfully in the investigation of internal oxides in carburised steels by the plan view of the oxides in the revealed layer and the depth profiling in GDOES. Most of the prior studies on internal oxidation have utilised cross-sections of the surface layers, either by SEM for a cross-sectional view of oxides on the micron scale, or by Transmission Electron Microscopy (TEM) to determine the type of the oxides (Mural *et al.*, 1997). However, these approaches cannot reveal a plan view of morphology and distribution and a depth location of the oxides. In the second part of Chapter 5, the internal oxides of the carburised steels were plan viewed in SEM after GDOES etching down to a surface layer with known depth. The oxides revealed in different layers showed different morphologies. Energy Dispersive Spectrometer (EDS) mapping in SEM identified that the oxide elements were Si, Cr and Mn, which is in agreement with the GDOES depth profiles for these elements.

Accumulation of hydrogen atoms in steel causes hydrogen embrittlement, which shows a loss in ductility and toughness of the steel. Hydrogen in metal can also produce cracks under the influence of stress before use as well as in service applications of the steels (Timmins, 1997). However, detection of hydrogen in steels often causes problems due to its immobility and light atomic mass. Hydrogen detection is impossible for most traditional surface analytical techniques (Lanford, 1982) and only a few techniques can be employed to do a surface analysis for hydrogen (Marwick, 1991; Tirira *et al.*, 1996 and Payling, 1997f). GDOES is one of the few analytical techniques that are sensitive to hydrogen. It is fast, easy to operate and relatively inexpensive

compared to others. With a relatively high sputtering rate, GDOES with a dc source can carry out bulk and depth profiling analysis of metal samples with tens of microns of depth, which makes it possible to use this method for hydrogen analysis of steels. Few applications in hydrogen detection have been found both in surface and bulk analysis (Alexandre *et al.*, 1981). The reasons are probably the lack of standards for the calibration of hydrogen and hydrogen contamination in the source that is inevitable in GDOES operation. In view of this, a research programme was set up to test the possibility of using GDOES for detection of hydrogen and to determine how sensitive the technique could be to hydrogen, so as to establish whether or not this could be used as, e.g., a routine test on steels or other metals that may suffer hydrogen attacks (Chapter 6).

Hydrogen contamination in the GDOES source was first tested, with the results showing that the hydrogen mainly came from water vapour deposited on the surfaces in the glow discharge source and measured samples, from hydrocarbons backstreaming into the chamber from the pumping system and from hydrogen contamination in the argon gas. These are in agreement with the observation of Payling (1997a). A minimum limit of the hydrogen intensity due to contaminants is hard to obtain as the hydrogen signal decays exponentially with an increase in the sputtering time, even after long etching times. However, after an appropriate 'warming up' period of the GDOES, a so-called 'hydrogen detection status' can be obtained: a condition in which the GDOES is optimally sensitive to the detection of hydrogen. In this status, different levels of hydrogen in steels were differentiated. Furthermore, the experiments in this chapter significantly revealed that differences in the intensities of the hydrogen contamination in GDOES can result from different sample matrices in the hydrogen detection status, even when the samples are believed to have no hydrogen. This phenomenon is named as matrix effects on the intensity of hydrogen contamination in GDOES in this study. It was followed by discussions in consideration of the relevant ionisation and excitation processes in the glow discharge. Then some results of hydrogen detection in GDOES were obtained. They show that the GDOES in the

hydrogen detection status has an ability to differentiate the hydrogen levels between steels with and without hydrogen loading. The GDOES can also detect the hydrogen at the interface between the coating and the substrate for electroplated samples.

On the other hand, hydrogen in the source can affect intensities of detected elements in GDOES measurements and, consequently, the apparent concentrations (Hodoroaba *et al.*, 2000a and 2000b). In Chapter 6, a simple experiment was also set up to confirm the hydrogen effect on the intensities and concentrations measured in the GDOES when using a fixed voltage and current with a variation in Ar pressure. The operation was without the addition of hydrogen by introducing a mixed gas. It was shown that the hydrogen mainly comes from the water vapour that is inevitable in GDOES measurements. The experimental results for two stainless steel standards indicated that, for the elements in the standards, the hydrogen has negative effects on the level of the signal for most of the metal elements and positive effects for non-metal and semiconductor elements, which could be due to the hydrogen in the plasma modifying the energy distribution of the energetic particles. After the quantification procedure, the effects on concentrations can be compensated to some degree by using the ratio values of the elemental intensities to that of argon. However, the results of the relative variations for Si, C, Cr and Mn show that the hydrogen effects on these elements should not be ignored in a quantitative analysis in GDOES. This is especially true for the analysis of layers a few microns thick, because the hydrogen contamination from the water vapour could be very high during the first tens of seconds of sputtering time. As a consequence of the hydrogen effect on intensities, the sputtered depth, which is calculated based on the elemental intensities, will also be affected.

The last chapter includes the conclusions of this study. Some ideas for future work are also presented concerning the subjects in this study. For example, experimental work could be done to combine the effects of surface binding energy and crystal orientation effects on the sputtering rate in GDOES in order to get a further understanding of sputtering rate parameters of importance in low ion energetic bombardment. For the

application of GDOES to the investigation of internal oxides of carburised steels, a combination of SEM imaging and the argon ion etching of the surface would give a 3-D image of the internal oxide. The plan view of oxide regions of relatively large size has also provided the opportunity to determine the crystalline structure using EBSD pattern detection.

Chapter 2 Background of GDOES

2.1 Introduction

Glow Discharge Optical Emission Spectroscopy (GDOES) is a chemical composition analytical instrument for solid samples. Combining sputtering and atomic emission in a Grimm source (Grimm, 1968), it provides a modern, extremely rapid technique for bulk analysis and depth profiling of samples. The Grimm source can work in conditions of direct current (dc) and radio frequency (rf) glow discharge. GDOES with a dc source is used in the analysis of conductive samples, while an rf source is used for both conductive and non-conductive samples. Light emitted by the glow discharge is analysed by an optical spectrometer. With a wide range of optical wavelength analysis from 110nm to 800nm, GDOES can analyse almost all of the elements in the periodic table. Relative standard deviations (RSD) of analytical precision are 0.1–1% for major and minor analytes and detection limits are in the range 1–10 ppm for bulk analysis (Bengtson, 1996). By employing the concept of emission yield, quantitative procedures of GDOES have been developed for sample analysis to produce characteristics showing elemental concentrations against analysed depth. For surface depth profile analysis, the analytical precision and the detection limit are very close to that for bulk analysis. GDOES can analyse up to a depth of ~100 μm within a single burn for steel samples, yet the minimum information in depth is in the scale of a few nanometres. The depth resolution of depth profiling in GDOES is believed to be about 15% of analysed depth. In recent decades, the technique has been successfully applied in routine tests and investigations of industrial surfaces of steels and alloys, thin films and hard coatings.

In this chapter, a general literature review on the GDOES technique is presented, which includes a description of the glow discharge source, the glow discharge process, the sputtering of the sample surface, the quantification procedures, analytical performance

and recent applications. The description focuses on GDOES instruments with dc sources as most of the studies in this thesis have been undertaken on this type of instrument.

Much of the introduction described here is covered in the major single-proceedings text edited by Payling *et al.* (1997). In what follows, the original literature is cited where possible, although most of the relevant chapters in Payling *et al.* (1997) would provide the reader with a more thorough, and up-to-date analysis. Works published later than 1997 are cited in full.

2.2 Glow Discharge Source and GDOES Instruments

2.2.1 The Grimm source in GDOES

All experimental work described later in this study has been performed in a GDOES which employs a standard Grimm glow discharge source. The Grimm source works on the same principle as a typical laboratory glow discharge source but with a different configuration. A typical laboratory glow discharge source, shown in Figure 2.1, consists of two planar, parallel electrodes, one the cathode and the other the anode, located inside a cylindrical glass vacuum tube filled with gas (e.g. argon) at low pressure. A voltage is applied between the cathode and the anode. When the conditions (gas pressure, voltage and current) are suitable and the discharge has ignited, the cathode is fully covered by a dark space. It is followed by the brightest band, called the negative glow, and a region of dark and bright bands, called the positive column, which extends to the anode. When the anode is close to the cathode, the positive column disappears and only the dark space and the negative glow remain between the cathode and the anode. This is the fundamental structure of glow discharge (Chapman, 1980).

The innovation of the Grimm source is probably the most important development in the GDOES technique. The principle of the source is based on the fact that the geometry

and the positioning of the electrodes strongly influence the distribution of the luminous zones inside the tube (Bouchacourt and Schwoehrer, 1997):

- the positive column diminishes and then disappears when the anode is sufficiently close to the cathode;
- the anode glow and the anode dark space also disappear and only the negative glow and the cathode dark space remain when the anode penetrates into the negative glow;
- the discharge ceases and no luminous phenomena are observed if the anode is brought into the plane of the cathode dark space.

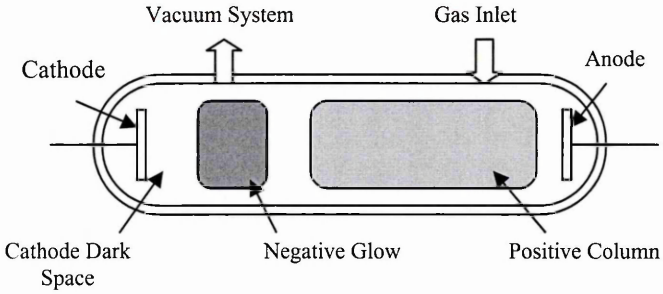

Figure 2.1. Schematic diagram of a typical laboratory glow discharge source.

A schematic cross-section of the Grimm source is shown in Figure 2.2. In the Grimm source, the anode is a hollow tube rather than the flat plate used with the laboratory glow discharge tube, and a flat sample acts as the cathode. The distance between the cathode and the anode is between 0.1 and 0.2 mm. The sample to be analysed is mounted onto an O-ring seal, completing a chamber. The chamber is first evacuated, then argon is bled continuously through the anode to maintain a low pressure (typically 300–1300 Pa). A voltage is then applied between the anode and the sample (400–1200 V) (Payling, 1997a). Interaction between electrons and the argon atoms causes positive ionisation of the argon. The argon ions are then driven by the negative bias in the cathode dark space to impact the sample, causing erosion (sputtering) of the sample surface. These sputtered atoms move away from the surface of the sample and are excited in the negative glow region through collisions with the electrons and metastable argon atoms, thus emitting photons. Energies of the emitted photons

correspond to those of electrons in the atoms falling from a higher level to a lower level. Hence, the emitted photons have the characteristic wavelength of the elements from which they were emitted. These photons pass through the window of the source and their energy is detected to analyse the materials being sputtered from the sample surface. The processes of glow discharge, cathode sputtering and de-excitation with the emission of light in the Grimm source are shown in Figure 2.3 (Bouchacourt and Schwoehrer, 1997). During an analysis, most of the sputtered material is deposited on the inside of the anode tube and the edge of the sputtered crater of the sample. After the analysis, the deposited materials inside the tube must be removed by a high speed drill.

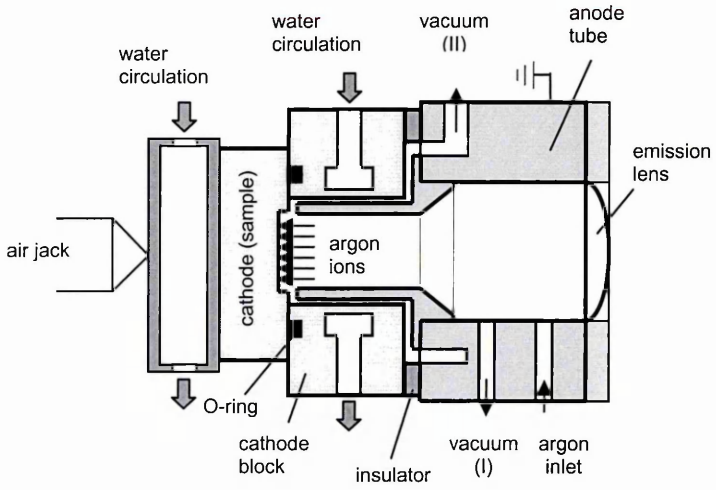

Figure 2.2. A schematic cross-section of the Grimm source

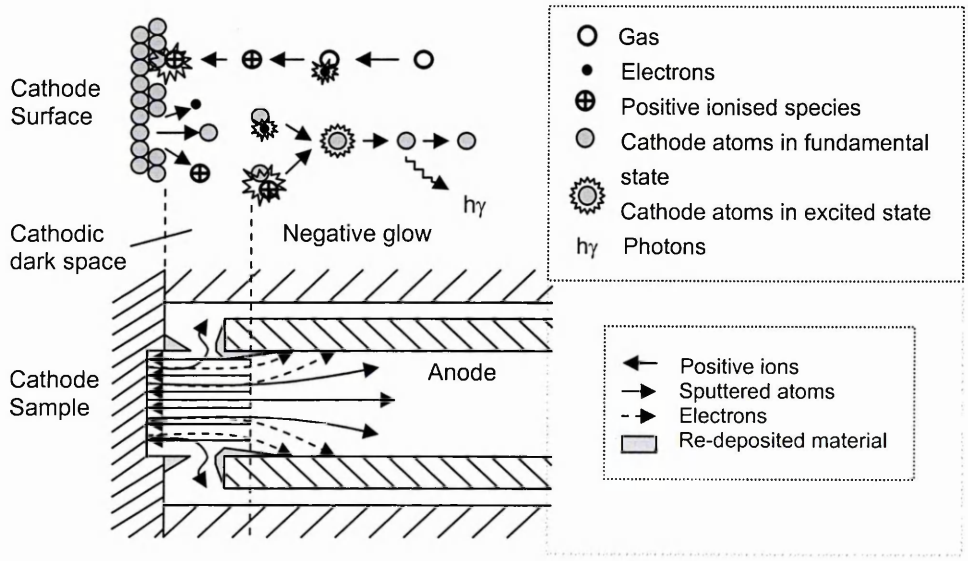

Figure 2.3. Schematic diagram of the glow discharge processes, cathode sputtering and de-excitation of the sputtered atoms with the emission of light in the Grimm source (after Bouchacourt and Schwoehere, 1997).

2.2.2 Current-voltage-pressure characteristics of glow discharge source

The glow discharge process and hence the sputtering of the cathode (sample) can be controlled by three operating parameters: voltage, current and gas pressure from outside of the source. In the abnormal glow region, the maintaining voltage U_g, i.e. the voltage between the anode and the cathode, is given by Weston (1968) as

$$U_g \approx U' + i_g R_g \ , \qquad (2.1)$$

where U' is the turn-on potential; i_g is the source current and R_g is the source resistance. No current flows until U_g exceeds U'. Comparing the effects of the gas pressure (P_g), cathode area and distance between the anode and the cathode, Eqn. (2.1) can be expressed in the GDOES system by (Payling, 1994 a and 1997a) as

$$U_g \approx U' + \frac{4k' i_g^a}{\pi D^m p_g^b} \ , \qquad (2.2)$$

where k' is a constant relating to the distance of anode to cathode; a is a constant between 1and 2; m and b are both approximately 2 and D is the inside diameter of the anode. Most of the constants in the equation appear to be dependent on the sample matrix. However, the three parameters, voltage, current and argon pressure, are not independent of each other. If two of the three parameters are kept constant, the third one will find its own value depending on the cathode matrix. In theory, the source can only work under the one of three operating modes: with either current, voltage or argon pressure as a variable. Figure 2.4 shows the current-voltage-pressure characteristics of the source operating with a steel sample. In practice, all of the three operating modes have been applied in GDOES measurements. For example, the mode of variable current could be used in a bulk analysis because of the rapid cleaning of the sample during a pre-burn which is required to remove surface contamination of the sample prior to analysis, and the mode of variable argon pressure is becoming increasingly important in quantitative analyses following improvements in quantitative theories of GDOES. Which mode is optimal will depend on the application and samples to be analysed (Bouchacourt and Schwoehrer, 1997).

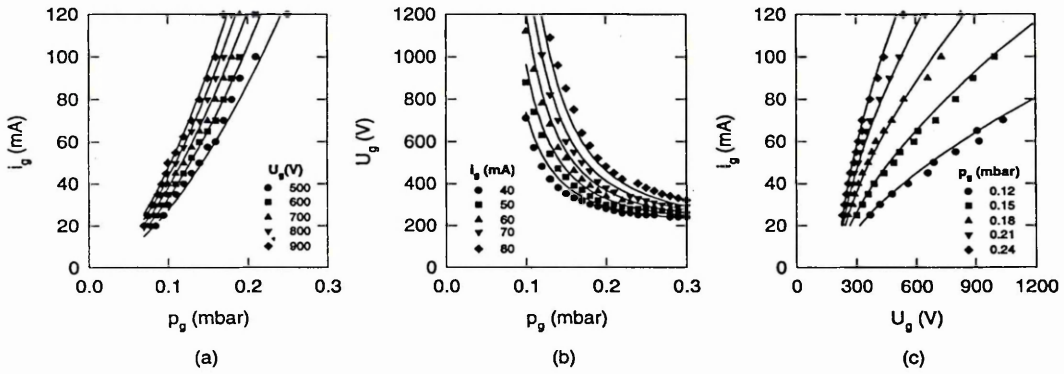

Figure 2.4. The current-voltage-pressure characteristics of the Grimm source in GDOES using steel as the cathode sample (Payling, 1994).

2.2.3 Instrumentation of GDOES

Figure 2.5 shows a schematic layout of the GDOES instrument used in the work presented in this thesis (Leco Corporation, 1992). The emitted photons pass through the window of the source, which is capable of transmitting photons in the wavelength range of 110–800 nm, and then into the optical spectrometer through an entrance slit. The photons with different characteristic wavelengths (and hence energy) are converted into intensity signals by the photomultiplier tubes in the spectrometer. The intensity signals for the elements to be analysed can be converted into elemental concentrations of the sample (for bulk analysis), or into the elemental concentrations as the function of sputtered depth (for depth profiling analysis), based on GDOES bulk or depth profiling calibration procedure using certified reference samples with known compositions and sputtering rates.

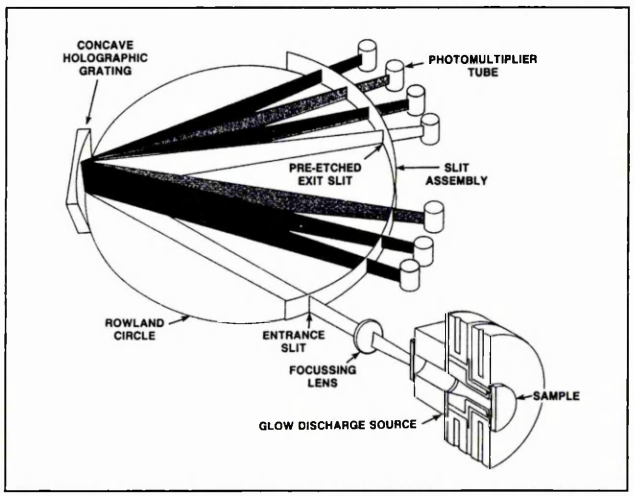

Figure 2.5. Schematic layout of the GDOES instrument used in this study.
(Leco Corporation, 1992)

There are two kinds of spectrometer. The first is a polychromator, with many fixed channels. It can record many elemental signals simultaneously. Another is a monochromator. It has only one channel but is tuneable over a wide wavelength range. The GDOES (Leco GDS 750), which was employed in this study, is equipped with a polychromator which is able to detect 44 individual elements and can analyse 24 elements in a single measurement.

2.3 Glow Discharge in GDOES

2.3.1 Structure of the glow discharge

Discharge is a breakdown phenomenon in a conducting ionised gas. In a voltage-current characteristic of gas discharges, as shown in Figure 2.6 (Wagatsuma, 1997), when the voltage increases to U_b, called the breakdown voltage, the discharge current increases rapidly and a dark discharge (region A-B) is produced. Gas discharge is a self-sustaining process. Initially electrons accelerate and collide with gas particles causing ionisation of the gas. The resultant charged particles can also contribute to the ionisation collision. When the discharge current is increased further, the voltage decreases and reaches a constant value U_n (the region C-D). In such discharges, a zone with visible light in the discharge body can be observed. Glow discharge corresponds to the region D-F, created at reduced pressures of several hundred Pa and discharge voltages of a few hundred volts, with characteristic 'glow', i.e. blue luminance in the case of argon as the carrier gas. The glow discharge can be divided into two regions, i.e. 'normal' glow (D-E) and 'abnormal' glow (E-F). The 'normal' glow discharge has the characteristic that the voltage remains constant as the current is changed by several orders of magnitude (e.g. from 10^{-4} to 10^{-2} A). Under these conditions, the current density at the cathode remains constant, while the area of the cathode covered by the glow expands proportionally with the current. When the cathode is fully covered, an increase in current is necessarily associated with a rise of the current density, so that a

larger cathode emission is required, and this again increases the cathode fall and the potential. The region with the positive characteristic, i.e. where the voltage increases as the current increases, is that of the 'abnormal' glow discharge. In analytical application of GDOES, it is the 'abnormal' glow discharge which is employed as a light excitation source (Boumans, 1972).

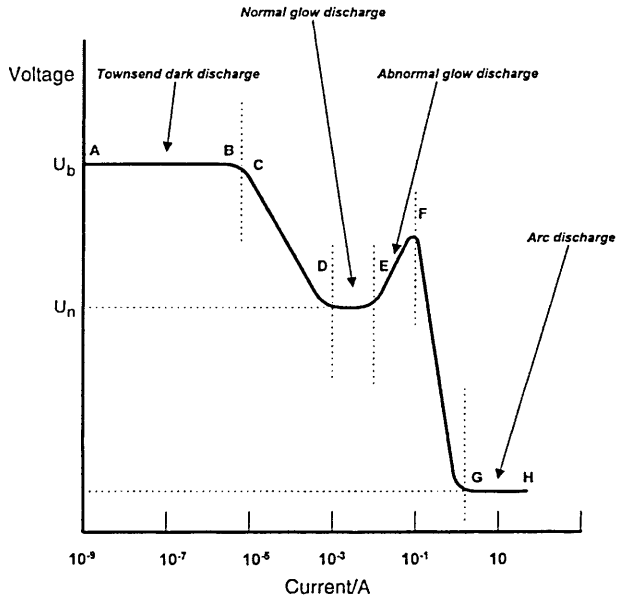

Figure 2.6. Voltage-current characteristic of gas discharges (Wagatsuma, 1997).

Region A-B: dark discharge;
Region C-D: visible light observed in the discharge body with a constant voltage;
Region D-F: glow discharge, which can be divided into two region: a 'normal' glow (D-E) and 'abnormal' glow (E-F). The 'abnormal' glow is employed as a light excitation source in GDOES analysis.

The glow discharge process depends on carrier gas, gas pressure, voltage, current, geometry and electrodes. In particular, the discharge structure may alter depending on the distance between the anode and the cathode. As the space between the electrodes is reduced, the positive column shrinks. When the space is reduced further (the space is just a few times the cathode dark space thickness and the minimum separation is about twice the dark space thickness), the positive column and the Faraday dark space finally disappear whilst leaving the cathode dark space and negative glow unaffected. Such a glow discharge is called the 'obstructed' glow, as described by Chapman (1980) and shown as Figure 2.7(a). This structure of glow discharge is a fundamental structure model of glow discharge, and is just the basic model in the Grimm source in GDOES. As can been seen in Figure 2.7(b), U_p is the plasma potential, which means that the glow region is at a small positive potential. Since a voltage U_g is applied between the

electrodes (the anode is grounded), there is an electric field produced in the cathode dark space, called cathode fall, the potential difference being close to U_g.

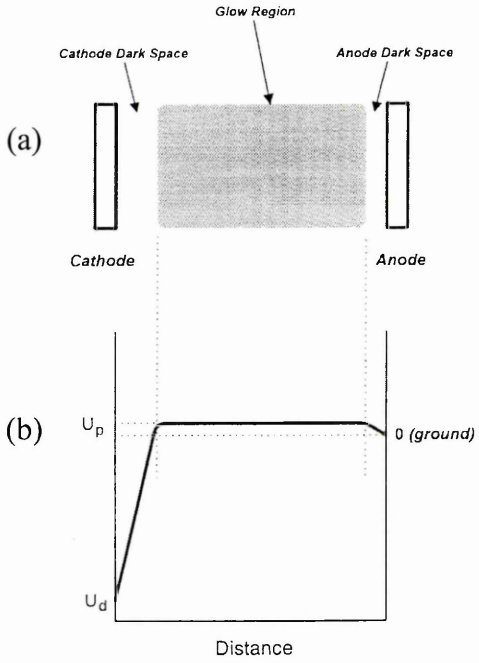

Figure 2.7. (a) The 'obstructed' glow, which is a fundamental structure model of glow discharges and is the basic model in the Grimm source in GDOES. (b) The plasma potential in this model (Chapman, 1980).

2.3.2 Collision processes and behaviour of electrons in the plasma

2.3.2.1 Collision processes

Collision processes in the plasma have been reviewed by Chapman (1980) and Bogaerts and Gijbels (1997), which include the most relevant processes in analytical glow discharges, i.e. ionisation (and recombination) and excitation (and de-excitation), and the plasma species playing a role in these processes: electrons, argon atoms, singly charged positive argon ions, argon atoms excited to a variety of energy levels including metastable levels, and atoms and ions of the cathode material. However, the collision processes are much more complicated, for example the collision processes may involve multiple-charged particles, clusters and negative ions, and probably not all processes are known and understood. Some of the collision processes are believed to play a dominant role and should not be neglected in a full description of the glow discharge of GDOES.

Electron impact ionisation of argon atoms is one of the most important and best-known processes in the glow discharge, simply expressed as

$$Ar^0 + e^- \rightarrow Ar^+ + 2e^- , \qquad (2.3)$$

where Ar^0 and Ar^+ are argon atoms in the ground state and argon ions with a single charge respectively. This collision is the essential process for the plasma being self-sustaining as it produces an extra electron which can ionise other argon atoms. The collision can have two effects: one is the ionisation of argon atoms from the ground level, which needs a minimum energy of 15.76 eV; the other is excitation to the metastable levels at 11.55 eV or 11.72 eV.

The metastable levels of an argon atom are created when energetic particles collide with it. **Electron impact excitation of argon atoms** is expressed as

$$Ar^0 + e^- \rightarrow Ar^* + e^- , \qquad (2.4)$$

where Ar^* is the argon atom in the metastable levels. The minimum energy transferred is 11.55 eV, which is less than the ionisation energy of an argon atom (15.76 eV). Therefore, the energy level is not high enough to eject an electron from the atom but can only excite the electron to a higher energy level within the atom. Sputtered atoms also can be excited to metastable levels. But the metastable argon atom has a longer life-time before it returns to the ground state than the metastable sputtered atoms.

In addition to processes involving argon atoms there are processes involving the analyte (sputtered) atoms. **Electron impact ionisation and excitation of sputtered atoms** are another two important processes in the glow discharge

$$M^0 + e^- \rightarrow M^+ + 2e^- , \qquad (2.5)$$

$$M^0 + e^- \rightarrow M^* + e^- , \qquad (2.6)$$

where M^0, M^+ and M^* represent sputtered atoms in the ground, a single positive charged and excited states, respectively. The mechanisms of these two processes are the same as for the processes of electrons impacting argon atoms. These processes will

depend on the average temperature, density of electrons and cross-section of the excitation. However, since the cross-section curve as a function of the electron energy is of comparable shape and magnitude for all elements, the ionisation and excitation processes are considered as rather unselective. Electron impact ionisation of sputtered atoms can also produce an extra electron for the plasma being self-sustaining. Electron impact excitation of sputtered atoms is one of the two excitation processes for sputtered atoms (the other is metastable argon atom impact excitation of a sputtered atom). Any excitation of the sputtered atom will directly affect its light emission and, hence, the intensity of the element recorded in GDOES analysis.

Metastable argon atom impact excitation of sputtered atoms is of the form

$$M^0 + Ar_m^* \rightarrow M^* + Ar^0 \ . \qquad (2.7)$$

In the glow discharge in GDOES, the metastable argon atoms can also excite the atoms in the source to produce emitted photons.

Penning ionisation involves a process such that

$$M^0 + Ar_m^* \rightarrow M^+ + Ar^0 + e^- \ , \qquad (2.8)$$

where Ar_m^* is the argon atom in the metastable state with energy 11.55 eV or 11.72 eV. Since most of the atoms of the periodic table have an ionisation potential lower than this value, then sputtered atoms can be ionised by collision with argon metastable atoms. Penning ionisation is another important process which results in the production of charged particles. These charged particles can again contribute to ionisation collisions for the self-sustained discharge. Elements that cannot be ionised by Penning ionisation in argon include H, N, O, F, Cl and Br.

2.3.2.2 Behaviour of electrons in the glow discharge

Electrons in the glow discharge in GDOES have been classified into at least three groups (Wagatsuma, 1997), i.e. the γ-electron, secondary electron and slow electron. The γ-electrons are the electrons which are ejected from a cathode surface when argon

ions impact the surface. Their energy is the highest among the electrons in the three groups. After the glow discharge has built up, the γ-electrons are the primary electrons, maintaining the glow discharge to be self-sustaining by collisions with argon and sputtered atoms in order to produce extra electrons which can contribute to the ionisation processes. The secondary electrons are produced from the ionisation processes of argon and sputtered atoms and collide with the argon and sputtered atoms in the plasma to cause the excitation of the atoms. The slow electrons, which are trapped by the plasma potential because of their low kinetic energies, are the largest part of the glow electrons. Electron temperature in the plasma is determined mainly by this group of electrons and is in the range of a few eVs down to 0.1 eV. On the other hand, the electrons are also lost mainly through electron-ion recombination. In fact, the glow discharge is self-sustaining in a balance of the production and reduction of electrons.

The energetic electrons also provide the only mechanism which enables energy coupling from the external power supply to the bulk plasma. The energy in the plasma is lost mainly through heating of the electrodes by energetic particles. In view of the balance of energy in the glow discharge, the lost energy must be compensated for through the energetic electrons in order to obtain a steady state discharge.

2.3.3 Properties of particles in the glow discharge

The particles involved in GDOES include the electrons, the positive ions, the excited atoms and the sputtered atoms. Fang and Marcus (1991) have investigated the properties of particles in the plasma using a single cylindrical Langmuir probe with a computer-controlled voltage driving system. The glow discharge sputtering device has a simple, diode-plane electrodes configuration. Different cathode matrices – copper, copper-zinc alloys, molybdenum, nickel, titanium and stainless-steel were sputtered in discharge conditions with constant current and argon pressure. The current and argon pressure were 8 mA and 2.7 mbar, respectively, at which the glow discharge was believed to be in the abnormal region. Axial distributions and the values of electron temperature, average electron energy, and electron and positive ion number densities in

a particular sampling position have been investigated. In this sampling position, at about 5.4 mm from the cathode, the plasma is quite luminous and the probe disturbs the plasma least.

Particular areas of interest lie within their experimental results about electron temperature, average electron energy, and electron energy distribution due to the relations to the discussion in Chapter 6 on hydrogen behaviours. Their experiments showed that the electron temperature decreased as the current and the voltage increased for the different cathode matrices, which was explained by the contribution of electrons produced by either Penning ionisation of sputtered atoms or electron impact ionisation of sputtered and argon atoms in the negative glow region. The secondary electrons produced by ionisation have quite low kinetic energy relative to the γ-electrons that have gained kinetic energy in the potential fall of the cathode dark space. In the abnormal glow region, the average electron energy increases with the current. However, for the different samples, the average energy values converged to a relative spread of only ~10%. This spread was within the sample-to-sample deviations for the analysis of the same alloys, which means that the cathode matrices have little effect on the average energy. The electron energy distribution functions for the different cathodes in the constant-current operating mode were also very similar.

A combination of different mathematical models for different plasma species in dc glow discharge have been produced by Bogaerts and Gijbels (1997). The models were one-dimensional, i.e. the quantities vary only with distance from the electrodes. For a dc glow discharge in argon with a copper cathode, at typical GDOES discharge conditions, i.e. a gas pressure of 500 Pa, a discharge voltage of 800 V and an electrical current of 40 mA, some typical results of the models were presented, such as density profiles of the plasma species, the electric field and the potential distribution throughout the discharge, different ionisation mechanisms in the plasma, energy distributions of the different plasma species and relative contribution to sputtering. The models are, in principle, also able to predict other quantities of the excitation to different levels and the

intensities of different spectral lines if there are enough cross-sectional data for the computer simulations, which are of interest for the glow discharge in GDOES.

In their further work, three-dimensional models for calculations of density profiles of sputtered atoms and ions (Bogaerts *et al.*, 1997a) and argon metastable atoms (Bogaerts *et al.*, 1997b) in a dc glow discharge have been established. The calculations, based on the models, also included the profile of electrons, the current-voltage characteristics, the flux energy distributions of positive ions, the profile of the sputtered crater on the cathode and the argon atomic optical emission spectrum (Bogaerts and Gijbels, 1998; Bogaerts *et al.*, 2000 & 2001). The calculated results were compared with experimental results obtained by laser-induced fluorescence spectroscopy (for the sputtered atoms, the ions and the argon metastable atoms), and Langmuir probe and optical emission spectrometry measurements (for the electrons). In general, satisfactory agreement has been qualitatively reached for most of the particles except the argon metastable atoms. Although exact quantitative agreement cannot be expected between the mathematical calculations and the experimental data, however, the modelling gives a better insight into the complex glow discharge as a complement to experimental plasma diagnostics.

2.4 Sputtering in GDOES

Most of the work described later in this study is related to sputtering of surfaces of samples in GDOES. Sputtering is the ejection of target atoms following the impact of energetic particles on the target surface. In GDOES, when the argon ions, driven by the negative bias in the dark space, impact the surface of the cathode, sputtering occurs. Figure 2.8 illustrates the interaction of an incident ion with a surface (Chapman, 1980). Generally, when an incident ion impacts on a solid surface, one or all of the following phenomena may occur:

- the ion may be reflected, probably in a neutralised state;
- electrons may be ejected from the surface, usually as secondary electrons (in this

work they are called as the γ-electrons);

- the incident ion may be implanted into the surface;
- the ion impact may be responsible for some structural rearrangements in the target material;
- atoms may be ejected from the surface.

This ejection process of the atoms is known as sputtering. Most ejected atoms (95–99%) are neutral, especially when the target material is a metal. It is these atoms which are normally analysed in GDOES.

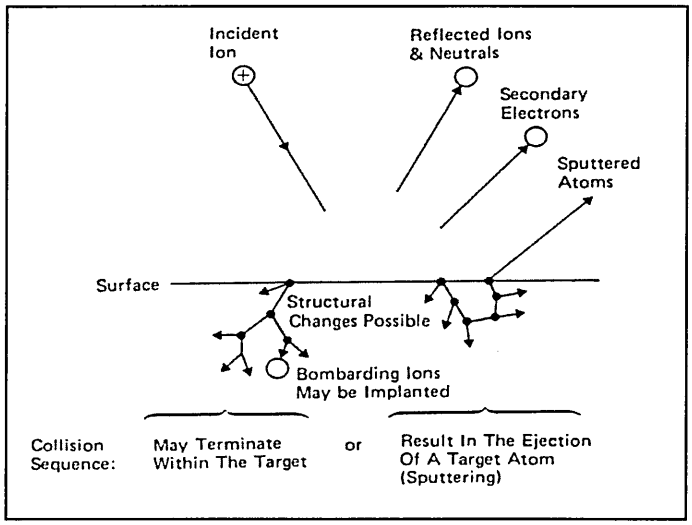

Figure 2.8. A diagrammatic sketch of interaction of an incident ion with cathode surface (Chapman, 1980).

2.4.1 Sputtering models

Sputtering theory has been reviewed by Payling (1994b and 1997b). The simplest model of sputtering is based on single elastic collisions, which was developed by Stark in 1909 (Payling, 1994b). In a simple binary collision the energy transferred from the incident particle to the target particle is given by Chapman (1980) as

$$\frac{E_t}{E_i} = \frac{4m_i m_t}{(m_i + m_t)^2}\cos^2\theta \ , \qquad (2.9)$$

where E_t is the energy transferred to a target in a single collision; E_i is the energy of an incoming particle; m_i and m_t are the masses of the incident and target particles, respectively; θ is the angle of velocity of the incident ion to the line joining the centre of

m_i and m_t at the moment of collision. Therefore, for a head-on binary collision, Stark determined a minimum threshold energy for sputtering, E_0, given by

$$E_0 = \frac{(m_i + m_t)^2}{4 m_i m_t} U_s \ , \qquad (2.10)$$

where U_s is the latent heat of sublimation, a measure of the energy required to break the surface atomic bond. U_s is typically 3-9 eV (Kaminsky, 1965), and for argon m_i = 40 amu, then m_t/m_i varies from 0.1 to 5. So E_0 in the Stark model typically varies from 3 to 20 eV.

In fact, the sputtering process is much more complex than the binary collision model. A single binary collision will only produce forward scattering of the target atom and not back-scattering as required for sputtering. Thus, following the initial binary collision between the incoming ion and the target atom, Langberg (1958) improved Eqn. (2.10) by multiplying E_0 with a factor L, which included the ejection of a near-neighbouring atom,

$$L = 10(1.1\frac{N}{n} + 0.2)(1 - \frac{1}{ad}\ln(1 + 0.83N^{\frac{1}{2}}))^{-2} \ , \qquad (2.11)$$

where N is the number of bonds of an atom in the lattice; n the number of nearest neighbours; a the Morse potential constant and d the closest-neighbour spacing. For most elements, the average value of L = 16 ± 3 (2 SD). Calculated values for the minimum threshold energy E_0 in the Langberg model vary form 31 eV for lead up to 152 eV for aluminium, and are typically around 100 eV (Payling, 1997b).

Sigmund (1969) presented a more rigorous theory for ion beam sputtering. In the Sigmund approach, a series of binary collisions occurs between the incident ion and the atoms in the target, causing multiple scattering of target atoms, and subsequent ejection of a neighbouring atom(s). Furthermore, Sigmund classified sputtering qualitatively by three regimes: single-knock-on regime, linear cascade regime and spike regime, as illustrated in Figure 2.9. In the single-knock-on, the atoms may be ejected from the target surface directly if the energy of the atom is enough to break down the binding

forces of the surface. In the linear cascade and spike regimes, the recoil atoms get the energies from the impact ions, which are enough to produce secondary and higher-generation recoils. Some of them may overcome the surface barrier and be ejected from the target surface. The difference between the linear cascade and the spike regimes is that the spatial density of moving atoms in a linear cascade is small but in the spike it is large.

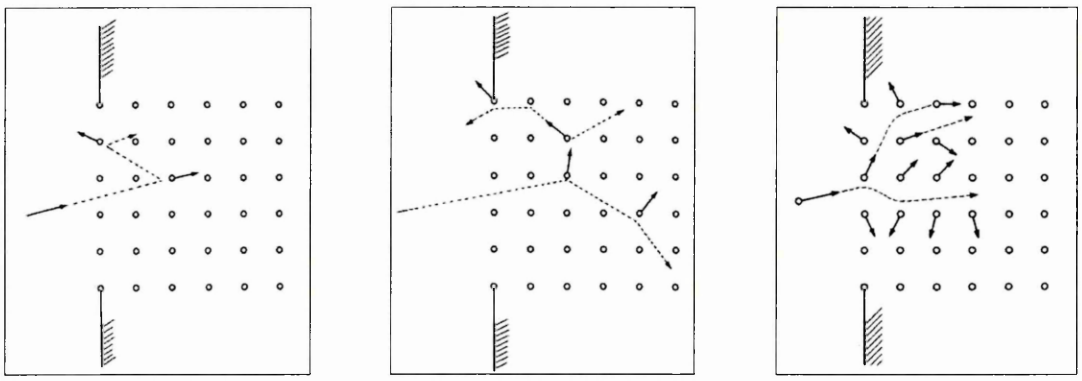

Figure 2.9. Three regimes of sputtering classified by Sigmund (1981):
(a) Single-knockon regime.
(b) Linear cascade regime.
(c) Spike regime.

2.4.2 Sputtering yield and sputtering rate

The sputtering yield S is defined as the number of sputtered atoms per incident ion, and the sputtering rate q is defined as the sputtered mass per second (μg sec^{-1}). For sputtering in the Grimm source of a GDOES system, the ion current is related to the total current by

$$i^{+} = \frac{i_g}{1+\gamma} , \tag{2.12}$$

where i_g is the glow discharge current (A); γ is the secondary electron yield (i.e. the number of extra electrons produced per incident ion). Then the sputter yield and the sputtering rate are related by (Boumans, 1972)

$$q = S\frac{i_g}{1+\gamma}\frac{m_t \times 10^6}{eN_A} , \tag{2.13}$$

where, m_t is the atomic mass of the sputtered atom; e the electronic charge (C); and N_A the Avogadro number (mole^{-1}). In most cases, $\gamma = 0.14 \pm 0.11$ (2SD), so that $(1 + \gamma)$ varies by only about ±10% for most elements and is often ignored (Payling, 1997b).

In the Langberg model of sputtering, sputter yield is quadratic at energies near E_0 and linear at higher energies. For energies $E >> E_0$ and normal incidence, the sputter yield was given as (Payling, 1997b)

$$S = b(E - E_0) \ , \tag{2.14}$$

where b is a constant and E the incident energy. Therefore, the sputter yield, in the Langberg theory, is related to the energy above the minimum threshold energy.

The sputtering yield was given, in the Sigmund theory as (Payling, 1997b),

$$S = \frac{3}{4\pi^2}\alpha(\frac{m_t}{m_i})\frac{S_n(E)}{U_s} \ , \tag{2.15}$$

where $\alpha(m_t/m_i)$ is an energy-independent function and varies form ~0.1 to >2 depending on the ratio m_t/m_i; $S_n(E)$ is the nuclear stopping cross-section and U_s is the binding energy of the target material. For incident energies below about 1 keV, which are the energies of interest in GDOES, but well above the threshold;

$$S_n(E) = \frac{4m_i m_t}{(m_i + m_t)^2}E \tag{2.16}$$

Therefore, in the Sigmund theory, the sputtering yield is proportional to incident energy rather than to the energy minus threshold value.

In the non-linear regime, experimental work showed that sputtering yields changed in a complex way with incident ion energy. In the range 50–150 eV, the sputtering yield is roughly quadratic with energy. In the range 150–250 eV, the sputtering yield is approximately linear with energy, and above 250 eV, it begins to bend over and eventually reaches a saturation level and then falls at much higher energies (Payling, 1994b). Therefore, the linear portion of Sigmund's theory does not extend as high in

energy as was originally envisaged. Matsunami *et al.* (1980) altered Sigmund's expression of the sputtering yield by considering the different dependence of sputtering yield on incident energy and gave the sputtering yield which could apply to both the near-threshold and linear regions by

$$S = S_{Sigmund}(1-(E_0/E))^{1/2} \tag{2.17}$$

They also found it necessary to include higher order terms in their equations and derived a sputtering yield equation as

$$S = 0.042\alpha^*(\frac{m_t}{m_i})\frac{S_n(E)}{U_s}\left[1-(E_0/E)^{1/2}\right]^N , \tag{2.18}$$

where N ≈ 2.8 (Payling, 1994b), and for argon ions in GDOES

$$\alpha^* \approx 0.257\left(\frac{m_t}{m_i}\right)^{0.4} \tag{2.19}$$

and

$$S_n(E) \approx 4.785\frac{4m_i m_t}{(m_i+m_t)^2}E^{1/2} \tag{2.20}$$

In the context of GDOES, the most important investigation of the sputtering yield and sputtering rate could be the work produced by Boumans (1972), which introduced a simple and well-known empirical relationship between the sputtering rate and the glow discharge current and voltage in the Grimm source of the GDOES system:

$$q = C_Q i_g (U_g - U_0) , \tag{2.21}$$

where C_Q is the reduced sputtering constant (μg watt^{-1} sec^{-1}); i_g the discharge current; U_g the operating voltage; and U_0 the threshold voltage for cathode sputtering. C_Q and U_0 depend on the cathode material and the plasma gas but are independent of the current, the voltage and the gas pressure. The Boumans equation now forms an essential part in the understanding, calibration, bulk analysis and depth profiling of GDOES. In his work, the experimental results of some pure metals and binary alloys showed that a linear relationship between the mass sputtered in unit time per unit of current strength (q/i_g) and the operating voltage (U_g) was established for both metals and alloys. The

reduced sputtering constant C_Q (i.e. slope of the linear relationship) for some pure metals and alloys is listed in Table 2.1.

Table 2.1. *Results of sputtering measurements for metals in the Grimm glow discharge with argon as a carrier gas (Boumans, 1972).*

Target	C_Q (μg W^{-1} sec^{-1})	U_0 (V)	i_g (mA)
Al	0.084	340	213-320
Cu	0.84	360	24-260
Mo	0.39	300	48-213
Ni	0.36	360	48-260
Ta	0.81	320	108-213
W	0.79	320	108-213
Zn	1.64	330	24-72
Brass	1.08	340	24-213
Cu-Ni	0.58	365	24-108
Cr-Ni-Steel	0.24	520	48-108

This linear relationship was confirmed in the experimental work by Bengtson (1985) by measurements of the sputtering rates with different materials. The results are listed in Table 2.2. Comparing the results of U_0 in Tables 2.1 and 2.2, the threshold voltages U_0 obtained by Bengtson were generally lower than those of Boumans. This was believed to be due to slight differences in the geometry of the individual source.

Table 2.2. *Experimental data of C_Q and U_0 of some pure materials and alloys (Bengston, 1985).*

Target	C_Q (μg W^{-1} sec^{-1})	U_0 (V)
Al	0.099	340
Fe	0.25	330
Cu	0.81	290
CuNi10	0.75	300
CuZn30	0.90	285
CuZnNi25/10	0.80	290
Sn	1.70	240
Zn	0.81	180
Cu_2O	0.61	320

Payling and Jones (1993) measured the sputtering rates of zinc-iron and zinc-aluminium alloys and concluded that, for pure elemental solids, U_0 varies from 220 V for chromium to 340 V for aluminium, and averages 308 ± 66V (2 SD) for 25 published values of metals and alloys. Payling (1994a) also calculated the turn-on voltage U' by multiple linear regression of the data from steel, copper and aluminium standards. The estimated values of U' vary from 205 V to 265 V, i.e. a range of 235 ± 30 V. He suggested that the threshold voltage U_0 in the Boumans equation is thus a sum of the turn-on voltage U' and a minimum voltage above U' for sputtering. As $U' \approx 235$ V and the average of U_0 is 308 V, this suggests that the minimum voltage for sputtering is ~73 V. From the equation of the incident ion energy related to voltage in GDOES (Payling, 1994a), which was obtained by regression of the experimental data by Suzuki (1988)

$$E = k(U_g - U') \,, \tag{2.22}$$

where k and U' are both constant with k = 0.5. The minimum sputtering voltage ~73 V corresponds to ~37 eV of incident energy, which is sufficient to break atomic bonds at the target surface and cause sputtering.

Equation (2.21) was also confirmed by Payling (1994b) by measurements of the sputtering rates with copper alloys. The review and the experimental data in (Payling, 1994b) suggested that the argon gas pressures in the source have no effect on the sputtering rate. It was also noted that in the experiments (Boumans, 1972) the sputtering time was kept constant, which would then result in different sputtered depths for different matrices. By keeping the sputtered depth constant, rather than the sputtering time, the experimental data in (Payling, 1994b) indicated that the sputtering rate is still proportional to the current i_g, but no longer to the U_g when the sputtered depth is in a range of 5–10 μm. Based on the non-linear dependence of sputtering with the operating voltage in the glow discharge, which was presented by Yamamura *et al.* (1983), Payling (1994b) altered the Boumans equation (2.21) as follows

$$q = C_Q i_g \left(U_g - U_0\right)^n \,, \tag{2.23}$$

where U_0 and n are constants, which were obtained by fitting the experimental data from copper alloys, stainless steels, nickel and the Boumans data to Eqn. (2.23). These values are listed in Table 2.3 and show a mean value for U_0 of 396 V, and n of 0.74.

Table 2.3. *Results of fitting data to Eqn. (2.23) (Payling, 1994b).*

Matrix	Data points	U_0 (V)	n	R^2
Copper alloy (i_g 40mA)	8	399	0.75 ± 0.02	0.9990
Copper alloy (i_g 60mA)	8	397	0.73 ± 0.02	0.9994
Stainless	9	364	0.74 ± 0.01	0.99992
Nickel	7	424	0.74 ± 0.04	0.998
Mean		396 ± 49	0.74 ± 0.02	
Zinc(Boumans)	5	373	0.72 ± 0.01	0.99995

The experimental data (Payling, 1994b) showed that the sputtering rate increased with sputtered depth in GDOES. Mechanisms for the changes with depth were explained by:

- The greater depth means that the sample surface is effectively further from the anode, and anode-to-sample spacing will affect the sputtering rate;
- The gas temperature near the target can be expected to increase with sputtering time. This will alter the plasma density near the target, hence the number of collisions and thus the impact energy; and
- During sputtering, material deposits on the sample surface opposite the annulus of the anode. This deposited material affects the argon flow by restricting the gap and therefore the pressure inside the anode, which in turn may affect the sputtering rate by changing the discharge conditions.

2.5 Quantification Procedure in GDOES

2.5.1 Quantitative theory

Some of the GDOES measurements described later in this study have been performed using the quantification procedure for GDOES in order to obtain information of

quantitative depth profiles of samples. When a measurement is made in GDOES, there are three processes involved in generating the analytical signal: 1) the supply of sputtered atoms; 2) excitation followed by de-excitation to emit photons of the sputtered atoms and 3) detection of the emitted photons. It is usually assumed that these processes are independent (Payling, 1997a). Therefore the recorded signal for a given emission line from element i is given by

$$I_i = k_i e_i q_i \ , \tag{2.24}$$

where q_i is the sputtering rate of element i, which represents the supply rate of the element into the plasma; e_i represents the emission process; and k_i is the instrumental detection efficiency.

The sputtering rate is defined as sputtered mass of the element per unit time, and will vary with the concentration c_i of the element i in the sample and with overall sputtering rate q of the sample,

$$q_i = c_i q \tag{2.25}$$

The emission term e_i can be described as

$$e_i = S_i R_i \ , \tag{2.26}$$

where S_i is a correction of self-absorption of the emitted photons in traversing the plasma to reach the source window; R_i is the emission yield, defined as the number of photons emitted per sputtered atom entering the plasma (Takadom *et al.*, 1984).

For a recorded elemental signal in GDOES, it should also include a background term, which is an intercept of a calibration curve (in concentration *vs.* intensity) on the axis of elemental intensities. After considering a background term b_i (Payling *et al.*, 1994), the recorded signal can be presented by

$$I_i = k_i S_i R_i c_i q + b_i \tag{2.27}$$

By assuming the signals from all of the elements with significant concentrations in a sample are recorded, i.e.

$$\sum c_i = 1 \ , \qquad (2.28)$$

all of the concentrations at a depth where the signals were recorded and the instantaneous overall sputtering rate q could be obtained through solving Equations (2.27) and (2.28) simultaneously.

2.5.2 The concept of emission yield in GDOES quantification

The emission yield term R_i, in Eqn. (2.27), which was first proposed by Takadom *et al.* (1984), is probably the most important term in GDOES quantitative analysis. The emission yield concept is based on the fact that the emission intensity of a spectral line in a glow discharge source is proportional to the sputtered mass of the corresponding element and is independent of the sample matrix (Payling and Jones, 1997). Experimentally, independence of the emission yield on the matrix has been investigated by Takadoum *et al.* (1984) with Zn-Fe alloys of different composition and by other authors (Pons-Corbeau, 1985; Takimoto *et al.*, 1987; Bengtson and Lundholm, 1988), and is now widely accepted to be valid.

The first application of the emission yield concept in GDOES depth profiling quantification is known as the integrated emission intensity method (IEI) by Takimoto *et al.* (1987). The emission yield of a spectral line of each element is experimentally obtained beforehand. From the emission yield concept there is

$$I_i = (\delta w_i / \delta t) R_i \ , \qquad (2.29)$$

where δw_i is the sputtered mass of an element i during a time increment of δt. Eqn. (2.29) is equivalent to Eqn. (2.24). The self-absorption S_i will vary depending on the elemental sputtering rate and can be neglected when $c_i q$ is small. Fortunately S_i is not a major factor in the GD source (Payling, 1997a and Bengtson, 1997a).

From Eqn. (2.29), the spectral intensity per unit sputtering time of an element in an analysed sample is directly converted into sputtered mass. The total sputtered mass in sample segment b in the unit sputtering time, δW_b, is given by

$$\delta W_b = \sum_i \delta w_i \qquad (2.30)$$

Then the elemental concentration (in weight percent) of an element i in the corresponding sputtered segment b can be expressed as

$$c_i = (\delta w_i / \ \delta W_b)100 \ , \qquad (2.31)$$

and the sputtered depth corresponding to the segment b can also be determined from the total sputtered mass as follows

$$\delta d_b = k \, \delta W_b / \ \rho_b \ , \qquad (2.32)$$

where δd_b is the sputtered depth; k is a geometrical conversion factor; and ρ_b is the density of the sample in the segment b. For the calculation of the sputtered depth, the density of analysed sample is also required. The density can only be obtained based on the information on the composition of the analysed sample, which is already obtained by Eqn. (2.31).

2.5.3 Differences between analyses of bulk and multi-matrix samples

The basic information obtained in a GDOES measurement is the signal intensity of elements in the measured sample against sputtering time. To obtain the elemental concentrations at a sputtered depth or variations of the concentrations as the function of sputtered depth, a calibration for GDOES must be done using a set of certificated reference materials (CRM) with known chemical compositions and sputtering rates.

For an analysis of a bulk sample, a set of CRMs with similar compositions (matrix) as analysed samples are generally needed. The parameters (voltage, current and argon pressure) used for the calibration burns must be the same as that in the analysis measurement. In bulk analysis in GDOES, only corrections for the temporal variations of the parameters of the source, the sputtering rate and the emission yields from sample to sample are necessary. This can be done by use of the ratio intensity of an element to an internal standard signal (Nelis, 1997). In theory, any signals which have a linear response to the variation of elemental intensities could be used as the internal standard, such as a spectral line of the major element or total emission of light, both of which

have been proven successful (Hunault and Bailly, 1990). Emission of an argon line was used as the internal standard in the multi-matrix quantification procedure (Bengtson, 1994), and the accuracy and precision of elemental determinations can be improved by taking the ratio.

When GDOES is applied to quantitative depth profiling for a coating sample, there are some differences compared to the bulk analysis (Bengtson, 1994):

- Coated samples normally contain a wider range of elemental concentrations in the coating and the substrate than homogeneous samples, which results in the selection of CRMs with very different compositions. So elemental intensities of the CRMs could be affected by the variation of sputtering rates of the CRMs;
- The matrix composition of analysed samples must vary as the sputtering penetrates through the interface between the layer and the substrate. So it is impossible to use a major elemental line as an internal standard with this multi-matrix problem;
- The parameters of the glow discharge source, the voltage, the current and argon pressure could change during sputtering through the layer to the substrate, due to parameters dependent on the sample matrix. This change also needs to be taken into account in the depth-profiling calibration;
- To calculate the sputtered depth in depth profiling analysis, the sputtering rate and the density of the analysed sample also need to be known.

2.5.4 The intensity normalisation quantification method of GDOES analysis

The intensity normalisation method for quantitative analysis in GDOES was developed at the Swedish Institute for Metals Research (SIMR) by Bengtson *et al.* (1994 and 1997b), and this is also used by the GDOES (Leco GDP 750) used in this study. The difference between this method and the emission intensity integration method is that the concentration of an element in the analysed sample is obtained from calibration curves as for bulk analysis, rather than from the ratio of sputtered mass of an element to the

total sputtered mass from the analysed sample. In practice, there are two different sorts of intensity normalisations:

(1) Normalisation of measured intensities from calibration samples to a reference sputtering rate in calibration procedure, that is

$$I_{im}(normalized) = I_{im} q_{ref} / q_s \,, \tag{2.33}$$

where I_{im} is the emission intensity of the spectral line m of an element i; q_{ref} and q_s are sputtering rates of a reference matrix (e.g. pure iron) and a calibration sample, respectively.

(2) Normalisation of measured intensities from analysed samples to reference excitation conditions (the voltage and the current) in an analytical measurement, that is

$$I_{im} = k_{im} c_i C_{Qb} i^{A_m} f_m(U), \tag{2.34}$$

where I_{im} is the normalised emission intensity of the spectral line m of an element i; k_{im} is an atomic- and instrument-dependent constant characteristic of the spectral line m of the element i; c_i is the concentration of the element i; C_{Qb} is a constant related to the sputtering yield of the material; in the term of i^{Am}, i is the excitation current, A_m is a matrix-independent constant, characteristic of the spectral line m only; and $f_m(U)$ is a polynomial of degree 1–3, also characteristic of the spectral line m, and given by

$$f_m(U_g) = a_0 + a_1 U_g + a_2 U_g^2 + a_3 U_g^3 \tag{2.35}$$

The A_m constants, and $f_m(U_g)$ for a large number of spectral lines have been measured by several laboratories with generally good inter-laboratory agreement (Bengtson, 1997c).

The quantitative procedure for GDOES depth profiling analysis in the intensity normalisation method is summarised in Figure 2.10. The true elemental concentrations need to be calculated by a sum normalisation of total elemental concentration determined by the calibration curves to 100% due to the intensities in the calibration curves having been normalised using the ratio of sputtering rates of q_{ref}/q_s. Meanwhile, the relative sputtering rate of the analysed sample to that of pure iron can also be obtained by the sum normalisation.

In order to obtain the corresponding sputtered depth, the real sputtering rate and the density of the analysed sample have to be known. Since the relative sputtering rate of the analysed sample to that of pure iron is obtained by the sum normalisation, the only information that needs to be known is the sputtering rate of pure iron at the actual excitation voltage and current which are used in the measurement of the analysed sample. For calculation of the sputtering rate of pure iron, the Boumans equation (2.21) has been employed in the method to provide a reliable solution. The density of analysed sample can only be calculated based on the information of the composition of the analysed sample, which is already obtained from the depth profiling measurement in GDOES. Böhm (1997) summarised four different ways to calculate the density by the elemental composition of the analysed sample (Böhm, 1997):

- the density is based on the mass percentage of the constituent elements

$$\rho_1 = \sum(c_i \rho_i) \tag{2.36}$$

- the density is based on the atomic percentage of the constituent elements

$$\rho_2 = \sum(n_i \rho_i) \tag{2.37}$$

- the density is based on a concept of constant atomic volume

$$1/\rho_3 = \sum(c_i / \rho_i) \tag{2.38}$$

- the density is based on the weighted densities of ρ_1, ρ_2, and ρ_3

$$\rho_4 = a\rho_1 + b\rho_2 + c\rho_3 \tag{2.39}$$

In Eqns. (2.36)–(2.39), ρ_1, ρ_2, ρ_3, and ρ_4 are the calculated densities in the different ways respectively, ρ_i is the density of a pure element i, c_i and n_i are fractions of the element i in mass percentage and atomic percentage, a, b and c are weighting factors. In the SIMR method, Eqn. (2.37) has been used to calculate the densities of analysed samples. It is believed that the density ρ_2 based on the atomic percentage provides very good results for many alloys, especially for oxides (Böhm, 1997). ρ_1, ρ_2, and ρ_3 were experimentally compared by Payling (1997c) using 50 metal alloys, 10 oxides and 10 organic materials. The overall results showed that the best approach was ρ_3 based on the constant atomic volume, slightly ahead of atomic fraction with mass fraction an

unsatisfactory third. The best results were obtained for metal alloys with relative errors less than 2%, but worst results for oxides with errors of about 40%.

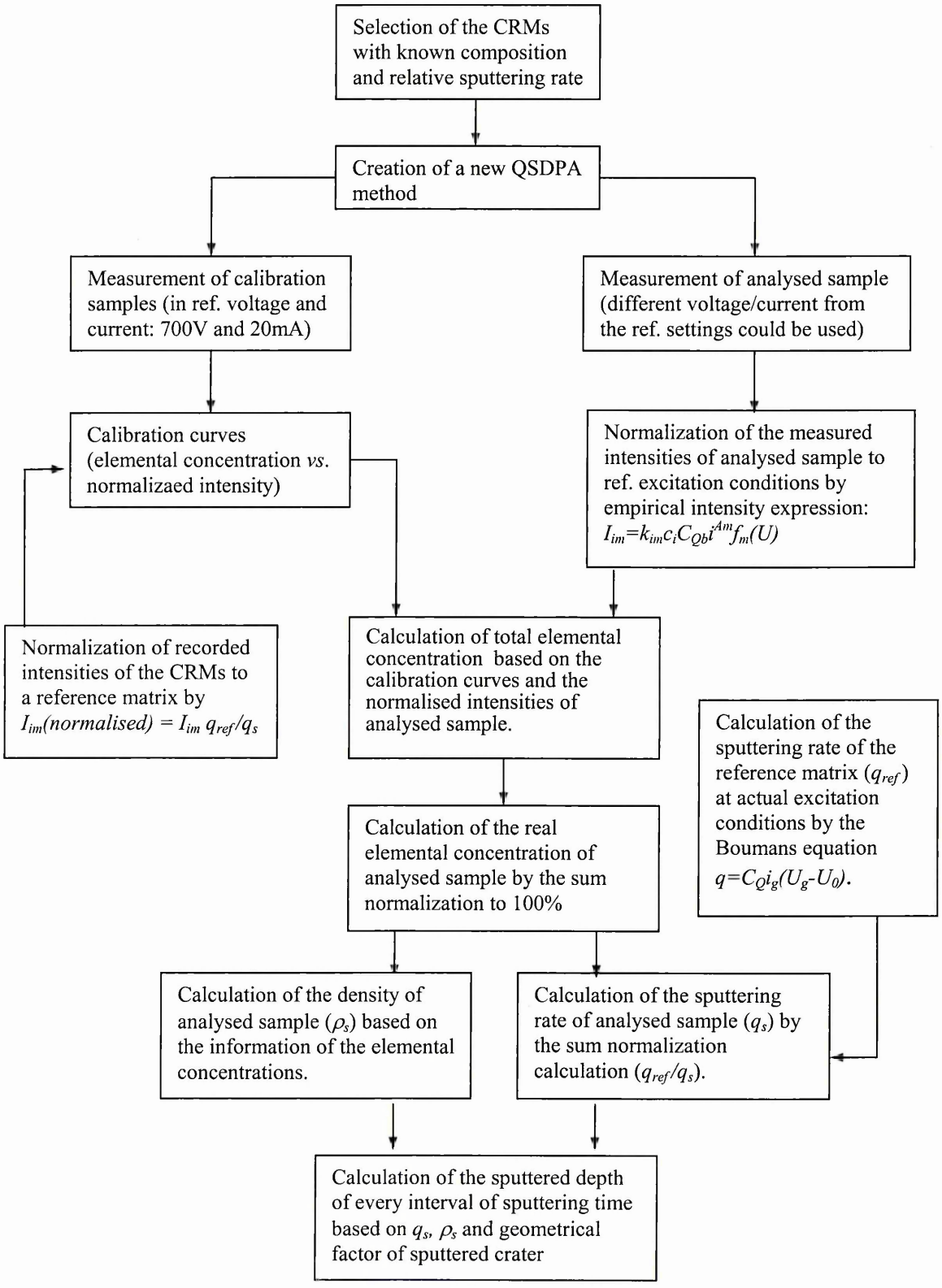

Figure 2.10. Flow chart of the quantification procedure in the GDOES used in this study, based on the intensity normalisation method for quantitative analyses in GDOES developed by Bengston *et al.* (1994 and 1997b).

2.5.5 Other investigations in GDOES quantification

2.5.5.1 Operating parameters' effects on the emission yield

Although the emission yields in GDOES are considered to be nearly matrix-independent quantities, it is a well-known fact that they do vary significantly with the excitation conditions. The excitation processes in the glow discharge source are determined by the operating conditions, which are the current, the voltage and the argon pressure of the source. During measurements of calibration and analysed samples in GDOES, the operating parameters could vary from sample to sample, even from layer to layer in one sample, because the parameters are not independent of each other: two of them are selected, and the third one will find its own value dependent on the sample matrix. The resulting variations of the emission yields must then be taken into account in a complete quantification model. There are various combination modes of operating parameters in calibration and analysis. Two of them are typical regarding the parameter effects. One is the mode of constant power and argon pressure, in which it is believed that the pressure is the only significant parameter affecting the emission yield (Payling and Jones, 1993a, 1993b). The other is the mode of constant voltage and current, in which it is assumed that the voltage and current have significant effects on the emission yields but the pressure does not (Bengtson, 1994 and Bengtson *et al.*, 1999).

Bengtson and Hänström (1998) have investigated the emission yield of Si using the 288.2 nm spectral line with three different matrices of steel, brass and aluminium for various operating conditions. The results showed that, compared to pressure, the current and the voltage have a considerably larger influence on the emission yield. The emission yield was found to increase with the current and decrease with voltage and pressure. For the investigated Si 288.2 nm line, it is concluded that the influence of pressure is nearly negligible within a normal operating range of discharge parameters.

The effects of experimental parameters on the emission yields have also been investigated by Marshall (1999). In this investigation, a multi-matrix calibration was

performed for constant voltage and current mode (VC mode) and constant power and pressure mode (PP mode) with 32 standards in four matrices: iron, copper, zinc and aluminium. Concentration for each standard, multiplied by the standard's known sputter rate, was then plotted against the average signal intensity recorded for that standard. Root-mean-square (RMS) errors of the linear least-squares curve fit in both operating modes for 15 elements, listed in Table 2.4, indicated that the VC mode was always at least as good as, and usually better than, the PP mode. The actual analytical results obtained from four check standards in both the VC and PP operating modes also indicated that the VC mode obtained significantly more accurate results on three of the four check standards; only on the iron standard is there little difference.

Table 2.4. *Comparison of multi-matrix calibrations between VC and PP operating modes.*

Element	Wavelength (nm)	VC RMS error (normalised mass%)	PP RMS error (normalised mass%)	PP/VC
Al	396.15	1.0	4.7	4.7
C	165.70	0.0044	0.0087	2.0
Cr	425.43	0.017	0.072	4.2
Cu	327.39	0.29	2.6	9.0
Fe	371.99	1.9	2.2	1.2
Mg	383.82	0.16	0.22	1.4
Mn	403.44	0.090	0.20	2.2
Mo	386.41	0.0021	0.0029	1.4
Ni	341.48	0.075	0.097	1.3
Pb	405.78	0.019	0.025	1.3
Si	288.15	0.021	0.074	3.5
Sn	317.50	0.027	0.032	1.2
Ti	337.27	0.0092	0.0093	1.0
V	318.54	0.0010	0.020	20.0
Zn	334.50	0.72	2.3	3.2

Payling *et al.* (1995) also compared the effects of operating mode on the emission yield using a set of steel and zinc-aluminium alloy standards for three different quantitative methods: the SIMR method, the IRSID method (invented separately by Cazet and

Hocquaux at the Institut de Recherches de la Sidérurgie Française) and the BHP method (Payling and Jones, 1993). In their investigation, a constant current was chosen for all of the three methods. Therefore, for the SIMR method, a constant current and a constant pressure with an emission yield correction for variation of the voltage was used; for the IRSID method a constant current and a constant voltage with variable pressure was used, and for the BHP method a constant current and a constant pressure without correction for variations of the voltage was used. The normalised emission yields, instead of the emission yields themselves, were calculated for the steel and the zinc-aluminium standards using the three methods at the chosen operating modes, and compared with a simple calibration curve using a constant current and a constant pressure without any corrections (i.e. no corrections for the sputtering rates and emission yields). Relative standard deviations (RSDs) for the normalised emission yields of some elements in the steel and the zinc-aluminium standards, listed in Table 2.5, indicated that for Mn, Ni and Cu in steel it is possible to get good workable calibration curves with any of the methods. However, this was not the case for copper and several other elements in zinc-aluminium alloys. The best calibration curves for zinc-aluminium were obtained with the IRSID and SIMR methods. This suggested that the effect of pressure is less important than voltage on the emission yield.

Table 2.5. *RSDs for the normalised emission yields in steels and zinc-aluminium alloys for three modes of operating conditions (Payling et al., 1995a).*

Elts	No correction		IRSID		SIMR		BHP		Conc. range (mass%)	
	Steels	Zn-Al	Steels	Zn-Al	Steels	Zn-Al	Steels	Zn-Al	Steels	Zn-Al
Mn	3.9		3.0		3.4		3.0		0.0057-1.5	
Ni	4.0		4.2		4.2		4.5		0.0058-0.5	
Cu	2.6	61.0	2.5	10.2	2.4	12.1	2.8	19.2	0.016-2.0	0.21-3.2
Mg		43.6		15.2		21.2		28.7		0.02-0.12
Al		53.4		14.8		11.9		9.0		0.047-13
Fe		53.5		21.8		16.5		24.7		0.01-0.12
Pb		55.8		7.0		10.7		18.5		0.0076-0.35
Mean	3.5	54.3	3.2	13.9	3.3	14.5	3.4	20.0		

However, when the IRSID and SIMR methods are corrected for pressure, or when the BHP method is corrected for voltage, all three corrected methods give comparable, good results, listed in Table 2.6. The work showed clearly that both pressure and voltage must be accounted for in a quantitative analysis using GDOES.

Table 2.6. *RSDs for the normalized emission yields in zinc-aluminium alloys with corrected IRSID, SIMR and BHP methods (Payling et al., 1995a)*

Method	Mg	Al	Fe	Cu	Pb	Mean
IRSID(corrected for pressure)	5.5	6.1	19.7	7.0	7.1	9.1
SIMR(corrected for pressure)	9.2	7.8	13.1	7.5	10.3	9.6
BHP(corrected for voltage)	12.1	8.8	13.1	9.2	10.4	10.7

In later work by Payling (1995b), an empirical equation was derived that describes the relationship between a recorded emission signal and the current, the voltage and the argon pressure in a model-independent way. The experimental results showed that the current, the voltage and the pressure all contribute significantly to the recorded signal and emission yield. Typically, the emission yield was proportional to the current, decreased as the square root of the voltage and increased linearly with the pressure at low pressures but decreased exponentially at higher pressures.

2.5.5.2 Background signal correction

There are still some problems that have not been well solved, although GDOES quantification has been successfully applied in bulk and depth profiling analysis. The effect of background signals in GDOES analysis is one of them. Although background signals in GDOES are very low, usually comparable with the photomultiplier dark current, and lower than with many other OES techniques such as spark or ICP (Payling, 1997e), at low concentrations the background cannot be neglected and needs to be corrected for in some way. In the quantitative theory of GDOES, the background signal is described as an independent term b_i, as in Eqn. (2.27), and is an additional

contribution to the intensity of an element i apart from the sputtered atoms of the element. Eqn. (2.27) can also be rewritten as

$$c_i = I_i /(k_i R_i q_i) - c_{BEC} \ , \tag{2.40}$$

in which,

$$c_{BEC} = b_i /(k_i R_i q) \ , \tag{2.41}$$

is known as the background equivalent concentration (BEC) (Payling, 1997d).

Only a few papers in the literature deal with background signal correction in GDOES quantification (Bengtson and Eklund, 1992; Payling *et al.*, 1994; Weiss, 1995). From bulk analysis in GDOES, it is known that the background signal varies with the sample matrices. If the matrix does not change, it is of no consequence in the evaluation of the concentration. However, in depth profile analysis, the matrix may change completely as different layers are penetrated, and consequently the BEC normally will change as well. In practice, it is very difficult to determine the "matrix-independent" BEC from the available calibration data. The BEC is also dependent on the discharge conditions in a different way from that of the line intensities. In the experimental work by Bengtson and Eklund (1992), they found the BEC of pure materials decreased with discharge current, but remained approximately constant with voltage. This difference in behaviour between the background signal and the emission yield dependence on discharge current and voltage makes GDOES calibration with a correction for the background signal difficult. Therefore, the BEC remains a constant in their quantitative method (the SIMR method) of GDOES.

The background signal in GDOES was also described by the sum of four terms (Payling *et al.*, 1994; Payling, 1997d): a constant component from the photomultiplier dark current and other instrumental noise sources, an argon term which varied with the argon pressure and the power of the source, and two matrix terms, a matrix continuum component largely associated with iron and a matrix line interference component. A background signal correction was presented by a general description of the behaviour of

the background signal as a function of the source parameters: the pressure, the current and the voltage (or the power). The success of these methods was demonstrated in the depth profiles of three commercial metallic and polymer-coated steel samples.

2.5.5.3 Gaseous impurity effects on the glow discharge

In Chapter 6 of this thesis the hydrogen signal in the glow discharge source and the effect of hydrogen on the measured elements will be discussed. Mixed gas effects on emission characteristics of the plasma in GDOES and on the cathode dark-space region of the Grimm source have been reported by Wagatsuma (2001), Videnovic *et al.* (1996) and Kuraica *et al.* (1997), which included argon-helium, argon-oxygen, argon-nitrogen, neon-helium and nitrogen-helium mixtures. For applications of GDOES, most interest lies with the gaseous impurities of N, O and H mixed into argon gas in the source of GDOES, since they are unavoidable in GDOES measurements, especially when analysing elements in the plasma from samples containing these elements.

Fischer *et al.* (1993) reported on the influence of a controlled addition of oxygen and nitrogen to argon on the effective sputtering rate, the emission intensities of aluminium, titanium, iron, nickel, copper and silver, and the discharge current with a Grimm glow discharge source in a constant-voltage operating mode. Additions of oxygen and nitrogen smaller than 0.1% by mass do not lead to any alternations of parameters relevant to GDOES analysis. Concentrations of oxygen and nitrogen in argon exceeding this value, which are believed to be easily reached when bulk compounds with nitrogen and/or oxygen (nitrides, oxides) or scales (coatings, corrosion scales) are sputtered, or which may be caused by air leakages occurring at the gasket between the sample and cathode plate, could alter the analytical line intensities of the elements of interest significantly. The line intensity may increase or decrease depending on the elements present in the discharge plasma. The presence of nitrogen and oxygen in the discharge may initiate chemical reactions in the plasma. The formation of compounds reduces the number of free atoms of the elements to be determined in the plasma and

hence their available number for excitation. The resulting reduction in intensity suggests a decrease of the elemental concentration in the sputtered layer of the sample.

Recently, the effects of adding hydrogen to argon on the glow discharge in GDOES have been investigated. Bengtson and Hänström (1999b) have observed that small amounts of hydrogen (< 0.1% partial pressure) added to an argon glow discharge can significantly alter analyte emission yields. The effects enhanced certain lines but quenched other lines of the same element. Hodoroaba *et al.* (2000a and 2000b) have investigated the effects of small amounts of hydrogen (up to 0.6% relative partial pressure) on the emission intensities of Ar I, Ar II, Cu I and Cu II lines. Different behaviours for different lines were observed. Most of the emission lines of Cu I increase strongly with the addition of even a small quantity of hydrogen, including the 327.40 nm line of Cu I used for the quantification of Cu in many commercially available GDOES spectrometers. They also presented evidence of the effects caused by hydrogen for the different matrix elements copper, stainless steel, titanium, aluminium and silicon. In an overview of various processes that may occur in an argon-hydrogen glow discharge plasma, the effect of H_2 molecules and H atoms on the argon analytical glow discharge were predicted (Bogaerts and Gijbels, 2000b), i.e. a drop in argon ion (and maybe electron) density, a drop in the argon metastable atom density and a change in the electron energy distribution function. However, because of the simplifications in the estimations, the authors suggested that these predictions need to be checked by experiment with analytical glow discharges.

2.6 Analytical Performance and Applications of GDOES

2.6.1 Analytical performance of GDOES

2.6.1.1 The detection limit

Analytical figures of merit of GDOES have been reviewed by Bengtson (1996) and Payling (1997e). Detection limits in GDOES are typically 0.1–10 ppm in steel and

copper matrices. Typically, detection limits of a few ppm normally are achieved in bulk analysis with long integration times of 5–10 sec. In depth profiling, detection limits at any particular point in a depth profile will be a factor of ten or worse compared to bulk analysis due to shorter integration times. Because of the high stability of the discharge, GDOES may analyse all elements (including C, N, O, H) present at a concentration above 10–100 μg/g (Hoffmann, 1993). In the case of the analysis for a steel sheet surface, experience has shown that 0.01% by mass is a practical detection limit for common steel-alloy elements with high dynamic detection ranges (Angeli *et al.*, 1993).

2.6.1.2 The sample-to-sample precision

Concerning the precision of GDOES analysis, sample-to-sample precision of GDOES is carried out in practice by recording from single or multiple burns for a number of identical samples and the precision is expressed as a relative standard deviation (RSD) for each element. A sample-to-sample precision of 0.4–3.7% RSD has been reported by Kruger *et al.* (1980) using ten identical steel samples for a range of ten elements. Sample-to-sample precision for the determination of major and minor elements in stainless steel (CRM JK-8F) is typically in the range 0.1–1% RSD (Bengtson, 1996).

2.6.1.3 The analytical accuracy

The accuracy of GDOES measurements can be expressed by the RSD of the differences between measured concentrations and the certified values. The reviewed accuracy of RSDs by Payling (1997e) show a range of spreads, which were believed to vary considerably, depending on the concentration range, number of samples, matrix effects, emission line interferences, etc. For example, typical RSD values are 0.2% for major elements and 1% RSD for minor elements (Cu in leaded bronze), and 1–13% RSD for Cr, Ni, Fe, and Zn in copper and aluminium matrices.

2.6.1.4 The depth resolution

Depth resolution in sputter-profiling was defined in terms of a characteristic depth (or sputtering time) necessary for the decrease of the normalised output signal from 84% to

16% if the measured profile is obtained by sputtering through a true rectangular concentration profile (Hofmann, 1977). Theoretically, sputtering in GDOES has a depth resolution of several nanometres (Angeli *et al.*, 1993; Bengtson, 1996), but in practice the depth resolution in GDOES depth profiling is dependent on the shape of the sputtered crater, which is mainly affected by the source parameters, i.e. the voltage, the current and the argon gas pressure (Angeli *et al.*, 1993; Quentmeier, 1994; Bengtson, 1996). It is believed that these effects result from the inhomogeneous distribution of the electric field between the anode and the cathode and of the pressure of the plasma gas in GDOES (Hamada *et al.*, 1995).

The crater shape was represented by a ratio of the depth at the edge to the depth in the centre of a sputtered crater (Angeli *et al.*, 1993). The experimental results in their work showed effects of the argon gas pressure and the source voltage on the shape of the crater and suggested that the excitation voltages between 600 and 800 V are preferable to obtain a near-flat material erosion by GDOES sputtering with a 4 mm diameter dc source.

The influence of the working conditions of a discharge source in GDOES on depth profiles and interface widths was investigated by Quentmeier (1994). Operating voltage and argon gas pressure were found to be the dominant parameters that determine the formation of the crater shape. Under the optimum discharge parameters (250 Pa argon gas pressure, 800 V discharge voltage and 8 mm anode), the crater remained nearly flat with increasing sputtered depths up to 37 μm, and this tendency was observed for nearly all matrices. Apart from the crater shape, the roughness of the bottom of the crater, which develops during sputtering due to the preferential sputtering of different crystal sizes and orientations, can deteriorate the depth resolution. The results showed that the surface roughness was also affected by the discharge voltage and the gas pressure. A low voltage is favourable for the reduction of sample roughness. The effects of crystal size and orientation on the depth resolution are studied in detail in Chapter 3.

The depth resolution was also estimated by the full width at half-maximum (FWHM) of a differentiated emission intensity-depth curve at a layer-substrate interface in GDOES analysis (Hamada *et al.*, 1995). The experimental results about dependence of the FWHM on the voltage and the current showed that the best depth resolution for the interface of a nickel coating on a copper substrate was obtained at a voltage of ~650 V (constant voltage mode) or a current of ~55 mA (constant current mode), and was almost independent of the measurement modes.

The correlation between the depth resolution and the crater formation process was also investigated by Präβler *et al.* (1995). By using multi-layer structure samples (five double layers with 100 nm Cu and 100 nm CrNi each), the depth resolution increased linearly with the sputtered depth and amounted to 5–10% of the depth under optimised conditions. Experimental results of the depth resolution for multi-layer samples, obtained by Ives *et al.* (1997) under the optimised conditions of 700 V and 30 mA, were similar to that of Präβler *et al.* GDOES measurements of the samples with Ni/Fe multiple layers consisting of 10 individual layers showed that the depth resolution was a linear function with the depth and amounted to ~10–15% of the total sputtered depth. As a general rule of thumb under good conditions the depth resolution is about 15% of the sputtered depth, i.e. about 15 nm at 100 nm depth and about 3 μm at 20 μm depth (Payling, 1997a).

2.6.2 Recent Applications of GDOES

In this study the Grimm source as a sputtering tool has been used to reveal the pitting phenomenon (Chapter 4) and to obtain surface layers with less structural damage for the collection of EBSD patterns and for plan views of internal oxides of steels (Chapter 5). However, applications of GDOES in the literature are mainly focused on depth profiling analyses. The first depth profiling analysis by GDOES was reported by Green and Whelan (1973) and concerned the measurement of Sb concentrations in thin films of GaAs-GaSb. Applications of GDOES in quantitative analysis and depth profiling have now been extended to a wide range in the fields of metallic coatings, industrial surfaces,

oxide scales, corrosion, semiconductors and PVD/CVD hard coatings (Payling, 1997a). Some applications of GDOES analysis in the last few years are summarised in Table 2.7.

Most of the applications were focused on the fields of modified surfaces, diffusion surfaces, thin films and hard coatings. The elements involved included not only common elements in analysis for steel samples but also Li, Na (Lindbergh and Zhu, 2000; Zhu *et al.*, 1998, 2001), and Ca, Cl (Olofsson and Dizdar, 1998). Wäckelgård (1998) showed GDOES can compare hydrogen content in the thin film of black nickel coatings (~100 nm thick) before and after heating the samples. Angeli (2001) showed the high detection sensitivity of GDOES where a concentration of ~20 ppm for Pb in a zinc layer was analysed. The spread of analysed depth in these measurements was in a wide range from a few tens of nanometres for thin films (Olofsson and Dizdar, 1998; Wäckelgård, 1998) to ~100 μm for nitrided stainless steel (Flis *et al.*, 2000). With multiple measurements by grinding repeatedly sputtered surfaces to the level of the bottom of the sputtered crater, GDOES analysis is able to profile the decarburised layer of steels to a depth of ~350 μm (Bellini *et al.*, 2001). Suchaneck *et al.* (1999) reported a depth resolution of a few tens of nanometres for ~200 nm-thick lead zirconate titanate ferroelectric films. A depth resolution of ~20 nm for ~100 nm black nickel coating was also obtained by Wäckelgård (1998).

Hard coatings, including titanium nitride, titanium carbide, and ternary and quaternary systems (TiN, TiC, CrN, AlN, TiCN, TiAlN, TiAlVN, etc.), have been widely applied in industry for cutting and forming tools and machine parts that are exposed to a continuous abrasive wear, due to their outstanding performance in corrosion- and wear-resistance and tribological properties. GDOES depth profiling has been successfully applied in the analysis of the composition and depth of the coatings (Payling, 1997a), due to its unique ability to analyse a wide range of elements with a depth resolution of only a few tens of nanometres. Some limitations which may affect the accuracy of

concentrations and depth resolution in GDOES analysis for hard coatings have been mentioned by Böhm (1997). For example,

- if a wide range of elemental concentrations in both the coating and the substrate exists and in conjunction with a high depth resolution, then this poses limitations in respect to the dynamic range of the photomultiplier;
- for some hard coatings, the optimised discharge conditions for the best depth resolution may be far from the normalised conditions of calibration (e.g. 700 V and 20 mA for the multi-matrix quantitative method). This strong deviation may exclude the use of the approximation to transform the measured intensities into normalised intensities;
- in the calculation of the density of a coating material in quantitative GDOES, which is based on the measured elemental concentrations, it is essential to transform a sputtering rate to a sputtered depth. This can provide reasonably accurate results for metallic alloys. However, errors can occur in the quantification of hard coatings because of differences in electronic and lattice structures of the compounds of light elements with metal atoms;
- a lack of calibration samples for some elements in the coatings, for example, CRMs with carbon between 5% and 20% by mass, nitrogen between 0.5% and 6.7% by mass, and with oxygen, makes the calibration of GDOES for hard coatings difficult.

Table 2.7. *A summary of some applications of GDOES depth profiling in the last few years.*

Sample	Application	Quali./Quant	Reference
1. Modified surfaces			
Corrosion layers of high aluminium steels and high chromium ferritic steels	The detected corrosion layers using GDOES were in the range of 0.5–20 μm for three different anode and cathode gas environments. In addition, GDOES composition profiles gave extra information for elements of Al, Cr, Li, Na, etc. in different depths, which was impossible for XRD investigations in the case of thin layers.	Quantitative	Lindbergh and Zhu, 2000; Zhu *et al.*, 1998, 2001
Pre-treated surfaces by sputtering etching	GDOES detection to compare oxygen signal on surfaces pre-treated by sputtering etching in direct current and medium frequency glow discharge for PVD coating	Qualitative	Faber *et al.*, 2002
Pre-treated surfaces for hot-dip galvanized and Galfan coated steel	Untreated and pre-treated surfaces were characterized by GDOES depth profiling for Fe, Al, Zn, Zr, O, C, Cr, Co, etc. in depths from 400 to 2000 nm . For Al, Cr and Zr, the GDOES depth profiles even gave information on outermost surfaces of only 10 nm in thickness.	Quantitative	Puomi *et al.*, 1999a and 1999b
Galvanized steel surfaces	GDOES detection of Zn, Al, Pb, Na, Ti, Mn, O and P in outermost surfaces of hot-dip galvanized steel substrates in different preparation stages. In the zinc layer the concentration of Pb was nearly 20 ppm.	Qualitative	Wolpers and Angeli, 2001
2. Diffusion surfaces			
Nitrided M2 tool steels	GDOES depth profiles for carbide-layer and nitride-layer and	Quantitative	da Silva Rocha

	diffusion zone of nitrided steel (da Silva Rocha *et al.*, 1999).		*et al.*, 1999
Nitrided medium alloy steels	GDOES depth profiles demonstrated that nitrogen concentrations were in the range of 10–16 mass% in outermost layers nearly 1 μm after a treatment for 3 hours.	Quantitative	Blawert *et al.*, 2000
Nitrided stainless steels and aluminium alloys	Comparison of nitriding results of stainless steels and aluminium alloys by plasma immersion ion implantation using GDOES depth profiling.	Quantitative	Möller *et al.*, 2001
Titanium-based materials	GDOES depth profiles of oxygen in outer layer of plasma nitriding (PN), thermal oxidation (TO), and palladium-treated thermal oxidation (PTO) treated materials showed there were relatively flat oxide layers of about 2 μm on the surfaces with oxygen diffusion zone about 20 μm in depth, which are of benefit to enhance corrosion resistance and improve anti-scuffing capacity of the materials.	Quantitative	Bloyce *et al.*, 1998
Nitrided stainless steels	GDOES results showed uniform elemental concentrations were throughout the nitrided layers. The deepest analysed depth reached 100 μm. In the region close to the substrate, C showed a maximum.	Quantitative	Flis *et al., 2000*
Phosphate coating on nitrided stainless steel	GDOES profiles of P, O, and Mn indicated that the thickness of the phosphate coating was about 10 μm with 1 μm thick outer layer composed mainly of the phosphates of Fe, Mn and Cr.	Quantitative	Flis *et al., 2001*
Boronised layers of steels	GDOES depth profiling for boronised layers of four steels showed boron concentrations in the layers were about 30 at.% with layer depth from a few microns to more than ten microns.	Quantitative	Küper *et al.*, 2000

Decarburized layer of hot-rolled cylindrical carbon steel rod	Hot-rolled cylindrical carbon steel rod was pressed using a 50 tons load to obtain a uniform flat surface free of cracks. It was confirmed that the pressing did not affect the extent of the decarburization and the decarburization layer. By grinding repeatedly the sputtered surface to the level of bottom of sputtered crater, GDOES analysis is able to profile a decarburized layer of ~350 μm.	Quantitative	Bellini *et al.*, 2001
Nitrided austenitic stainless steels	Depth profile of the surface for N, C, O, Cr, Ni and Fe. Thickness of the diffusion layer was 14 μm.	Quantitative	Mändl *et al.*, 1998
3. Thin films			
Housing washer of spherical roller thrust bearing	GDOES depth profiling of a boundary-lubricated surface for the elements of Fe, Cr, Ca, Zn, O, N, P, and S to 100 nm of depth.	Quantitative	Olofsson and Dizdar, 1998
Lead zirconate titanate (PZT) films on silicon	GDOES depth profiles indicated that the film consisted of PbO, TiO_2 and ZrO_2. Thickness of the film was 200 nm and the depth resolution was only a few tens of nanometres at the interface.	Quantitative	Suchaneck, *et al.*, 1999
Black nickel solar absorber coatings on copper	Thickness of the film characterised in GDOES depth profile was about 100 nm with a depth resolution ~20 nm. The GDOES analysis also showed hydrogen content decreased by a factor of two throughout the whole layer after heating the sample at 200 °C for 24 h. This result was in correspondence with that obtained by nuclear resonance reaction technique.	Quantitative	Wäckelgård, 1998

Black chromate conversion coatings	GDOES depth profiling of the coating, combining with other surface analysis methods, showed a role of anions in a chromate electrolyte and effects of the transituon elements in zinc electrodeposits.	Qualitative	Gigandet *et al.*, 1997
Oxide layers grown at high temperature on a nickel-based super-alloy	GDOES depth profiles demonstrated that thickness of the oxide layer increased from a few hundreds of nanometres to 2 μm, by characterising the elements of Cr and Ti growing in the layers, as temperatures of air thermal treatment increased from 700 °C to 950 °C in 4 hours.	Quantitative	Ingo *et al.*, 2001
Oxide films on stainless steels	GDOES quantitative depth profile of the films.	Quantitative	Pan *et al.*, 1998
$CuInSe_2$ thin film on Ti substrate	GDOES depth profiling showed different profiles between films as-deposited and excessively annealed.	Qualitative	De Silva *et al.*, 2001
4. Hard coatings			
PVD coating with TiN-TiCN-TiC layer structure	The GDOES analysis revealed a narrow titanium nitride peak close to substrate, corresponding to the pure TiN first deposited. However, the GDOES profile for Ti, Cr, C, and N could be strongly affected by presences of hydrogen and oxygen in the source.	Quantitative	Wänstrand *et al.*, 1997
TiCN coatings on M2 steel, medium carbon steel and Si substrate	GDOES depth profile of the coating showed that the composition were in overall agreement with that obtained by Rutherford backscattering spectrometry (RBS). In additional, the GDOES results indicated that deleterious effects of the target poisoning are not only the reduction of the deposition rates, but it also affects the homogeneity of the coating layer.	Quantitative	Senna *et al.*, 1997 and Freire Jr. *et al.*, 1998

TiN/AlN multiple layers	GDOES depth profiles for multi-layers with six AlN and six TiN layers revealed clearly the interfaces for layer thickness of 360 nm without post layer-deposition ion bombardment (PLDIB) etching and was able to reveal the interfaces with the PLDIB etching very sharply even thickness of the layer was only 240 nm.	Qualitative	Thobor *et al.*, 2000
Carbide-doped hydrogen DLC coatings (WC/C)	GDOES depth profiling showed the chemical composition of the coatings and hydrogen signals at the interfaces between the coating and the substrate. The GDOES results only were semi-quantitative, owing to the presence of hydrogen in the coating. This is because hydrogen has a strong influence on the recorded signal of the other elements.	Quantitative	Wänstrand *et al.* 1999
PVD TiAlN films	GDOES profile showed fairly three layers of TiAlN outer layer, TiAl interlayer with thickness of TiAl layer of 1 μm and HSS substrate.	Quantitative	Lii *et al.*, 1998
PVD TiN coating on low alloy cast steel	The GDOES depth profile for the coating revealed the Ti interlayer with thickness of only 200 nm in spite of a high substrate roughness.	Quantitative	Schulz *et al.*, 1997
PVD TiAlN coating on HSS	GDOES depth profile for the coating showed carbonitride in outer layer.	Quantitative	Smith *et al.*, 1997
PACVD TiN, TiC and $Ti_{1-x}Al_xN$ coatings on steels and WC/Co hard metal substrates	GDOES depth profiles for the coatings were employed in a study on the coatings deposited by unipolar and bipolar pulsed d.c. plasma activated CVD under various process conditions.	Qualitative	Täschner *et al.*, 2001

Machinable TiN_x coatings for ultraprecision cutting	Thickness of the coating was 20 μm (whereas normal PVD coatings up to only 5 μm). GDOES depth profiling, using Ti and TiCN as calibration samples, were used to determinate the dependence of coating composition on the nitrogen pressure in the PVD process.	Qualitative	Kohlscheen *et al.*, 1999
PVD TiN, CrN, TiAlN, NbN-(TiAl)N, CrN-TiCN and AlN/TiN coatings on magnesium alloys	GDOES results exhibited constant distributions of the different elements through the coating's thickness. Additionally, an oxygen peak up to 40 at.% was measured at the interface of the NbN-(TiAl)N-coating.	Quantitative	Hollstein *et al.*, 2003
Cr-based hard coatings	Quantitative depth profiles of the coatings for Cr, N, C, O and Fe.	Quantitative	Čekada *et al.*, 2002
5. Others			
Corrosion products on ancient bronzes	GDOES analysis showed the depth profiles for elements of Cu, Pb, Sn O, Si up to a depth of 120 μm.	Quantitative	Ingo *et al.*, 2000, 2002
Fe, Ni and Ti-base alloys	Determination of macro-segregation patterns by GDOES.	Quantitative	Johnson *et al.*, 1998
EDT roll surface	GDOES depth profiling of electrical discharge texturing hardened roll surface, which was alloyed/modified using WC/Co and TiC/WC/Co powder metallurgy green compact and sintered electrodes. The profile gave information of Fe, Cr, Mo, V, C, W and Ti for up to 100 μm thick.	Quantitative	Simão *et al.*, 2002

Chapter 3 Crystal Orientation Effects on the Sputtering Rate in GDOES

3.1 Introduction

For quantitative depth profiling in GDOES, the sputtering time is converted into a depth on the assumption that the sample surface is eroded layer-by-layer uniformly. In fact, material is often removed non-uniformly due to uneven sputtering of the sample surface. In the case of the analysis of surface structures, such as coatings and nitrided layers, this results in a degradation in depth resolution. The principal cause of low depth resolution in GDOES is the formation of crater curvature, i.e. the shape of the crater (Quentmeier, 1997), which is affected by the discharge parameters of voltage, current and argon gas pressure (Angeli *et al.*, 1993; Hamada et al, 1995; Präßler *et al.*, 1995). The depth resolution is believed generally to worsen as the depth of the burn increases (Präßler *et al.*, 1995). The crater shape can most easily be controlled by the voltage, the current and argon gas pressure above the sample (Quentmeier, 1994). Roughness of the crater bottom can also affect the depth resolution in GDOES depth profiling. The roughness is thought to depend on the composition of the sample and orientation of crystallites within it. For example, selective sputtering was found to be responsible for the apparent enrichment of the alloying elements Cu, Mg, Mn, and Si in aluminium cast-alloys and considered to be caused by distinguishable metallurgical phases, which were heterogeneously distributed in the base material (Dessenne, 1993). Crystal orientation effects on the sputtering rate are also believed to increase the roughness of the crater bottom in GDOES (Quentmeier, 1997), but no evidence in the range of low ion energies (below 500 eV) to support this can be found in the literature.

It is well known that sputtering rates at high ion energies (1–20 keV) are affected significantly by crystal orientation (Robinson, 1981; Roosendaal, 1981). GDOES typically operates at a voltage of around 500–1200 V, and the corresponding ion energies are believed to be below at most ~1 keV, where crystal orientation effects generally are regarded as less important. Furthermore, most ion impacts are at rather lower energies than 1 keV due to scattering and charge-exchange processes within the plasma. The results presented in this chapter clearly demonstrate that crystallite orientation does significantly affect sputtering rates at these low ion energies, at least in iron. Furthermore, crystal orientation affects the surface roughness of the crater on a sub-grain scale: both these effects may reduce the depth resolution of the technique when it is used for depth profiling.

SEM images are seen to reveal different topographical structures on the bottom surface of a GDOES crater using pure iron as the test sample. Combined with the depth measurements of individual crystallites using a profilometer and their orientation detection by the EBSD technique, a correlation between the sputtering rate, the crystallite orientation and the micro-texture has been found.

3.2 Experimental

High purity (99.995%) rolled iron was chosen as the test sample in this investigation. The reason for choosing pure iron was due to its metallurgical significance and the fact that, relative to other elements, its sputtering rate is average. Also, the influence of non-uniformly distributed impurity elements in the sample on the sputtering can be eliminated by the high purity. The iron was 1 mm thick and was first cut into several 15×15 mm pieces. The iron samples were then mounted in bakelite, which facilitates sample polishing and GDOES sputtering. The samples were mechanically polished to a 1 μm-grade diamond paste finish before sputtering in GDOES.

The sample erosion was performed in the GDOES (LECO 750 GDS) with a 4 mm-diameter anode and Grimm dc source. The glow discharge source (GDS) was operated in the discharge mode of constant voltage and current. Because the three parameters are not independent in GDOES, once the voltage and current are both kept constant, the argon pressure will be dependent on the sample matrix (Payling, 1997a). In fact, the discharge conditions used in the GDOES are that the voltage and the current are chosen using a fixed voltage value, and the argon pressure is controlled automatically by a gas-flow controller to maintain a constant current as the matrix changes. In this work the argon pressure did not change significantly because of the homogeneity of the sample matrix.

Profiles of sputtered craters were measured by a laser probe profilometer (UBM). The sample was moved in the X and/or Y direction by a computer-controlled stepper motor, so that a line profile scan and a 3-D surface scan of the crater could be obtained. The depth resolution of the profilometer depends on the measuring range chosen and is about 0.5 μm at the 50 μm height range used here. At first, the voltage and the current parameters (between the ranges of 500–1000 V and 15–35 mA) of the glow discharge source were determined in order to optimise the flatness of the gross crater shape. The sputter time was adjusted from 200–700 seconds to yield mean sputtered depths between 13.5 and 18.8 μm. The dependence of the gross crater shape on the voltage and current is shown in Figure 3.1. From the different profiles with varying voltage, it can be seen that a concave shape is sputtered at 500 V and a convex shape at 1000 V. From the profiles with different currents, it can be seen that the influence of the current on the shape of the crater is less than that of voltage. Therefore, a flat crater bottom can be obtained at optimum conditions with a voltage of 600–800 V and a current of 25–30 mA for the iron sample. The results presented for the rest of the chapter are from craters sputtered at 600 V and 30 mA.

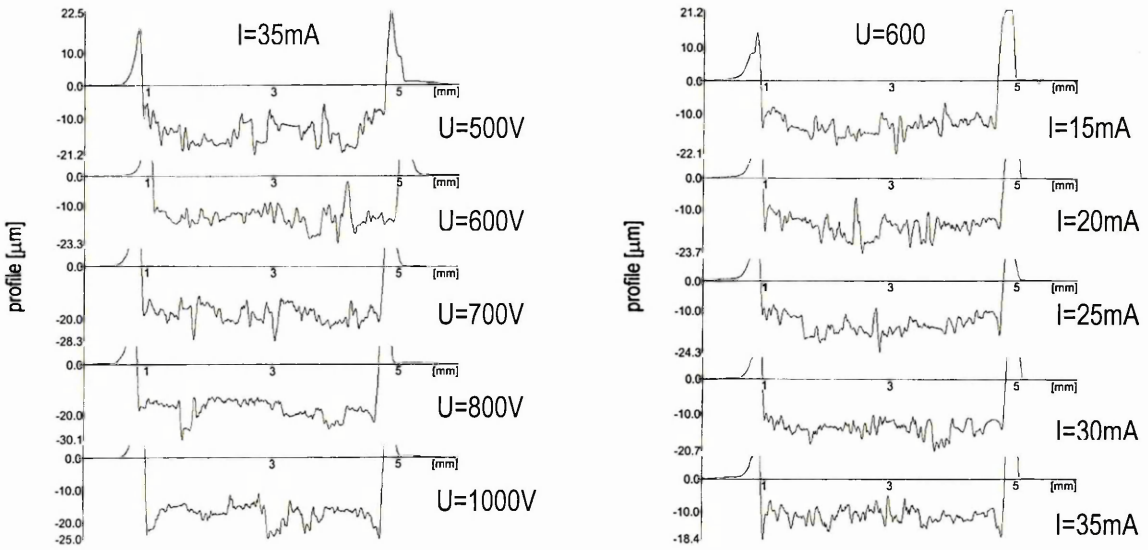

Figure 3.1. The profiles of craters measured by the profilometry (UBM) with varying voltages and currents in the glow discharge. The profiles on left column show the shape of crater changing from concave (at the voltage of 500V) to convex (at 1000V). On the right, it is shown that the current has less effect on the shape of crater.

In addition to the gross crater shape described above, scanning electron microscopy (SEM/JEOL 840) was employed to reveal detailed topographical structure in the base of each crater. Figure 3.2 illustrates the morphologies of the crater bottoms under different GDS conditions and sputtered depths obtained in SEM images. Most of these features seem to have a size that corresponds to the crystallite size within the iron. In order to confirm this, electron back-scattered diffraction (EBSD) was employed to determine the crystalline orientation of the iron substrate at many different positions on the surface of the eroded samples. EBSD is performed simultaneously with conventional SEM imaging. High energy electrons (20 keV) are focused into a beam approximately 50 nm in diameter onto the specimen surface. Some high energy electrons are back-scattered directly from sub-surface atomic nuclei. These high-energy electrons may then be further diffracted by the crystal structure on their way out of the specimen. A two-dimensional EBSD detector mounted to one side of specimen can record the angular distribution of these emergent diffracted electrons (Figure 3.3) to form a Kikuchi pattern. Standard analysis of such patterns, which consist of parallel lines

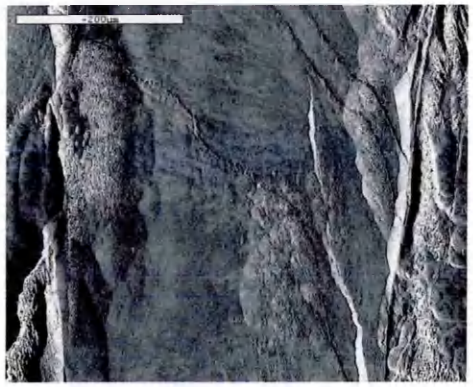

(a) 600V/30mA/500s/18.3μm

(b) 700V/35mA/100s/8.6μm

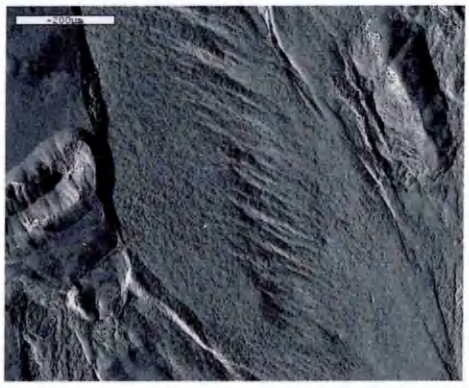

(c) 700V/35mA/800s/39μm

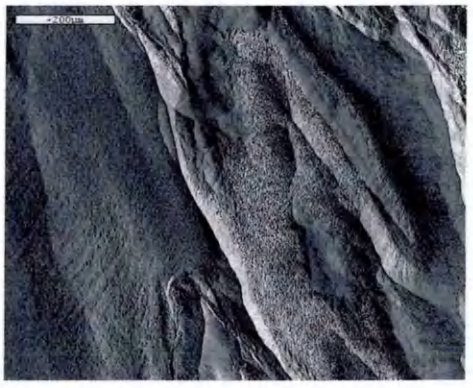

(d) 700V/35mA/1000s/44μm

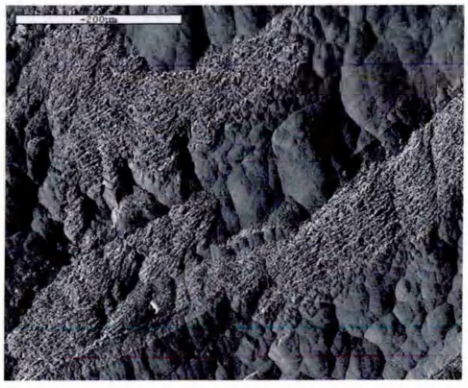

(e) 700V/35mA/2000s/98μm

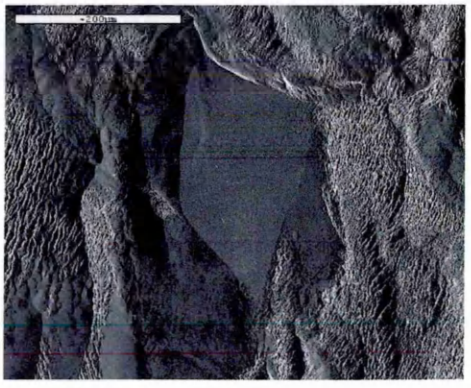

(f) 1100V/35mA/500s/63μm

Figure 3.2. SEM images illustrate morphologies of bottoms of the craters under different GDS conditions and sputtered depths.

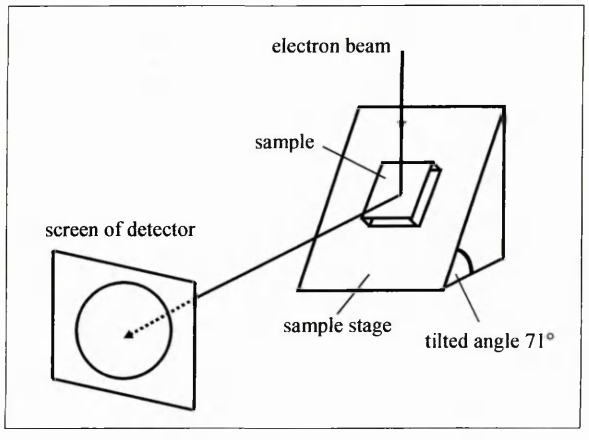

Figure 3.3. Schematic diagram of collection of back-scattered electrons to form the EBSD pattern. A two–dimensional EBSD detector mounted to one side of specimen can record the angular distribution of emergent diffracted electrons to form a Kikuchi pattern.

corresponding to low-index planes, yields the crystalline orientation of the volume of material irradiated by the electron beam (Randle, 1993). In pure iron, this sampling volume was expected to be about 1 μm in size below the incident spot on the surface of the sample. The method can therefore easily differentiate between crystallites on the scale found in the iron samples (about 50–100 μm). Scanning the probe can allow all the crystallites in the field of view to be indexed. The technique has opened up the detailed study of crystallite texture in metals or other materials. In this work, the SEM (Philips XL30) with the Oxford EBSD detection system was used to index the crystal orientation of individual crystallites revealed by GDOES sputtering. As correlating sputtering rate with the crystal direction normal to the surface sample is of interest, care was taken to measure the geometrical calibration of the EBSD detector, which ensured that the measuring was in the sample normal.

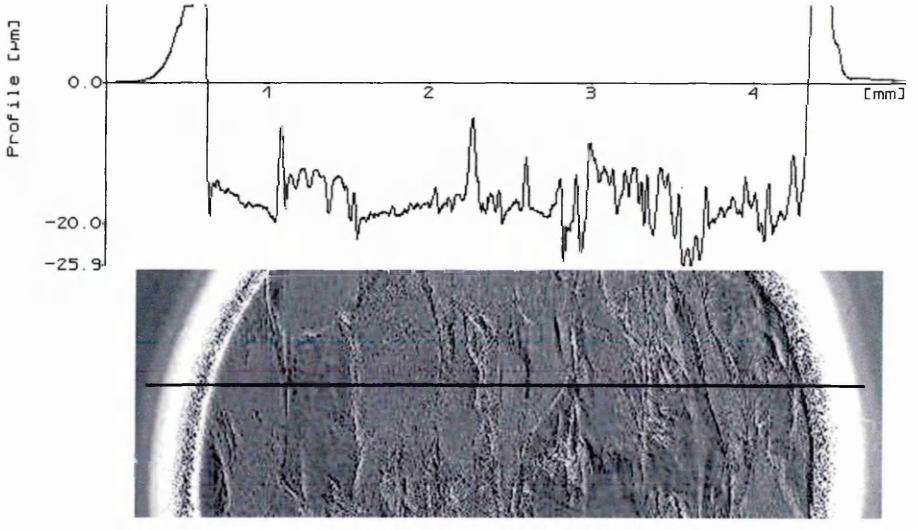

Figure 3.4. Correlation between the profile of crater and the SEM image. The profile was obtained along the reference line shown on the SEM image below.

The profilometer data (Figure 3.1) also contains significant microstructure on about the same scale as the crystallites seen in the SEM images. The depth of the surface of each crystallite was correlated by superimposing a profilometer scan taken along a line, and comparing this directly with the SEM image, as shown in Figure 3.4. Registration of these separate data is difficult, but accurate correlation can be achieved routinely with

full confidence. In this way, each crystallite which is observed in the SEM image can have its absolute depth measured (via the profilometer scan) – from which the effective sputtering rate can be inferred, assuming the crystallite depth is larger than the crater depth – and at the same time its crystal orientation can be determined (via the EBSD detector). Thus, crystal orientation can be correlated with sputtering rate and the surface texture that results from the sputtering process.

3.3 Results and Discussion

The topographical structures of bottom surfaces of the GDOES craters were first revealed in SEM images. The low-magnification SEM image illustrating a quarter of a sputtered crater is shown in Figure 3.5. It demonstrates clearly crystallite grain boundaries and coarse crystal grains with different topography on the bottom of the crater.

Figure 3.5. Low magnification SEM image shows a range of different textures within about one quarter of a typical GDOES crater. Different regions correspond to different crystallites, each with a distinct surface texture. GDS parameters: 600V/30mA/500s.

○ —'rough' texture; △ —'smooth' texture;

□ —'concaved' texture; ▭ —'ripple' and 'concaved' texture.

For the sake of this discussion, the different surface textures are classified arbitrarily into a number of different types. Figure 3.6 demonstrates the common textures in the bottom surfaces of GDOES craters at different sputtering times. The most typical micro-texture is the so-called 'rough', as shown in Figure 3.6 (a), (e) and (i). It is most commonly found on the flat surface of coarse grains relative to the other textures. Another common texture consists of shallow hollows, referred to as 'concaved' texture: this appears much smoother than the 'rough' texture in the low-magnification SEM images. But in the SEM image at a magnification of ×1000 (Figure 3.6 (b), (f) and (j)), it appears to have many adjacent concave surfaces. Note that the eye may deceptively interpret the image as a series of convex domes, but knowledge of the detector geometry in the SEM ensures that these features are indeed concave. The third texture, called 'smooth', appears completely flat in the low-magnification SEM image. In fact, at higher magnification it can be seen to consist of a very finely jagged laminated microstructure, as shown in Figure 3.6 (c), (g) and (k). Occasionally a 'ripple' texture appears, as shown in Figure 3.6 (d), (h) and (l): this is often adjacent to the 'concaved'

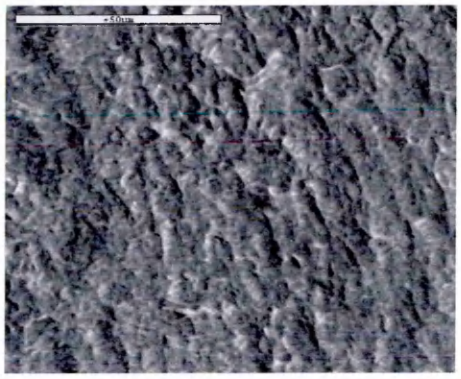

(a) 'rough' texture

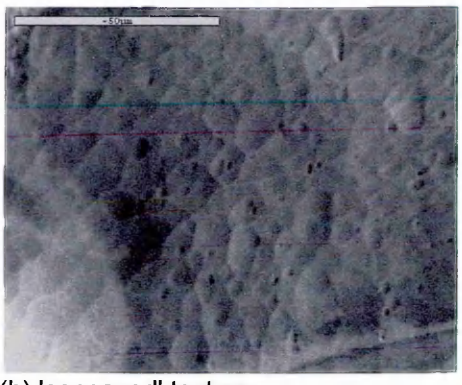

(b) 'concaved' texture

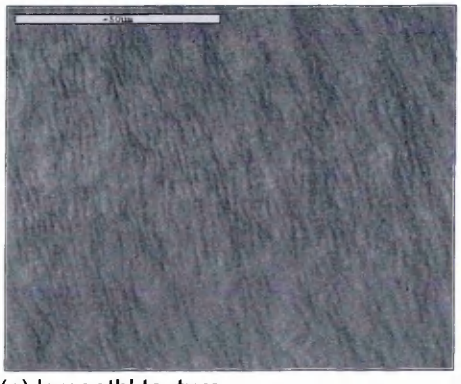

(c) 'smooth' texture

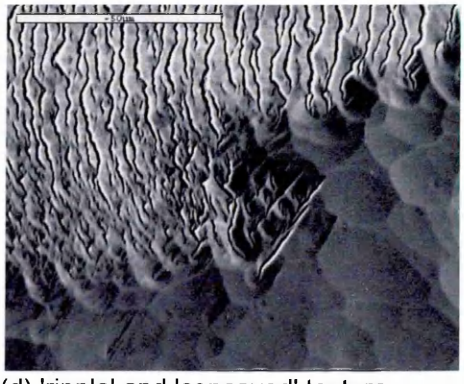

(d) 'ripple' and 'concaved' texture

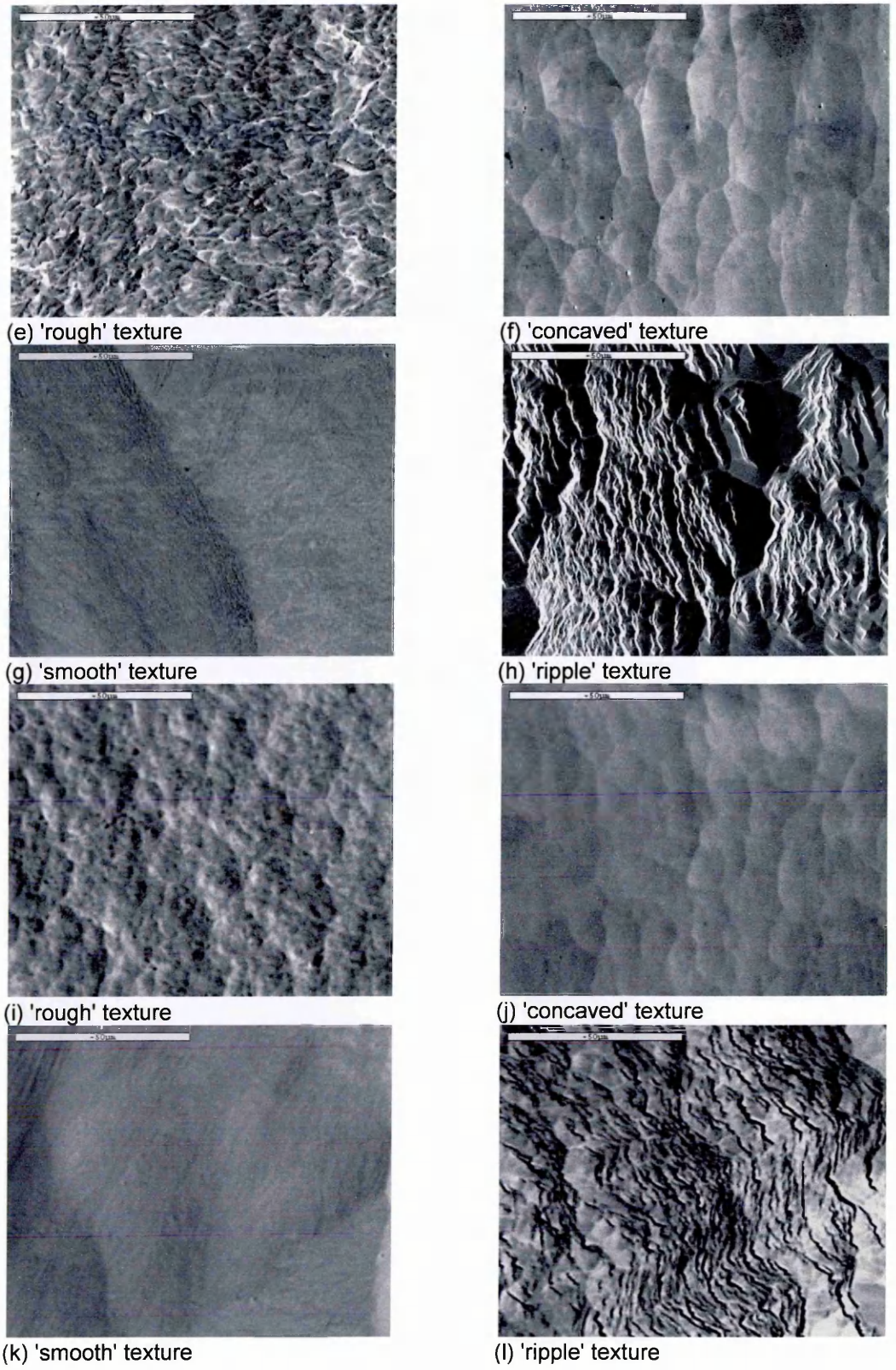

Figure 3.6. SEM images of the typical micro-textures on the high purity iron sample sputtered by GDOES. (a), (e), (i) 'Rough' texture, which is easily found on flat coarse grains, (b), (f), (j) 'concaved' texture appears to have many adjacent concave surfaces, (c), (g), (k) 'smooth' has fine structure compared with 'rough' and 'concaved', (d), (h), (l) 'ripple' is often found adjacent to 'concaved'. GDS: 600V/30mA/4 mm anode.

(a) ~ (d) sputtering time: 500 s, depth: 20.3 μm;
(e) ~ (h) sputtering time: 1000 s, depth: 38.1 μm;
(i) ~ (l) sputtering time: 1300 s, depth: 41.8 μm.

areas. These types of micro-textures have also been observed when the pure iron has been sputtered at different source voltages and currents. Note that the proportion of the area of the crater bottom displaying the 'ripple' texture reduces as the sputtering time increases from 500 s to 1300 s, but as yet there is no explanation for this.

The results from the GDOES craters in the high-purity iron samples with different sputtering times, 500 s, 1000 s and 1300 s, were selected to show the sputtered depth, micro-textures and orientation. The average sputtered depth corresponding to the stated sputtering times are 20.3 μm, 38.1 μm and 41.8 μm, respectively. From the three craters of different depths, a total of 70 micron scale areas, with different textures of 'rough', 'concaved' and 'smooth', were selected and the crystal orientations normal to the sample surface of these areas were then measured via EBSD. The results are presented in the form of an inverse pole diagram, as shown in Figure 3.7. Despite the arbitrariness of the classification of texture, there is significant correlation between orientation and the different micro-textures. Most areas with the 'rough' texture have a surface-normal close to the [111] pole and 'concaved' textures tend to be close to the [001] pole. 'Smooth' textured areas range between the [111] and [001] poles, although the correlation is less clear in this case.

This correlation can also be seen in the orientation maps obtained on the EBSD system, as shown in Figure 3.8. Figure 3.8(a) shows a typical SEM micrograph of the surface texture observed in the bottom of a GDOES crater. In Figure 3.8(b), the same area is shown, but in this picture the colour coding corresponds to sub-surface crystalline orientation calculated by the EBSD technique. In other words, for every pixel in the colour part of this image, a whole back-scattered diffraction pattern has been collected and its crystalline orientation has been indexed. The colour-schematic pole diagram in Figure 3.8(c) shows how these colours correspond to the crystal orientation. Because the iron is a bcc structure, only a small segment of angle space (between the [001], [110] and [111] poles) represent truly unique crystalline orientations (Sutton and Balluffi, 1995). It is evident that the visible surface texture is correlated directly with

the underlying crystallography of the sample: each orientation gives a different surface texture.

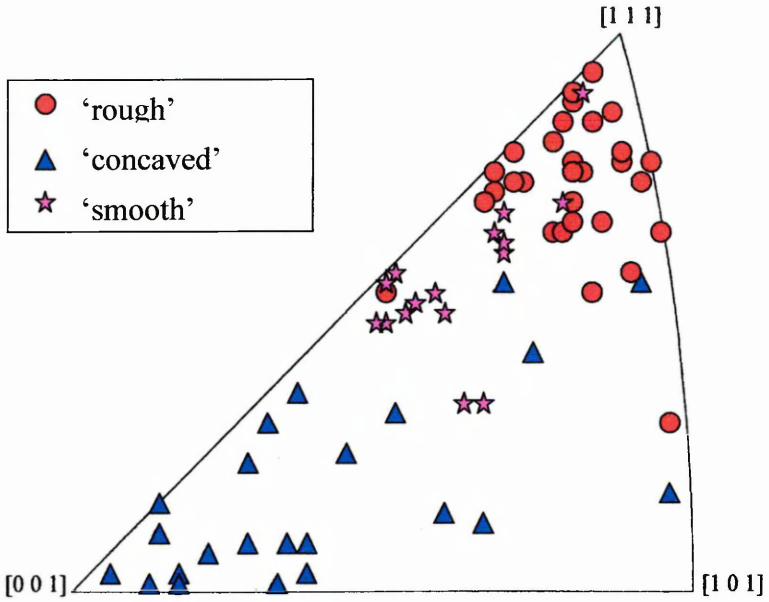

Figure 3.7. Correlation between the 'rough', the 'concaved' and the 'smooth' textures and the measured orientations normal to the sample surface by EBSD. The orientation for the most of micro-areas with 'rough' texture are close to [111], 'concaved' close to [001] and 'smooth' stay in the region between [111] and [001].

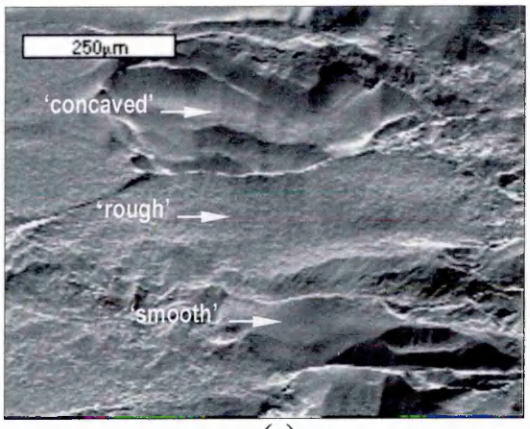

(a)

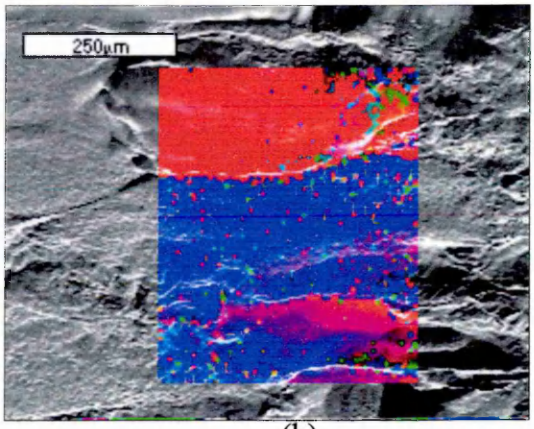

(b)

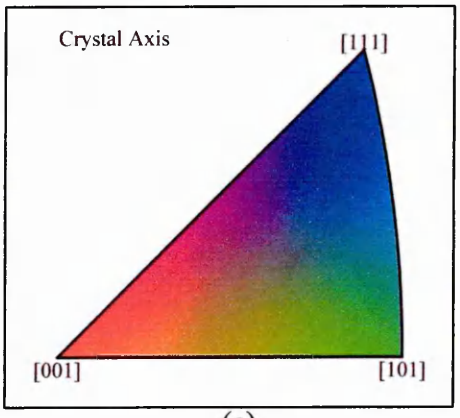

(c)

Figure 3.8. The mapping result by the EBSD for three crystallites with the 'rough', the 'concaved' and the 'smooth' textures.
(a) shows a typical SEM image in bottom of GDOES crater;
(b) the colour coding superimposed on the SEM image indicates the different orientation corresponding to the underlying grain;
(c) shows how these colours correspond to the crystal orientation.

The average sputtered depth with the orientation of a crystallite as a function of sputtering time can also be correlated, as shown in Figure 3.9(a). Figure 3.9(b) shows the relationship between the average depth and the different textures. The configuration of Figure 3.9(b) is similar to Figure 3.9(a), which emphasises the correlation between the orientations and the textures. It is noted that the spread in the measured depth of burn for the crystallites at first increases, and then ceases to increase as the sputtering time increases. This is particularly true of crystallites with 'rough' and 'concaved' surface textures. The depth difference at 1300 s is 5.0 μm compared with 5.3 μm at 1000 s. One possible explanation for this is that as sputtering proceeds, some fast-eroding crystallites are completely removed to reveal lower crystallites which, being of different orientation, sputter more slowly. To determine the average crystallite depth, a cross-section view of the crystalline arrangement in the sample is shown in Figure 3.10, which is an optical image obtained after etching the cross-section of the iron specimen in 2% nital. It is seen that the crystallites are flat in shape and are around several tens of microns deep: much less than their size in the other two dimensions, and about the same depth as the bottom of the GDOES crater after a long burn. In other words, the reduction of the spread of measured depths across the crater surface occurs at around the same depth as the average crystallite depth. The reason the sample is anisotropic is that it was manufactured by a rolling process. Hence when sputtering starts, the roughness of the crater increases until such a time when, on average, more than one crystallite has been sputtered from each point of the surface.

(a)

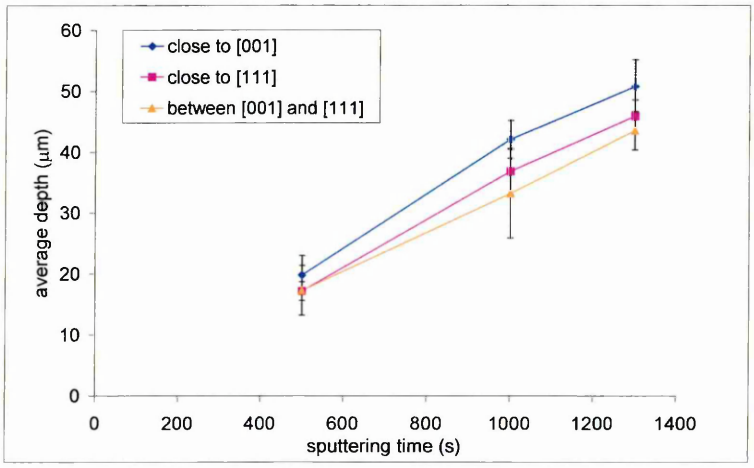

(b)

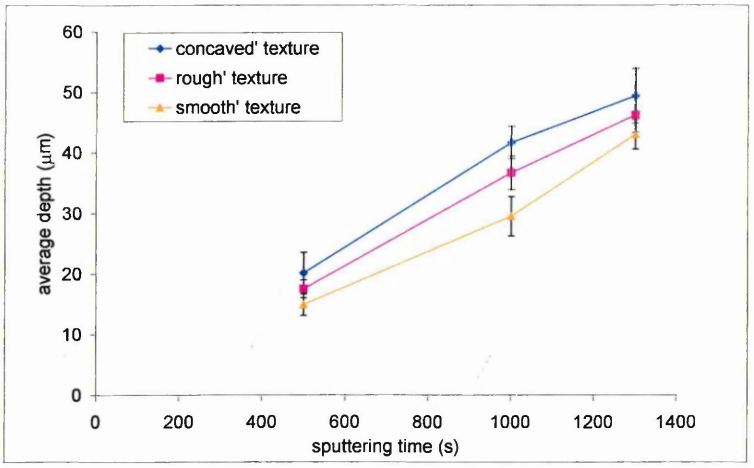

Figure 3.9. Average sputtered depth for crystallites with different orientations and textures as a function of the sputtering time. The spread in the sputtered depth tends to increase with time with both different orientations, as shown in (a), and for the different textures (b). The error bars are obtained from the standard deviations (STDEV) of the average depth measured over many grains and are in the region of 1.5–4.5 μm, except for the depths of orientations between [001] and [111] at a sputtering time of 1000 s, for which there was a large STDEV of 7.3 μm.

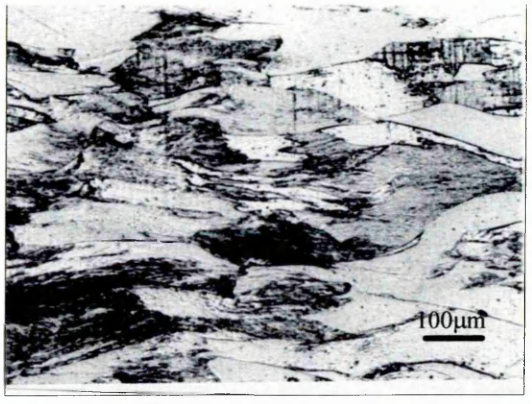

Figure 3.10. A view of cross-section of the high purity iron sample after etching with nital (2%). It shows that the crystallites are flat in shape and are around several tens of microns deep.

Figure 3.9(a) reveals that the average depth of regions with zone-axes close to [001] is deeper than that of regions with zone-axes close to [111] (i.e. the sputtering yield is 10–15% greater in areas close to [001]). One possible explanation for this observation is the existence of channelling of the incident Ar ions. It is well known (Robinson, 1981) that for ion energies exceeding ~1 keV, the sputtering yield shows a strong dependence on crystallographic orientation. This has been explained in terms of

channelling, which is where a high-speed particle is incident on a crystal and nearly parallel to a row of atoms. Rather than undergoing hard collisions, these ions undergo glancing collisions and are channelled deep into the material. Channelled ions result in collision cascades occurring deeper in the material than for non-channelled ions, resulting in the reduction of the sputtering yield. Obviously some crystal orientations are more transparent (i.e. channel more readily) than others. In the case of bcc Fe, one would expect the [111] zone axes to be more transparent than the [001] and hence the [111] zone axes would have a lower sputtering yield, which is what is observed experimentally.

The problems of using channelling alone to describe the observations are twofold. The theoretical model used to describe channelling was developed to explain observations at energy levels of a few keV. To the best of our knowledge, the energy distribution of the Ar ions in the plasma in the GDOES has not been measured. Computer models (Bogaerts and Gijbels, 1997) predict a wide range of incident ion energy ranging from 50 to 600 eV. The other problem of using channelling alone to describe the results in Figure 3.9(a), is that the sputtering yield of high-index planes is lower than that of the low-index planes. These high-index planes are less transparent than the low-index planes and should have a higher sputtering rate, in contrast to what is actually observed. Unfortunately, there are few studies in the literature of sputtering at lower energies. However, the sputtering of Cu with Ar ions has been studied (Robinson, 1981) at energies of less than 500 eV. Differences in sputtering yields of around 20% for different orientations have been reported, which is similar to the different erosion rates reported here. Furthermore, high-index planes showed a lower sputtering rate than lower-index planes, in general agreement with the results shown here. The phenomenon is poorly understood, but it has been suggested that as well as channelling, the surface binding-energy plays an important role at these lower energies.

3.4 Conclusions

Pure iron samples have been used to investigate the crystal orientation effect on the sputtering and the depth resolution in depth profiling analysis by the GDOES. The SEM images of the GDOES crater bottom revealed three main classes of surface textures; 'rough', 'concaved' and 'smooth'. Electron back-scattered diffraction was used to determine the crystal orientation of the typical micro-areas. The depths of these areas were measured using profilometry, and these depths were correlated with crystal orientation and surface texture.

Most of the areas with 'rough' texture are close to [111], the 'concaved' areas are close to [001], whilst the 'smooth' areas have higher-index planes in a region between the [111] and [001] zone-axes. The fastest erosion occurred when the normal surface vector is parallel to [001]. The difference in the sputtered depth between [001] and [111] increases as the sputtering time increases from 500 s to 1000 s. As the sputtering time increases further, the differences in the sputtering depth of different areas does not continue to increase but rather begins to decrease. This may be because the erosion rate in different regions balances when the sputtered crater depth is over the mean crystal depth (as it becomes likely that a mixture of faster and slower crystallites have been encountered).

The results imply that samples with small grain size will have the best possible depth resolution in GDOES. For iron samples with larger crystallite size, depth resolution will be compromised by about 20% of the total crater depth, although this tends to a constant resolution at greater than the average crystallite depth.

Chapter 4 Pitting Phenomena in Surface Evolution of Coated Samples

4.1 Introduction

Sputtering in GDOES, as with other ion etching techniques, can induce micro-textures on etched surfaces (Payling, 1997a and Quentmeier, 1997). When a carbon-coated silicon wafer was etched in the GDOES, an interesting surface morphology, the 'pitting' phenomenon, was found, as seen in Figure 4.1(a). No pits were found on silicon wafers without carbon films after GDOES etching, an example of which is seen in Figure 4.1(b). The etched surface of the silicon wafer, which had a grill mask during the carbon-coating process, clearly shows that the pits are only present in the region with the carbon film, as seen in Figure 4.1(c).

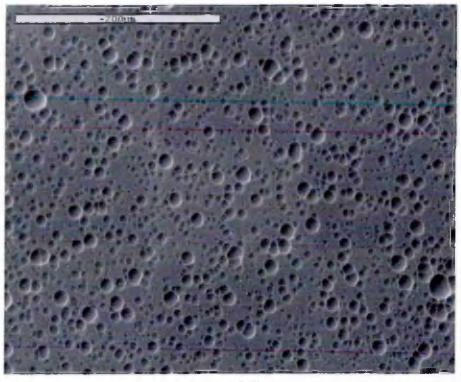

(a)

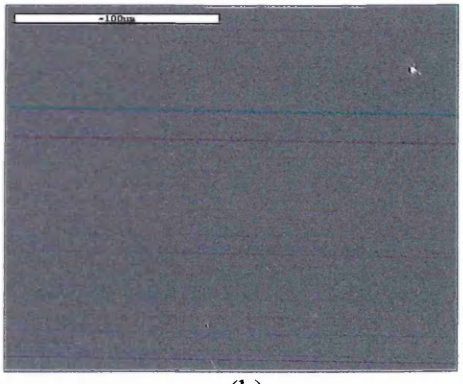

(b)

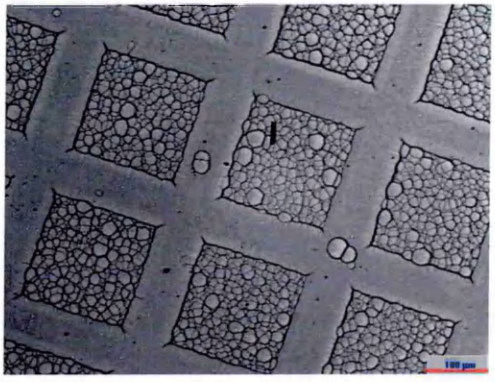

(c)

Figure 4.1. (a) SEM image shows pitting phenomena on a silicon surface after GDOES etching of the carbon-coated silicon wafer.
(b) SEM image shows that there are no pits on a silicon surface without carbon film after GDOES etching.
(c) Optical microscopy image shows pits only in the region with carbon-coated film before GDOES etching.

The development of surface topography under heavy ion-bombardment is well known. It is dependent on the ion flux and energy, initial surface state, and crystalline structures and defects in grains. Carter *et al.* (1983) have classified the stages of development of surface topography and its dependence on the ion flux. The process of ion bombardment-induced sputtering creates at least atomic-scale discontinuities at the surface, and such effects may be observed for ion fluence of up to 10^{16} ions cm^{-2}. As ion fluence increases above this level, the features become microscopically observable with a size in the range 100–10,000 Å. At a fluence of 10^{17} ions cm^{-2}, when sufficient bombardment-induced defects are built up within the crystal, local variations in sputtering yield occur, resulting in major changes in surface topography. In this stage, the development of etch pits, cones and ripples and a further striking three-dimensional mosaic was observed. At very large ion fluence above 10^{19}–10^{20} ions cm^{-2}, the features assume macroscopically observable dimensions of sub-millimetre size. For etched pits, which are of more interest in the investigation here, it is suggested in the literature that they originate presumably from intrinsic defects, and have very well-defined shapes that are identical within each grain but differ in shape from grain to grain. An increase in the fluence of bombarding ions usually results in the appearance of more small pits and the already-existing pits grow in size, eventually overlapping with others but, until that happens, always retaining their characteristic shape. Examples can be seen in Figure 4.2 (Cater *et al.*, 1983), obtained from Cu, W and Si by Ar ion bombardment with ion energies of either 4 or 40 keV.

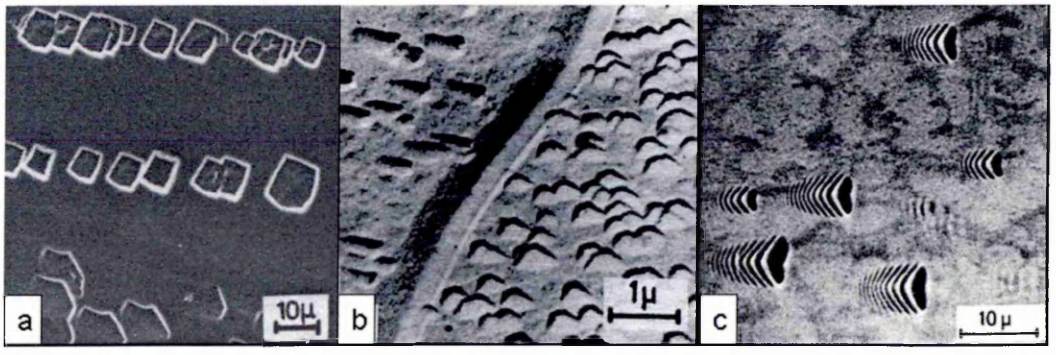

Figure 4.2. Pitting phenomena caused by bombardment with high energy Ar ions (Carter *et. al.*, 1990). (a) 40 keV argon ion bombardment on Cu. (b) 4 keV argon ion bombardment on W. (c) 40 keV argon ions bombardment on Si, 10^{20} ions cm^{-2} at 45° to surface normal.

In GDOES sputtering, using the conditions 600 V/25 mA and using a 4 mm anode, an ion flux in the order of 10^{18} (ions cm^{-2} s^{-1}) is expected. Computer modelling indicates that the ion energies typically lie in the range 50 to a few hundred eVs (Bogaerts and Gijbels, 1997). Some features, like cones or pyramids, ripples, concaved dots and mosaic patterns can also be observed in the bottom of craters sputtered by GDOES (Chapter 3), which are very similar to those mentioned in the literature. However, for the pitting phenomenon, which will be discussed later, no reports on this or similar have been found in the literature. The pits may have different mechanisms of formation and geometric characteristics compared with the pits formed on well-defined surfaces under high-energy ion bombardment. Further investigations on the characteristics and development of the pits also showed that the pitting phenomenon has a potential application as a random array of micro-lenses. With a parallel light beam irradiating the pitted surface, a set of luminous spots, which are focused on a layer at a certain distance above the surface by pit surfaces, can form a unique luminous pattern. Figure 4.3 shows a set of luminous spots that correspond to the pits in optical images of a pitted surface. Due to the stochastic nature of the creation of the micro-lens, the luminous pattern created is unique and could be used in marker technology applications.

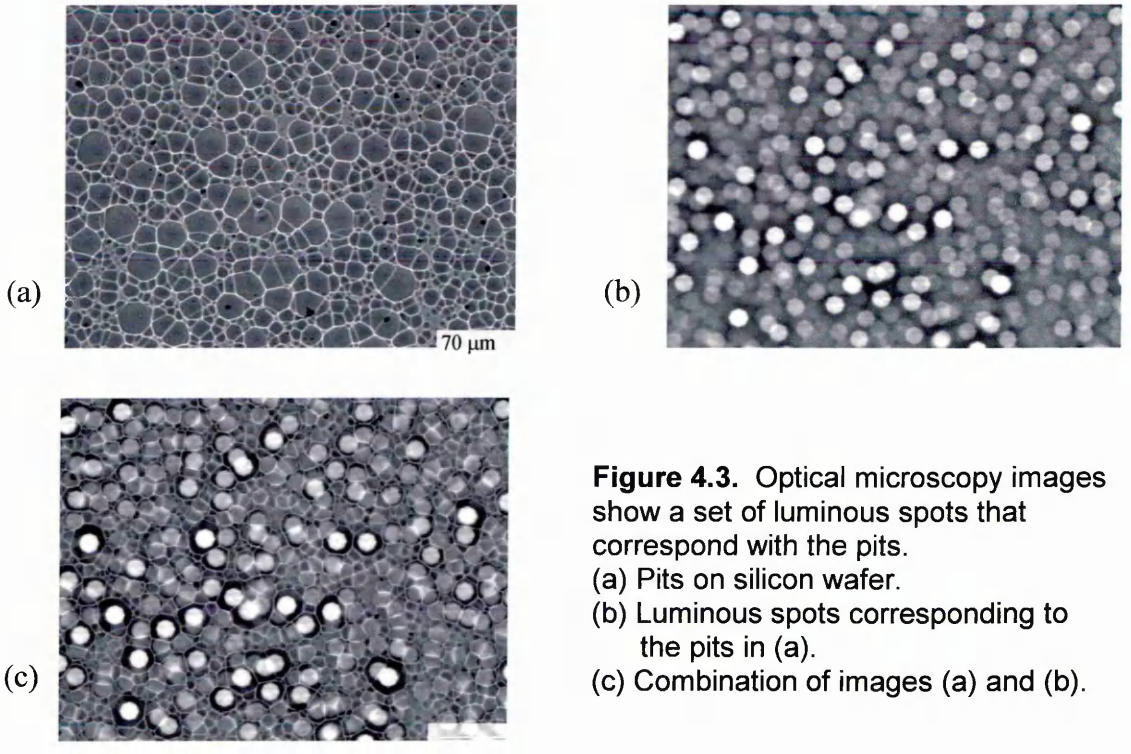

Figure 4.3. Optical microscopy images show a set of luminous spots that correspond with the pits.
(a) Pits on silicon wafer.
(b) Luminous spots corresponding to the pits in (a).
(c) Combination of images (a) and (b).

In this chapter, the mechanism of pit generation on surface-coated silicon wafers will first be discussed. It appears that pit formation is mainly due to a large difference in the sputtering rates between the coating and the substrate. The density of pits determined from SEM images revealed different processes of pit development in etched layers of carbon film and silicon substrate. Finally, geometries and the development of the pits on silicon surfaces were investigated in detail. A model for the pitting phenomenon is given based on AFM results.

4.2 Experimental

4.2.1 Coating processes

All films in this investigation were grown in a vacuum coating system (Edwards E306A). Different materials of carbon, aluminium, silver, germanium and silicon were deposited onto silicon wafers. For carbon film preparation, the evaporation source consisted of two carbon electrodes. One of them was fixed and another, sliding in an insulated bush, was pressed against the fixed electrode by a light spring. The contact region was tapered to a reduced cross-section so that passage of an electric current resulted in local resistive heating of the contact area. The heating is sufficient to cause the carbon to sublime from the narrowest part. For other coated materials, a resistance-heated filament made from a basket-shaped tungsten wire was used as the evaporation source. Coating materials were cut into chips of millimetre size so that it was able to fit the chips into the basket.

4.2.2 Estimation of thickness of the coatings

The thickness of the film deposited by the vacuum coating system was in the range of tens to hundreds of nanometres. It is difficult to measure the thickness by a profilometer or other common techniques. In this study, the thicknesses of the films were estimated by calculation. Given that the coated material was vaporised and

deposited on the substrate surface in an evacuated chamber under a vacuum of $<10^{-5}$ bar, the vaporised particles in the chamber can be expected to diffuse isotropically. Then, in any part of a sphere with the vaporising point as the centre, the thickness should be same. Therefore, assuming that the sample surface is a part of the sphere, the thickness of the film can be calculated from the mass loss of the coating material and the density of the film. In this study, the mass loss of coating materials was obtained with a microbalance. For carbon film, the density is 2.2 g/cm^3 (Watt, 1985). However, densities for other films in this study were not found in the literature. Therefore, the densities of bulk materials of aluminium, silver, germanium and silicon were chosen as the densities of the films. The use of bulk densities may result in errors in the calculations of thickness of the films. Coarse particles vaporised from coating materials can also cause the calculated thickness of the coating to be less than that of real values.

The accuracy of the calculated thickness of the carbon film on the silicon wafers was tested by sputtering the coated samples in the GDOES. Silicon wafers with different calculated thicknesses of the carbon film of 110, 180, 215 and 260 nm were sputtered until the carbon films were completely removed. Figure 4.4 shows GDOES profiles of carbon and silicon intensities versus sputtering time for the carbon-coated silicon wafers. If the midpoint of silicon intensity between its lowest and highest levels is considered as a reference point for the interface between the coating and the substrate, the sputtering times corresponding to the points for those samples were 65, 110, 131 and 163 seconds. Figure 4.5 shows a good correlation between the thickness and the sputtering time. If the midpoint is considered as a reference of the interface, the thickness of the carbon film could be indirectly measured by subtracting the sputtered depth of silicon wafer only from the depth of the sputtered crater. For example, for the silicon wafer with the 260 nm-thick carbon film, the total sputtering time was 241 seconds. The depth of the sputtered crater was measured by a profilometer as 1.20 μm. In the sputtering conditions used in this study the etching rate, defined as etched depth in nanometres per second, of the silicon wafer was measured as ~12 nm/sec. Therefore,

the thickness of the carbon film would be 265 nm, which is close to the calculated thickness of 260 nm.

(a)

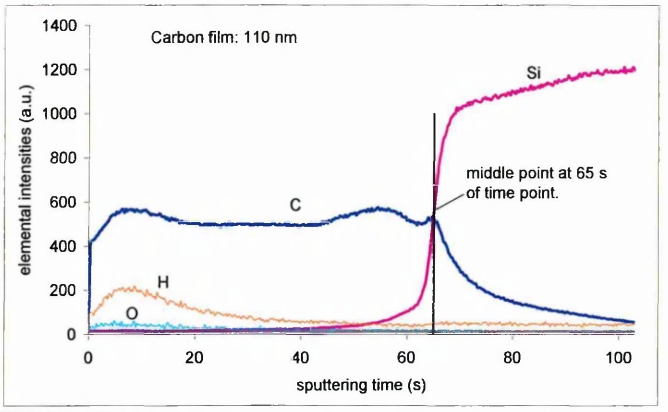

(b)

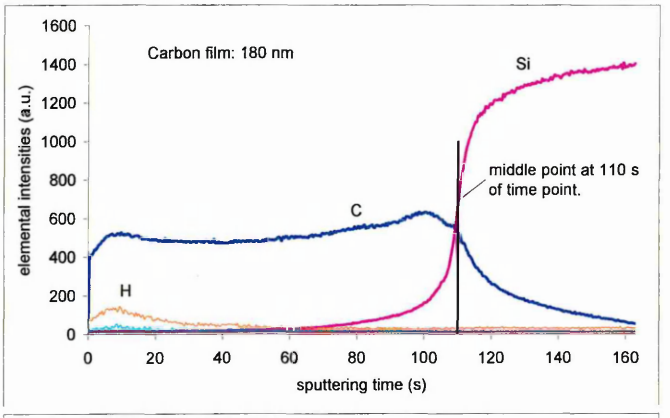

(c)

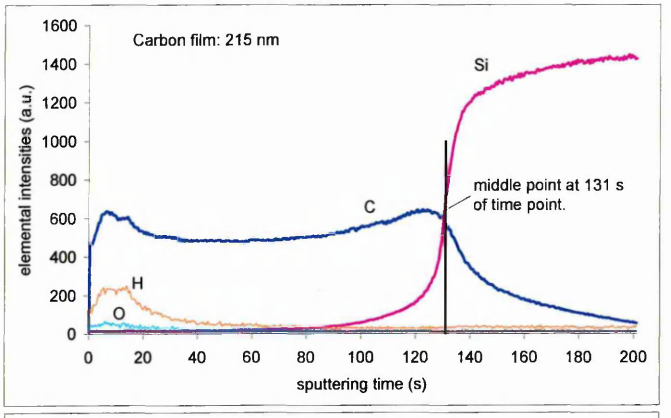

(d)

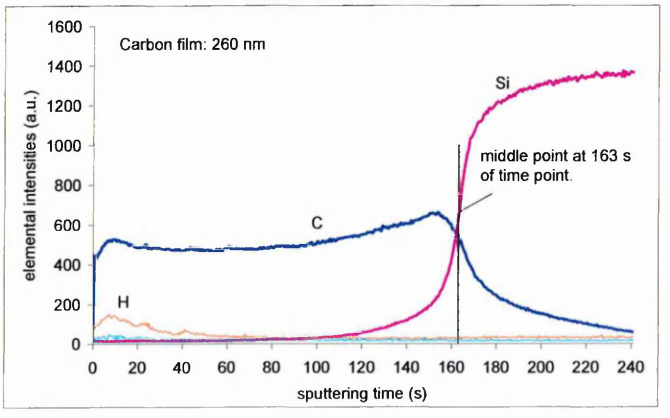

Figure 4.4. GDOES depth profiles of carbon-coated silicon wafers with different thicknesses of carbon film. The thicknesses were (a) 110 nm, (b) 180 nm, (c) 215 nm and (d) 260 nm. GDS parameters: 600V/25mA/4 mm anode.

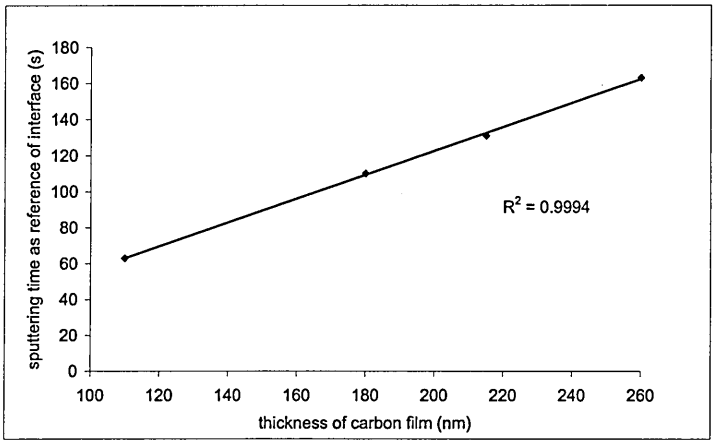

Figure 4.5. Calculated thickness of carbon film against the sputtering time at the mid point of the profile of the silicon intensity. The good correlation shows the reliability of the calculated thickness of the carbon film.

4.2.3 AFM measurements

The pitting phenomenon was identified by optical microscopy and SEM images of the sputtered surfaces. Nevertheless, they cannot provide 3-D data of the pits. 3-D scanning by a laser-beam profilometer can give some information for relatively large pits, but its resolution is not good enough to give information on the geometry of smaller pits. The Atomic Force Microscope (AFM) makes it possible to measure the details of the pits in three dimensions even when pits' diameters are only of the order of a micron or less. AFM probes the surface of a sample with a sharp tip a couple of microns long and usually around five nm in diameter. The tip is located at the free end of a cantilever that is 100 to 200 μm long. Forces between the tip and the sample surface cause the cantilever to bend, or deflect. A detector measures the cantilever deflection as the tip is scanned over the sample, or the sample is scanned under the tip. The measured cantilever deflections allow a computer to generate a map of surface topography (Howland and Benatar, 1993). Figure 4.6 shows a schematic diagram of an AFM. A laser beam bounces off the back of the cantilever onto a position-sensitive photodetector (PSPD). As the cantilever bends, the position of the laser beam on the detector shifts. The PSPD itself can measure displacements of light as small as 10 Å. The ratio of the path length between the cantilever and the detector to the length of the

cantilever itself produces a mechanical amplification. As a result, the system can detect sub-angstrom vertical movement of the cantilever tip.

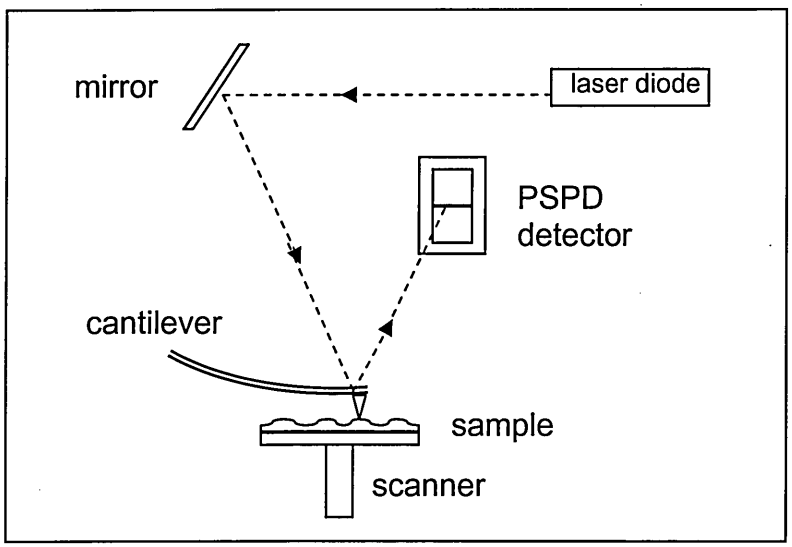

Figure 4.6. Schematic diagram of an AFM

Once the AFM has detected the cantilever deflection, it can generate the topographic dataset by operating in one of two modes: constant-height or constant-force mode. In this study, the AFM was working in the constant-force mode. In this mode, the deflection of the cantilever is used as input to a feedback circuit that moves the scanner up and down vertically, responding to the topography by keeping the cantilever deflection constant. In this case, the image is generated from the scanner's motion. With the cantilever deflection held constant, the total force applied to the sample is constant.

AFM images of the pits on surfaces of silicon wafers showed that the pits have circle-like edges before joining with others. Section profiles of a pit along two cross-diameters of the circle were symmetrical about their centre lines. Examples are shown in Figure 4.7(a) (the circle edge) and Figure 4.7(b) (the symmetric feature of the profile of a pit). The observations of the circle edges and the symmetric feature led to an assumption that the pit's surface could be a part of a sphere. The assumption can be proved by calculating the radii of the profile based on any three points on it, as any three

points in a plane can define a unique circle. If the calculated radii based on the points on two cross-profiles of a pit have similar values, the pit surface should be regarded as an approximate sphere.

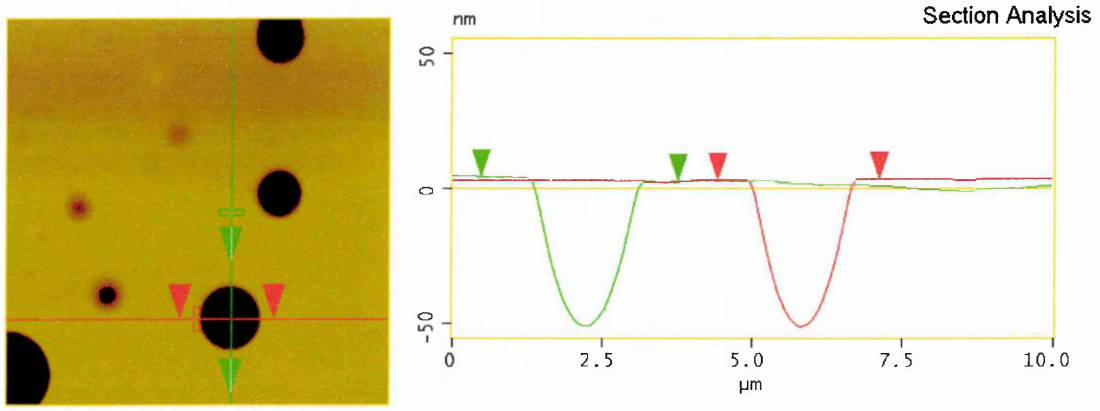

(a) (b)

Figure 4.7. AFM image of a pit and two profiles obtained by cross-cutting the pit along its diameters.

4.3 Experimental Results and Discussion

4.3.1 Experiments with different coatings

The 'Pitting' phenomenon was first found on the surface of a carbon-coated silicon wafer after the GDOES etching. When the carbon film was completely removed, a random array of pits of characteristic shape was present on the etched surface of the silicon substrate, as seen in Figure 4.1(a). A carbon-coated silicon wafer covered with a grill mask during the coating process was also prepared. Figure 4.1(c) clearly shows that the pits were only present in the regions with the carbon film after the surface was etched by GDOES sputtering. No pits can be found in the areas without carbon film after the GDOES etching. It seems that the pitting phenomenon only occurs when silicon wafers are coated with a thin film of carbon. It is known that the sputtering rate of carbon is the lowest among the elements in common use. For example, the measured sputtering rate of carbon in the GDOES is 18 times lower than that of pure iron, while silicon is only about 6 times lower. The etching rates (nm/sec) in GDOES (under the

conditions of a 600 V/25 mA/4 mm anode) for carbon film and silicon wafers are ~1.65 nm/sec and ~12 nm/sec, respectively.

A series of samples with different coatings of silver, aluminium, silicon and germanium were produced in order to study why and how the pitting phenomenon occurs. The pure metals silver and aluminium were selected as coating materials because these metal films are expected to have a crystalline structure. However, carbon, silicon and germanium films are believed to be amorphous. On the other hand, the sputtering rate of aluminium in GDOES is the lowest among the common metals. The measured sputtering rate of aluminium in the GDOES in this study is about 2.5 times lower than that of pure iron and comparable to that for Si.

In GDOES etching, a display of elemental profiling is simultaneous with the etching evolution. This allows the etching to be stopped in a particular layer of the evolution. For example, the etched surface could stay in the coating, or the etched surface could reveal the substrate material just after the coating is completely etched away or the etched surface could be the substrate surface that has experienced a long etching time after the coating has been completely removed.

Silver and aluminium were first coated onto silicon wafers. The calculated thickness of the aluminium film was around 150 nm. The GDOES etching parameters were 600 V and 25 mA with a 4 mm anode tube. As the etching rates in GDOES are different for the silver and aluminium films, the etching times to the interface between the film and the silicon substrate were ~1 second and ~4.5 seconds for silver and aluminium, respectively. Therefore, a variety of etching times were chosen, which were 2, 5, 8 and 30 sec for the silver-coated silicon and 5, 8, 10 and 30 sec for the aluminium-coated silicon, in order to observe morphologies of the surfaces in different etched layers. GDOES profiles of the silver- and the aluminium-coated silicon wafers indicated that all the burns with the different etching times mentioned above had removed all the coating material and revealed substrate surfaces completely. The etched surfaces were observed

in the SEM (JEOL 840). With short etching times (etching times up to 8 sec for the silver-coated silicon wafer and up to 10 sec for the aluminium), no pits were found on the etched surfaces of both coated silicon wafers (Figure 4.8(a) and (c)). These short etching times corresponded to at most 7 sec and 6 sec of substrate etching times for the silver- and aluminium-coated silicon wafers, respectively. With a long etching time of 30 sec, very few pits were found on the etched surface for Ag-coated silicon, as seen in Figure 4.8(b). This time was corresponded to ~29 sec of substrate etching time for the silver-coated silicon wafer. However, after 30 seconds' etching for the aluminium-coated silicon (corresponding to ~25 sec of substrate etching time), a pit-like topography on the surface was produced, an example of which can be seen in Figure 4.8(d), but at a much lower density than for the carbon-coated silicon wafer.

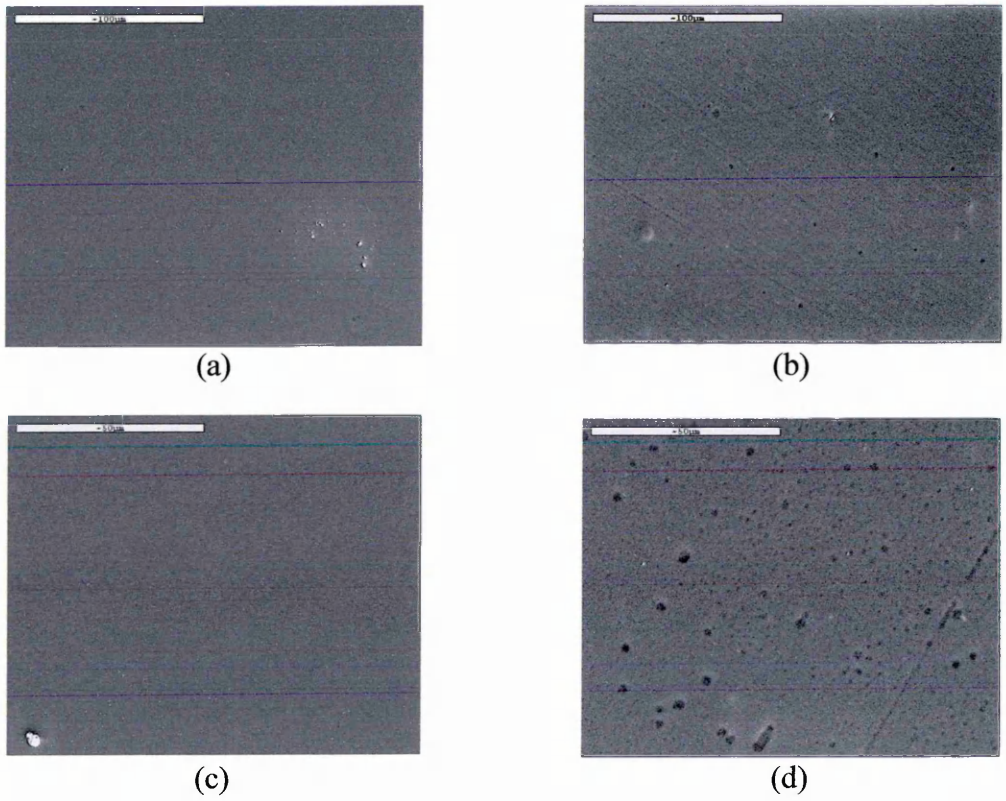

Figure 4.8. SEM images of etched surfaces of Ag- and Al-coated silicon wafers after short and long times of GDOES etching. GDOES parameters: 600 V/25 mA/4 mm anode.
(a) Sample: Ag-coated silicon wafer, etching time: 8 sec, no pits were found on the etched surface.
(b) Sample: Ag-coated silicon wafer, etching time: 30 sec, very few pits on the surface.
(c) Sample: Al-coated silicon wafer, etching time: 10 sec, no pits on the surface.
(d) Sample: Al-coated silicon wafer, etching time: 30 sec, a pit-like topography was found on the surface.

A germanium film was deposited onto silicon wafer with a calculated thickness of around 90 nm. The GDOES setting was the same as above. The etching time to the interface is about 1.5 seconds, therefore different etching times of 2, 5, 10 and 30 seconds were selected to obtain the etched surface in different layers of the substrate. SEM images of the etched surfaces showed no pits on the etched surfaces with short etching times up to 10 seconds (corresponding to at most ~8 sec etching for the substrate only), e.g. see Figure 4.9(a). With a longer etching time of 30 seconds (corresponding to an etching time of ~28 sec for the substrate only), small pits with low density were again observed in the SEM image of the etched surface, as seen in Figure 4.9(b).

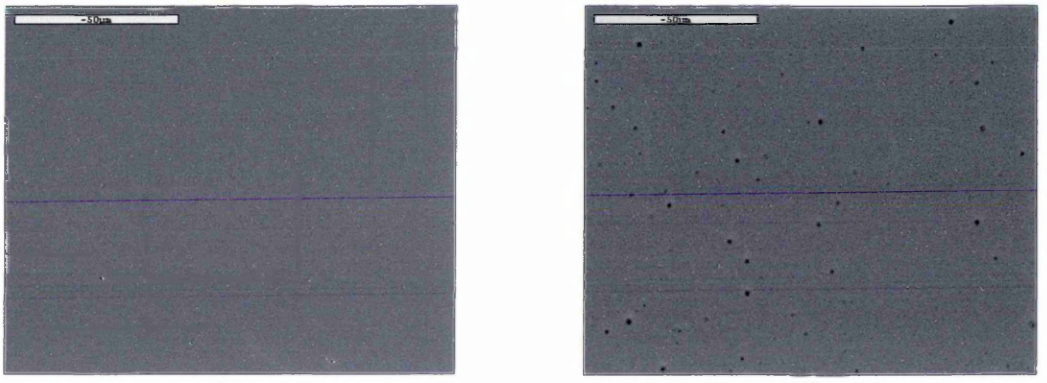

(a) (b)

Figure 4.9. SEM images of etched surfaces of Ge-coated silicon wafers after 10 and 30 seconds of GDOES etching respectively. GDOES parameters: 600V/25mA/4 mm anode.
(a) Sample: Ge-coated silicon wafer, etching time: 10 sec, no pits were found on the etched surface.
(b) Sample: Ge-coated silicon wafer, etching time: 30 sec, small pits on the surface.

Figure 4.10 shows an SEM image of the pits on an etched surface of a silicon wafer. The silicon wafer was coated with carbon film 135 nm thick. The same etch conditions of GDOES as that in Figures 5.8 and 5.9 were used. The total etching time was 107 seconds and the etch time for the substrate only was about 25 seconds. From Figure 5.10, it can be seen that the density and the size of the pits are much larger than those with Ag, Al and Ge films.

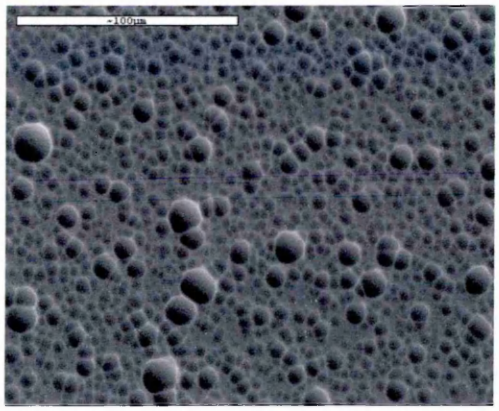

Figure 4.10. Pits on an etched silicon wafer. The silicon wafer was coated with carbon film 135 nm thick and etched in GDOES under the same conditions as that in Figures 5.8 and 5.9, but much higher pit density was obtained. The total etching time was 107 sec and the etching time for the silicon substrate was ~25 sec. GDS: 600V/25mA/4mm anode.

The topography of the sputtered surface is mainly dependent on the characteristics of argon ions, the original surface definition and the microstructures of the sample. In this case, the GDOES parameters were set to keep the ion energy and fluence constant. Single-crystal silicon wafers were selected as the substrates. Therefore, the only difference was the coated film, which could act as a mask on the surface. Differences in film structures and defects were almost inevitable in the coating process. These differences will introduce a difference in sputtering yields in some localised areas and consequently result in a specific topography on the surface when the film is etched away. The experimental results above show that no pits were observed on the etched surfaces with short etching time, which does not mean there is no sputtering-induced surface topography. In fact, the topography on the etched surfaces could be at less than the micro-scale, which cannot be distinguished in the SEM images. With a long substrate etching time after the film is etched away, the topography on the sub-micron scale is developed up to the micro size. It is the pitting phenomena introduced by the etching under GDOES sputtering that were observed on silicon surfaces with metal-, non-metal- and semiconductor-coating in SEM images with long etching times.

The 'pitting' phenomenon was also confirmed by etching Si-coated silicon wafers. The Si coating has an amorphous structure when grown at room temperature, as do the carbon and germanium films. Two silicon wafers with different calculated thicknesses

(~50 nm and ~160 nm) of the silicon coating were prepared by evaporation. The interface between the silicon film and silicon substrate was identified in GDOES depth profiling by a peak in the carbon signal and a step in the silicon signal at the interface. Under the same GDOES conditions, the etching time to the interface for the silicon films of 50 nm and 160 nm thickness were less than 0.1 and ~1.2 seconds, respectively. It can be seen in SEM images in Figure 4.11(a) and (b) that a pit-like topography was revealed on the etched surfaces with the thick silicon film after only eight seconds of etching. However, for the thin silicon film, no pits were observed even after 10 seconds of GDOES etching, as seen in Figure 4.11(c) and (d). The significant pit-like topography in Figure 4.11(a) and (b) is mainly due to the thick silicon film providing a longer time than the thin film for the ions to etch the silicon surface in some local areas. Therefore, the etching rate of the coating material should play a key role in the pit formation. Although the pit-like topography can be introduced on silicon surfaces coated with silver, aluminium, germanium and silicon films using GDOES sputtering, the pit size was much smaller and the pit densities were lower than that on the carbon-coated silicon surface. The reason for this difference can be explained by the difference in etching rates between the film and the substrate. For the carbon film, the etching rate was measured as ~1.65 nm/sec at GDOES conditions of 600 V/25 mA with a 4 mm anode. It is seven times lower than that of the silicon wafer (~12 nm/sec). Etching rates of other films in this study cannot be obtained due to the inaccuracy of the calculated thickness of the films and much shorter etching time than the carbon film. However, sputtering yields of carbon, silver, aluminium, germanium and silicon under argon ion bombardment were obtained by the computer simulation (SRIM, 2003), with the ion energy of 500 eV and for 100 atomic layers, and are listed in Table 4.1.

Table 4.1. *Calculated sputtering yields (atoms/ion) of carbon, silver, aluminium, germanium and silicon by the computer simulation (SRIM, 2003) and estimated etching rates (nm/sec) for silicon, aluminium, germanium and silver films according to the etching rate of the carbon film 1.65 nm/sec and the simulated sputtering yields.*

	Carbon	Silicon	Aluminium	Germanium	Silver
Sputtering yield	0.13	0.50	0.68	1.30	2.50
etching rate	1.65	14.0	16.3	43.1	59.8

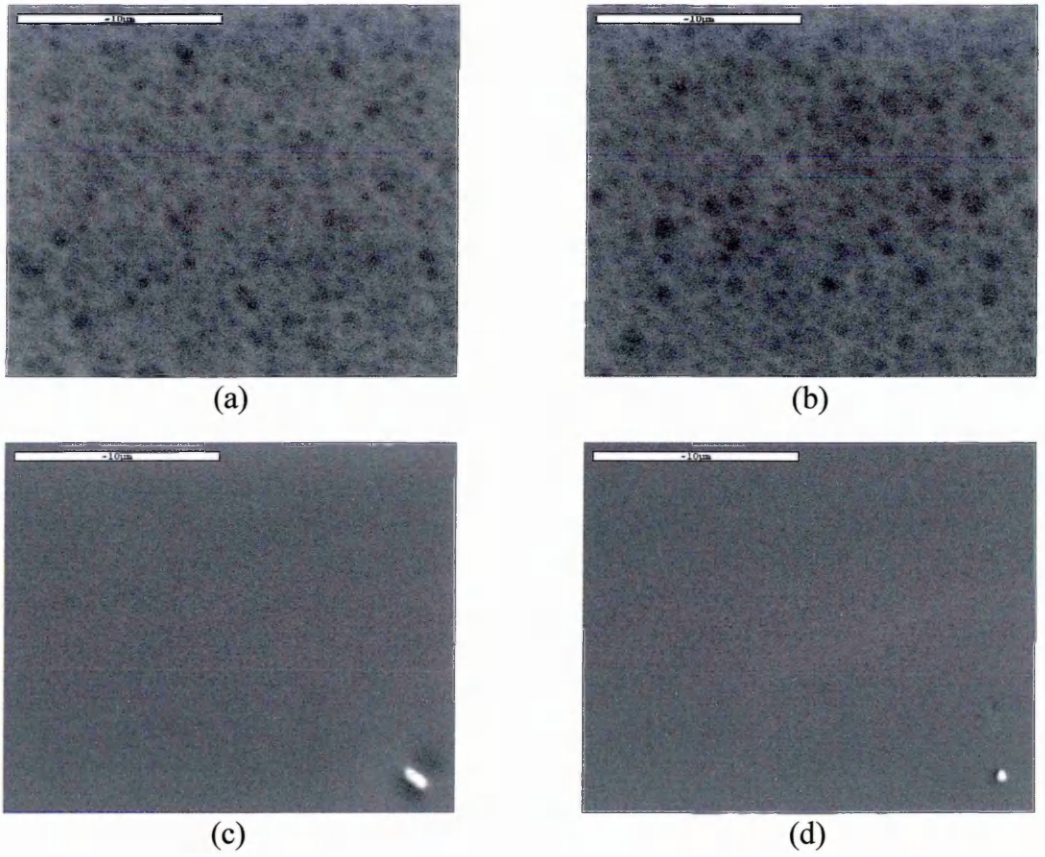

Figure 4.11. SEM images show pits-like topography on the etched surfaces with the thick silicon film even after 8 seconds of etching. However, for the thin silicon film, no pits can be observed even after 10 seconds etching. GDS: 600V/25mA/4mm anode.
(a) sample: silicon wafer with coated Si film in 160 nm thick, etching time: 8 sec;
(b) sample: silicon wafer with coated Si film in 160 nm thick, etching time: 23 sec;
(c) sample: silicon wafer with coated Si film in 50 nm thick, etching time: 5 sec;
(d) sample: silicon wafer with coated Si film in 50 nm thick, etching time: 10 sec.

To compare the etching rates of two materials, the sputtering yield must be converted to the sputtering rate based on Eqn. (2.13). Therefore, a ratio of etching rates of two different targets 1 and 2 can be expressed as:

$$\frac{P_1}{P_2} = \frac{S_1}{S_2}\frac{m_{t1}}{m_{t2}}\frac{\rho_2}{\rho_1}, \tag{4.1}$$

where P is the etching rate of the target; S is the sputtering yield; m_t is the atomic mass of the target and ρ is the density of the target. In the case of the carbon film and the silicon wafer, the ratio of the etching rates of the silicon wafer to the carbon film was calculated as 8.5 based on the sputtering yields in Table 4.1. That is, the etching rate of

carbon film is 8.5 times lower than that of the silicon wafer, which is close to the measured results (seven times lower). The etching rates of the silicon, aluminium, germanium and silver film were calculated according to the etching rate of the carbon film (1.65 nm/sec) and the sputtering yields in the table, which are also listed in Table 4.1.

Figure 4.12 shows the SEM images of a carbon film on pure iron after GDOES etching. The calculated thickness of the carbon film was ~600 nm. After 155 seconds' etching in the GDOES at 700 V/30 mA, the surface layer was still in the carbon film, which was confirmed by GDOES profiles for the Fe and C intensities. From Figure 4.12(a) it can be clearly seen that the pits formed initially. Occasionally we can even see the pits on the substrate where the carbon film was broken over a relatively large area, as seen in Figure 4.12(b).

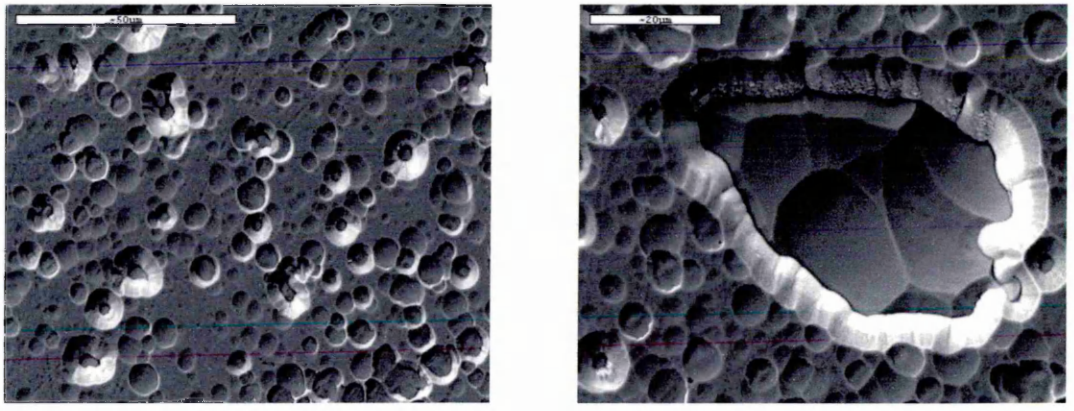

(a) (b)

Figure 4.12. SEM images of pits on a surface of carbon-coated pure iron after GDOES etching. The surface layer was still in the carbon film. Original thickness of the carbon film: ~600 nm. Etching time: 155 sec. GDOES parameters: 700V/30mA/4mm anode.
(a) The pits formed initially in carbon layer.
(b) The pits on the substrate where the carbon film was broken over a relatively large area.

The pitting phenomenon was observed not only on single-crystal silicon surfaces, but also occurred on pure polycrystalline iron. Figure 4.13 shows an SEM image of a surface of carbon-film-coated pure iron after the film has been completely etched away

by GDOES sputtering. In the image, the ripple and smooth textures represent different crystallites with different orientations (Chapter 3). The pits formed on both the ripple and smooth areas, suggesting that the crystal structure has no effect on the pitting phenomenon.

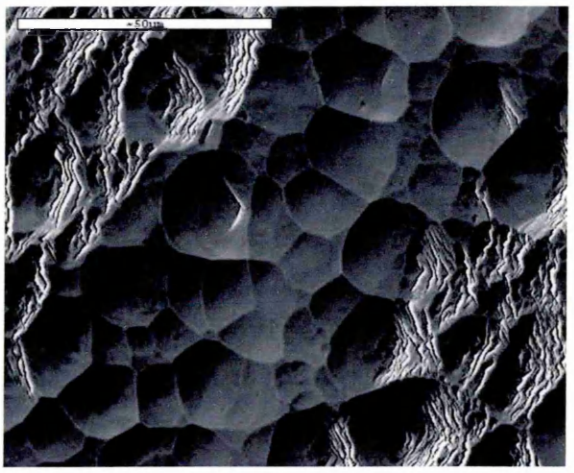

Figure 4.13. SEM image of pits on a surface of carbon-coated pure iron after the film was completely etched out in the GDOES. The pits generated on the 'ripple' and the 'smooth' areas imply crystal structure has no effect on the pitting phenomenon.
Thickness of the carbon film: ~600 nm.
Etching time: 200 seconds.
GDS: 700 V/30 mA/4 mm anode.

4.3.2 Effect of carbon film thickness on pit formation

Silicon wafers with different thicknesses of carbon film have been prepared to investigate the effect of film thickness on pit formation. The calculated thicknesses of the films were 50, 110, 215 and 260 nm. The etching parameters used in the GDOES were 600 V/25 mA and a 4 mm anode. The samples were etched in the GDOES until the silicon signal just began to rise. The burns were stopped when the silicon intensity reached 0.2 V, which is only ~4% of the Si signal on a pure silicon wafer. This implies that a few of the argon ions were only just penetrating the carbon film in some local areas and were bombarding the silicon surface. In this stage, most of the ions were still bombarding onto the carbon film. SEM images in Figure 4.14 show pits on the etched surfaces of the carbon-coated silicon wafers with original thicknesses of the carbon film of 50, 110 and 260 nm respectively. From the SEM images, it can be seen that diameters of the biggest pits increase as the original thickness of the carbon films increases. However, the smallest pits have similar size, which can be seen more clearly in the SEM images in Figure 4.15. Densities of the pits were determined for each of the

samples corresponding to that in Figures 4.14 and 4.15, which are shown in Figure 4.16. The density decreases as the original thickness of the carbon film increases.

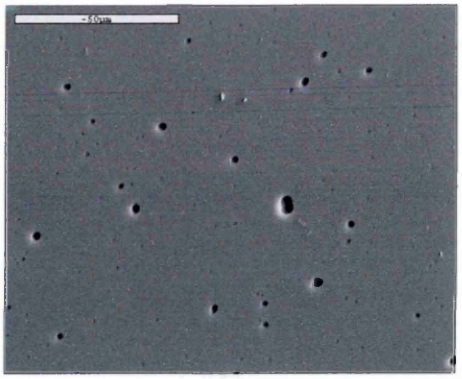

(a)

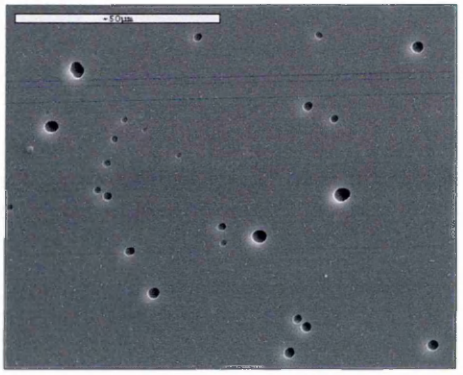

(b)

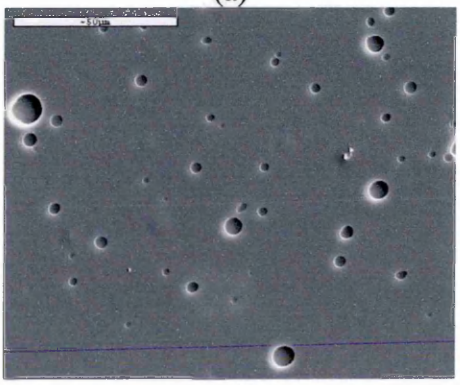

(c)

Figure 4.14. SEM images of pits on etched surfaces of carbon-coated silicon wafers with different original thicknesses of the films. The surfaces were in the layers in where argon ions just penetrated through the films and silicon atoms began to be sputtered out. GDOES parameters: 600 V/25 mA/4 mm anode. Original thickness of carbon films and etched times: (a) 50 nm/20 sec.
(b) 110 nm/39 sec.
(c) 260 nm/106 sec.

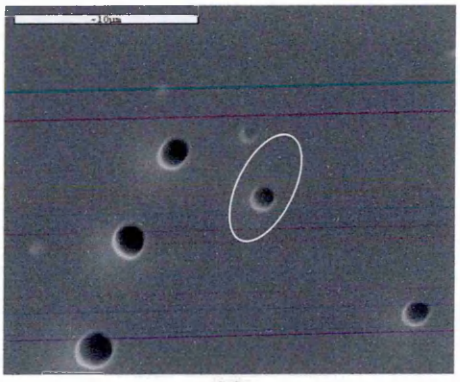

(a)

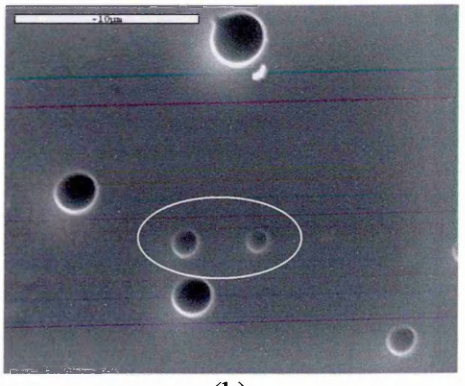

(b)

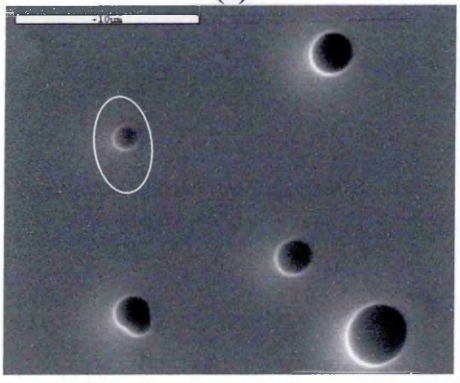

(c)

Figure 4.15. SEM images of the smallest pits on the surfaces of carbon layers. Sizes of the smallest pits in the different layers were almost same, around one micron. GDOES parameters: 600 V/25 mA/4 mm anode. Original thicknesses of carbon films and etched times were:
(a) 110 nm/39 sec,
(b) 215 nm/83 sec,
(c) 260 nm/106 sec.

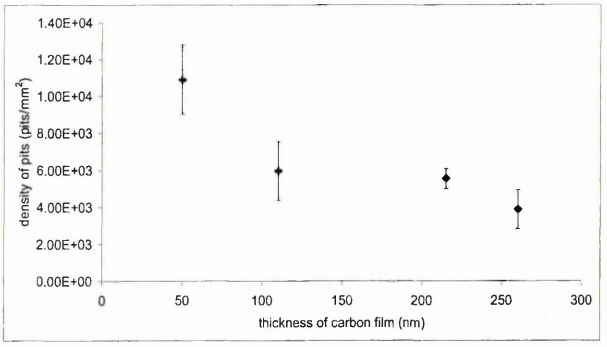

Figure 4.16. Densities of the pits on the surfaces of carbon layers of the samples corresponding to that in Figures 4.14 and 4.15.

The sputtering times for the samples in Figures 4.14 and 4.15 suggested that thicknesses of the remaining carbon films differ according to the original thicknesses of the carbon film. For example, the sputtering times for the samples with thicknesses of 110 nm, 215 nm and 260 nm were 39 sec, 83 sec and 106 sec, respectively. However, the GDOES profiles of the samples (see Figure 4.4) show that sputtering times to the interfaces between the carbon film and the substrate were 65 sec, 131 sec and 163 sec, respectively. Therefore, the thicknesses of the remaining films could be estimated as ~45 nm, ~80 nm and ~95 nm, based on the etching rate of the carbon film of ~1.65 nm/sec.

This phenomenon, i.e. the pit density decreasing as the original thickness of the carbon film increases, could be explained by the stochastic roughening model for ion bombardment of surfaces (Carter, 1995). In this model, ion bombardment is considered to erode surfaces only by sputtering in the absence of all other effects. The incident ion flux consists of a random statistical arrival in time and space of individual ions at the surface with each ion sputtering a fixed number of atoms at the point of incidence (the sputtering yield). The model suggested that the 'macroscopic' surface becomes increasingly rough with increasing time (or mean sputtering depth). The surface roughness of the samples in Figures 4.14 and 4.15 were measured and plotted in Figure 4.17. The roughness does increase as the etching time increases, which supports the stochastic roughening. As schematically illustrated in Figure 4.18, shorter sputtering

time will result in a relatively smooth surface structure, which will result in higher pit-densities (Figure 4.18a) than longer sputtering time and a rough structure (Figure 4.18b). Therefore, the stochastic roughening resulted in the higher pit-density and the thin remaining carbon film for the sample with the thin original carbon film. However, the thicker original carbon film required a longer sputtering time before the ions reached the silicon surface, which resulted in the rougher surface and the lower pit-density.

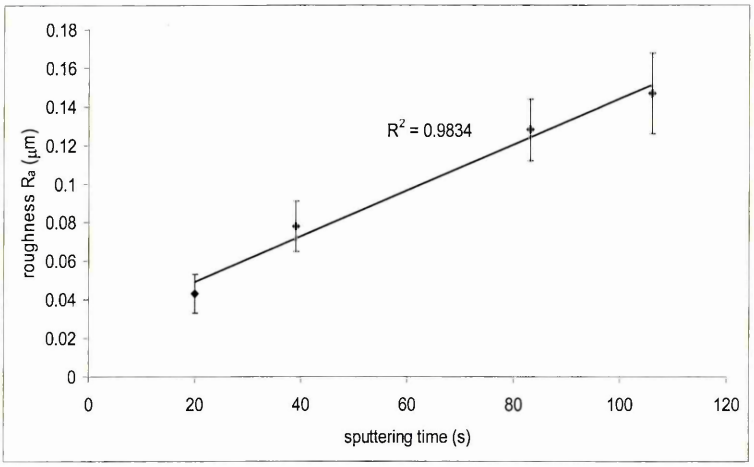

Figure 4.17. Measured roughness of etched surfaces of the samples corresponding to that in Figure 4.16. The roughness increases as the sputtering time increases. A best fit straight line has been fitted to the data with $R^2 = 0.9834$.

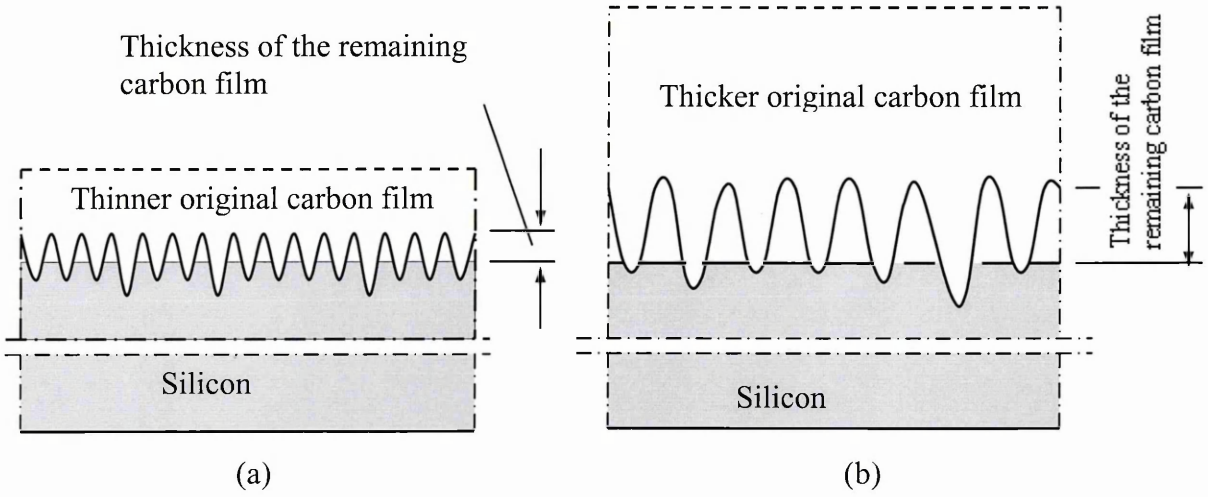

Figure 4.18. Schematic illustration of the stochastic roughening model.
(a) With thinner original carbon film, the stochastic roughing results in a higher density of pit and leaves a thinner remaining thickness of carbon film.
(b) The thicker carbon film requires a longer sputtering time and leaves a rougher surface, which produces the pits on the silicon surface with lower density.

4.3.3 Effect of thickness of carbon film on pits developing in the silicon substrate

By etching the carbon film completely away, pits with different appearances were left on completely exposed surfaces of silicon wafers. Figure 4.19 shows the difference on the surfaces of the silicon wafers with different original thicknesses of the carbon film of 50, 110, 180, 215 and 260 nm. The etching evolution of the samples were monitored by the GDOES depth profiling so that the etching was stopped when the carbon signals were down to ~0.1 V, as shown in Figure 4.4. Variations of densities of the pits and the

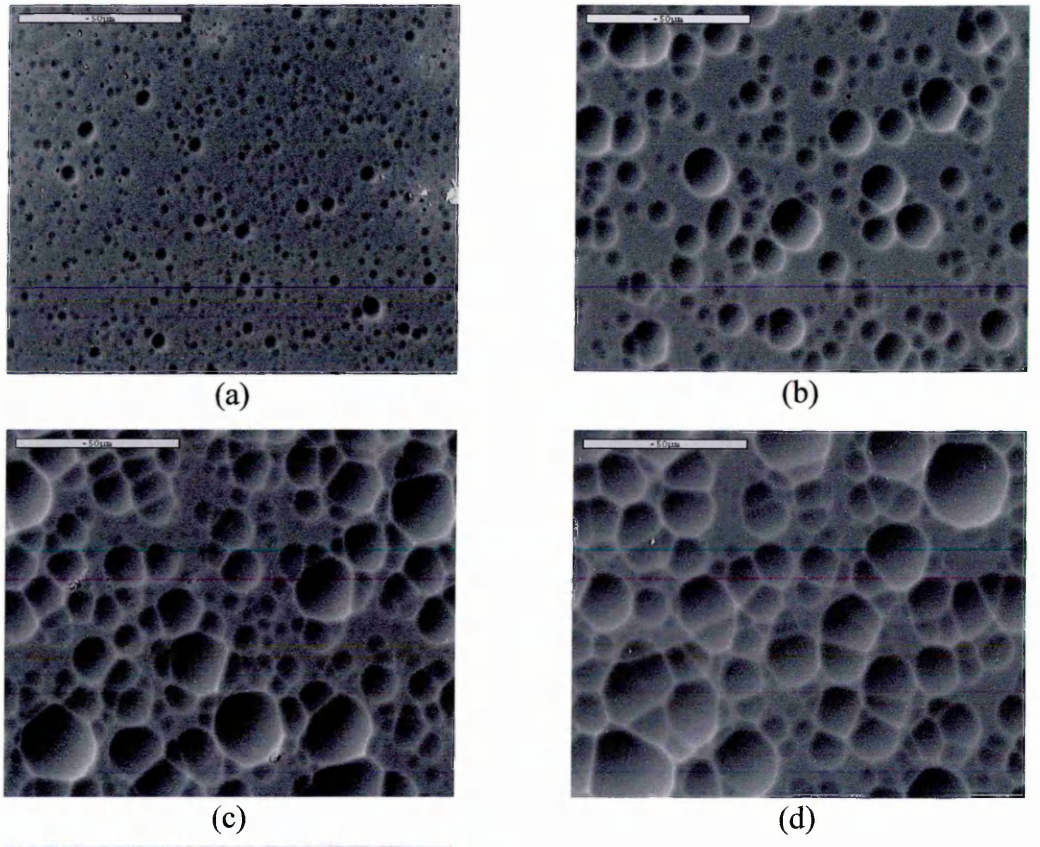

Figure 4.19. SEM images of pits on silicon wafers with different thicknesses of original carbon films when the films were etched out completely. GDOES parameters:600 V/25 mA/4 mm anode. Thicknesses of carbon film and etched times: (a) 50 nm/36 sec.
(b) 110 nm/103 sec.
(c) 180 nm/163 sec.
(d) 215 nm/201 sec.
(e) 260 nm/241 sec.

diameter of the biggest pit corresponding to the thicknesses of the carbon films were plotted in Figure 4.20 and Figure 4.21 respectively. There are two possible explanations for the observed decrease in pit density. First, the density of the pits originally formed on the silicon surface decreases as the thickness of the carbon film increases (Figure 4.16), due to the stochastic roughening effect of the ion bombardment on the carbon film. Second, some small pits have been engulfed by the development of bigger pits (Figure 4.19), as the pits initially formed on the silicon surface with a thicker carbon film have a longer developing time before the film is completely etched away.

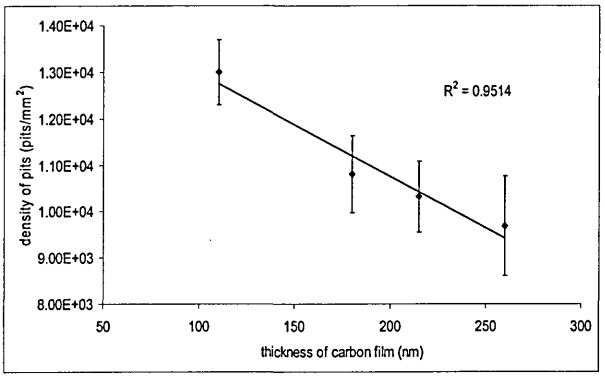

Figure 4.20. Densities of the pits corresponding to the samples in Figure 4.19. A best fit straight line has been fitted to the data with R^2=0.9514.

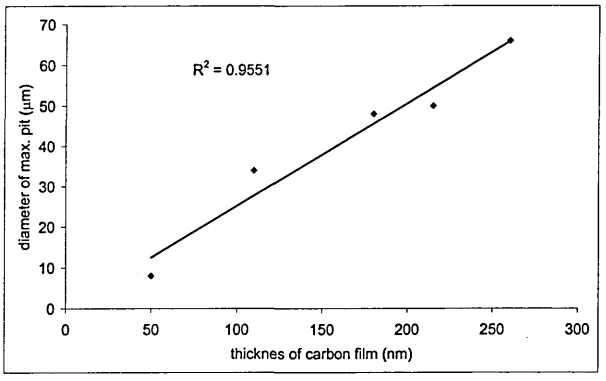

Figure 4.21. Diameter of the largest pit in the samples in Figure 4.19. A best fit straight line has been fitted to the data with R^2 = 0.9551.

4.3.4 Identification of characteristics of pits on silicon wafers by AFM

4.3.4.1 Diameters and depth of the pits

SEM and optical images have shown all of the pits have circular edges before joining with other pits, even the smallest ones that can just be observed in the SEM images (Figure 4.15). The circular edges have also been confirmed using AFM images. Figure

4.22 shows typical AFM images of the pits on silicon wafers after the carbon films were just etched away by GDOES etching. The thicknesses of the original carbon films were 65, 105 and 180 nm respectively. The diameters of the circle and depth of 42 individual pits selected from the three samples were measured directly from the AFM measurements and listed in Table 4.2. Each of the selected pits has an entire circular edge, which means the pits had not joined with others. The measured diameters are in a range from less than one micron to nearly 20 microns. Nevertheless, the measured depths vary from 10 nm to 610 nm.

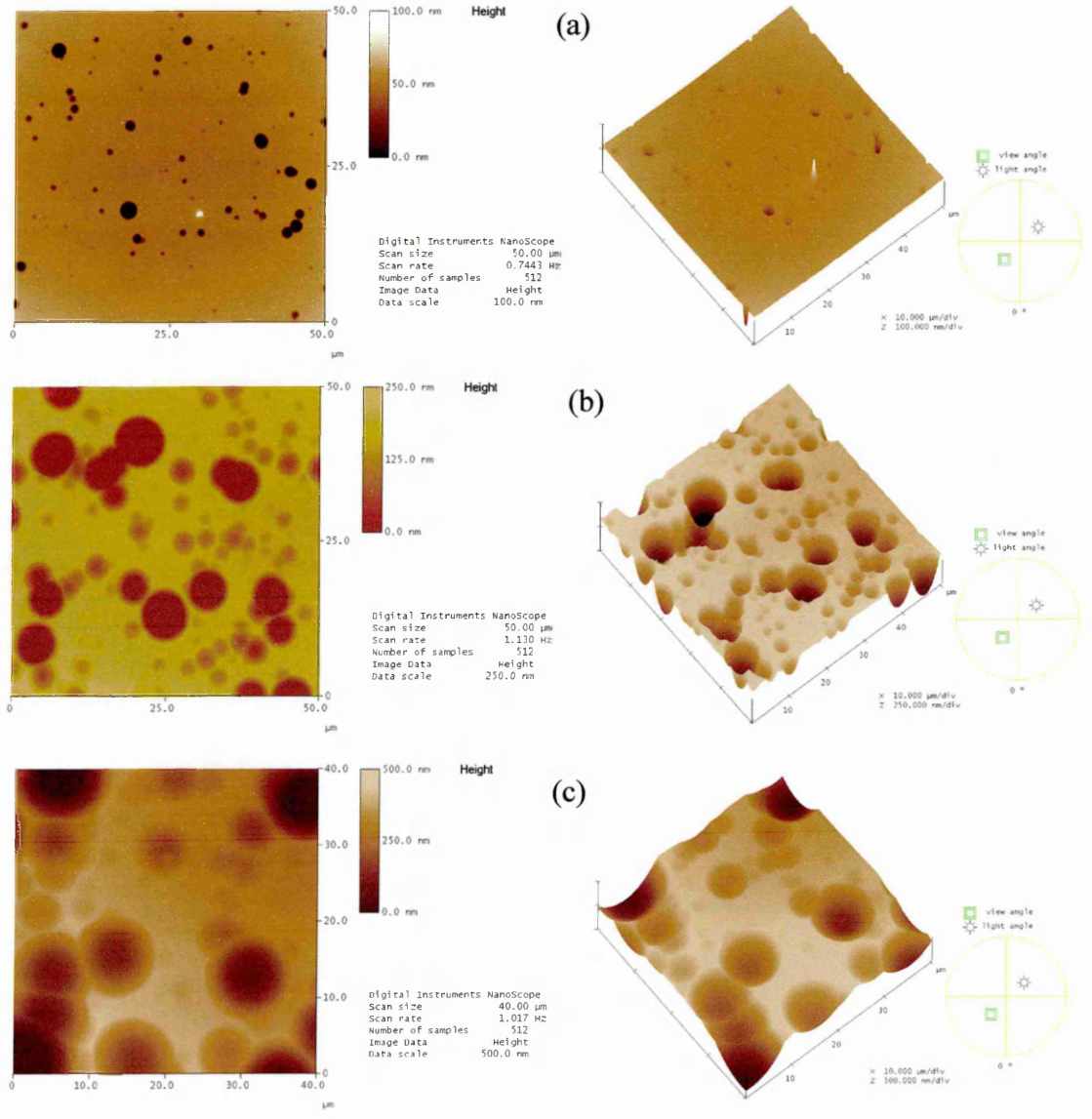

Figure 4.22. AFM images of pits on silicon wafers with different original thicknesses of the carbon film. GDOES parameters: 600 V/25 mA/4 mm anode. Thickness of original carbon films and etched times: (a) 65 nm/21 sec. (b) 105 nm/90 sec. (c) 180 nm/163 sec.

Table 4.2. *Measured diameters, depths and calculated mean radii with corresponding relative standard deviations for all of 42 pits from three carbon-coated silicon wafers with different thicknesses of original carbon film.*

Sample with 65 nm thick carbon film				Sample with 105 nm thick carbon film				Sample with 180 nm thick carbon film			
Diameter (μm)	Depth (nm)	Radius (μm)	Rel.STDEV (%)	Diameter (μm)	Depth (nm)	Radius (μm)	Rel.STDEV (%)	Diameter (μm)	Depth (nm)	Radius (μm)	Rel.STDEV (%)
0.809	10.5	5.30	14.3	2.311	20.9	22.59	5.0	11.512	257.8	62.16	1.2
1.020	15.4	4.59	15.7	2.337	20.9	23.49	6.2	11.893	270.8	63.29	1.9
1.042	19.2	4.94	10.8	2.643	29.5	21.77	3.0	13.390	299.8	70.16	1.9
1.237	24.7	5.02	3.1	2.937	36.0	22.99	3.9	15.116	431.3	68.38	2.6
1.310	29.9	5.28	5.8	3.542	53.8	23.16	2.8	18.226	552.5	73.13	2.7
1.324	28.4	5.15	5.8	3.709	56.7	22.73	2.9	18.500	610.0	71.35	3.0
1.420	34.1	5.33	4.8	3.962	66.5	23.94	2.2				
1.436	34.7	6.02	2.9	4.113	68.1	24.83	1.4				
1.533	38.9	6.05	4.2	4.480	94.3	25.18	1.2				
1.644	47.3	5.48	3.1	4.566	96.3	25.68	4.0				
1.839	59.7	5.51	4.9	4.839	115.8	24.15	1.6				
1.947	67.8	5.66	3.1	5.644	136.9	25.72	0.4				
2.147	74.6	6.01	2.9	6.212	191.8	25.44	0.8				
2.325	88.9	6.30	4.0	6.756	204.4	28.08	5.1				
2.746	130.5	6.84	1.2	7.232	204.7	27.56	1.6				
2.995	144.8	6.20	8.2	7.990	272.3	27.98	2.5				
3.220	153.4	7.71	1.1	9.512	407.8	28.50	3.3				
4.054	221.1	8.70	0.9	9.603	346.9	30.66	0.8				

4.3.4.2 Identification of the surface of the pit

The surface of the pit was initially assumed to be a part of a sphere and the assumption is further proved using the method mentioned in Section 4.2.3. In this study, for each of the pits listed in Table 4.2, two section-profiles along two cross-diameters of the pit circle were obtained from the AFM measurements. Five points on each of the profiles were selected evenly, and then divided into six different combinations with three of the five points. Six radii based on the six data combinations were calculated. For two cross-profiles of one pit, 12 radii were obtained. Therefore, the sphere of the pit surface can be confirmed when a mean radius of the 12 radii has a small relative standard deviation. The mean radius for each of the pits in Table 4.2 was calculated. The mean radii and their relative standard deviations are also listed in Table 4.2. Results in the table show that the relative standard deviations of the mean radii for most of the pits are less than 5%, with the exception of pits with diameters below one micron. This implies the surface of the pit is very close to a part of a sphere when the diameter of the pit is larger than one micron.

4.3.4.3 Developments of pits in silicon wafers with different thicknesses of carbon film

Diameters, depth and radii of the pits in Table 4.2 were measured from the AFM measurements. The diameters were measured from the circular edges of the pits. The depth represents a distance from the plane of the circular edge to the deepest point on the surface of a pit. The radius of the pit surface is an average of 12 calculated radii from two profiles of the pit along two cross-diameters. The results in Table 4.2 were also plotted as pit depth and pit radius versus pit diameter respectively, as shown in Figure 4.23(a) and Figure 23(b). From the figures, it can be seen that the depths and radii of the pits in any one of the three samples increased with increasing pit diameter. A linear relationship was followed, with the exception of a few lower data points of the samples with carbon film thicknesses of 65 nm and 105 nm in Figure 4.23(a). Slopes of the lines for both the depth and the radius are almost the same for the samples with the different thicknesses of carbon film. The gradient slope represents the developing speed

of the pit in pit depth or pit radius. In the graph of depth *vs.* diameter, the higher the gradient of the line, the faster the pit depth develops. Therefore, the fact that the gradients are nearly constant indicates that the variation of thickness of the carbon film has no effect on the pit development speed in the silicon wafer. For the coated samples etched in GDOES, once the pits have formed, the development of the pit on a substrate should only depend on the density, energy and incident angle of the argon ions and substrate materials. As these parameters were kept constant in this study, the gradient of the slope is constant.

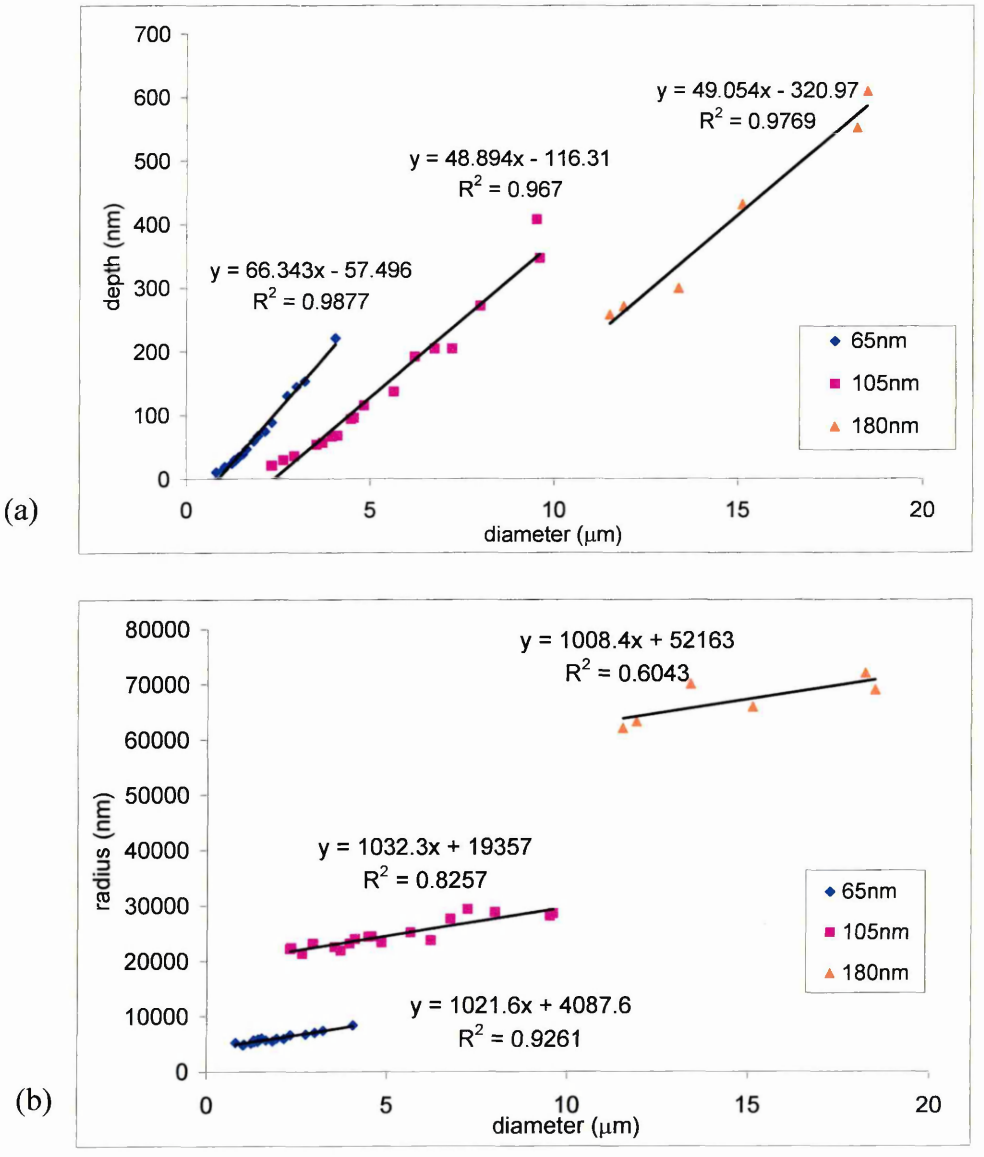

Figure 4.23. Depths (a) and radii (b) against diameters of pit based on the AFM results listed in Table 4.2.

4.3.4.4 Developing speeds of the pits in pit diameter and pit depth

The data in Table 4.2 also show a difference in the developing speeds of the pits between directions of the diameter and the depth. For example, considering the 18 pits from the sample with the 105 nm-thick carbon film, the diameters varied from 2.3 μm to 9.6 μm, while the depth ranged from 21 nm to 347 nm. This implies the developing speed in the direction of the diameter is much faster than the depth. There are two explanations for this observation. First, consider the profile of a pit as a part of a circle, as shown in Figure 4.24, and assume that etching in the direction normal to the pit surface occurs at the same rate anywhere on the surface. This means that circle enlargement takes the same point as its centre. Using geometry, a ratio of the developing speeds of the pit in the diameter and the depth can be obtained as,

$$\frac{\Delta x}{\Delta h} = \frac{n-1}{\sqrt{2n-1}}, \tag{4.2}$$

where Δx and Δh are the developing speeds in the directions of pit diameter and pit depth; n is a ratio of the radius to the depth of the pit. When $n = 40$, the minimum of the ratio for all of the pits in Table 4.2, the developing speeds have $\Delta x/\Delta h = 4.5$. Hence, the developing speed of the pit diameter in Table 4.2 is at least nine times faster than the pit depth.

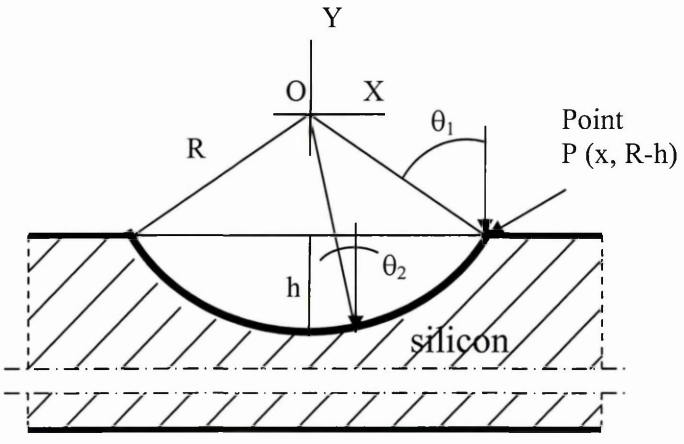

Figure 4.24. Schematic diagram of a pit profile in geometry. The origin point *O* is located at the centre point of the circle. The pit profile is a part of the circle. *h* is depth of the pit. P is the point of intersect of the profile and the line of the flat surface. θ_1 and θ_2 are the angles between ion incidence and normal of the surface.

During the development of the pits, the flat surface of the silicon wafer was etched layer by layer, which should engulf some of the diameter more than the depth. From Eqn. (4.2) it can be calculated that when the ratio of $n > 3.4$, the erosion of the flat surface will cause more reduction of the diameter than of the depth of the pit. This is the case with the pits listed in Table 4.2. Even so, the experimental results still indicate the developing speed of the pits by pit diameter is much faster than by pit depth.

Second, the developments of the pits could be affected by the angular dependence of sputtering yield (Chapman, 1980). The angle is defined as the angle between direction of ion incidence and normal to the etched surface. In the literature, it is indicated that the sputtering yield is not a maximum at an angle of zero. It will increase as the angle increases from zero and reach a maximum at an angle of around 60°, as shown in Figure 4.25. As it is expected that most of the argon ions in the GDOES sputtering were along a direction normal to the sample surface, θ_1, the incident angle at the edge of the pit, is bigger than θ_2, at a point close to centre of the pit, as shown in Figure 4.24. For the pits listed in Table 4.2, the angle θ_1 is in a range of 2.9°–13.5°. These angles could cause the sputtering yield from the outside area of the pit surface to be higher than in the central area, and did result in this phenomenon. This could aggravate the increase in pits' diameters.

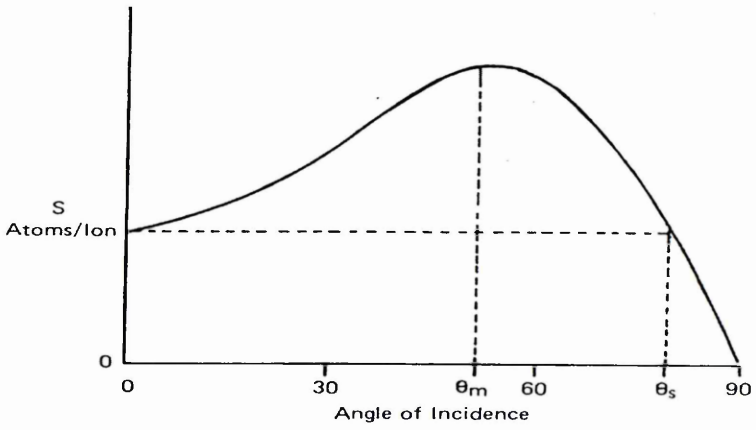

Figure 4.25. Sputtering yield dependence on angle of ion incidence (Chapman, 1980).

The different developing speeds of the pit in the diameter and the depth resulted in a growth in the pits' diameters and shallowness in their depths. Figure 4.26 shows measured roughness of silicon surfaces with the pits after different times of etching. The roughness decreases with increased etching time, which gives indirect evidence for the difference in the developing speeds.

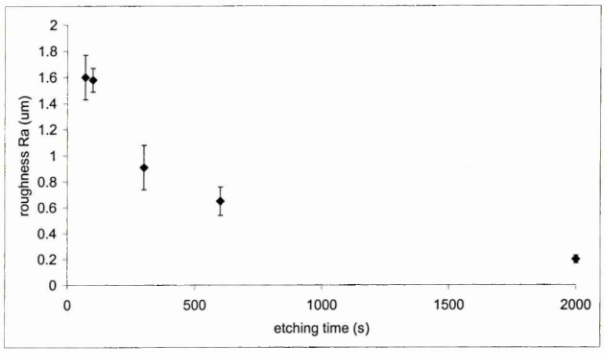

Figure 4.26. Roughness of pitting surface of silicon wafer decreases as etching time increasing.
GDS: 700V/30mA/4mm anode.

4.3.4.5 A model of the pit formation and development

Based on the results obtained in AFM, a model for how the formation and the development of the pits on the silicon substrate was built up as seen in Figure 4.27. Pits are first formed on a surface of a layer of the carbon film. The size and density of the pits depend on the original thickness of the film. After the carbon film is completely removed by GDOES etching, the pits develop in a different way than on the surface of the carbon layer. The developing speed in pit diameter is much faster than in pit depth. This results in the pit enlarging in diameter and becoming shallower in depth as the etching time increases. Some small pits (later formed) will be engulfed by the development of bigger pits (early formed). The etched surface will become smoother and smoother.

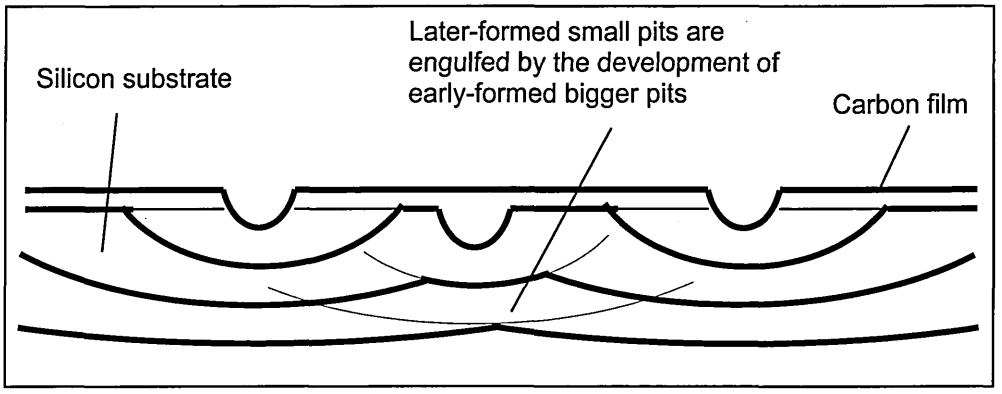

Figure 4.27. The model for the formation and the development of the pits on the silicon substrate.

4.4 Conclusions

A pitting phenomenon was found when a carbon-coated silicon wafer was etched in GDOES. After the carbon film was completely etched away, pits in a random array with a variety of sizes were formed on the silicon surface. Experimental results from the samples coated with Ag, Al, Si and Ge films confirmed that some of the pit-like topography on silicon surfaces could be developed as the etching time increases. However, the pits with high density and bigger size were only produced on the silicon surfaces under carbon films. A big difference in sputtering rate between the film and the substrate appears to play a crucial role in pit formation. The experiments also indicate that the structure of the film or the substrate has little effect on the pitting phenomenon.

The silicon wafers with different thicknesses of carbon films were etched in GDOES. The pitting phenomena of the surfaces were observed using SEM. For the surfaces of etched layers still in the carbon film, the pit density decreased as the thickness of the carbon film increased. This could be due to the stochastic roughening by ion bombardment of the carbon film. The measured roughness of the surfaces increased as the etching time increased, which supports stochastic roughening. For the etched

surface of a silicon wafer, the density of pits also decreased as the thickness of the carbon film increased. Possible explanations for this could be that the density of the pits originally formed on the silicon surface decrease as the thickness of the carbon film increases, and some small pits have been engulfed by the development of bigger pits.

Detailed geometrical data for the pits were obtained from AFM measurements. The sphere-like surface of the pit was confirmed by the mean radius, which was calculated based on the data points on the two cross-profiles of the pit, with small relative standard deviations. The measured diameters, depths and the calculated mean radii for each of the 42 pits from three samples with different original thicknesses of the carbon film revealed that;

(1) the original thickness of the carbon film has no effect on the development of the pits in the silicon surface;

(2) the developing speed of the pit by its diameter is faster than that by its depth, which results in the pit enlarging in diameter and becoming shallower in depth as the etching time increases. Based on the results obtained in AFM, a model for the formation and the development of the pits was built up.

Chapter 5 The Applications of GDOES in Collection of EBSD Pattern and Investigation on Internal Oxides in Carburised Steels

5.1 Introduction

Although GDOES is principally used as a surface analysis technique and most applications of GDOES are focused on the depth profiling of surfaces, GDOES with a dc glow discharge source is also a powerful tool in removing materials from sample surfaces layer by layer on an atomic scale. This chapter is concerned with the use of the glow discharge itself to alter the surface of a specimen. The sputtering process involves a high flux of low-energy argon ions incident on a surface. These ions typically have energies of a few hundred eV that only bombard the surface in the range of a few nm in most materials. This leaves an ion etched surface with little damage to the underlying crystal structures. By appropriate depth measurement of the sputtered craters either by a profilometer or in GDOES quantitative depth profiling with a proper calibration, a fresh surface with known depth from a few nanometres to around a hundred microns can be easily obtained. In the first part of this chapter it is demonstrated that GDOES can successfully be used to etch the surface to remove the damaged surface layer so that electron back-scattered diffraction (EBSD) patterns can be collected. In the second part it is shown that GDOES etching combined with quantitative depth profiling is a powerful tool in investigations of internal oxides of carburised steels by plan views of the oxides revealed by etching.

Electron back-scattered diffraction is a well-developed technique that allows measurements of the orientation of individual crystallites in bulk samples (Randle, 1993). Specimen preparation for EBSD is fast relative to other competing techniques

for measuring grain size and orientation (such as plan view TEM) but the need for not disturbing the crystallinity of the specimen within the depth of the back-scattered signal (typically about 20 nm) can still require considerable care. The usual method is to employ mechanical polishing followed by a chemical etch or electro-polishing. Non-metallic samples often require lengthy ion milling. In the following section (5.2), it is shown that GDOES etching with plasma glow discharge in the Grimm source is a very effective method for removing any surface damage prior to EBSD work. The technique has the advantages of speed (sample preparation can be less than 20 seconds), flexibility and of not requiring the use of any toxic chemicals. It also allows us to assess the depth of surface damage in metals, and so could also be useful in the microscopy of surface wear phenomena.

In Section 5.3, the application of GDOES in the research of internal oxides in carburised steels is demonstrated. The internal oxidation of carburised steels has long been known to degrade component properties. In particular, it leads to low surface hardness and reduced component strength (Natio *et al.*, 1984). Moreover, internal oxides are stress-raisers and are known to act as fatigue crack initiation sites, resulting in poor fatigue properties of the components (Dowling *et al.*, 1995). Most prior studies on internal oxidation have utilised cross-sections of the surfaces, either by SEM for a cross-sectional view of oxides on the micron scale, or by TEM to determine the type of the oxides (Mural *et al.*, 1997). However, these approaches cannot reveal a plan view of the morphology and distribution of the oxides. For a plan view of internal oxides, the necessary preparation of a sample surface by polishing will damage internal oxides. Internal oxides in a sample could be revealed after deep etching of the sample surface by electrochemical etching (Stott *et al.*, 1984). The electrochemical etching for different sample matrices needs a number of attempts in order to result in a proper surface. But it also cannot reach a particular surface-layer accuracy. In this study, two types of steels were studied. They had been carburised in three different thermal cycles. By GDOES etching, fresh surfaces in different layers of the carburised steels were obtained. Morphologies and distributions of internal oxides in the eroded surfaces were

observed in SEM images. EDS/SEM analysis of the surfaces also gave information of the relevant elements of the internal oxides, which were in agreement with the corresponding results of the GDOES depth profiles.

5.2 Collection of EBSD Pattern by Etching Surface in GDOES

5.2.1 Experimental

The principle of the EBSD analysis has been described in Chapter 3. In this study, the SEM (Philips XL30) equipped with the Oxford EBSD detection system was employed. Pure rolled iron (Fe: 99.999%) and single-crystal copper were employed as test specimens. The iron specimens were 1 mm thick and cut to a size of 15 × 15 mm. The biggest grain size in the iron was around a few millimetres in the rolling direction by a few hundred microns width by ~50 μm in depth, which was established by the SEM image of a GDOES etched surface and the optical image of a cross-section view after a conventional chemical etch, as shown in Figure 5.1. Mechanical polishing for EBSD work is usually finished with 1 μm-grade diamond paste. In order to deliberately retain significant surface damage, the specimens were only polished to a 6 μm-grade diamond paste finish. Examination in the SEM revealed extensive surface scratching. In this state, no recognisable EBSD patterns are expected to be obtained from anywhere on the surface at an electron accelerating voltage of 20 keV. Given that at this energy the EBSD signal emanates from approximately the first 20 nm of the sample, it can be inferred that the polishing process has severely distorted the lattice structure within this initial depth.

The specimens were then placed in the GDOES (Leco GDS 750) using a 4 mm anode in dc discharge. This device is usually employed to measure atomic concentrations in bulk samples by bombarding a surface with a high-flux plasma glow discharge and then measuring the intensity of various optical emission lines to quantify the presence of particular elements. In the present discussion, the spectroscopic capability is redundant:

what is of concern here is the ability of the high-flux glow discharge to etch away the surface of the sample without introducing any artefacts into its underlying crystallinity. The source parameters of the voltage of 600 V and the current of 25 mA were chosen in the sputtering for a flat bottom. Under these conditions, the flux of the Ar ions was expected to be in the order of 10^{18} ions cm^{-2} s^{-1} (see Eqn. (2.12) in Section 2.4.2).

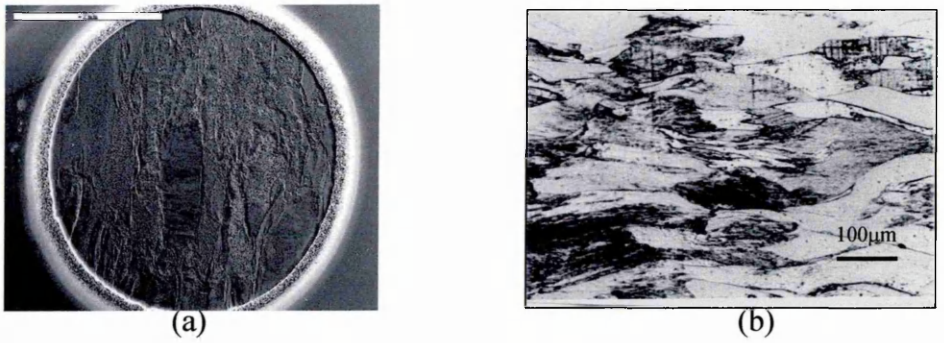

Figure 5.1. SEM and optical images show sizes of crystallites of the pure iron sample in the plan view and the cross-section.
(a) SEM image of the bottom of a GDOES crater on the pure iron specimen. GDS: 600V/30mA, depth of crater: ~45 μm.
(b) Optical microscope image shows the size of the crystallites in cross-section after chemical etching with 2% nital.

5.2.2 Results and discussion

The EBSD patterns obtainable in the SEM, as shown in Figure 5.2, are very greatly enhanced by subjecting the specimen to a relatively short exposure in the GDOES etch. Figure 5.2(a) shows an unprocessed EBSD pattern taken from the mechanically polished region of an iron specimen prepared as described above: no Kikuchi lines are visible. In Figure 5.2(b), 5.2(c) and 5.2(d) the EBSD patterns were taken under identical conditions to Figure 5.2(a) (i.e. the same beam current, spot size, working distance, detector position, detector gain and contrast) from the same specimen, but after it has been etched in the Grimm source for 10 seconds, 25 seconds and 50 seconds, respectively. The patterns obtained from the 10-second etch are definitely of inferior quality, but still give rise to recognisable Kikuchi patterns that are easily indexed by the automatic software.

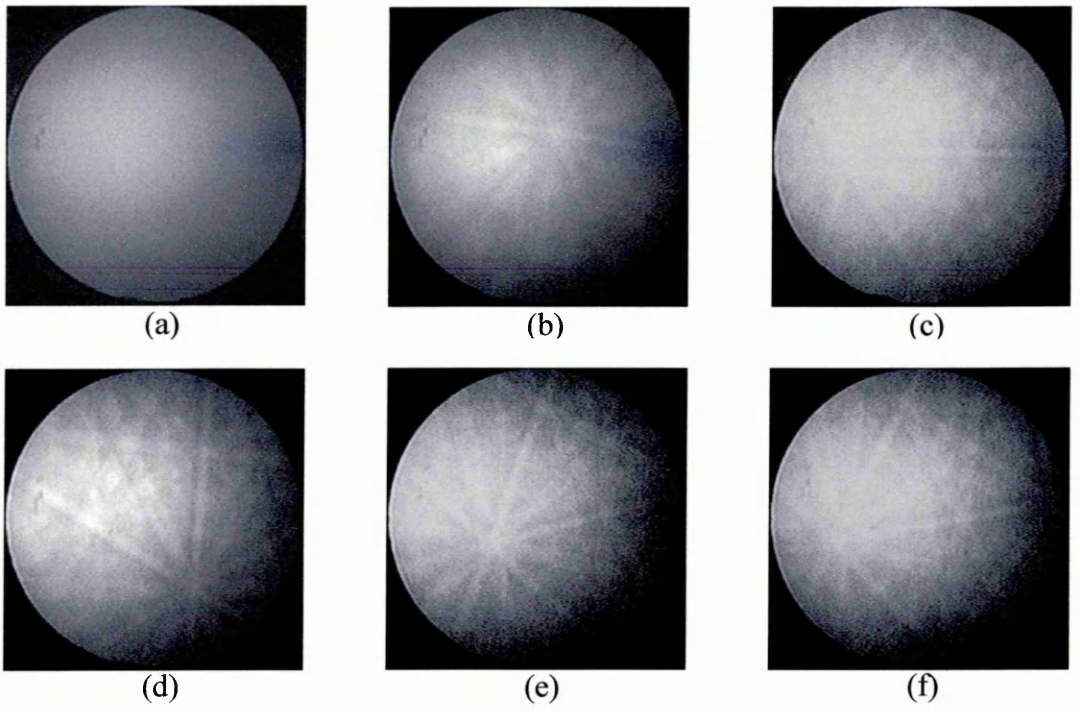

Figure 5.2. The EBSD patterns obtainable in the SEM with the pure iron specimens before and after GDOES etching.
GDS: voltage: 600 V, current: 25 mA, diameter of anode: 4 mm.
EBSD detection: electron beam: 20 keV, spot size: 6, gains: high gain 6.2, integration time: 1.3 sec, average frame: 5.
(a) Mechanical polished surface to a 6 μm-grade diamond paste finish.
(b) Etching time: 10 sec.
(c) Etching time: 25 sec, depth: 0.37 μm.
(d) Etching time: 50 sec, depth: 0.80 μm.
(e) Etching time: 200 sec, depth: 5.3 μm.
(f) Etching time: 1470 sec, depth: 42.3 μm.

A profilometer (UBM) was used to measure the depth of the crater obtained in a GDOES etch. Erosion rates were calculated as a function of the etching time, as shown in Figure 5.3. The erosion rate of the pure iron in the conditions in this study is divided clearly into two parts. In the first 100 seconds' sputtering, the erosion rate increases with increasing time more sharply than after 100 seconds. Thus, the removal of a surface layer of the iron corresponding to the 10-second etch was calculated as approximately 150 nm thick. Without resorting to very detailed image analysis methods, it can be observed that EBSD patterns collected after a 10-second etch are not nearly as crisp as those collected after 50 seconds. Patterns collected after a 25-second etch were clear but still of noticeably lower quality than the best available. More

lengthy etch times (up to 1470 seconds) do not result in any noticeable improvement or degradation of pattern quality (see Figure 5.2(a) and 5.2(f)). That would imply that the polishing process with 6 μm-grade diamond paste has damaged the specimen to a depth of between 0.2 and 1.0 μm, which agrees broadly with earlier TEM work on the surface damage of copper (Turley and Samuels, 1997).

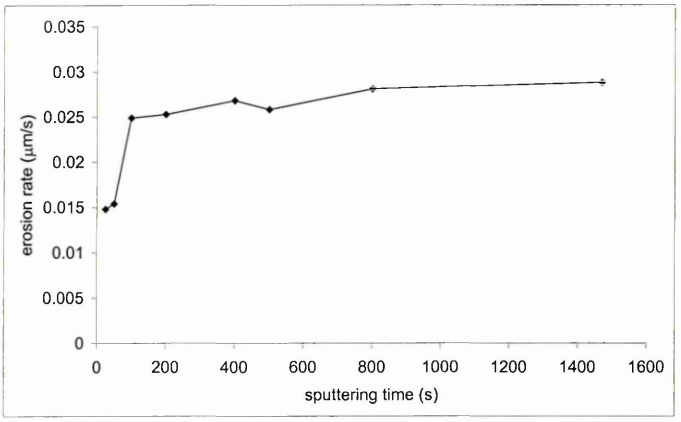

Figure 5.3. The erosion rate of the GDOES etching for the pure iron specimen as a function of etching time. GDS conditions: voltage: 600 V and current: 25 mA.

The enhancement of the EBSD pattern by GDOES etching was also obtained using single-crystal copper as the specimen. The GDOES etching for 10, 30 and 50 seconds produced etched depths of 0.7 μm, 2.1 μm and 3.5 μm respectively. The patterns and corresponding surface morphologies are shown in Figure 5.4 and Figure 5.5. The pattern taken from the mechanically polished region of the copper specimen also showed no visible Kikuchi lines. The patterns collected after 30 seconds' and 50 seconds' etching show crisper Kikuchi lines than that after a 10-second etch, although the pattern after a 10-second etch is close to the best quality. This implies that the damage layer by a polish with 6 μm-grade diamond paste could damage the surface to a depth up to ~2 μm for the copper sample. The fact that the damage layer by the polishing with 6 μm-grade diamond paste in a copper surface was double that of iron also agrees with the fact that the hardness of iron is nearly double that of copper.

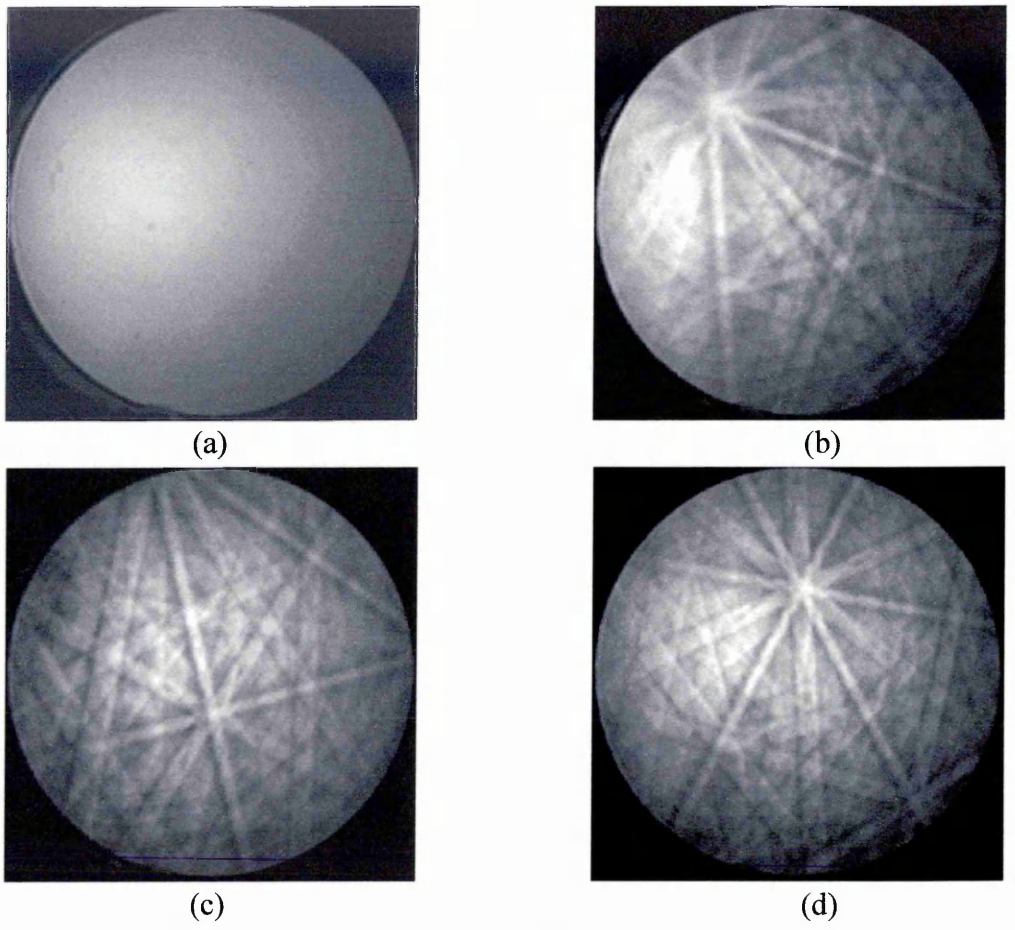

Figure 5.4. The EBSD patterns collected from surfaces of the single crystal copper with and without the GDOES etching.
GDS: 600V/25mA/4 mm anode.
Microscope beam: 30keV, spot size: 6, magnification: 2481, working distance: ~10mm.
EBSD detection gains: high gain 4.5, integration time: 1.3 sec, average frame: 25, background subtract: 80%
(a) From polished surface with 6 μm-grade diamond paste finish.
(b) From the surface after 10 sec of the etching, the depth was 0.7 μm.
(c) From the surface after 30 sec of the etching, the depth was 2.1 μm.
(d) From the surface after 50 sec of the etching, the depth was 3.5 μm.

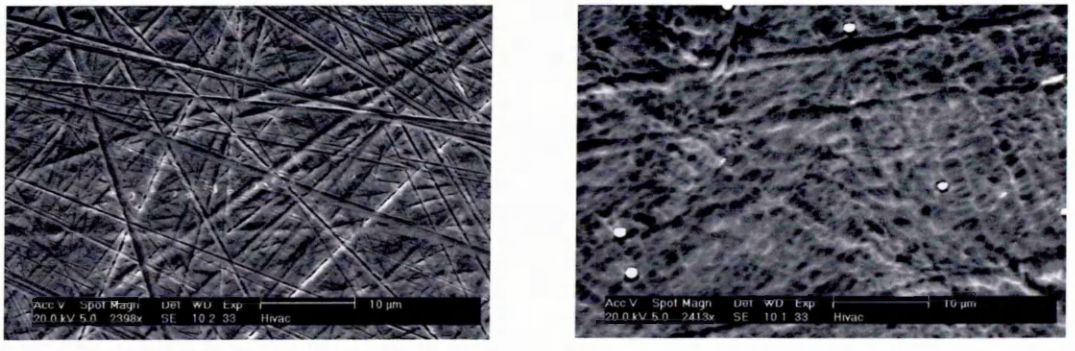

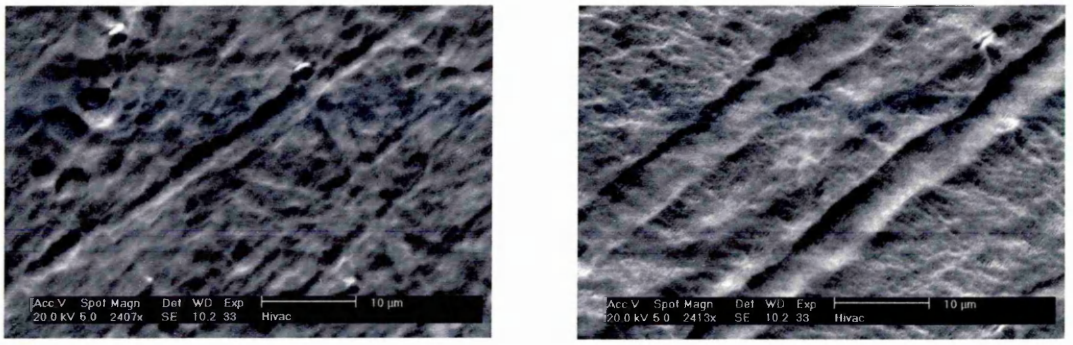

(c) (d)

Figure 5.5. Surface morphologies of the single crystal copper corresponding to the surfaces in Figure 5.4.
(a) Polished surface to a 6 µm-grade diamond paste finish.
(b) After 10 second-etching, depth was 0.7 µm.
(c) After 30 second-etching, depth was 2.1 µm.
(d) After 50 second-etching, depth was 3.5 µm.

There may be various factors affecting the quality of the diffraction pattern other than simply the removal of the damaged material. The most debilitating of these would be that the high-power Grimm source actually heats the specimen surface, inducing re-crystallisation. However, this is unlikely to be a problem with such short etch times for iron and copper specimens. It should be noted that in general, materials like Al, Cu, Ni, Cr and steels tend to develop their grain boundary microstructures after the etching by the Grimm source, and this depends on the different grain orientations (Angeli, 1997). Therefore, in the case of the copper and iron specimens here, it would seem very unlikely that re-crystallisation could have occurred. There may also be re-crystallisation induced by the ion bombardment itself. However, the average ion energy is likely to be less than 200 eV (see Section 2.4). Simulation calculations suggest that the range of Ar ions and any associated deposition of energy and ion-vacancy defects are restricted to less than 1 nm in depth (King, 1997). This compares with the fact that the EBSD signal comes from about 20 nm below the specimen surface.

There can be confidence, therefore, that after a 10-second etch in GDOES a good representation of the actual crystal structure was obtained, which was at about 0.2 µm below the (original) surface of the pure iron and 0.7 µm of the copper, and that the

improvement in pattern quality is due solely to the removal of the most severely damaged layer.

5.3 Investigation of Internal Oxides in Carburised Steels by Plan View and GDOES Depth Profiling

5.3.1 Experimental

Three carburised steels were used in this study. Chemical compositions of the steels before carburising are shown in Table 5.1. The main difference in the compositions between specimen A and specimens B and C is the concentration of Si. Specimen A has a higher concentration of Si (0.31%) than do specimens B and C (each 0.19%). The specimens had already been carburised in a commercial furnace using different thermal cycles outlined in Figure 5.6. In the figure, the base process (from A to D) is only aiming to heat parts in the furnace evenly to a required temperature. The carbon potential required for the carburising process was not introduced at this stage. A fully carburising atmosphere was introduced into the furnace in the boost process (from D to F). Specimen A was only heat-treated at 800 °C for 2.0 hours in the heat-up stage (from point A to B). Specimen B was treated from the beginning of the thermal cycle for a total exposure time of 9.0 hours (from point A to E), which means that specimen B experienced both heat-up and carburising processes. Specimen C was directly put in the furnace at the beginning of the boost process and was carburised for a total time of 12.0 hours (from point D to F). Oxygen partial pressures in the furnace were 5E-21 atm. at 800 °C and 2E-19 atm. at 900 °C in the base process, and 2E-20 atm. in the boost process.

Table 5.1. *Compositions of the steels before carburising processes (mass%).*

Sample	Steel type	C	Si	Mn	Cr	Ni	Cu	Al	P	S
A	Commercial	0.19	0.31	1.00	0.96	1.07	0.21	0.025	0.012	0.047
B & C	Commercial	0.19	0.19	1.02	1.01	1.14	0.17	0.019	0.010	0.049

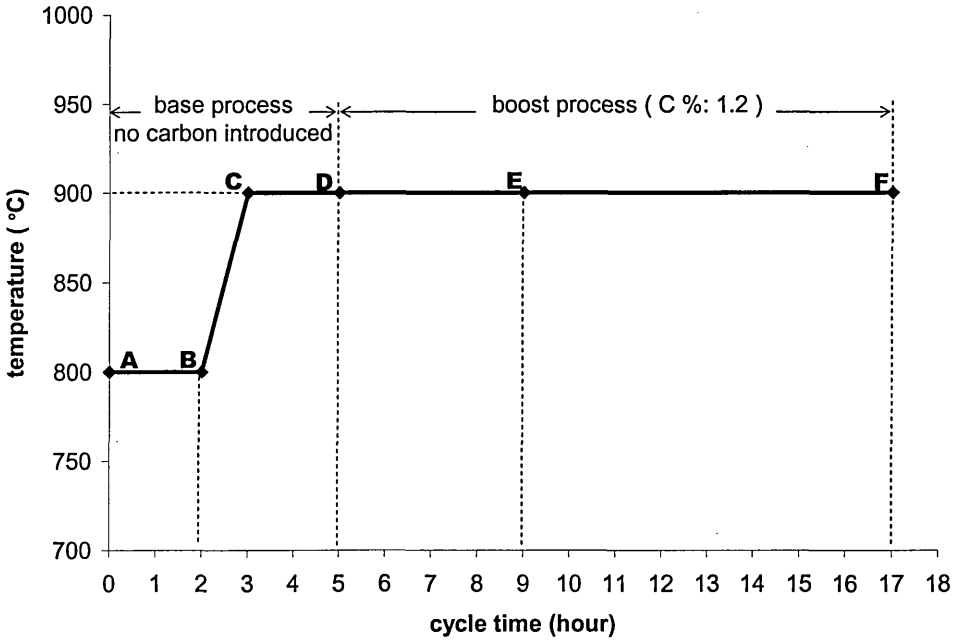

Figure 5.6. The thermal cycles of carburising process in a commercial furnace.

For GDOES depth profiling of the carburised steels, a set of certified reference materials (CRMs), listed in Table 5.2, was used for the calibration of the GDOES. The calibration did not include oxygen due to the lack of suitable standards. Coefficient factors and data points of the calibration curves for the elements of interest are listed in Table 5.3. The compositions of specimens A and B were measured in the GDOES and are listed in Table 5.4. This shows a general agreement with the supplied chemical compositions. The conditions of the GDOES sputtering were 600 V of voltage and 25 mA of current. The argon pressure was controlled by a gas-flow controller to keep the current as constant as possible. A 4 mm anode was used in this study, which can produce an analysed area of ~12.6 mm^2 per burn. In this condition, a sputtered crater with a relatively flat bottom can be obtained for the sample. Profiles of the craters were obtained by the laser profilometer (UBM); examples of such profiles are shown in Figure 5.7.

Table 5.2. *CRMs of GDOES calibration for depth profiling of the carburised steels (the elemental concentration is mass% and SR is the relative sputtering rate to that of pure iron standard).*

Standards	SR	Fe	C	Si	Mn	P	S	Cr	Mo	Ni	Al	As	Co	Cu	V	W	Mg
SS481/1	0.59	80.325	0.680	0.150	0.250	0.023	0.022	3.400	0.280				0.31		0.560	14	
SS486/1	0.65	81.276	0.740	0.270	0.210	0.029	0.021	4.540					0.08		1.820	5.800	
SS487/1	0.82	74.273	1.020	0.180	0.260	0.022	0.029	3.910							1.140	1.800	
SS406/2	0.91	94.070	0.173	0.342	0.447	0.0102	0.043	2.001	0.980	1.620	0.013	0.012		0.289			
SS407/2	1.05	93.586	0.490	0.660	0.195	0.038	0.0105	3.030	0.830	0.527	0.040			0.397	0.190		
SS408/2	1.02	93.564	0.289	0.237	0.557	0.056	0.030	0.111	0.098	4.130	0.154	0.0046		0.694	0.067		
SS409/2	0.92	92.888	0.086	1.180	0.559	0.0141	0.0179	1.318	0.599	3.020	0.094			0.205			
SS410/2	0.95	92.784	0.428	1.100	0.419	0.074	0.041	1.684	0.432	2.070	0.046	0.0053	0.0248	0.436	0.440		
SCRM666/7	2.04	93.070	3.370	1.720						1.710							0.089
SCRM667/7	1.67	92.698	2.870	2.850	0.180					1.330							0.072
SCRM668/7	1.58	93.758	3.750	1.560	0.730					0.190							0.012
SCRM669/7	1.65	93.279	3.060	2.500	0.610					0.520							0.031
SCRM670/7	1.69	93.025	3.450	2.190	0.340					0.950							0.045
SS405/1	0.97	96.226		1.710	1.280	0.018	0.069	0.150		0.220					0.280		
SS409/1	0.93	93.170	0.082	1.460	0.440	0.025	0.021	0.940	0.650	3.060			0.014		0.090		
NBS-1761	0.92	95.085	1.030	0.180	0.678	0.040	0.035	0.220	0.103	1.990	0.055	0.011		0.300	0.053		
NBS-1763	1.04	95.019	0.203	0.630	1.580	0.012	0.023	0.500	0.500	0.510	0.043	0.055	0.095		0.300		

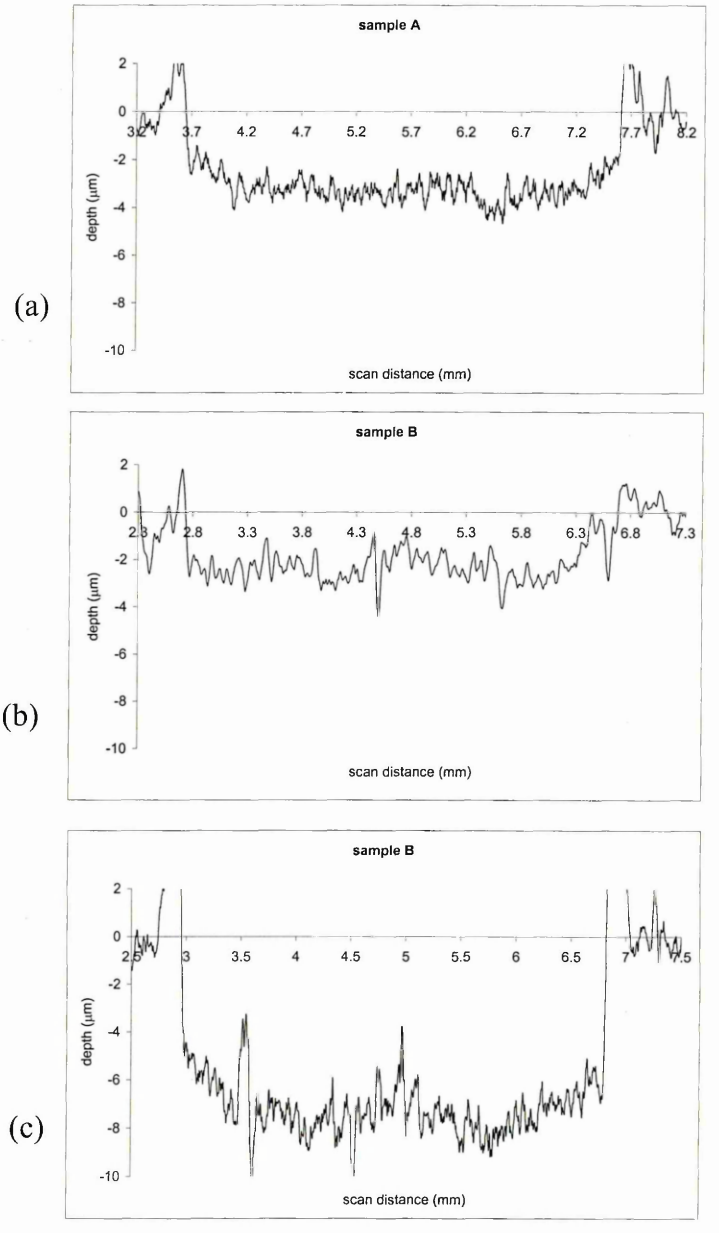

Figure 5.7. Profiles of craters obtained by the laser profilometer (UBM) for specimens A and B. Depths of the craters calculated by the GDOES quantification procedure were: (a) specimen A: 3.26 μm, (b) specimen B: 2.85 μm, (c) specimen B: 8.40 μm. GDS conditions: 600 V/25 mA/4 mm anode.

Table 5.3. *Coefficient factors and data points of the calibration curves for the elements of interest.*

Element	C	Si	Mn	Cr	Ni	Cu	Al
Coefficient	0.9901	0.9735	0.9813	0.9923	0.9687	0.9943	0.9953
Data points	16	17	16	8	13	7	7
Element	**P**	**S**	**As**	**Co**	**V**	**Mo**	
Factor	0.9776	0.9843	0.8866	0.9975	0.9930	0.9410	
Data points	12	12	5	5	11	9	

Table 5.4. *Compositions of specimens A and B measured in the GDOES (mass%).*

Sample	C	Si	Mn	Cr	Ni	Cu	Al	P	S	As	Co	V
A	0.30	0.39	0.97	0.88	0.91	0.25	0.015	0.008	0.042	0.020	0.037	0.003
B	0.31	0.29	0.99	0.88	0.99	0.21	0.009	0.007	0.045	0.019	0.010	0.005

The morphology of the sputtering eroded surface and internal oxides revealed by the etching were observed by secondary electron and back-scattered electron images in the SEM (JEOL 840) under an operating electron voltage of 20 keV. The qualitative elemental distribution of the internal oxidation zone was analysed by EDS (Oxford ISIS system) with the operating setting 15 or 20 keV for the electron beam and 1 or 3 nA for the probe size.

5.3.2 Results and discussion

Plan view SEM images of the sputtering eroded surface of the three specimens in different layers were obtained, as shown in Figures 5.8 to 5.10. Different surface morphologies were revealed in the secondary electron images (in left column). From the back-scattered electron images (in right column), different morphologies and distributions of internal oxides were also displayed. A relative uniform distribution of the oxides can be seen from these images. However, morphologies of the oxides in different layers in a specimen were changed. For example, in Figure 5.9 the oxides' morphologies in specimen B changed from a large size within grains and on grain-boundaries in the layer 2.85 μm below the surface to intergranular oxides at 8.40 μm below the surface. While, for sample C, even in the layer 1.53 μm below the surface, the oxides appeared as uniform intergranular oxides.

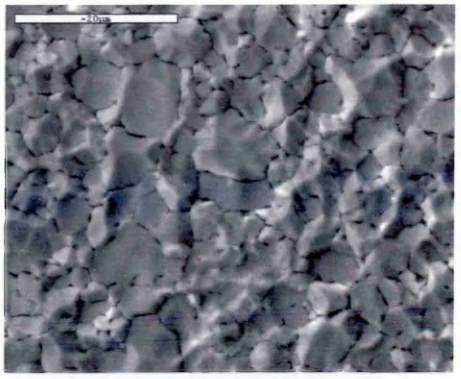

(a) SE image at the depth of 3.26 μm

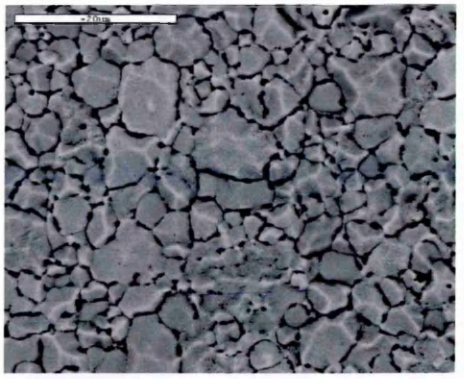

(b) BS image

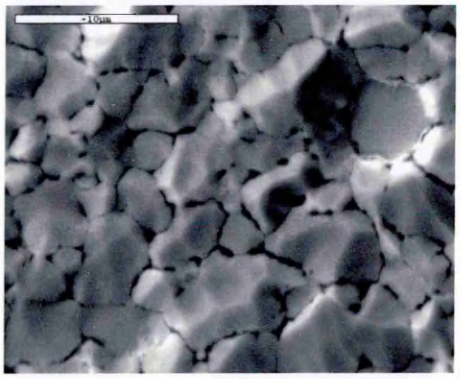

(c) SE image at the depth of 3.26 μm

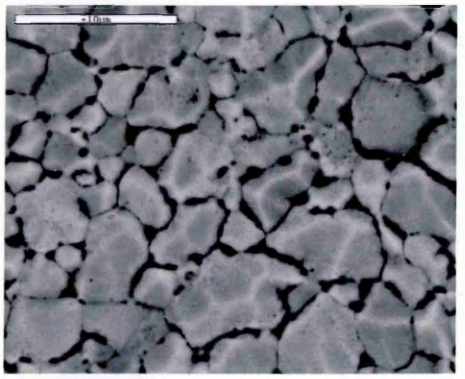

(d) BS image

Figure 5.8. SEM secondary electron (SE) and back-scattered electron (BS) images for plan views of the eroded surface of specimen A at the depth of 3.26 μm.
GDS conditions: 600V/25mA/4mm anode.

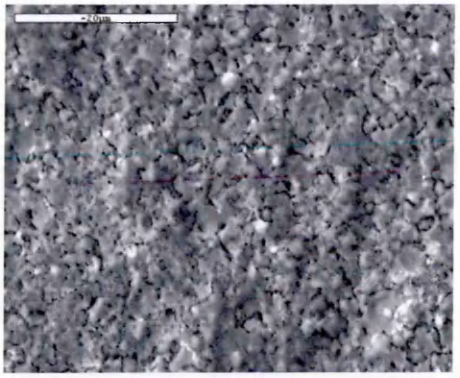

(a) SE image at the depth of 2.85 μm

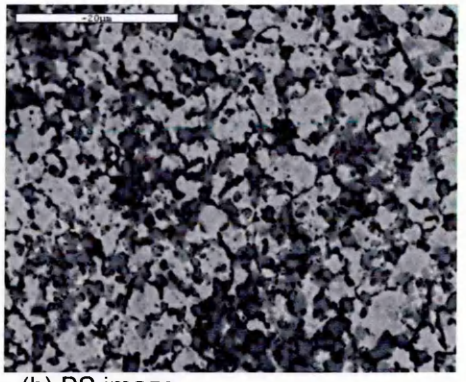

(b) BS image

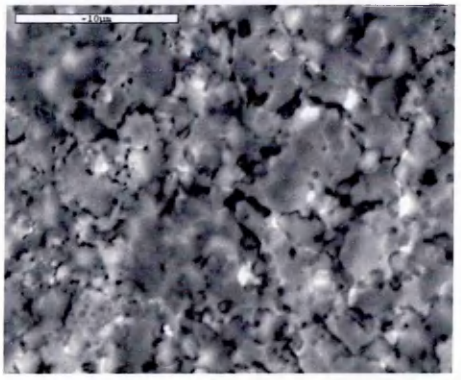

(c) SE image at the depth of 2.85 μm

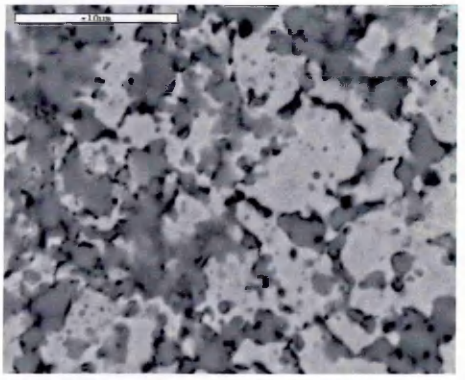

(d) BS image

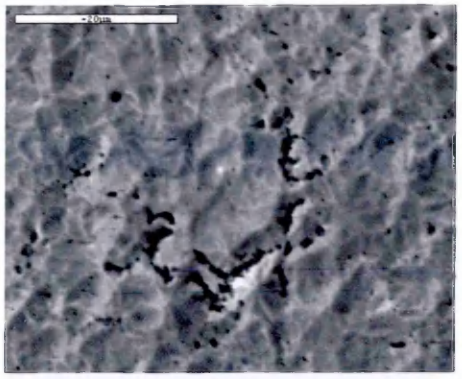

(e) SE image at the depth of 5.87 μm

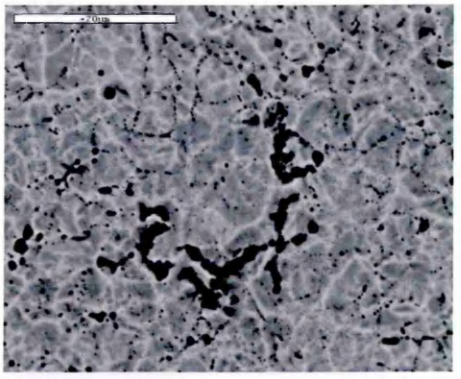

(f) BS image

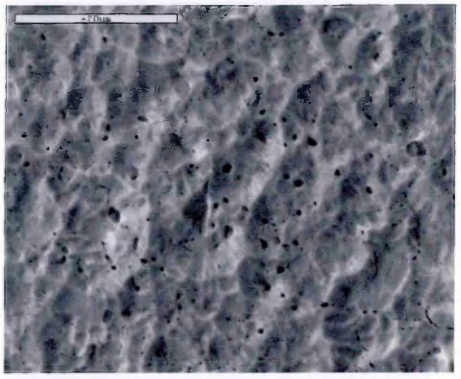

(g) SE image at the depth of 5.87 μm

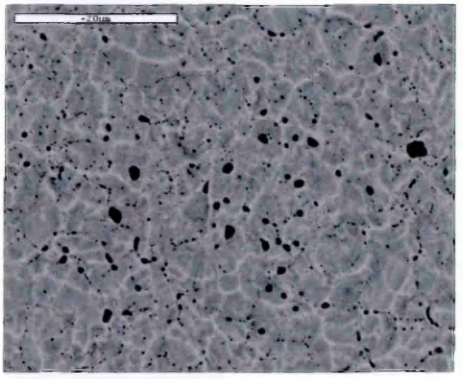

(h) BS image

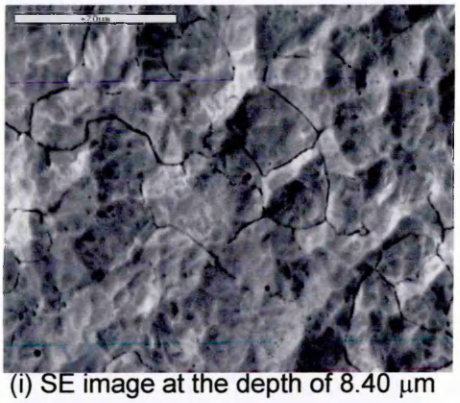

(i) SE image at the depth of 8.40 μm

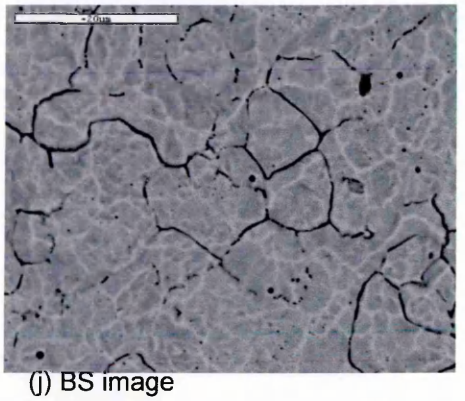

(j) BS image

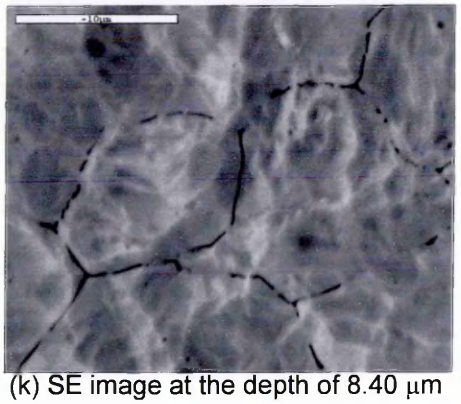

(k) SE image at the depth of 8.40 μm

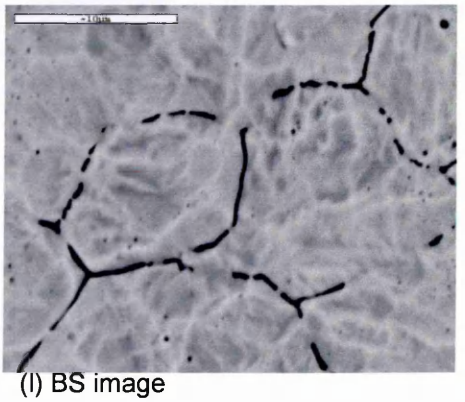

(l) BS image

Figure 5.9. SEM secondary electron (SE) and back-scattered electron (BS) images for plan views of the eroded surfaces of specimen B at the depth of 2.85 μm (a)–(d), 5.87 μm (e)–(h) and 8.40 μm (i)–(l) respectively.
GDS conditions: 600V/25mA/4mm anode.

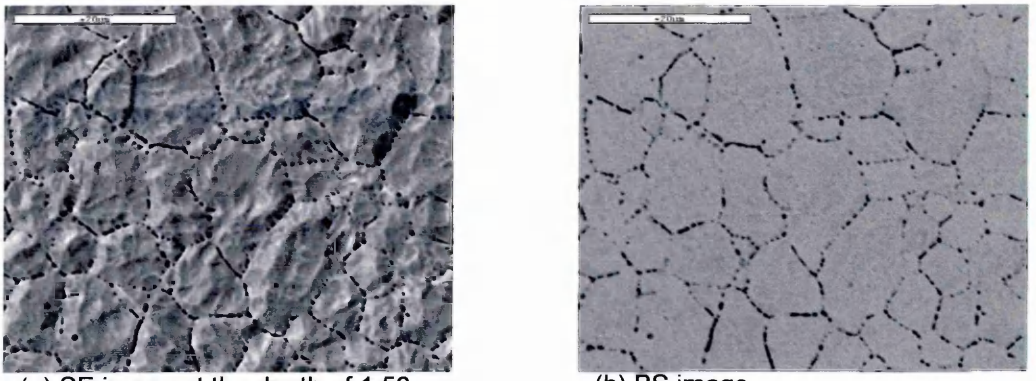

(a) SE image at the depth of 1.53 μm (b) BS image

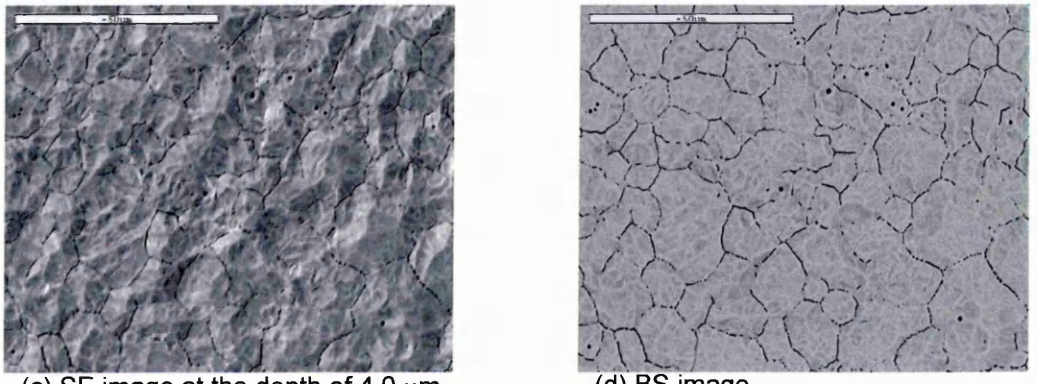

(c) SE image at the depth of 4.0 μm (d) BS image

Figure 5.10. SEM secondary electron (SE) and back-scattered electron (BS) images for plan views of the eroded surfaces of specimen C at the depth of 1.53 μm (a), (b), 4.0 μm (c), (d) respectively.
GDS conditions: 600 V/25 mA/4 mm anode.

Elemental mapping results using the SEM/EDS for the area containing internal oxides are shown in Figures 5.11 to 5.13, which correspond to the back-scattered electron images in Figure 5.8(d), 5.9(d) and 5.9(l) respectively. The results confirmed the oxides existed by their oxygen counts and gave extra information that the oxide elements were Si, Cr and Mn. Figure 5.12 shows the mapping results for the layer 2.85 μm below the surface of specimen B. The oxygen enrichment was associated with elements Cr and Mn, and with depletion of Fe. This indicates that the large size of oxides in the upper layer mainly consists of the oxides of chromium and/or manganese. In fact, the TEM analysis of the oxides indicated that they could be Cr and Mn complex oxides (An *et al.*, 2003). In the deep layer 8.40 μm below the surface, the mapping results shown in Figure 5.13 indicated clearly that the oxides with the characteristic of

elongated morphology were intergranular oxides of silicon. The mapping results in Figure 5.11 in the layer 3.26 μm below the surface of specimen A revealed that the oxides were relevant to the elements Si, Cr and Mn.

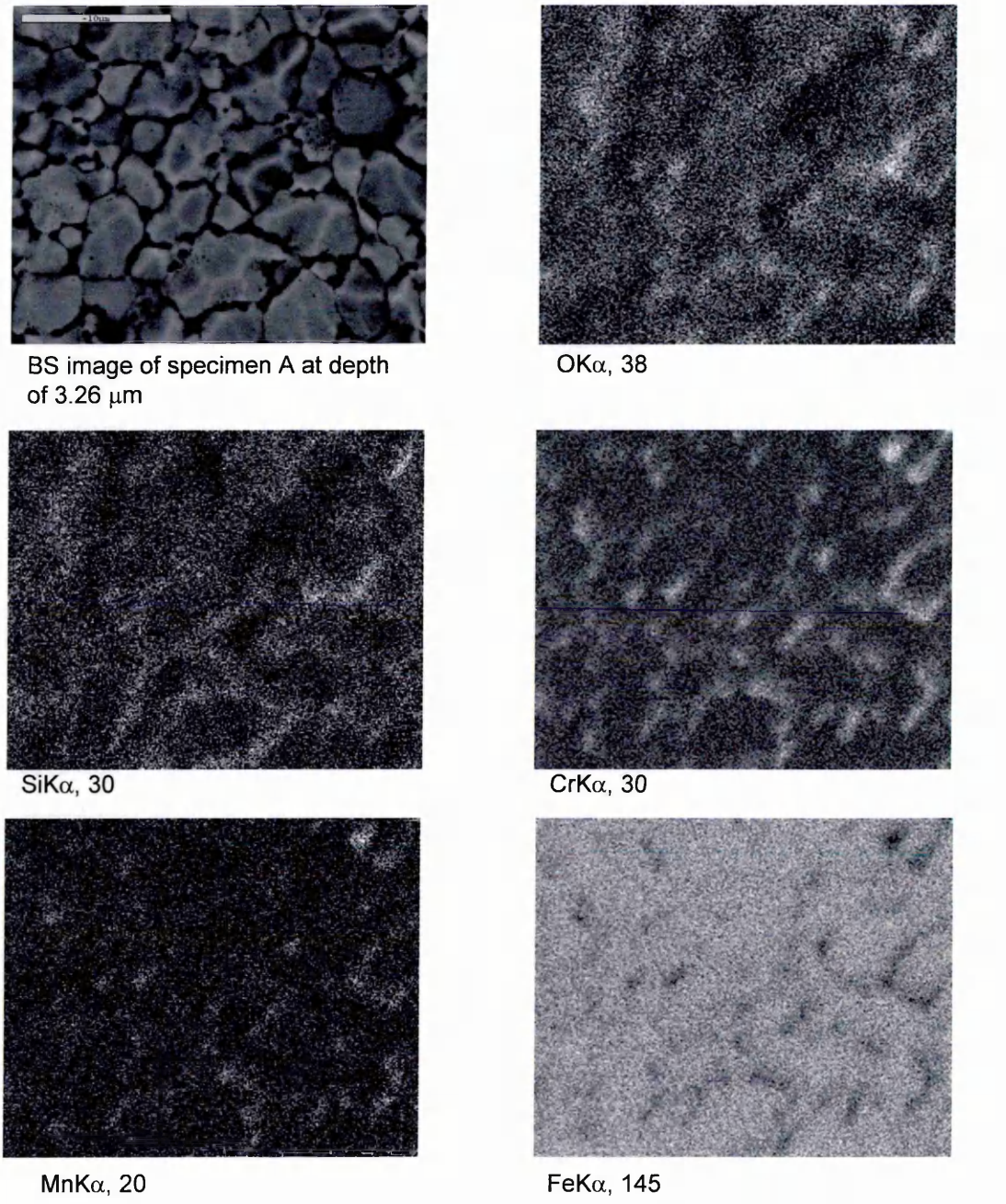

Figure 5.11. SEM/EDS elemental mapping results for an area in specimen A at the depth of 3.26 μm show that the oxides were relevant to the elements Si, Cr and Mn, whereas Fe was depleted.

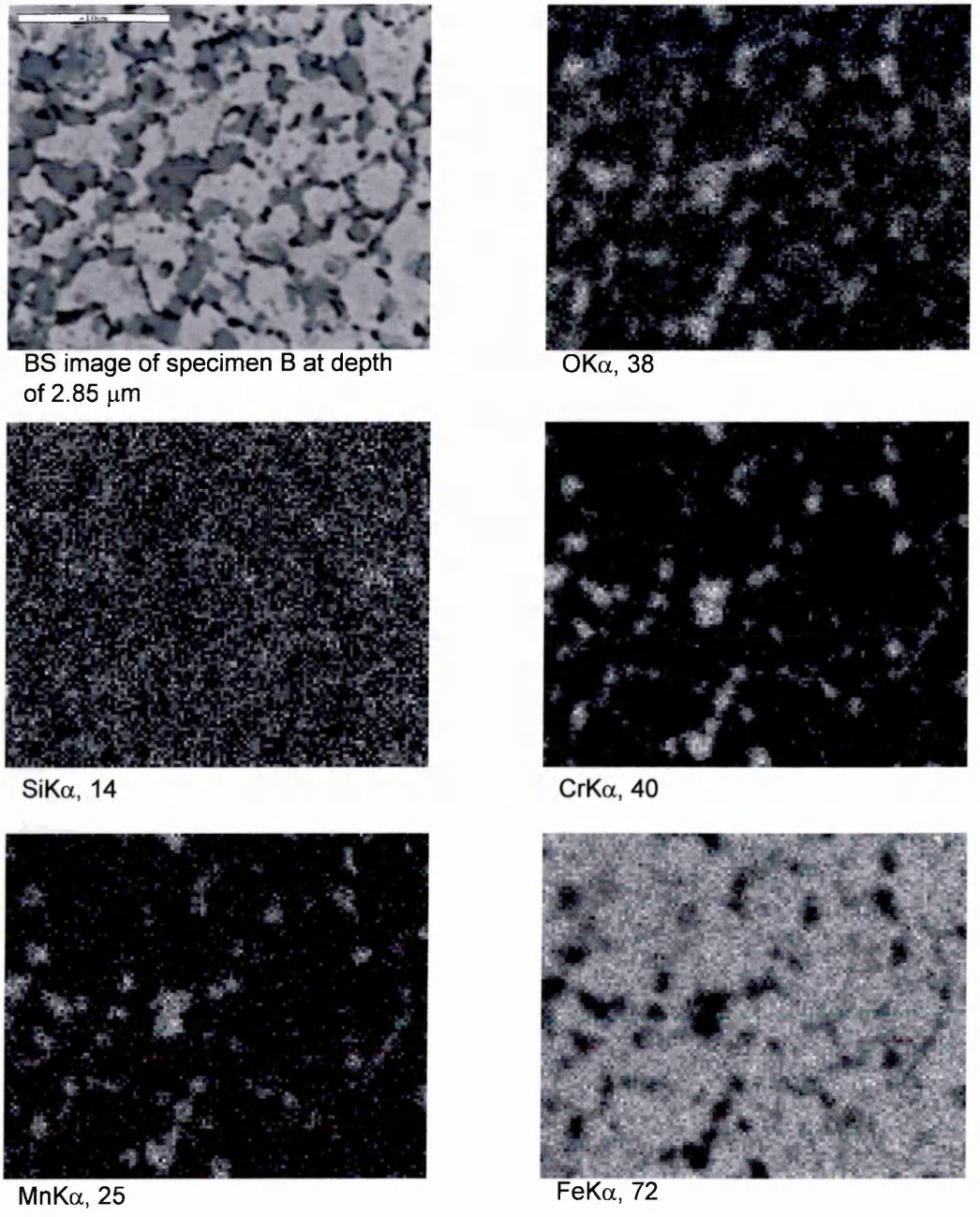

Figure 5.12. SEM/EDS elemental mapping results for an area of specimen B at the depth of 2.85 μm show that the oxides were relevant to the elements Cr and Mn, whereas Fe was depleted.

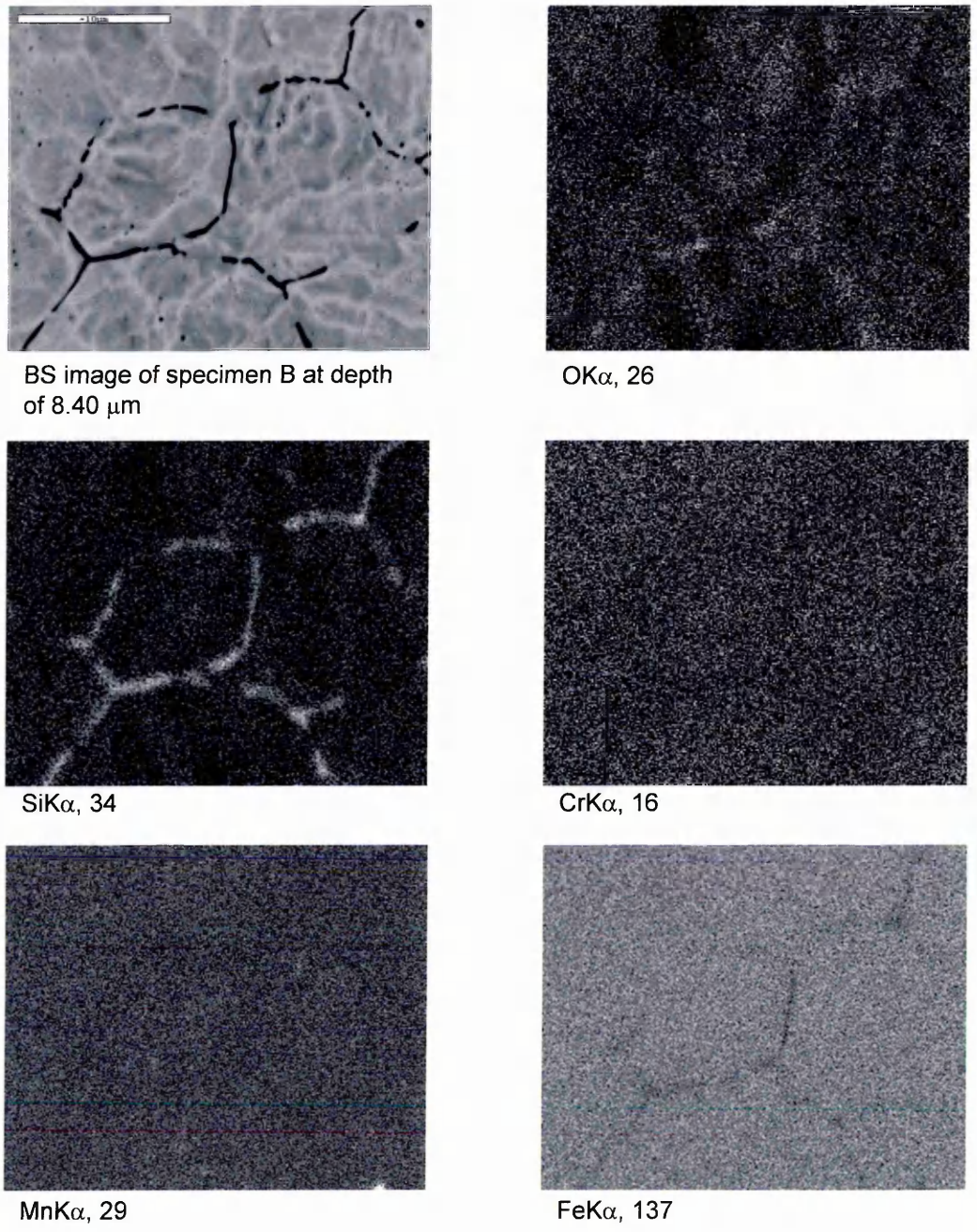

Figure 5.13. SEM/EDS elemental mapping results for an area of specimen B at the depth of 8.40 μm show the silicon oxides, whereas in where Fe was depleted.

Depth profiles obtained using the GDOES for the specimens showed similar results with that of the EDS mapping. Figure 5.14(a) is the GDOES depth profile of specimen A to the depth of 3.26 μm. Figures 5.14(b) and (c) are the depth profiles of specimen B to the depths of 2.85 μm and 8.40 μm respectively. The elemental concentrations in the final layers of the depth profiles are listed in Table 5.5. These final layers also correspond to those of the EDS mapping in Figure 5.11 to 5.13.

(a)

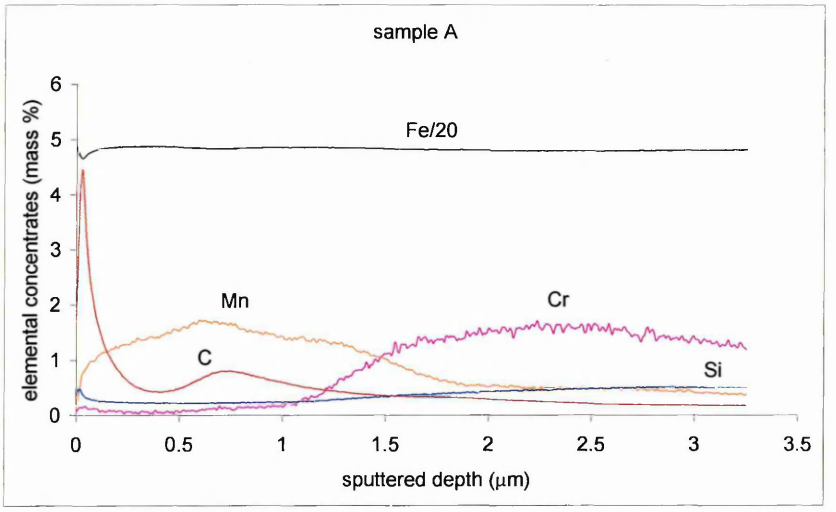

(b)

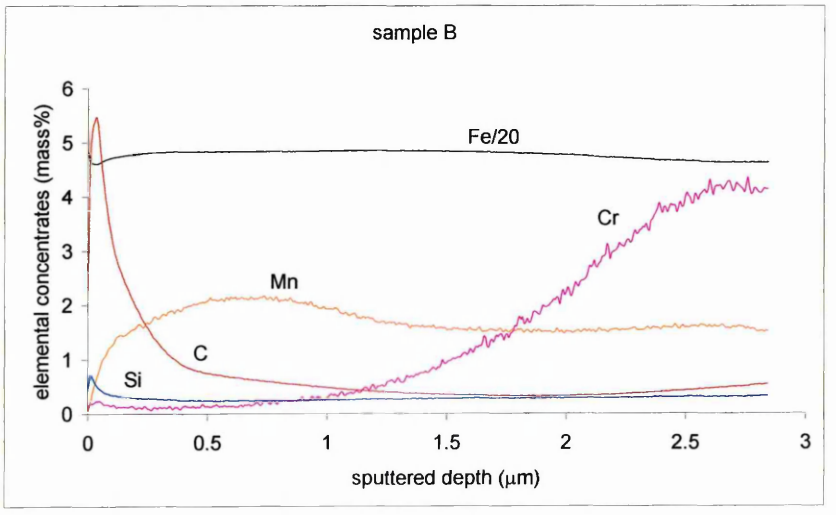

(c)

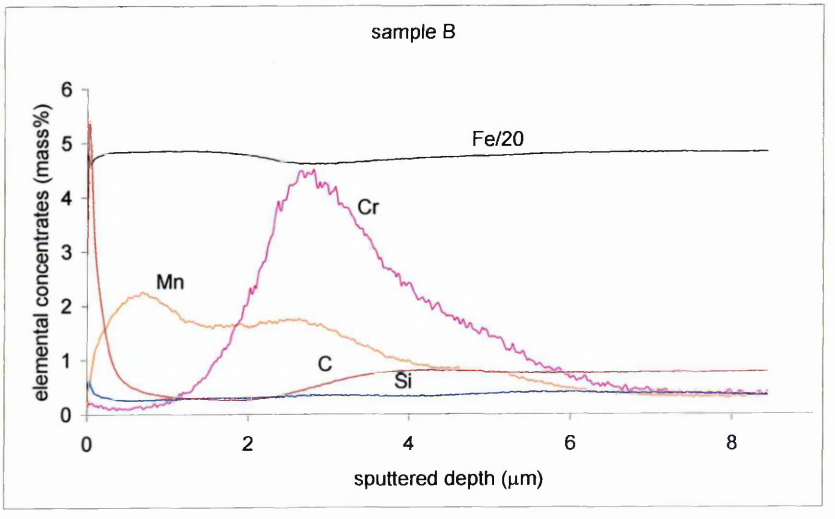

Figure 5.14. GDOES depth profiles for specimen A to the depth of 3.26 μm (a) and for specimen B to the depth of 2.85 μm (b) and 8.40 μm (c) respectively.

Table 5.5. The elemental concentrations of specimens A and B in the layers corresponding to those of the EDS mapping in Figure 5.6 to 5.8 and the depth profiles in Figure 5.9. (elemental concentration: mass %)

Sample	Depth (μm)	C	Si	Mn	Cr	Mo	Ni
A	3.26	0.176	0.50	0.382	1.26	0.119	0.94
B	2.85	0.535	0.323	1.531	4.123	0.069	0.539
B	8.40	0.78	0.353	0.324	0.378	0.142	1.128
Sample	**Depth (μm)**	**Cu**	**Al**	**P**	**S**		
A	3.26	0.21	0.019	0.072	0.02		
B	2.85	0.127	0.009	0.007	0.022		
B	8.40	0.196	0.015	0.009	0.029		

From the table, in the layer of 3.26 μm below the surface of specimen A, the enrichment of the elements Si and Cr corresponded to the oxides of Si and Cr as shown in Figure 5.11. The depletion of Mn was due to diffusion of Mn toward to the oxidation front. This, consequently, resulted in the matrix depletion of the element, which can be clearly seen in the depth profile in Figure 5.14(a). In different layers of specimen B, the enrichment of Cr and Mn in the layer 2.85 μm below the surface corresponded to the oxides of Cr and Mn. Meanwhile, Si in the layer 8.40 μm below the surface corresponded to the oxides of Si. These are clearly showed in Figures 5.12, 5.13, 5.14(b) and 5.14(c). From Table 5.5 and Figure 5.14(c), in the layer 8.40 μm below the surface of specimen B, there were also depletions of Cr and Mn resulting from the diffusion of Cr and Mn toward the oxidation front. Figure 5.14(c) also reveals a decarburised zone within a depth of ~3 μm, corresponding to the zone of oxides of Mn and Cr, and a depletion of Fe corresponding to the peak of Cr. Peak concentrations of C in the outermost surfaces were due to the contamination of C in the anode (see Section 6.2) and on the original surfaces of the specimens.

The profiles in Figure 5.14(b) and (c) were from different burns of the same specimen. The depth of the profile in Figure 5.14(b) is up to 2.84 μm. For the same depth range in Figure 5.14(c), the elemental profiles of Cr, Mn, Si, C and Fe are quite similar to those in Figure 5.14(b). This indicates that the GDOES measurements have good

reproducibility. All of the depth profiles in Figure 5.14 show that there were always Si peaks close to the outer surfaces, followed by strong Mn peaks, and then Cr peaks. Internal oxidation is driven by the oxygen in the furnace atmosphere. The difference of alloying element affinities for oxygen and oxygen partial pressure in the different heating stages led to the formation of different internal oxides. The results in Figure 5.14 agreed with the thermodynamic data, reported by Kozlovski *et al.* (1967), that alloy elements' affinities for oxygen should be in the order of Si, Mn and Cr in the gas carburising atmosphere, while Fe, Ni, Mo are not expected to oxidise.

Combined with observations on the oxides' morphology, it is clearly indicated that Cr and Mn oxides are formed at larger sizes in the outer layer zone close to the surface and Si oxides are formed as intergranular oxides remote from the surface. These different morphologies related to different heat processes and stages, in which the oxygen partial pressure was different. Thermodynamically, for the three elements, the free energy of formation of Si oxides is lowest, followed by Mn and Cr (Birks and Meier, 1983). Therefore, growth of the silicon oxides was prevented from their nucleation and then stable silicon-oxides were formed in the boundaries, as seen in Figures 5.9(j) and (l). They can form even in a lower oxygen-activity region. As a result, Si oxides formed in the deep region as a network of uniform intergranular oxides. Meanwhile, the oxides of Cr and Mn tended to growth rather than nucleation, so the oxides of Cr and Mn with a large size were seen in the layer in front of the region of Si oxides.

For the surface analysis of steels, GDOES has an ability to do a depth profiling at a depth from hundreds of nanometres down to ~100 μm. The depth resolution is generally about ~15% of sputtered depth. For example, the depth resolution is less than 0.5 μm for a depth of 3 μm. The region of internal oxides in carburised steels is generally less than ~30 μm. This is just the favoured range of depth profiling in GDOES. Through the depth profiling for the oxidation-affinities elements such as Si, Cr, Mn and the elements C and Fe, GDOES depth profiles can be used to identify different oxidation zones in the whole range of oxidation by the concentration changes

of the elements. This is very helpful in the investigation of mechanisms of internal oxidation and the choice of thermal cycle in the carburising process. This ability, then, cannot be replaced by traditional analysis methods for internal oxides, for example, cross-section line scans in SEM/EDS and electron probe microscopy analysis (EPMA), and a depth profile in X-ray photoelectron spectroscopy (XPS). Moreover, GDOES provides unique plan view images of the oxide structure to a known depth when the eroded surface is subsequently examined in SEM, allowing direct correlation of chemical information with oxide distribution and a potential use of other complementary techniques, such as the EBSD (see Section 5.2).

5.4 Conclusions

1. The results of the EBSD patterns collected from the surfaces of the pure iron and the copper after GDOES etching have shown that a high-power Grimm source, as generally employed in GDOES, is an excellent tool for removing surface damage in iron specimens prior to study using EBSD. The technique is extremely fast and can in principle be applied to any sample, without the use of any chemicals; non-conducting specimens would require the use of a radio-frequency plasma source. The Grimm source itself is a simple system (as, say, compared to an ion beam thinner), and so could represent a very cheap and fast specimen preparation route.
2. GDOES has proved a powerful tool for the study of internal oxidation, combining excellent depth resolution with good elemental sensitivity and rapid specimen analysis. A secondary benefit of the GDOES sputtering technique is the ability to sputter to a known depth and hence to reveal the oxide morphology in a plan view.

Chapter 6 Hydrogen Detection in GDOES

6.1 Introduction

Hydrogen can enter the surface of solid metal in its mono-atomic form. At room temperature this commonly occurs during the electrochemical evolution of hydrogen such as in corrosion cells, in the electroplating processes, acid cleaning and cathodic protection. At higher temperatures, hydrogen enters the surface of solid metal bases through a different mechanism known as chemisorption. Molecular hydrogen gas can readily enter a molten metal surface via water contained in the ambient atmosphere. The dissolved molecular hydrogen can be retained as a mono-atomic solute on solidification (Cater *et al.*, 2001). At normal pressures and low temperatures, it is difficult to form metal hydrides. As an interstitial solute, hydrogen remains in its mono-atomic form and exists in the microstructure of metals (Hill, 1961). The atomic hydrogen can be trapped in the lattice defects, usually dislocations and interfaces between the metal and a second phase, or grain boundaries. Molecular hydrogen can also be formed in voids in the metal, which is very dependent on the energy of motion of the hydrogen atoms and the nature of the lattice defects. As atomic hydrogen accumulates in a steel, it becomes hydrogen embrittled and shows a loss in ductility and toughness. The hydrogen contained in metals can also cause cracks under the influence of stress and results in the premature failure of parts before and while in service (Timmins, 1997).

Hydrogen in metal samples can be detected in different ways. Hydrogen embrittlement of steel is evidenced as a reduction in ductility. Therefore, mechanical tests which actually measure or evaluate reduction in ductility in combination with residual or applied stresses are mostly applied in studies of hydrogen embrittlement. Standard

embrittlement testing methods have been modified to incorporate fracture mechanics. Since 1980, various types of hydrogen damage have been further classified in terms of crack nucleation, crack growth rates, and threshold stress-intensity measurements (Raymond *et al*, 1987). Hydrogen contained in steels can also be detected by the tin-fusion method (Snavely, 1961), which involves dissolution of the steel samples in molten tin to free the contained hydrogen as a gas. The tin-fusion method combines the advantages of accuracy, relative ease of performance, and short time for completion; however, its cost and complexities have often been stumbling blocks in embrittlement studies. The concentration of hydrogen in metal pieces can be detected by the barnacle electrode (Fullenwider, 1983), which is an electrochemical device. This device can cause any hydrogen near the surface of a specimen to diffuse out, resulting in a decay transient, recorded as a current. Provided that the diffusion coefficient for hydrogen in the specimen is known, the recorded current can be used to directly calculate the concentration of hydrogen in the specimen.

Hydrogen detection is impossible via most traditional surface analytical techniques. For example, hydrogen has no X-ray or Auger transition; it does not neutron-activate, and it is too light for Rutherford back-scattering analysis (Lanford, 1982). Only a few techniques can deal with hydrogen detection in the near surface, for example, Secondary Ion Mass Spectroscopy (SIMS), Nuclear Reaction Analysis (NRA) and Elastic Recoil Detection Analysis (ERDA). However, these all suffer from disadvantages in that they are limited to the outermost surface, are time consuming and expensive. SIMS can be used in hydrogen detection in metals (Suzuki and Ohtsubo, 1984; Oya *et al.*, 2001). For hydrogen depth profiling, SIMS is sensitive but difficulties may arise in layered samples, due to both the mobility of hydrogen under the analysing beam and differences in the ionisation probability of the sputtered atoms in different layers (matrix effects) (Bishop, 1986). It is also generally only suited for relatively shallow depth profiling (<1 μm).

Higher-energy ion beam techniques rely on binary collisions between the beam ions and hydrogen nuclei. Although the sensitivity of hydrogen is usually not as good as SIMS, matrix effects are small or negligible, and the requirement for standards is reduced or even eliminated (Marwick, 1991). Methods for quantitative analysis for hydrogen based on nuclear reaction analysis were developed in the 1970s (Lanford *et al.*, 1976; Ziegler *et al.*, 1978; Clark *et al.*, 1978; and Lanford, 1982). The NRA technique makes use of a narrow isolated resonance in the nuclear reaction: $^{15}N + {}^{1}H \rightarrow {}^{12}C + {}^{4}He + 4.4$ MeV gamma-ray. The sample to be analysed is bombarded with ^{15}N from a nuclear accelerator with an energy equal to the resonance energy (6.4 MeV) or above. The yield of characteristic 4.4 MeV gamma-rays is a measure of the hydrogen concentration on the surface or within a certain depth of the analysed sample. Applications of NRA in hydrogen detection are found in the field of semi-conductors (Marwick, 1991). This technique has good near-surface depth resolution, as high as 12 Å in theory. But it would degrade to 200 Å f.w.h.m. at a depth of 580 Å in practice for Si samples (Hjörvarsson and Rydén, 1990). Sensitivities to hydrogen in silicon as low as 50 appm (Damjanschitsch *et al.*, 1983) or 20 appm (Kuhn *et al.*, 1990) have been achieved.

Elastic recoil detection analysis is another high-energy ion beam technique applicable in the detection of hydrogen, especially when the hydrogen concentration is rather high and poor depth resolution is not a disadvantage. The essence of the method is to knock hydrogen atoms out of a target using an MeV beam, so that the recoiling hydrogen atoms have MeV energies, then their energy spectrum is measured to get the hydrogen depth profile. Reflection ERDA was introduced by Tirira *et al.* (1996) and is an accurate and convenient method of hydrogen depth profiling. With the techniques of the channel-depth conversion and the energy-spread correction (Verda *et al.*, 2001; 2002a; 2002b), the channel axis of ERDA spectra can be converted directly to units of depth. With MeV He^{+} beams the sensitivity of ERDA is usually quoted as being of order 0.1 at.% (1000 appm) (Marwick, 1991). The depth resolution of ERDA using MeV He^{+} beams is quite poor. Comparing experimental results between ERDA and

NRA by Wielnski *et al.* (2002) shows that the best depth resolution and sensitivity for hydrogen detection are offered by resonance NRA. MeV-He^+ ERDA only has good depth resolution for the near surface, and rapidly reduced with depth.

GDOES is one of the few analytical techniques that are sensitive to hydrogen. It is also fast, easy to operate and relatively inexpensive. GDOES has been successfully applied in depth profiling analysis for both conductive and non-conductive materials. However, there are only a few applications involving hydrogen detection for surface analysis reported in the literature. In an early study on GDOES, Alexandre *et al.* (1983) compared GDOES, SIMS and AES (Auger Electron Spectroscopy) depth profiles of the first few nanometres of passive films formed on iron surfaces after a borate treatment. They showed that only GDOES provided a hydrogen depth profile. Hydrogen cannot be detected directly in AES and can be difficult in SIMS, although SIMS provided some additional molecular evidence, namely the presence of OH^-. Recently, Shimizu *et al.* (2002) reported a hydrogen depth profile using GDOES with an rf-source in an analysis of a boron-doped diamond film, ~13 μm thick, deposited onto a mirror-finished n-Si(100) substrate by microwave plasma chemical vapour deposition. After 2000 seconds of sputtering, hydrogen was detected both in the diamond film and in the silicon substrate. In the film, the intensity of hydrogen decreased rapidly during the first 200 seconds, and then to a steady and low value after 400 seconds of sputtering. In the silicon substrate, a hydrogen peak was detected near to the film. The significance of the hydrogen intensity in the first few hundred seconds of sputtering time suggested that it was genuine and not associated with moisture layers adsorbed on to the diamond surface. The hydrogen peak detected in the silicon substrate suggested that hydrogen had diffused into the silicon substrate during the early stage of film deposition. The hydrogen profile is quite similar to those that have been detected in electroplated samples in this study, which will be described in Section 6.3.2. GDOES also has a relatively high sample-erosion rate. It can do bulk and depth profile analysis of metal samples with tens of microns of depth, which makes it possibly suitable for the hydrogen analysis of steel samples. In view of this, a programme of research was set up

to test the possibility of using GDOES and how sensitive the GDOES technique could be in the detection of hydrogen in steels, so as to establish whether or not this could be used as, say, a routine test on steels or other metals that may suffer hydrogen attack.

Background signals always exist in most detection techniques. For common applications of GDOES analysis, the background term is known as consisting of five separate components: a constant component from photomultiplier dark current and other instrumental noise sources; continuum and line components from the argon plasma; and from the sputtered matrix (Payling, 1997a). It can be dealt with, however, in the quantification procedures at certain levels (Weiss, 1995 and 1997). But for hydrogen detection in GDOES the results also suffer, apart from the background signal mentioned above, from contamination due to the hydrogen which already exists in the glow discharge source (GDS) before the sample is analysed and the hydrogen contamination that keeps entering the GDS during GDOES measurement. With the addition of the effects of hydrogen contamination, the background signal of GDOES in hydrogen detection becomes more complex and variable, and is the main problem of GDOES applications for hydrogen detection. In GDOES, the hydrogen contamination is believed to come from water vapour, hydrocarbons and the argon gas (Payling, 1997a). In this investigation, the origins of the hydrogen contamination were classified and quantified. The data indicated that the hydrogen mainly comes from water vapour. Unfortunately, this is inevitable during the first tens of seconds of sputtering time in GDOES measurements. However, in this investigation, it is shown that with a proper warming up of the instrument, a so-called "hydrogen detection status" can be obtained. In this status, intensities of the hydrogen contamination at a selected sputtering time, say two hundred seconds, can be kept nearly constant for different burns. Therefore, a comparison of hydrogen contained in different steels can be carried out. Furthermore, the experiments in this chapter revealed that significant differences in the intensities of the hydrogen contamination in GDOES can be the result of different sample matrices in the hydrogen detection status, even when the samples were heated and were believed to have no hydrogen in them. These different hydrogen intensities detected using samples

with different matrices are collectively named as the "matrix effect" on the intensity of hydrogen contamination in GDOES in this study, and will be discussed in Section 6.2.3 in consideration of the relevant ionisation and excitation processes in the glow discharge. Some results of hydrogen detection in GDOES were obtained and show that the GDOES in the hydrogen detection status has an ability to differentiate the hydrogen contained in bulk samples with similar matrices.

It was found in this study that the hydrogen contamination in the source can also affect quantitative results for some elements in the GDOES measurements. Hodoroaba *et al.* (2000a) have reported experimental results on the influence of hydrogen in the case of copper as a cathode sample by means of the addition of small quantities of molecular hydrogen (<1% relative partial pressure) to the argon carrier gas. The glow discharge was controlled by keeping the voltage and gas pressure constant. The progressive addition of molecular hydrogen caused different intensity changes particular to the individual lines of different species such as atomic (Cu I) and ionic (Cu II) copper, and also atomic (Ar I) and ionic (Ar II) argon. Most of the emission lines of Cu I increased strongly with the addition of even small quantities of hydrogen. They also presented evidence of the effects caused by hydrogen for the different matrix elements in copper, stainless steel, titanium, aluminium and silicon (Hodoroaba *et al.*, 2000b). In general, the lines of most of the sputtered elements, Fe I (371.9 nm), Fe II (249.3 nm), Cr I (425.4 nm), Ni I (349.2 nm), Mn I (403.4 nm), Mo I (386.4 nm), W I (429.4 nm), Ti I (365.3 nm), Al I (396.1 nm) and Cu II (219.2 nm), decreased in intensity as hydrogen increased, but at different rates. However, many lines such as Cu I (327.3 nm) and Si I (288.1 nm) increased in intensity when a copper sample and a silicon wafer were sputtered.

Not many papers can be found in the literature on correction for the hydrogen effects on the measured elemental concentrations in GDOES. An improved method for quantitative GDOES depth profiles of hard coatings has been developed to account for all known variables in the plasma, notably the electrical plasma parameters, pressure

and especially for the hydrogen effect (Payling *et al.*, 2001; Payling *et al.*, 2002). The experimental results by Hodoroaba *et al.* (2000b) have been taken from this method and were normalised to a general form of hydrogen effect on an inverse relative emission yield. It is aimed principally at radio-frequency (rf) operation, while the method is applicable to direct current (dc) operation. The method with hydrogen correction has been successfully applied in TiCN, TiN, TiC, Cr_7C_3, TiAlN, CrN and MoS_2+Ti coated steels.

To test the hydrogen effects on measured elements in normal operation, i.e. without a special mixture of hydrogen with the argon, and what level of the effect occurred in the normal operation, GDOES measurements were carried out using two steel standards in GDOES conditions of fixed voltage and current. The hydrogen effects on measured elements and depth in the GDOES using the standards will be discussed at the end of this chapter.

6.2 Hydrogen Signal in GDOES Analysis

If a sample contains hydrogen, whether as molecules, atoms, ions or in hydride compounds, the hydrogen in the sample should be included in the intensity of hydrogen detected in GDOES. Figure 6.1 shows a typical plot of a hydrogen signal detected from a carbon steel that may reveal the hydrogen contained in the sample. This is a simple plot of elemental intensities recorded as corresponding photomultiplier responses, without further processing in any way. The hydrogen signal starts high, and appears to decay exponentially, approaching an asymptote at about 200 units. The most naïve interpretation of this behaviour would be that this exponential represents the actual hydrogen profile in the steel measured as a function of depth. Detailed experiments described in Section 6.2.1 will show that the main cause of the high intensity of hydrogen at the beginning of the sputtering and the decay is to do with various types of gaseous and surface contamination. The warming-up procedure of GDOES before

detection of hydrogen also severely affects the hydrogen value as it decays asymptotically. However, it is possible to reach a 'hydrogen detection status' in GDOES, which will be described in Section 6.2.2. Effects of the sample matrices on the hydrogen intensity in GDOES detection will also be discussed in the last part of this section.

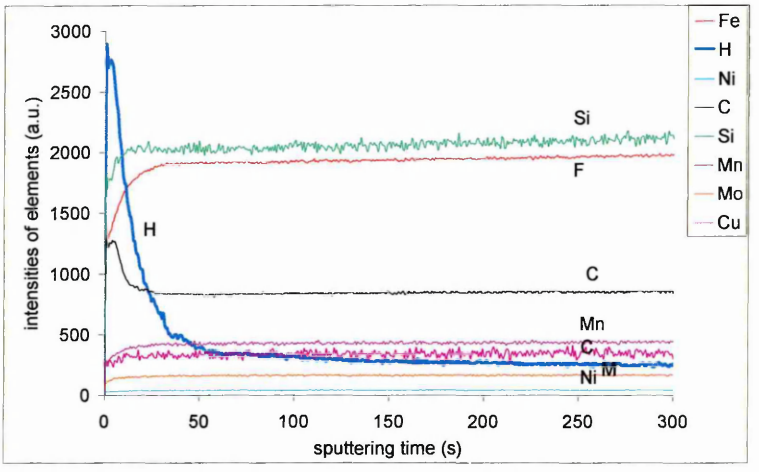

Figure 6.1. A typical profile of a hydrogen intensity detected from a carbon steel using GDOES.

6.2.1 Hydrogen contamination in GDOES measurements

6.2.1.1 Experimental technique and results

Due to the working principle of GDOES and the procedure of operation, the hydrogen contamination comes mainly from the water vapour deposited on the surface of the GDS chamber and the sample, hydrocarbons that have back-streamed into the chamber from the pumping system, and the hydrogen contamination of the argon gas. To confirm the contamination of hydrogen intensity in GDOES, pure silicon wafers were chosen as samples because they are manufactured under a process with strict controls and their perfect mirror-like surfaces can provide a uniform surface and also seal the GDS chamber as tight as possible. The discharge conditions and gain of the photomultiplier (PMT) for hydrogen were also fixed with a voltage of 700 V, a current of 30 mA and gain of the PMT for hydrogen of 10.

Water vapour

In GDOES measurements, exposure of the sample surface and the source to ambient water vapour is unavoidable as the source must be sealed from the air by a measured sample forming a vacuum chamber. When the source is open (i.e. no sample is in place), argon gas is blown through the source continuously to minimise contamination from outside of the source. However, water vapour still has a chance to deposit onto the annular space between the anode and the cathode and the end surface of the source facing the cathode sample. So the exposure time, ambient moisture and temperature can affect the water vapour deposited on these surfaces, and consequently affect the hydrogen intensity in GDOES detection.

The effect of the exposure time on the hydrogen intensity was tested by a series of measurements using silicon wafers. A warm-up procedure was first carried out for about a thousand seconds' sputtering before the test to reduce the hydrogen already existing in the source to a low level. Between the measurements, the source was exposed to ambient conditions for different times. Figure 6.2 shows how the hydrogen intensities change with different exposure times of the source to the atmosphere from 20 seconds to 30 minutes. For each of the measurements, a peak of hydrogen intensity is always detected within the first 10 seconds of sputtering. The hydrogen intensities then decrease as the sputtering time increases. All the hydrogen intensities of the different measurements are similar after etching has proceeded for about 100 seconds. From 20 seconds to 30 minutes, the longer the exposure time, the higher the peak of the hydrogen intensity. This implies that the exposure times have an effect on the hydrogen intensity, particularly during the first few tens of seconds' sputtering, due to the water vapour. The integrated values within 300 seconds of sputtering time for the hydrogen intensities in Figure 6.2 indicate a saturated status of the water vapour diffused onto the surfaces as the source is exposed to the atmosphere for a longer time (after 600 seconds), as shown in Figure 6.3.

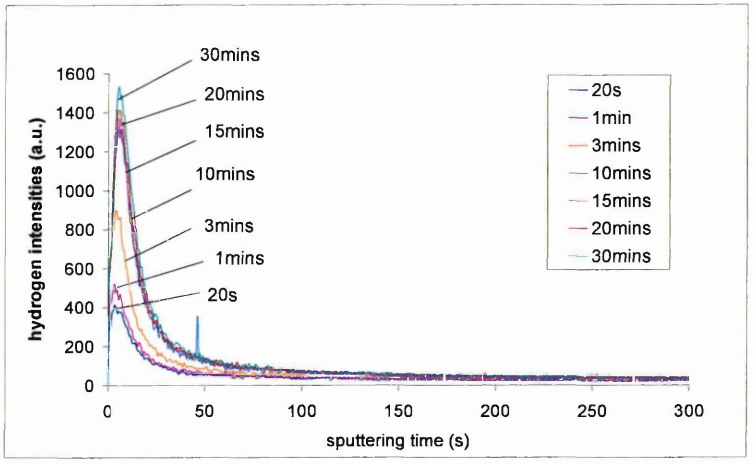

Figure 6.2. The hydrogen intensities change as different exposure times of the source to the atmosphere from 20 seconds to 30 minutes. Samples: silicon wafers. GDS: 700V/30mA/4mm anode. Gain of the PMT for hydrogen:10.

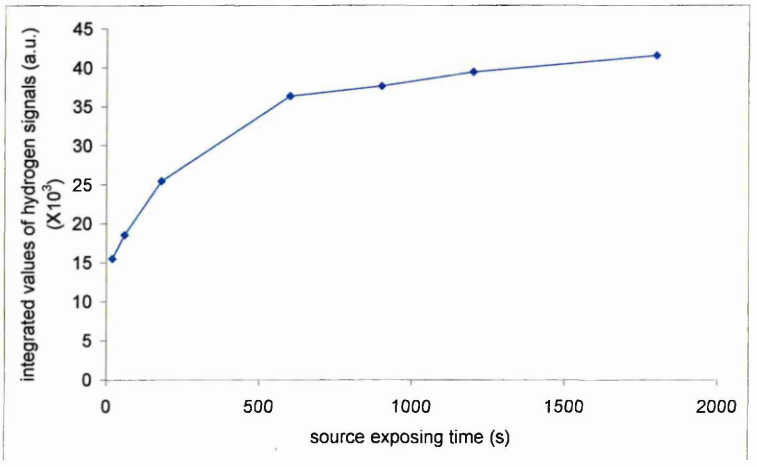

Figure 6.3. Integrated values for the hydrogen intensities in Figure 6.2 indicate a saturated status of the water vapour diffused onto the surface as the source is exposed to the atmosphere for a longer time.

The hydrocarbons

Rotary pumps were used in the GDOES equipment employed in this research. They maintain the vacuum in the spectroscopy chamber and are used for the evacuation of the source chamber. Hydrocarbons from the oil in the pump that evacuates the source chamber can diffuse back into the source. To test the hydrocarbon effect on the hydrogen intensity, the water vapour effect must be removed as much as possible. In the GDOES, it is possible to make multiple burns on one spot without the source being

exposed to the atmosphere, called 'same spot' burns. With this kind of procedure, the sample can be held on the source under the vacuum and kept on the source after the prior burn until the next burn is ready to be done after an interval of time. An experiment with multiple-burns procedure was done at different intervals between the burns. Each of the burns has 300 seconds of sputtering time and the intervals were 100s, 1hrs, 2hrs, 4hrs, 10hrs and 20hrs. During these intervals, the source vacuum was kept at 1.3 Pa. At the beginning of sputtering, the vacuum of the source was ~1.5 × 10^2 Pa. In this procedure, most of the hydrogen signal in the GDOES measurements is expected to come from the hydrocarbons' back-diffusion as the source was isolated from the ambient environment. Figure 6.4 shows results of the measurements of the hydrogen intensities in the procedure of multiple burns. The longer the time interval, the higher the peak value of the hydrogen intensity. This suggests that hydrocarbon back-streaming into the source does exist. Figure 6.5 shows the carbon signals of the burns corresponding to those in Figure 6.4. The similarity of the configuration between the curves of hydrogen and carbon signals in the two figures confirms that hydrocarbons are back-streaming and discounts the possibility of the increase being due to hydrogen build-up in the pumping system (such as out-gassing of water in the pumping lines, etc.).

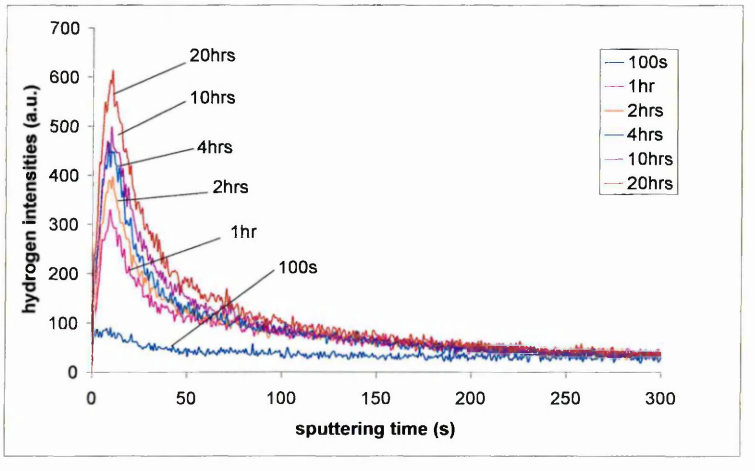

Figure 6.4. The hydrogen intensities in the procedure of multiple burns with different intervals between the burns from 100 seconds to 20 hours. Samples: silicon wafer. GDS: 700V/30mA/4mm anode. Gain of the PMT for hydrogen: 10.

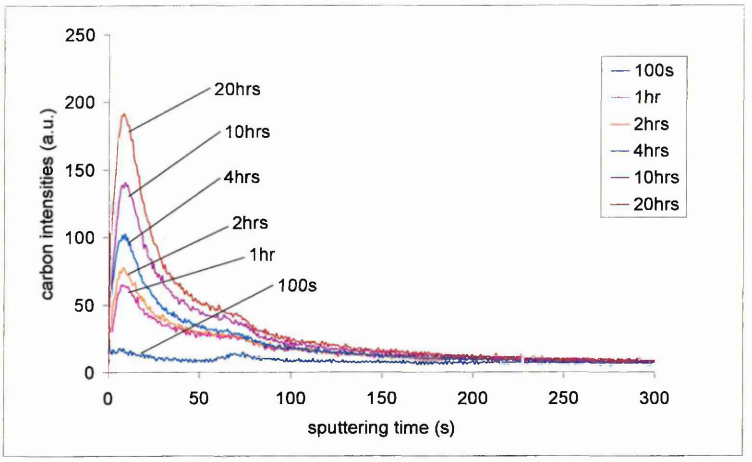

Figure 6.5. Carbon signals of the burns corresponding to those in Figure 6.4. The similarity of the configuration between the curves of hydrogen and carbon signals in the two figures confirms that hydrocarbons are back-streaming.

The argon pressure during the sputtering (~1.5×10^2 Pa) mentioned above seems not to be in the range of the argon pressure of the glow discharge (Section 2.2.1). In the GDOES, the displayed argon gas pressure of the source corresponds to the pressure on the annular space side of the anode-cathode block. The actual pressures in the glow discharge were measured during a simulation test without discharge by a vacuum gauge installed in place of the cathode sample (Bouchacourt and Schwoehrer, 1997). The results indicated that the pressure in the discharge region was around 10 times greater than that measured in the annular anode-cathode space for a 4 mm anode. Therefore, the argon pressures displayed in the GDOES should be around 10 times lower than the actual pressures in the discharge region.

Hydrogen in the argon gas

During sputtering in GDOES, argon gas is continually bled into the source to maintain the glow discharge. The argon pressure in the GDOES is controlled by a gas controller to keep the current constant in accordance with changes of the sample matrices. Since the same sample matrix (silicon wafers) was used, the argon pressure in this experiment should not change significantly either during a measurement or from sample to sample. Therefore, the hydrogen atoms in the source from the argon gas should be fairly constant if the argon flow does not change during the sputtering. Experimental results

using high-purity argon gas and normal analysis argon respectively are shown in Figure 6.6. Peak values of hydrogen intensity can be seen in the first few tens of seconds' sputtering for both argon gases although the GDOES was well warmed up. This is due to the water vapour effect since the procedure of same-spot burns could not be employed in this test. After 100 seconds' sputtering, the two lines decay with increasing sputtering time parallel to each other, with a difference of ~15 (a.u.) on average between 100s and 1200s, and about 10 (a.u.) after 1300 seconds of sputtering time. Comparing the results in Figures 6.2 and 6.4, whatever the peak values of hydrogen intensities at the beginning of sputtering are, after more than 200 seconds of sputtering, the intensities are very close. So the difference of ~15 (a.u.) can be considered as an effect on the hydrogen intensity due to the hydrogen coming from different purity argon gases.

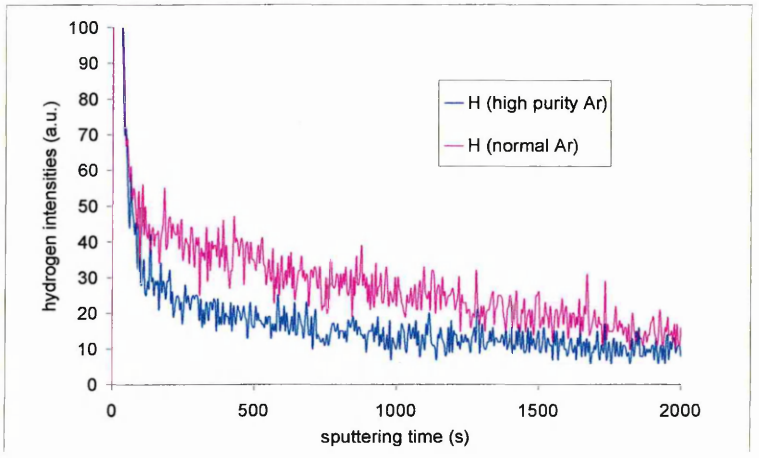

Figure 6.6. Hydrogen intensities detected in the GDOES using high-purity argon gas and normal analysis argon gas, respectively. Samples: silicon wafers.
GDS: 700V/30mA/4mm anode. Gain of the PMT for hydrogen: 10.

6.2.1.2 Discussion

It is noted that the hydrogen intensities in Figures 6.1, 6.2 and 6.4 decrease as the sputtering time increases, even within the long sputtering time of 2000 seconds as shown in Figure 6.6. The peak values of hydrogen intensities are normally present at about 10 seconds of sputtering time, and then decay exponentially. The hydrogen contamination from the hydrocarbons is quite small compared with that from the water

vapour diffusion. The highest peak value in Figure 6.4 with a 20-hour interval is only 600 (a.u.), which is even lower than the peak value with 3 minutes of source exposure time in Figure 6.2. The hydrogen level in the GDOES due to the hydrogen contaminants in the argon gas should change little if the argon flow is kept constant. For the hydrogen contamination tests in the source here, only silicon wafers were used and the argon pressure should be constant. Therefore, the hydrogen contaminants in the argon are not expected to contribute to the decay. Actually, the hydrogen contaminant in argon gas is the smallest component in the three sources of hydrogen contamination. Comparing Figures 6.2, 6.4 and 6.6 it can be seen that the water vapour is the most significant contribution to the hydrogen signals in GDOES measurements within the first hundred seconds of sputtering.

In the operation of the GDOES, there is a pumping time after the source is sealed by a sample and before the sputtering starts. In this study the pumping time was 20 seconds. The source chamber was evacuated by the pumping to a vacuum in the range of 1.2–2.0 Pa, which should have removed some of the hydrogen existing in the source before the sputtering started. However, there was still residual hydrogen in the source chamber, which came from the water vapour and the hydrocarbons that have back-streamed into the source during the pumping time. During sputtering, therefore, the decay of the hydrogen intensity as the sputtering time increases should be a dynamic process which involves hydrogen entering the source and exiting the source simultaneously. Since the hydrogen intensity showed decay as the sputtering time increased, it suggested that a minimum limit of hydrogen intensity should principally be obtained with a long sputtering time, when a hydrogen balance status between the hydrogen entering and leaving the source is reached. However, this condition is almost impossible to reach in practice due to the sputtered materials being deposited on the edge of the sputtered crater during the sputtering. After an extended sputtering time the material eventually leads to an electrical circuit between the anode and the cathode (sputtered sample), which will form a short circuit and interrupt the sputtering. Under

normal conditions the sputtering time cannot exceed about 2000 seconds when steel samples are sputtered.

6.2.2 The hydrogen detection status in GDOES

The peak value of hydrogen intensity is inevitable during the first tens of seconds of sputtering time and a minimum limit of the intensity of hydrogen contamination in GDOES is impossible to reach. However, it is found in this study that when the GDOES is in the low hydrogen background status after proper warming-up of the GDOES, the hydrogen intensity at a selected sputtering time, for example two hundred seconds, is nearly constant over multiple measurements of the same sample. This status is called the 'hydrogen detection status' of GDOES in this study.

6.2.2.1 Experimental and results

In order to test the hydrogen detection status of GDOES, two groups of samples were prepared. One of the groups was used to obtain the status of the low hydrogen background, and named the warm up (WUP) samples. The WUP specimens were cut from a steel block into a size of 30×30×3 mm and mechanically polished using grade 600 grinding-paper to get a uniform surface finish and to provide a good surface to seal the source chamber. Before GDOES measurements, the specimens were baked in an oven at 250 °C for 20 hours in order to remove possible hydrogen in the specimens. The baking temperature of 250 °C was chosen so that most of the hydrogen in the steel (i.e. the more mobile or diffusible part) could be removed before the temperature reached 250 °C (Smialowski, 1962). Another group consisted of five steel specimens (STL 1–STL 5), which may contain hydrogen. The STL specimens were cut into a size of 30×30×6 mm with lubricant to prevent the samples from overheating during the cutting process. Compositions of the steel specimens were measured in the GDOES and are listed in Table 6.1. All of the samples in the two groups were at room temperature before measurement and were then sputtered in the GDOES for 300 seconds. Hydrogen intensity at 200 seconds and 300 seconds respectively for each of the measurements were collected and are shown in Figure 6.7. The hydrogen intensities are averages of 10

data points around the selected sputtering times. The 10 data points correspond to about 6 seconds of sputtering.

Table 6.1. *Compositions of the steel specimens measured in the GDOES (mass%).*

	Fe	C	Si	Mn	Cr	P	S	Ni
Steel 1	94.17	0.227	0.484	1.510	3.165	0.032		
Steel 2	93.66	0.135	0.420	2.012	2.993	0.030		0.117
Steel 3	94.11	0.200	0.458	1.568	3.110	0.031		0.006
Steel 4	95.94	0.070	0.101	0.337	3.135	0.032	0.011	
Steel 5	90.60	0.512	1.538	0.777	3.740	0.032		1.928
	Mo	**Co**	**Cu**	**V**	**Ti**	**Pb**	**Nb**	**Zr**
Steel 1		0.009	0.174	0.052	0.053	0.095	0.002	0.026
Steel 2	0.288	0.010	0.175		0.044	0.071	0.010	0.033
Steel 3		0.012	0.360		0.024	0.092		0.028
Steel 4		0.013	0.185		0.025	0.125		0.027
Steel 5	0.395	0.015	0.247	0.053	0.023	0.117		0.023

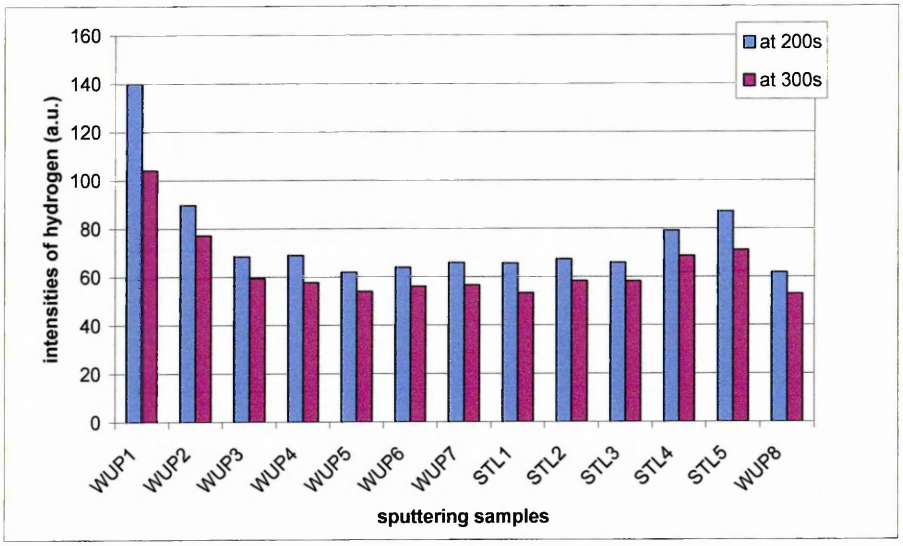

Figure 6.7. Hydrogen intensities of the warm-up specimens (WUP) and the steel specimens (STL) at 200s and 300s of sputtering time, respectively. The intensities of WUP3 to WUP8 indicate that the GDOES was in a status of low background of the hydrogen intensity (the status of hydrogen detection of GDOES).
GDS: 700V/30mA/4mm anode. Gain of the PMT for H: 10.

From Figure 6.7 it can be seen that the hydrogen intensity of the warm-up specimens reduced from WUP 1 to WUP 3 and the GDOES reached a stable and low level of

hydrogen intensity from specimen WUP 3. The average hydrogen intensity of the warm-up samples from WUP 3 to WUP 8 at sputtering times of 200 and 300 seconds were 65.2 and 56.1 (a.u.) with standard deviations of 3.16 and 2.38, respectively. This small standard-deviation implies the GDOES was in a status of stable background signal of the hydrogen intensity. The steel specimens were sputtered following the warm-up specimens in the order STL 1 to STL 5. The hydrogen intensities of STL 5 and STL 4 were a little higher than the other steels and the averages of the warm-up specimens, both at 200 and 300 seconds. In order to remove the effect of the sampling order in the results in Figure 6.7, another round of measurements in the GDOES for the same samples and under the same parameters of GDOES was undertaken. In the second round of measurements, sampling of the steels was in the order STL 5 to STL 1, in the reverse order to the last round. The results are shown in Figure 6.8. The average of the hydrogen intensities of the warm-up specimens WUP 2 to WUP 5 at 300 seconds was 40.6 (a.u.) with a standard deviation of 1.20, which confirmed the status of the GDOES. The hydrogen intensities of STL 5 and STL 4 were still a little higher than the others. Similar results to those of the last round of measurements were obtained.

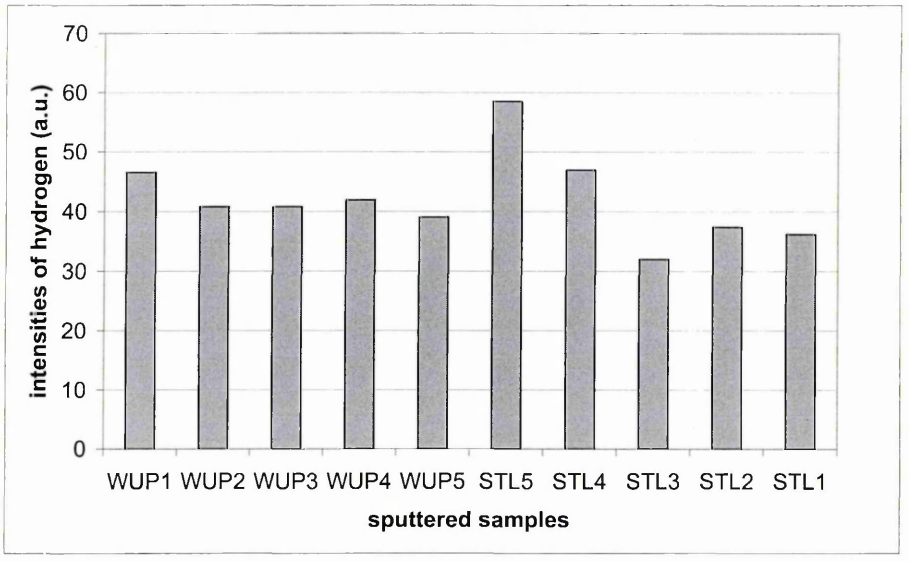

Figure 6.8. The hydrogen intensities of the second round of measurements using the same specimens with those in Figure 6.8 but in a reverse sampling order for the steel specimens confirmed the status of stable background of the hydrogen intensity of the GDOES. The setting of the GDOES were same with that in Figure 6.7.

6.2.2.2 Discussion

The intensities of hydrogen contamination in the stable condition are very low and do not change significantly with the sputtering time in the different measurements. This means that the hydrogen contamination in the source at the selected sputtering time (reasonably far from the hydrogen peak at the beginning of sputtering time) can be kept almost constant. Therefore, this low and stable hydrogen-level status can be employed as a hydrogen detection mode in GDOES. Samples containing differing amounts of hydrogen could be compared by GDOES measurements using this hydrogen detection status at a selected sputtering time, for example 200 or 300 seconds. For pure iron, 300 seconds' sputtering in GDOES with the parameters of 700 V and 30 mA and with a 4 mm anode can erode the sample's surface to a depth of 11.5 μm. The eroded surface is far from the outermost surface of the sample and thus there is little effect upon the hydrogen intensity from water vapour on the sample surface.

It was noted that there is a difference of 15.5 (a.u.) between the two hydrogen averages of the warm-up specimens at 300 seconds in the two rounds of measurements as seen in Figure 6.7 and Figure 6.8. This could be due to cleanliness of the lens in the source, which can have an affect on the transmission of light. Cleanliness of the lens not only affects the sensitivity of the emission transmission but also the relative sensitivities for different elements. Jones (1997) gave an example in which the lens was not cleaned for three weeks. Loss of transmission is most evident at the shortest wavelengths. The wavelength for hydrogen in the GDOES used here was 121.57 nm, which is the shortest wavelength used in this GDOES. The result in Figure 6.13 obtained with a newly cleaned lens shows an average for the hydrogen intensity of 86.3 (a.u.) for the warm-up specimens; two times higher than that in Figure 6.8.

6.2.3 Sample matrix effects on intensity of hydrogen contamination in GDOES

The differences in the hydrogen intensities between STL 5 and the other steel specimens and the average values of the warm-up specimens, shown in Figure 6.7 and Figure 6.8,

seem to indicate that there is more hydrogen in STL 5 than the others. However, from Table 6.1 it can also be seen that there are significant differences in composition between the specimens, for example the concentration of Fe in STL 5 is only 90.6%, lower than that in STL 1 to STL 4 (93.66–95.94%), while the concentrations of Fe in STL 1 to STL 4 are similar. This implies the matrix of the specimen STL 5 is significantly different from the other steels, which suggests that the different intensities of the hydrogen contamination could have been affected by the different matrices of the sample, i.e. the different hydrogen intensities in the measurements under the hydrogen detection status could have resulted from the different cathode matrices even when there was no hydrogen contained in the samples. This is called the 'matrix effect' on the intensity of hydrogen contamination in GDOES detection in this study.

6.2.3.1 Experimental details and results

In order to test for the matrix effect on the hydrogen intensity in GDOES detection, three types of sample, steel, pure iron and a silicon wafer, were used. Five specimens for each type were prepared, so that in total there were 15 specimens. Surfaces of the steel and the pure iron specimens were mechanically polished to a 1 μm-grade diamond paste finish to obtain a surface as close as possible to the mirror-like surface of the silicon wafer. Before sputtering in the GDOES, the steel specimens were baked at 250 °C for 20 hours to remove possible hydrogen contained in the specimens. The pure iron and silicon wafer are considered to have little hydrogen due to their strict production process. Each of the specimens was at room temperature before sputtering in the GDOES. The 15 specimens were divided into five groups. Each group contained three specimens with one from each type. Classification of the samples is listed in Table 6.2. The 15 specimens in the five groups were sputtered in the GDOES for 300 seconds, in a sampling order from group 1 to group 5 and from the steel to silicon wafer in each of the groups. In this way, the hydrogen contamination effects on the intensities in the GDOES were expected to be as similar as possible between the three types of samples. The hydrogen intensities at 300 seconds for each of the specimens were collected as shown in Figure 6.9. The sputtering rates corresponding to the measurements, as shown

in Figure 6.10, were obtained by weighing the sputtered mass using a micro-balance. Averages of the sputtering rates and the hydrogen intensities for each of the three types of samples are shown in Figure 6.11. Standard deviations of the average sputtering rates for the steel specimens and the pure iron specimens were 1.42×10^{-1} and 6.80×10^{-1} respectively. It was impossible to obtain a standard deviation of the sputtering rate for the silicon wafers due to the precision-limitation of the micro-balance, which is only to 0.1 mg. It was noted that the standard deviation of the average sputtering rates of the pure iron specimens was larger than that of the steel specimens. This could be caused by the orientation effect on the sputtering rates due to coarse grains with different orientations in the pure iron specimens (Chapter 3).

Table 6.2. *Classification of the samples in five groups for the test of the different matrices effects on the intensities of hydrogen contamination.*

Type of samples	Group 1	Group 2	Group 3	Group 4	Group 5
Steel	WUP01	WUP02	WUP03	WUP04	WUP05
Pure Iron	PFE01	PFE02	PFE03	PFE04	PFE05
Silicon Wafer	SIW01	SIW02	SIW03	SIW04	SIW05

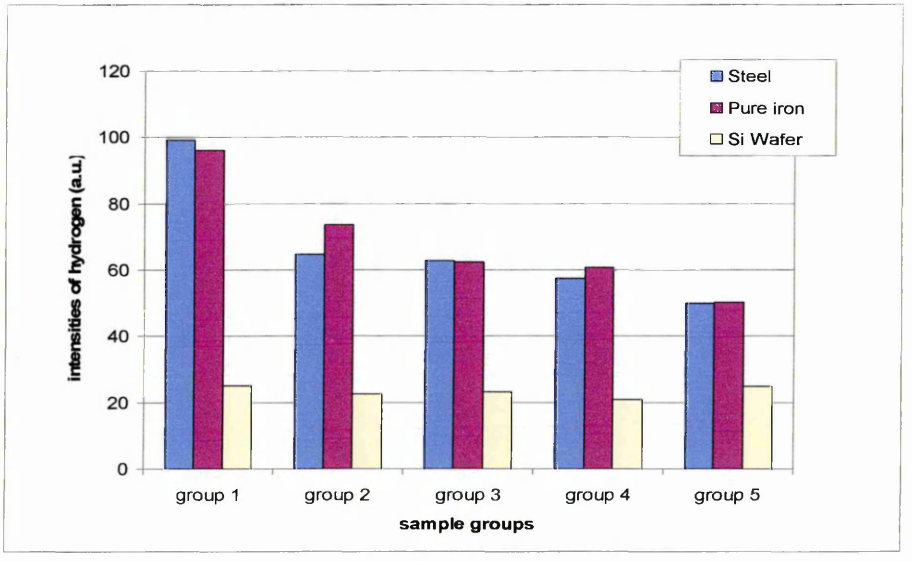

Figure 6.9. Hydrogen intensities at 300 seconds of sputtering time. The 15 specimens in the five groups were sputtered in a sampling order from group 1 to group 5 and from the steel to silicon wafer in each of the groups.
GDS: 700V/30mA/4mm anode. Gain of the PMT for hydrogen:10.

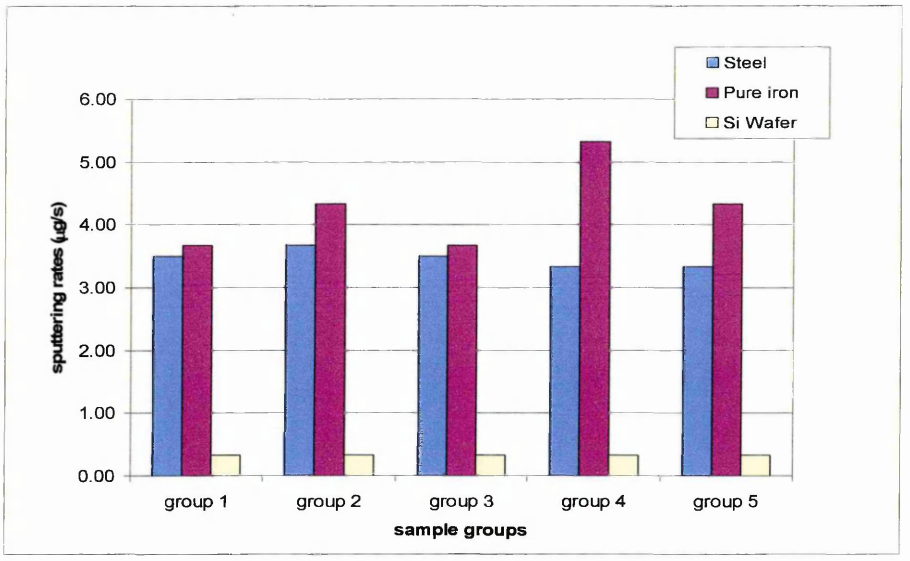

Figure 6.10. Sputtering rates corresponding to the measurements in Figure 6.9, were obtained by weighing the sputtered mass using a micro-balance and divided by 300 seconds of sputtering time.

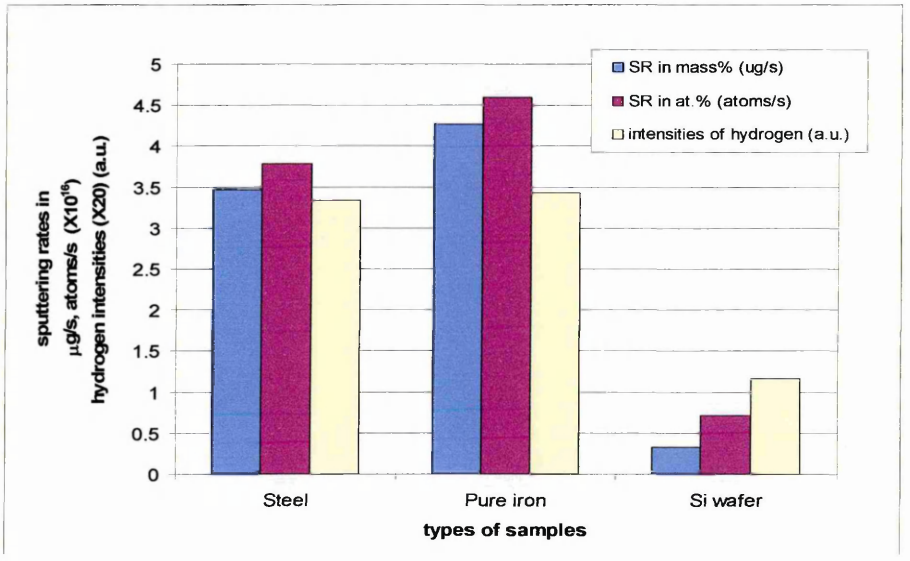

Figure 6.11. Averages of the hydrogen intensities and the sputtering rates in µg/s and atoms/sec corresponding to the measurements in Figure 6.9. Standard deviations of the sputtering rates in µm/s for the steel and the pure iron specimens are 1.42E-01 and 6.80E-01, respectively.

In Figure 6.9, the hydrogen intensities of the steel specimens and the pure iron specimens are clearly higher than that of the silicon wafers in each of the sample groups. There was no big difference in the intensities between the steel specimen and the pure iron. Minimal differences in the intensity between the steel specimens (or the

pure iron specimens) and the silicon wafers were obtained in group 5, in which the intensities of the steel and the pure iron are about 50 units, twice as high as that of the silicon wafer at 24.8 units. From Figure 6.11, the average of the sputtering rates of the pure iron specimens is 4.27 μg/s, a little higher than that of the steel at 3.47 μg/s, but ten times higher than the silicon wafers at ~3.33×10^{-1} μg/s.

From the averages of the hydrogen intensity and the sputtering rates of the three types of sample, as shown in Figure 6.11, it seems that the sample matrix effect on the hydrogen intensity is relevant to the sputtering rate of the measured sample. In order to further understand this, a further experiment was carried out. In this experiment, types of sample included steel, silicon wafer, and pure metals of copper, aluminium, molybdenum, titanium, cobalt, tin, and nickel. The specimens of the steel, pure copper and aluminium were baked at 250 °C for 20 hours. All of the specimens were at room temperature before being sputtered in the GDOES. The GDOES was well warmed-up until it reached the hydrogen detection status. The hydrogen intensities when sputtering the samples in GDOES were also collected at 300 seconds of sputtering time. The sputtering rates were obtained by known densities of the samples and sputtered depth measured using a laser profilometer. Averages of the hydrogen intensities, the sputtering rates and argon pressures for each type of sample are shown in Figure 6.12. From the figure it can be seen that the averages of the hydrogen intensity are as high as 205 and 61 (a.u.) for the aluminium and the copper, and as low as 10 and 9 (a.u.) for the silicon and the tin. The resulted sputtering rates are also varied in a range of 18.3 μg/s of the pure tin to 0.68 μg/s of the silicon wafer.

In the GDOES employed here, the voltage and the current were fixed. The argon pressure was automatically adjusted to keep the selected current as a constant. Therefore, the argon pressure could change by some level in accordance with the different matrices to be sputtered. The argon pressures of the different specimens were also recorded in Figure 6.12. It could be argued that the baking temperature and time (250 °C, 20 hours) were not high enough and long enough to release the hydrogen from

the specimens. Therefore, measurements in the GDOES using samples of the steel, the pure metals of copper and aluminium, which were baked at the temperature of 400 °C and for 48 hours, were also undertaken. The averages of the hydrogen intensities measured in the GDOES with the same conditions as the samples at 250 °C, 20 hours were 37.8, 76.6 and 246.1 (a.u.) for the steel, the pure copper and the pure aluminium, respectively. This result is similar to that in Figure 6.12. The similarity of the results between the samples heated in the two baking conditions means that the results in Figure 6.12 are validated, at least for samples of the steel, the pure copper and the pure aluminium.

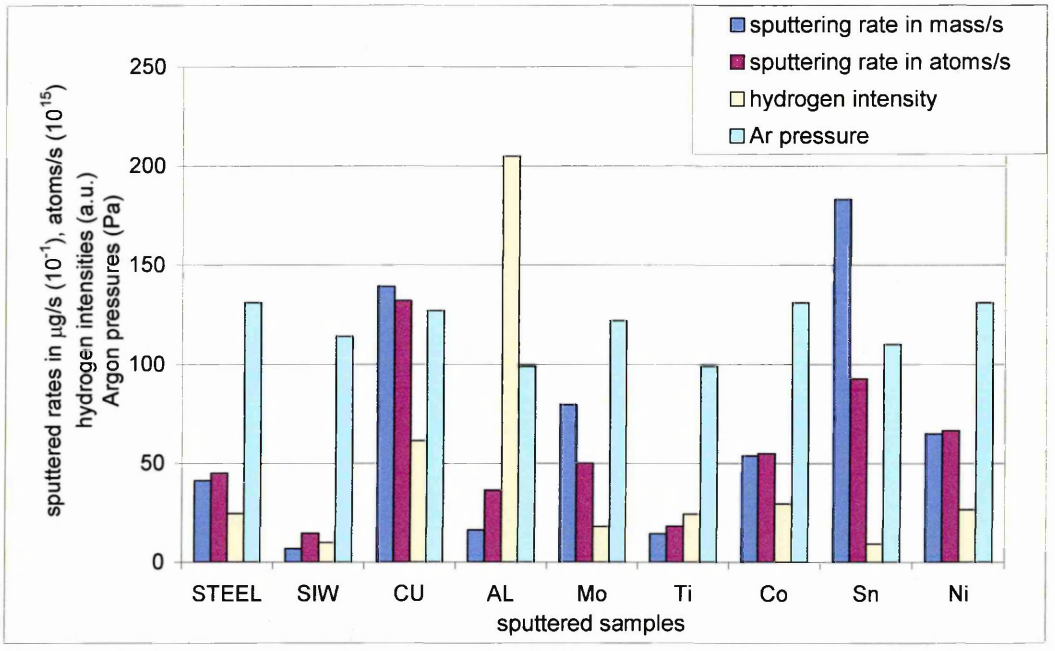

Figure 6.12. Averages of the hydrogen intensities, the sputtering rates and argon pressures for steel, silicon wafer, and pure metals of copper, aluminium, molybdenum, titanium, cobalt, tin, and nickel.
GDS: 700V/30mA/4mm anode. Gain of the PMT for hydrogen: 10.

6.2.3.2 Discussion

The results in Figure 6.12 clearly show that the hydrogen intensities do vary with the different cathode matrices. However, the results of the aluminium and the tin give a result opposite to that expected from the hypothesis that the matrix effect on the hydrogen is relevant to the sputtering rate of the measured sample. The hydrogen

intensities and the sputtering rates of the other matrices in Figure 6.12 also do not support this hypothesis. This then refutes the previous prediction that the intensity of hydrogen contamination was affected by the sputtering rate.

How does the cathode matrix affect the hydrogen intensity in GDOES detection? It may be helpful to understand this phenomenon by reviewing the processes of ionisation and excitation in the GDOES source (Section 2.3). During sputtering in GDOES there are three major particles in the source, i.e. neutral atoms, ions, and electrons (Mehs and Niemczyk, 1981). It is known that only the energetic particles, i.e. high energy electrons and metastable argon atoms, are major contributors in the emission of photons when they collide with atoms in the source (Eqns. 2.6 and 2.7).

For the three groups of electrons in the glow discharge, the energies of the γ-electrons cannot be transmitted in the excitation of the atoms directly due to their low cross-section of electron collision with higher energy. It is the secondary electrons that make a contribution to the atomic excitation in the glow discharge (Wagatsuma, 1997). The secondary electrons result from ionising collisions, have considerably lower energies on average than the γ-electrons, and have appropriate kinetic energies for excitation of the atoms in the discharge. However, the γ-electrons' impact ionisation of argon atoms (Eqn. 2.3) and the Penning ionisation of sputtered atoms (Eqn. 2.8) are the main ionisation processes in the production of secondary electrons.

In the ionisation of the argon atoms, the γ-electrons play a key role in the collisions. Although most of the primary electrons reach the anode surface without any loss of their kinetic energy in the plasma, (their energy results simply in heating of the anode), only a small share of their energy is essential for the maintenance of the glow discharge (Wagatsuma, 1997). Bogaerts and Gijbels (1998) have reported that maximum cross-sections of electron impact ionisation of argon atoms are 3×10^{-16} cm^2 and 8×10^{-16} cm^2 at the electron energies of 80 eV and 10 eV respectively, and the density of the argon ions in the glow region is 2×10^{13} cm^{-3} at 800 V of voltage, 40 mA of current and

500 Pa of argon pressure. The cross-section of the Penning ionisation between argon metastable atoms and analysed atoms are generally in the order of 5×10^{-15} cm^2. This is about one order higher than that of electron impact ionisation of argon atoms, and most of the atoms in the periodic table have an ionisation potential lower than the argon metastable level (11.55 or 11.72 eV). However, it is suggested that the Penning ionisation is only dominant in low pressure discharge glow discharge (Bogaerts and Gijbels, 1998). Therefore, the γ-electrons (which produce most of the secondary electrons) should play an important role in the excitation of the analysed atoms in the glow discharge. The γ-electrons are ejected from the cathode sample during the sputtering and their number can vary depending on the specimen matrix. The efficiency of the γ-electron emission resulting from ion bombardment is higher for non-conductive cathode materials than for metals. It also does not vary much for clean metals and is almost independent of the kind of metal (Champman, 1980; Wagatsuma, 1997). The γ-electron emission coefficient (i.e. the number of ejected electrons per incident ion) is nearly independent of the argon ion kinetic energy at energies below 500–1000 eV and is typically in the order of 0.1 for most clean metal surfaces (Chapman, 1980). The hydrogen intensities collected here are after 300 seconds of sputtering time, so the corresponding etched surfaces could be considered as the clean surfaces. In Figure 6.12, the hydrogen intensities for the steel and the pure metals of Mo, Ti, Co, and Ni are 24.4, 18.0, 24.2, 29.6, and 26.6 (a.u.), respectively. They are not very different from one another and are also more similar than the corresponding sputtering rates, which are 44.9, 50.0, 18.2, 54.8, and 66.5 ($\times 10^{15}$) in atoms per second. The fact that the sputtering rates do not match the corresponding hydrogen intensities could imply that the different hydrogen intensities are more related to the γ-electron emissions from the surface during the sputtering rather than the sputtering rate. However, the γ-electron emission coefficients in GDOES sputtering for the metals considered here cannot be found in the literature. This limits further discussion of the correlation between the γ-electrons and the hydrogen intensities. In the figure mentioned, the dramatic results of the hydrogen intensities for other pure metals of Cu, Al and Sn can also be seen. This leaves further questions to improve understanding in this area.

The metastable argon atoms can also excite other atoms to emit photons. They are created by excitation in the collisions between argon atoms and the secondary electrons (Eqn. 2.6). The cross-section of the secondary-electron impact excitation of argon atoms has a maximum of 1.6×10^{-16} cm^2 (at 20 eV), which is of the same order of that of the γ-electron impact ionisation of argon atoms. But the density of the metastable argon atoms in the glow is much lower compared with that of the secondary electrons (Bogaerts and Gijbels, 1998). Therefore, the metastable argon atoms should have a lesser effect on the variation in the hydrogen intensities than the secondary electrons. This has been confirmed by comparing the different argon pressures when measuring the different samples in the GDOES, because the density of the metastable argon atoms should be partly related to density of the argon atoms in the source chamber and hence the argon pressure. The results in Figure 6.12 indicate that the argon pressures change from 98.8 to 131 Pa and do not match the variation in the hydrogen intensities. This implies the density of the argon atoms or, by implication the metastable argon atoms, are not important to the variation in the hydrogen intensities.

To understand the matrix effects on the hydrogen intensity, it is also necessary to pay attention to the different types and densities of sputtered atoms apart from argon atoms in the glow region, since in principle the same processes that cause the ionisation and the excitation of argon atoms also apply to the ionisation and the excitation of the other atoms in the glow discharge. What is of interest in this case is the electron impact ionisation and excitation of the sputtered atoms. They should have the same or higher probabilities of being ionised as the argon atoms, at least for copper atoms as they are much more efficiently ionised than the argon atoms (Bogaerts and Gijbels, 1997). Differences in the energy level of the ionisation and excitation and densities of the atoms could alter the energy distribution in the glow region and consequently result in variation of the excitation of the hydrogen atoms in the source. From the point of view of only the densities of the atoms, there are no correlations between the sputtering rates (in atomic percent) and the corresponding hydrogen intensities in Figure 6.12.

Unfortunately, no data can be found in the literature about energy levels of electron impact ionisation and excitation of sputtered atoms in GDOES.

The results in Figure 6.12 do imply that there is a variation in the hydrogen intensities with the different sputtered samples, which clearly indicates that the different cathode matrices have an effect on the intensities of the hydrogen contamination in GDOES detection. In view of what has been discussed concerning the ionisation and excitation processes of argon and the analysed atoms, it is hard to give a conclusion about which process dominates in this effect. The γ-electrons ejected by argon ions impacting the cathode surfaces should play an important role in the measured data. The hydrogen intensities for the samples of the steel, and the pure metals of Mo, Ti, Co, and Ni in Figure 6.12, may support the proposed γ-electron effect. However, the experimental results for the pure metals of Cu, Al and Sn still cannot be explained. On the other hand, different sputtered atoms in the glow discharge, i.e. different densities and energy levels of the ionisation and excitation of the atoms, can alter the energy distribution in the glow region and result in variation of the excitation of the hydrogen atoms in the source.

6.3 Detection of Hydrogen in GDOES

Hydrogen contamination signals in GDOES measurements are unavoidable within the first few tens of seconds of sputtering time due to the effects of water vapour on the sample surface and in the annular space of the anode-cathode block. However, in the hydrogen detection status of GDOES, the hydrogen intensities at a fixed sputtering time (a few hundred seconds) are stable for samples with similar matrices in different measurements. Therefore, it is possible to compare the hydrogen content between bulk samples with similar matrices. Samples with big differences in their matrices could not be compared due to matrix effects on the hydrogen intensity. Since the hydrogen intensity only has a peak in the first few tens of seconds of sputtering time, and decays

as the sputtering time increases, then for plated samples with a thick layer, GDOES has the ability to detect the hydrogen that could diffuse into the interface between the plated coating and the substrate in the plated process. Two experiments have been performed to detect hydrogen by GDOES. One is the detection of hydrogen in steels that were loaded with hydrogen in an electrochemical process. Another is the hydrogen detection of carbon steels that have been plated with pure chromium and nickel layers.

6.3.1 Hydrogen detection in bulk samples using GDOES

6.3.1.1 Experimental

To test the ability to detect hydrogen in GDOES on bulk samples, the warm-up specimens (cut from a steel block with a uniform matrix) were employed to obtain and confirm the hydrogen detection status of the GDOES. Two of them were loaded with hydrogen in an electrochemical process for 2 hrs and 4 hrs of loading time, respectively. The solution and conditions employed to load the hydrogen were as follows:
Conditions: −1.2 V of voltage; −205 mA of current;

Solution: 0.1 mol H_2SO_4; 3.5 g/l $CS(NH_2)_2$— thiourea; 3.5 g/l NaCl.

The hydrogen-loaded specimens were immersed in liquid nitrogen to prevent the hydrogen from escaping, and were then given the same exposure time to the ambient environment to reach room temperature before being measured in GDOES. In this way, it was hoped that the real differences in the hydrogen contained between the samples with and without the hydrogen loading, and between the samples with different loading times, could be revealed in the hydrogen detection status. The GDOES was first properly warmed up using the warm-up specimens to reach the hydrogen detection status. The specimens with 2 hrs and 4 hrs of the hydrogen loading time were then measured. After the hydrogen-loaded specimens, two of the warm-up specimens were measured again to make sure that the GDOES was still in the hydrogen detection status. All specimens were measured in the GDOES for 300 seconds of sputtering time with similar time intervals between the specimens. The averages of hydrogen intensities at 300 seconds of sputtering time were collected. The hydrogen intensities at 300 seconds are not expected to show the influence of water vapour on hydrogen intensity.

6.3.1.2 Results and discussion

The recorded hydrogen intensities are shown in Figure 6.13. The average of the hydrogen intensities of the warm-up specimens from WUP 1 to WUP 7 is 86.3 (a.u.) with a standard deviation of 2.7. The small standard deviation confirmed that the GDOES was in the hydrogen detection status during the measurements of the hydrogen-loaded specimens. The hydrogen intensity of the specimen with 2 hrs of hydrogen loading time is 167.8 (a.u.), twice as high as that of the warm-up specimens. The hydrogen intensity of the specimen with 4 hrs of hydrogen loading time is 491.0 (units), nearly three times higher than that of the specimen with 2 hrs of hydrogen loading time and about six times as high as the specimens without the hydrogen loading.

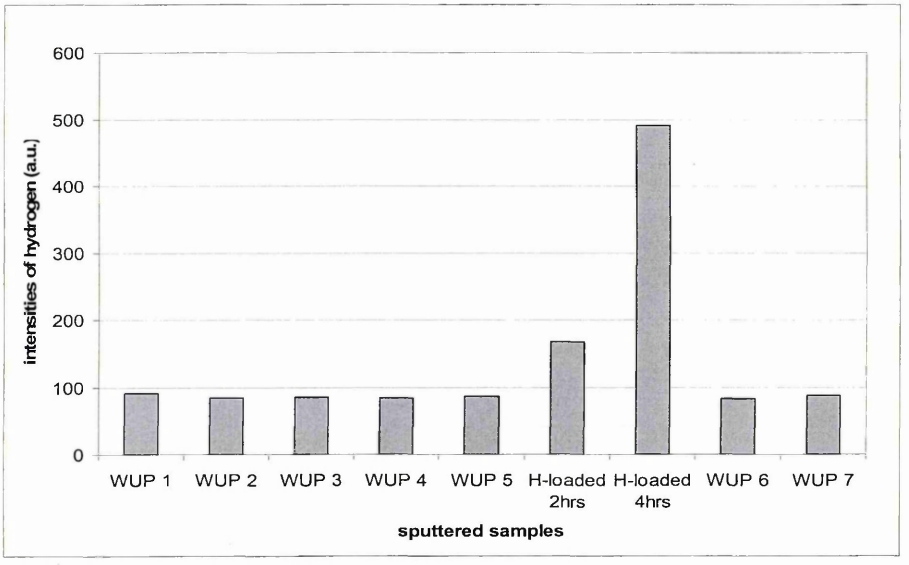

Figure 6.13. Comparison of the hydrogen intensities detected in the GDOES between the carbon steel specimens without hydrogen loading and with hydrogen loading in different loading times.
GDS: 700V/30mA/4mm anode. Gain of the PMT for hydrogen: 10.

Carbon steels with longer hydrogen loading time (16 hours) have been measured in the GDOES. The hydrogen intensities of the specimens were plotted in Figure 6.14, which shows some sharp peaks in the hydrogen profiles. These sharp intensities may indicate that there is a possible forming of hydrogen bubbles in the specimens with longer exposure to the hydrogen loading process. The interesting point is that the detection of

hydrogen in GDOES can reveal not only the hydrogen bubbles in the sample but also can give depth information on the bubbles. In Figure 6.14, the sharp intensities that appear at ~30 seconds and ~300 seconds of sputtering time could indicate that hydrogen bubbles existed at depths of ~1μm and ~11 μm, respectively, below the surface of the steel sample.

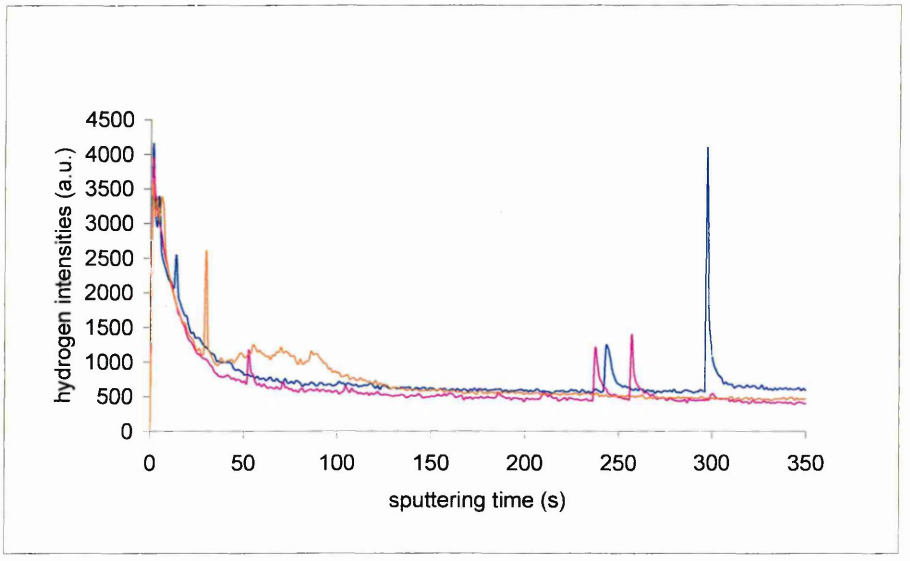

Figure 6.14. Hydrogen profiles detected in the GDOES using carbon steel specimens with 16 hours hydrogen loading in the electrochemical process. The sharp peaks of hydrogen intensity show that there is a possible forming of hydrogen bubbles in the specimens.

6.3.2 Hydrogen humps in plated samples detected by GDOES

Hydrogen humps were found in GDOES depth profiles of plated samples at interfaces between the coating and the substrate. An example is shown in Figure 6.15. The hump of hydrogen intensity at the interface between the Ni coating and the steel substrate is clearly seen. However, the hydrogen hump cannot be identified as straightforwardly as a hydrogen profile in a bulk sample can. The sputtering rate vs. sputtered depth of the sample in Figure 6.15 was plotted by the quantification procedure in the GDOES, and is shown in Figure 6.16. It indicates that the sputtering rate also increases at the interface. This increase in the sputtering rate was due to the matrix of the sample at the interface changing as the GDOES sputtered from the coating to the substrate.

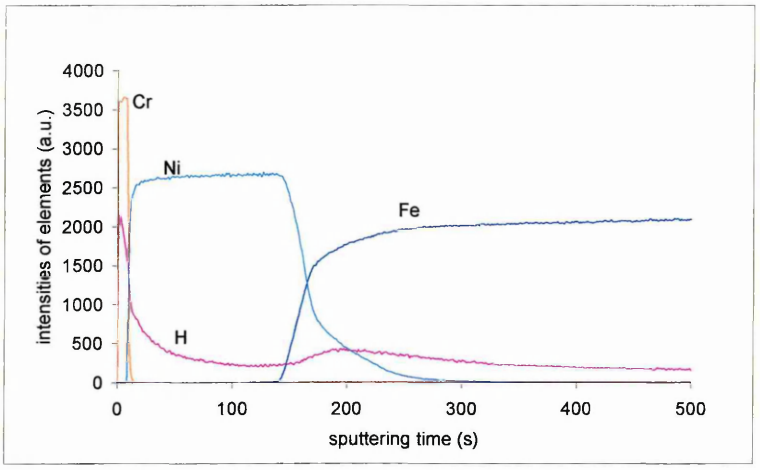

Figure 6.15. Hydrogen hump appears at the interface between Ni layer and carbon steel substrate.
GDS: 700V/30mA/4mm anode. Gain of PMT for hydrogen: 10

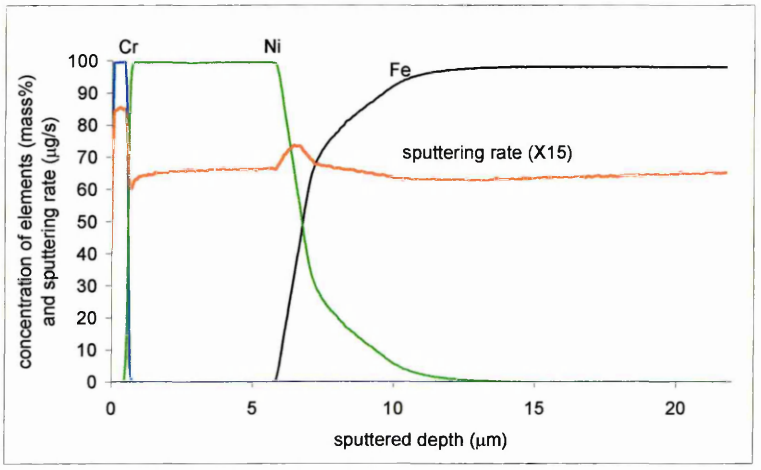

Figure 6.16. The sputtering rate calculated by the quantitative procedure in the GDOES shows there is a hump at the interface between the Ni layer and the substrate.

In GDOES measurements, increasing the sputtering rate could cause an increase in the intensities of the measured elements. For example, if an element has a uniform concentration throughout the coating in a sample of zinc-coated steel, the intensity of the element measured in GDOES in the coating will be higher than in the substrate because the sputtering rate of the zinc coating is higher than steel. However, after a quantification procedure in GDOES, the measured concentration of the element should not be affected by a variation in the elemental intensity, because the variation is corrected by the normalisation of sputtering rates (Section 2.5.4). Unfortunately, the

quantification procedure in the GDOES cannot carry out a quantitative analysis for hydrogen due to a lack of hydrogen calibration standards. Therefore, in order to understand the hydrogen humps, it is necessary to differentiate between two possible causes for the humps:

- In principle, the hydrogen hump could be caused by a sputtering rate rise at the interface, even though the concentration of hydrogen throughout both the substrate and the coating is constant;
- Alternatively, the hydrogen concentration really does increase at the interface.

6.3.2.1 Experimental and results

In order to identify the hydrogen hump, three groups of Cr/Ni plated steel, groups A, B and C were prepared. All of the samples were plated in an industrial plating line. The substrates were carbon steels. The surfaces of the substrates were first cleaned before being coated by nickel and chromium layers. The cleaning process included an anodic clean, cold water rinse and acid dipping to remove the oxide scales and grease on the surface. The surfaces were then polished in a rumbling barrel, which is a vibrating box containing grinding particles that polish the surface of the samples. The specimens in group C were cut from commercial products into a size of 15×30×4 mm. Group A consisted of a batch of testing samples with a size of 30×30×4 mm, which were specially prepared for this experiment in the same line as the specimens in group C. The substrates, the cleaning and the plating processes of the specimens in group A were the same as that of commercial products (in group C). After the specimens in group A were plated, they were immediately immersed into liquid nitrogen until ready for GDOES detection. The specimens in group B were another batch of testing samples prepared by the same process as groups A and B. These specimens were not immersed into liquid nitrogen but were exposed to the ambient environment before GDOES detection.

The GDOES was first calibrated using a set of certified reference materials (CRMs) with known elemental compositions and sputtering rates. The CRMs are listed in Table

6.3. Because there are no suitable CRMs for hydrogen in GDOES calibration, it is impossible to obtain the concentration of hydrogen in GDOES depth profiles. In this experiment, the GDOES was generally warmed up. The gain of PMT for hydrogen, the voltage and the current of the source, and the pumping time, were all kept constant. Temperatures of the specimens were at room temperature before being measured in the GDOES.

Table 6.3. *CRMs of GDOES calibration for Cr/Ni plated samples measurements in the GDOES. (Elemental concentrations in mass%, SR is the relative sputtering rate to a pure iron sample).*

	SR	Fe	C	Si	Mn	P	S	Cr	Mo	Ni	Al	Cu	Nb
K756	0.72	43.17			0.55	0.007		20.09	2.89	26.3	0.01		
K757	0.94	43.82		0.91	1.75	0.005	0.003	17.87		29.4			
K2009	1.29	71.86		1.05	0.98	0.005	0.004	18.07		7.95	0.005	0.01	
K2010	1.29	64.40	0.73		0.99	0.014	0.014	28.64	0.49		0.02	0.02	
K2249	1.14	66.26	0.52	1.01	1.15	0.049	0.016	18.64	0.98	8.86	0.015	0.31	1.06
JK-8F	0.80	66.94		0.424	1.552	0.0161	0.0183	16.91	2.775	11.04		0.0523	
NBS1763	1.04	95.02	0.203	0.63	1.58	0.012	0.023		0.5		0.043	0.043	0.10
NSC3-G	0.90	61.44	0.87	1.07		0.029	0.017	21.1					2.28
SS287-1	1.32	67.44		0.569	1.48	0.027	0.0014	18.61	0.247	10.35		0.203	
SS483/1	0.61	84.28	0.65	0.16	0.22	0.023	0.023		0.18				
SS484/1	0.54	61.30	0.76	0.18	0.21	0.025	0.015		1.08				
SS486/1	0.65	81.28	0.74	0.27	0.21	0.029	0.021		5.2				
SS487/1	0.82	74.27	1.02	0.18	0.26	0.022	0.029		9.41		0.006		
SS406/2	0.91	94.06	0.173	0.342	0.447	0.0102	0.043		0.98		0.013	0.289	
SS407/2	1.05	93.59	0.49	0.66	0.195	0.038	0.0105		0.83		0.04	0.397	
Pure Ni	0.98									99.9			

The specimens from group A were measured in the GDOES with different exposure times to ambient conditions from several minutes to a few tens of hours. The intensities of hydrogen from specimens A1 to A5 were plotted in one graph of hydrogen intensity vs. sputtering time, as shown in Figure 6.17. From the graph it can be seen that there is a difference in the peak values of the hydrogen intensities between the specimens. This is probably due to the effect of the background signal from hydrogen contamination. The heights of the hydrogen humps are similar, which clearly implies that the different

exposure times have little effect on the hydrogen humps. The humps were also shifted on the axis of sputtering time, which indicates that the thickness of the coatings were not uniform. The sputtering rates of the specimens in group A in the GDOES measurements were also plotted in one graph of sputtering rate vs. sputtered depth, which is shown in Figure 6.18.

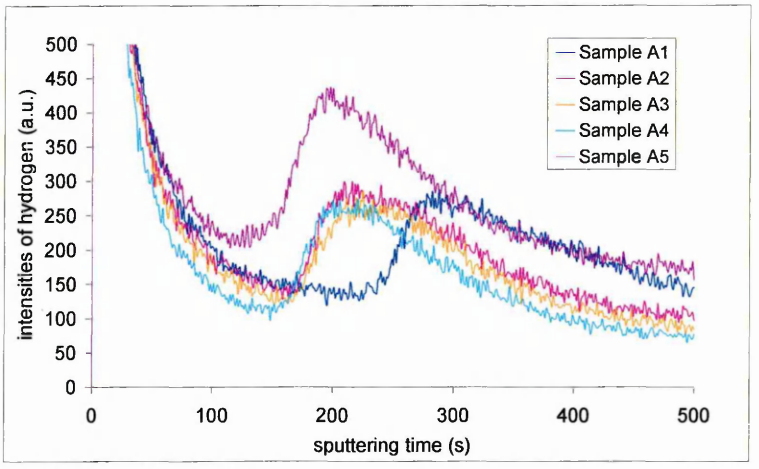

Figure 6.17. Hydrogen humps detected in GDOES at the interfaces between the Ni layer and the substrate of the carbon steel specimens in group A.
GDS: 700V/30mA/4mm anode, PMT gain of hydrogen: 10.

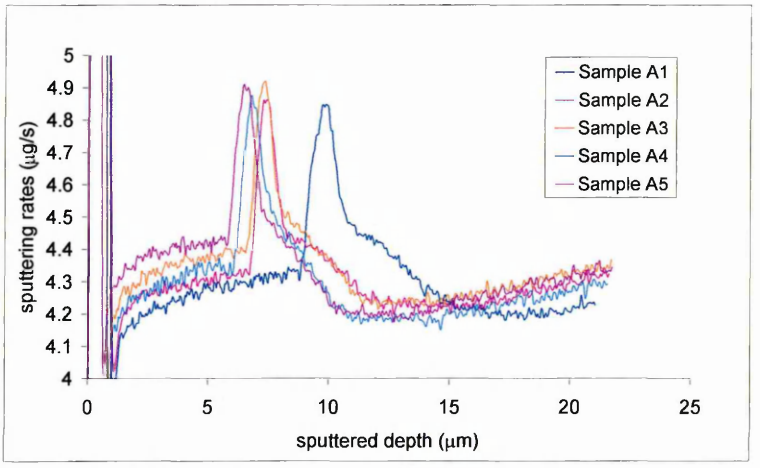

Figure 6.18. The sputtering rates in the GDOES measurements corresponding to those in Figure 6.17 show the peak values at the interfaces.

Five specimens from each of the groups B and C were measured in the GDOES to obtain comparisons for the different coating batches. One specimen from group A was

also measured, following the measurements of the specimens in groups B and C respectively, in order to compare their hydrogen humps in a similar status of GDOES. The detected hydrogen humps and corresponding sputtering rates are shown in Figures 6.19 to 6.22.

The raised values (heights) of the humps of the hydrogen intensities and the sputtering rates at the interfaces were calculated to represent the increases of the hydrogen intensities and the sputtering rate. The initial values (the values at the point just before they start to rise), the peak values and the raised values of the intensities and the sputtering rates at the interfaces for all of the specimens in the three groups were calculated and are listed in Table 6.4. In this table, the initial values of the intensities and the sputtering rates, H_0 and SR_0, and the peak values H_p and SR_p are all averages of five data points. ΔH and ΔSR are the raised values of the intensities and the sputtering rates, respectively, at the interfaces. The raised value equals the difference between the peak value and the initial value.

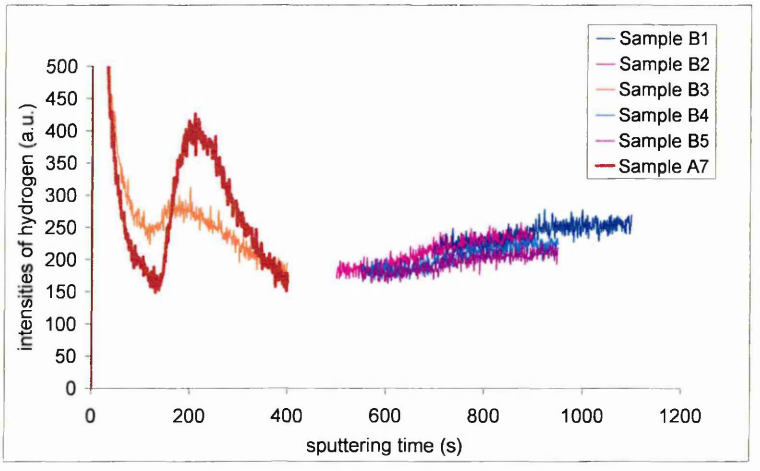

Figure 6.19. Hydrogen humps detected in the GDOES at the interfaces between the Ni layer and the carbon steel of plated samples in another batch.
GDS: 700V/30mA/4mm anode. Gain of the PMT for hydrogen: 10.

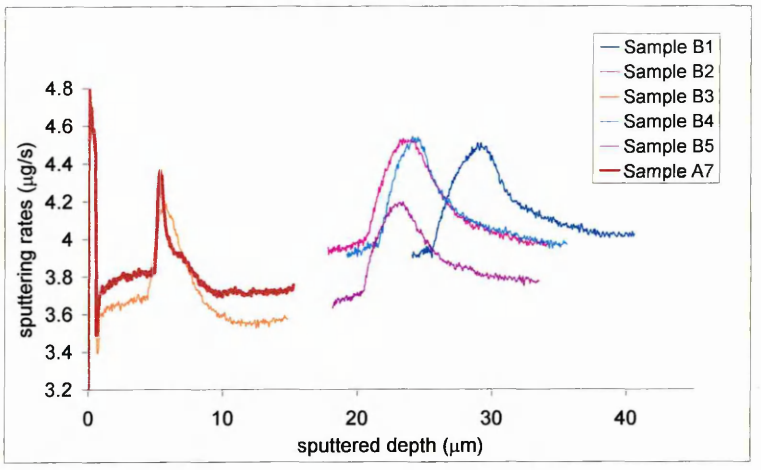

Figure 6.20. The peaks of the sputtering rates at the interfaces corresponding to the measurements in Figure 6.19. The sputtering rates and the depths were calculated by the quantitative procedure in the GDOES.

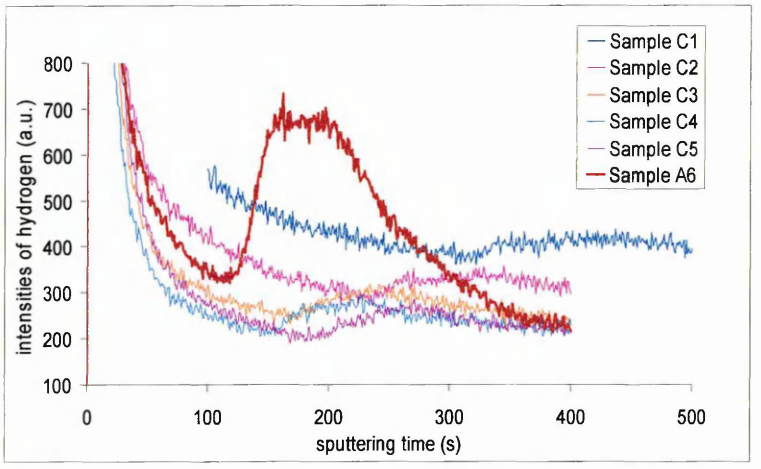

Figure 6.21. Comparison of the hydrogen humps of the specimens in groups C and A at the interfaces between the Ni layer and the carbon steel.
GDS: 700V/30mA/4mm anode. Gain of PMT for hydrogen: 10.

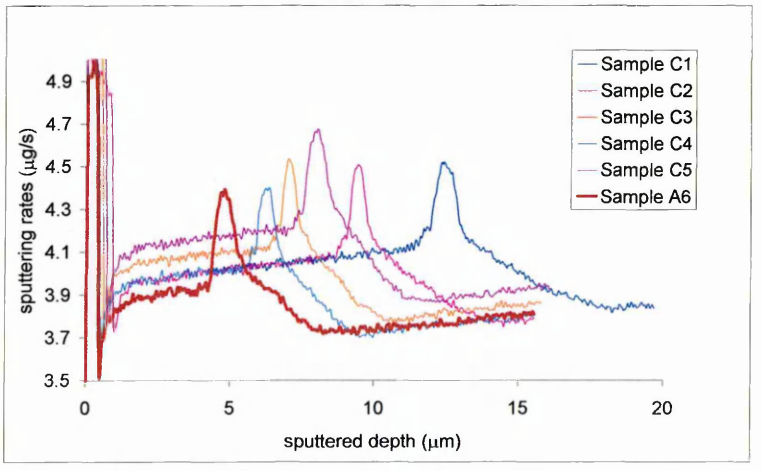

Figure 6.22. The peaks of the sputtering rates at the interfaces corresponding to the measurements in Figure 6.21, The sputtering rates and the depths were calculated by the quantitative procedure in the GDOES.

Table 6.4. The initial, peak and raised values of the hydrogen intensities (a.u.), H_0, H_p, and ΔH, and the sputtering rates (μg/s), SR_0, SR_p, and ΔSR, at the interfaces between the Ni layer and the substrate of the specimens in the three groups.

Samples	H_0	H_p	ΔH	SR_0	SR_p	ΔSR
A1	139	271	132	4.32	4.84	0.52
A2	140	278	138	4.33	4.86	0.53
A3	132	258	126	4.40	4.91	0.51
A4	115	258	143	4.34	4.85	0.51
A5	222	425	203	4.43	4.90	0.47
B1	225	258	33	3.94	4.49	0.55
B2	187	239	52	3.98	4.52	0.54
B3	242	280	38	3.69	4.17	0.48
B4	183	227	44	3.96	4.53	0.57
B5	177	216	39	3.72	4.19	0.47
A6	161	390	229	3.83	4.35	0.52
C1	383	419	36	4.21	4.51	0.30
C2	281	341	60	4.18	4.50	0.32
C3	248	312	64	4.23	4.52	0.29
C4	217	286	69	4.11	4.40	0.29
C5	203	268	65	4.28	4.67	0.39
A7	331	690	359	3.95	4.38	0.43

6.3.2.2 Discussion

On an initial examination of the results in Figures 6.17 and 6.18, the correlation of the humps in the hydrogen intensities and the sputtering rates seems to show that the hydrogen humps are caused by an increase of the sputtering rates at the interfaces. However, comparison of the results in Figures 6.19 to 6.22 shows evidence that the hydrogen humps were not a result of the raised sputtering rate. It can also be seen that the raised values of the hydrogen humps of the specimens in group A are significantly higher than the specimens in groups B and C, but the raised values of the sputtering rates look the same. The results in Table 6.4 indicate that the raised values of the hydrogen intensities of the specimens in group A are much higher than those of the specimens in groups B and C. The raised values of the sputtering rates do not correlate with the variation of the corresponding hydrogen humps, not only between the groups but also between specimens in any one of the groups. This confirms that there is more

hydrogen at the interfaces of the specimens in group A than the specimens in groups B and C. The detected hydrogen humps have been less affected by the rising of the sputtering rates at the interfaces.

It is also noted that the raised values of the sputtering rates of the specimens in group C are a little smaller than those of the others, but as yet there is no explanation for this. All the hydrogen humps detected at the interfaces shifted relative to the carbon steel substrates, an example of which is shown in Figure 6.15. Hydrogen may have entered the substrate during the plating process and in particular during the cleaning process before the plating. In the cleaning procedures, the acid dipping to remove the oxide scales and grease on the surface could be the main origin of the hydrogen. Further experiments are needed to confirm sources of the hydrogen at the interfaces.

The two experiments above have demonstrated that GDOES has the ability to detect the hydrogen in both the bulk samples and plated samples. However, there is still a long way to go to achieve a quantitative analysis of hydrogen using GDOES. For the bulk analysis, the results obtained show only the comparative difference of the hydrogen intensities between the samples with and without hydrogen loading. The experiments in this study do not tell us the sensitivity of the GDOES technique to the detection of hydrogen in steels.

6.4 The Hydrogen Effects on Emission Intensities and Concentrations of Elements in GDOES Measurements

While performing routine measurements with steel samples in the GDOES, it was noticed that some measured elements showed a lower intensity in the first few tens of seconds of sputtering time, particularly when the GDOES was not properly warmed up. An example can be seen in Figure 6.1: intensities of the elements of iron, manganese and copper in the first 30 seconds are significantly lower than their stable levels after

100 seconds. Although an unstable voltage, current or argon pressure in the source and/or contamination on the surface of the sample could cause variations of the elemental intensities, they should be limited to the first few seconds of sputtering. However, the high level of hydrogen intensity in the first 30 seconds suggests that there may be some effects of the hydrogen on the variations of the elemental intensities, and consequently on the measured concentrations.

The behaviour of the hydrogen contamination in the source has been discussed in Section 6.2.1. It is known that this hydrogen contamination is unavoidable in GDOES measurements, and could even remain at a very high level in the first few tens of seconds of sputtering time if the GDOES is not properly warmed up. This period of sputtering time is crucial for applications of GDOES in depth profiling of multi-layer samples. For a steel sample, 30 seconds of sputtering in GDOES would remove a layer of about 1 μm thick. Therefore, the hydrogen effects on elemental concentrations in GDOES measurements should receive special attention.

6.4.1 Experimental and results

An experimental procedure was set up to test the hydrogen effects on the intensities and concentrations of elements in a GDOES measurement with fixed voltage and current. The GDOES was in a normal condition, i.e. without the addition of molecular hydrogen to the argon gas in the source. Therefore, the hydrogen originated mainly from water vapour, which is unavoidable in GDOES measurements. Two steel standards, SS 410/2 and JK-8F, were chosen as samples to investigate the hydrogen effects. The certified elemental compositions of the standards are shown in Table 6.5. The GDOES was calibrated with a set of CRMs, which are listed in Table 6.6 with selected gains of PMTs and correlation coefficients of the calibration curves for each of the elements concerned. Surfaces of the standards were mechanically polished to a 1 μm-grade diamond paste finish before the GDOES measurements. The source conditions of the GDOES were 700 V of voltage and 20 mA of current and included a 4 mm anode. The gain of the PMT for hydrogen was 10.

Table 6.5. *The certificate and measured compositions of the standards samples SS410/2 and JK-8F (mass %).*

Samples		Fe(bal.)	C	Si	Mn	P	S	Cr	Mo	Ni	Al	As	Co	Cu	V
SS	Certificate	92.784	0.428	1.1	0.419	0.074	0.041	1.684	0.432	2.07	0.046	0.0053	0.0248	0.436	0.44
410/2	Measured	92.815	0.517	0.885	0.353	0.066	0.044	2.007	0.424	2.028	0.035	0.002	0.023	0.391	0.34
JK-8F	Certificate	66.936	0.0389	0.424	1.552	0.0161	0.0183	16.91	2.775	11.04		0.0108	0.125	0.0523	0.022
	Measured	67.596	0.21	0.374	1.279	0.016	0.024	17.54		10.49		0.007	0.132	0.076	0.066

Table 6.6. *Compositions and sputtering rates of the CRMs for the GDOES calibration, gains of the PMT and correlative coefficients of calibration curve for the elements.*

CRMs	SR	Fe (bal.)	C	Si	Mn	P	S	Cr	Mo	Ni	Al	As	Co	Cu	V
SS481/1	*0.59*	80.325	0.68	0.15	0.25	0.023	0.022	3.4	0.28				0.31		0.56
SS482/1	*0.56*	75.396	0.67	0.14	0.26	0.027	0.027	3.95	0.4				0.29		1.04
SS483/1	*0.61*	84.284	0.65	0.16	0.22	0.023	0.023	2.9	0.18						0.22
SS484/1	*0.54*	61.3	0.76	0.18	0.21	0.025	0.015	4.98	1.08						1.05
SS485/1	*0.48*	69.779	0.94	0.3	0.41	0.043	0.039	4.02	0.66						1.02
SS486/1	*0.65*	81.276	0.74	0.27	0.21	0.029	0.021	4.54					0.08		1.82
SS487/1	*0.82*	74.273	1.02	0.18	0.26	0.022	0.029	3.91			0.006				1.14
SS406/2	*0.91*	94.06	0.173	0.342	0.447	0.0102	0.043	2.001	0.98	1.62	0.013	0.012		0.289	0.01
SS407/2	*1.05*	93.586	0.49	0.66	0.195	0.038	0.0105	3.03	0.83	0.527	0.04		0.0068	0.397	0.19
SS408/2	*1.02*	93.564	0.289	0.237	0.557	0.056	0.03		0.098	4.13	0.154	0.0046		0.694	0.067
SS409/2	*0.92*	92.888	0.086	1.18	0.559	0.0141	0.0179	1.318	0.599	3.02	0.094			0.205	
SS410/2	*0.95*	92.784	0.428	1.1	0.419	0.074	0.041	1.684	0.432	2.07	0.046	0.0053	0.0248	0.436	0.44
Gain of PMT		3	5	8	10	9	8	8	10	10	10	10	10	10	10
Correl.coefficient		0.9350	0.9888	0.9814	0.9201	0.9710	0.9317	0.9758	0.8985	0.9561	0.9985	0.7347	0.9982	0.9950	0.9866

The standards of SS410/2 and JK-8F were measured in the GDOES for nine and six burns, respectively. Each of the measurements had 100 seconds of sputtering time. As expected, the hydrogen intensities decreased, not only in just one of the measurements as the sputtering time increased, but also from the first burn to the last. As an example, profiles of the hydrogen intensities of JK-8F in the six burns are shown in Figure 6.23.

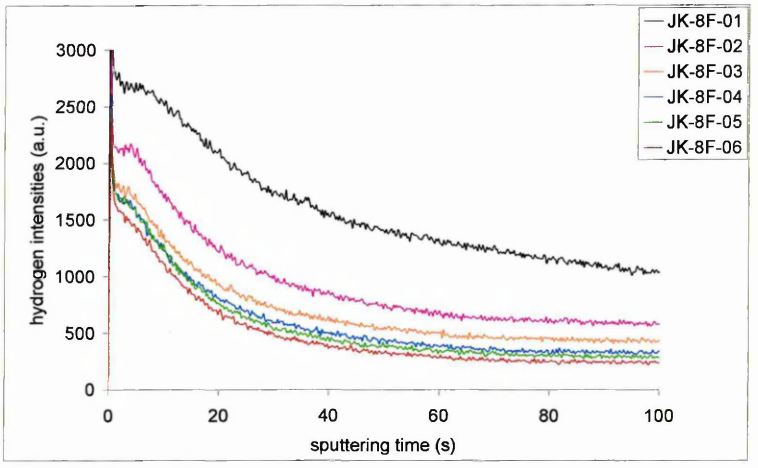

Figure 6.23. Profiles of the hydrogen intensities in the GDOES measurements using the standard JK-8F. The intensities vary not only in one measurement as the sputtering time increases, but also from the first to the last at a same sputtering time.
GDS: 700V/20mA/4mm anode, Gain of the PMT for hydrogen: 10.

At the same time, intensities for all of the elements in the standard could also be obtained. For each of the burns, 10 data sets between 10 and 100 seconds of sputtering time for each of the elements were selected. Every data set included the elemental intensities and the corresponding hydrogen intensity. In this way, for each of the elements in the standards, 90 data sets for SS410/2 and 60 for JK-8F were obtained, which are plotted in Figures 6.24 and 6.25, respectively, in elemental intensity vs. hydrogen intensity.

In Figures 6.24 and 6.25, the data sets, which were from the different burns and the different sputtering times between 10 to 100 seconds, show a good correlation between the elemental intensities and the corresponding hydrogen intensities. Variations of the hydrogen intensities were in a wide range, from 80 (a.u.) to 2700 (a.u.) for SS410/2, and

from 240 (a.u.) to 2500 (a.u.) for JK-8F. From the figures, it can also be clearly seen that the intensities of all the metal elements (Fe, Mn, Ni, Al, Cu, V, Mo and Co), apart from Cr, decrease as the hydrogen intensities increase. Intensities of all of the non-metal elements (C, S and P) and semiconductor elements (Si and As), however, increase as the hydrogen intensities increase. The results are generally in agreement with those reported by Hodoroaba *et al.* (2000a and 2000b).

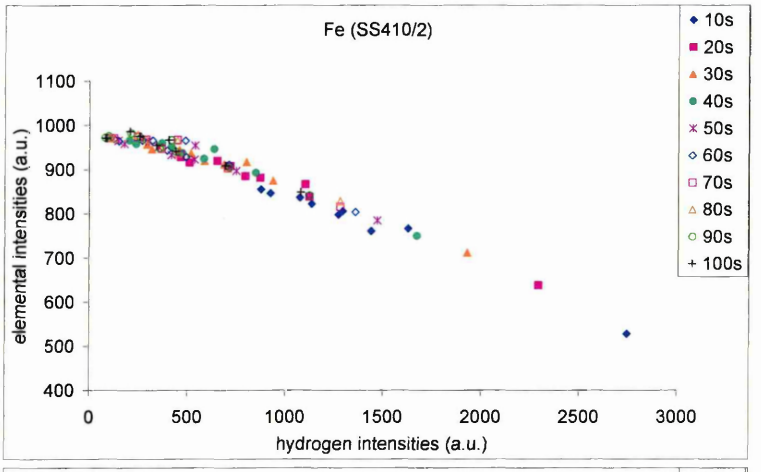

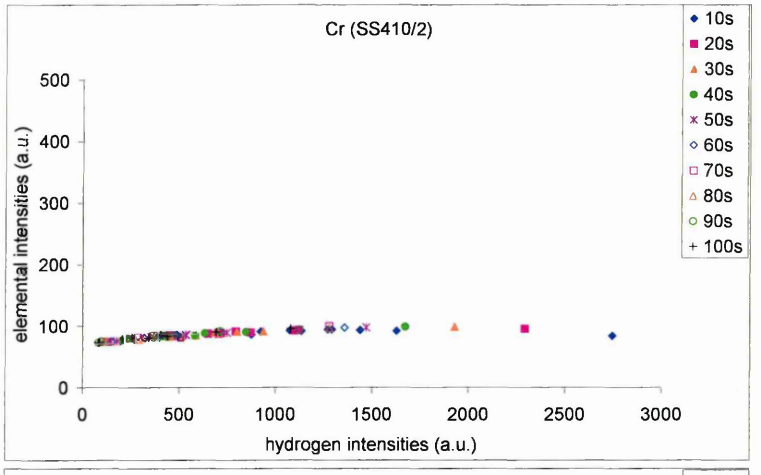

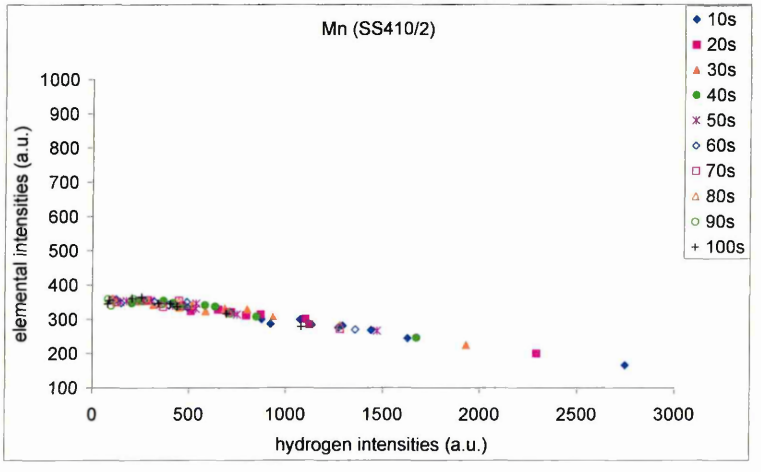

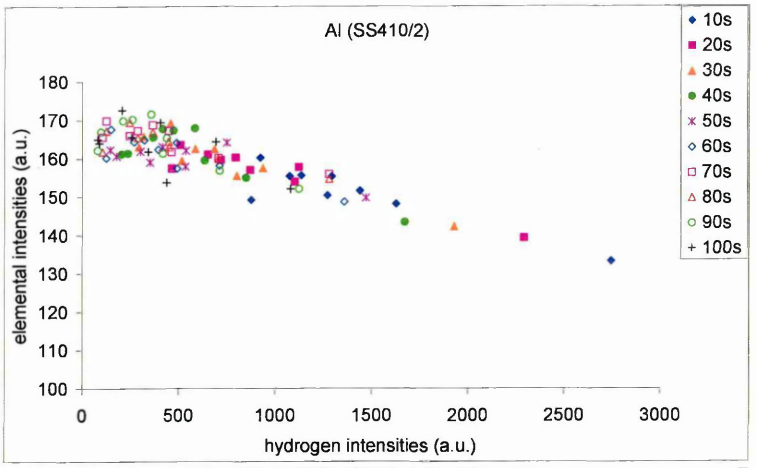
Al (SS410/2)
elemental intensities (a.u.)
hydrogen intensities (a.u.)
10s
20s
30s
40s
50s
60s
70s
80s
90s
100s

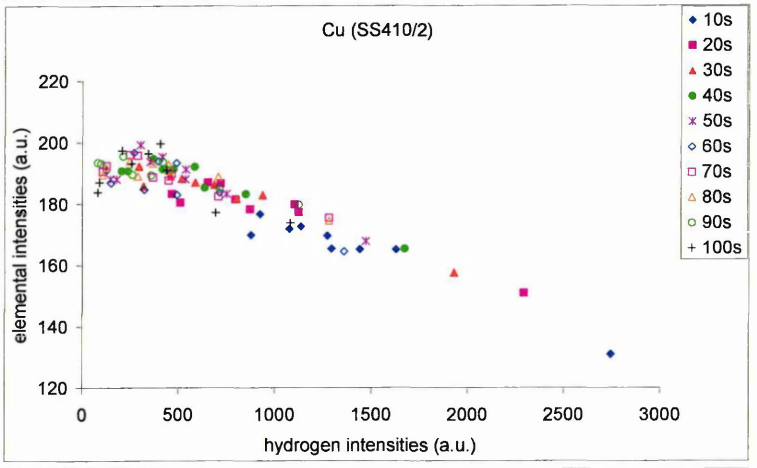
Cu (SS410/2)
elemental intensities (a.u.)
hydrogen intensities (a.u.)
10s
20s
30s
40s
50s
60s
70s
80s
90s
100s

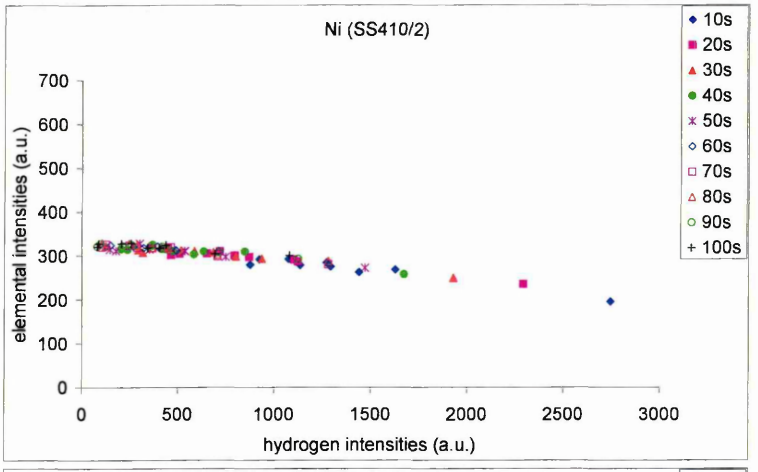
Ni (SS410/2)
elemental intensities (a.u.)
hydrogen intensities (a.u.)
10s
20s
30s
40s
50s
60s
70s
80s
90s
100s

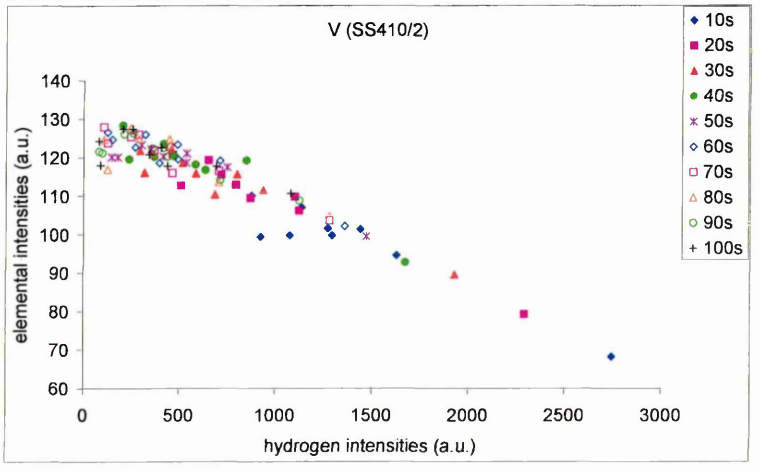
V (SS410/2)
elemental intensities (a.u.)
hydrogen intensities (a.u.)
10s
20s
30s
40s
50s
60s
70s
80s
90s
100s

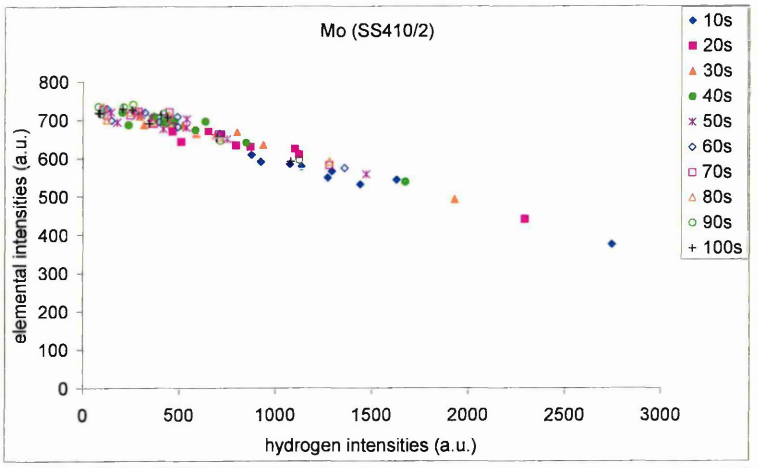
Mo (SS410/2)
elemental intensities (a.u.)
hydrogen intensities (a.u.)
10s
20s
30s
40s
50s
60s
70s
80s
90s
100s

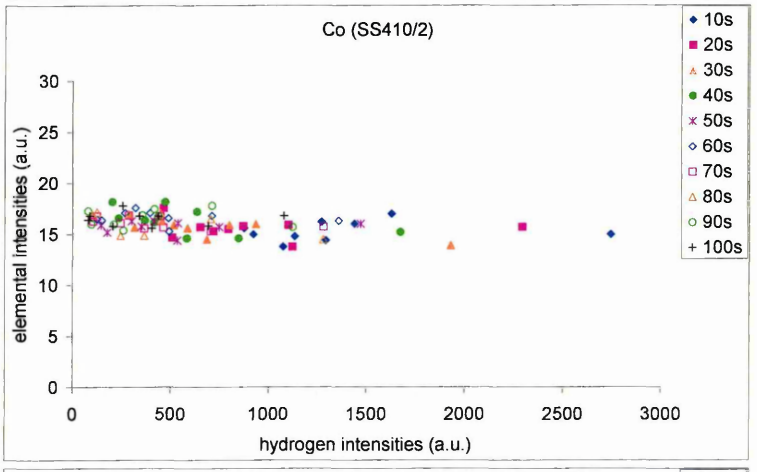
Co (SS410/2)
elemental intensities (a.u.)
hydrogen intensities (a.u.)
10s
20s
30s
40s
50s
60s
70s
80s
90s
100s

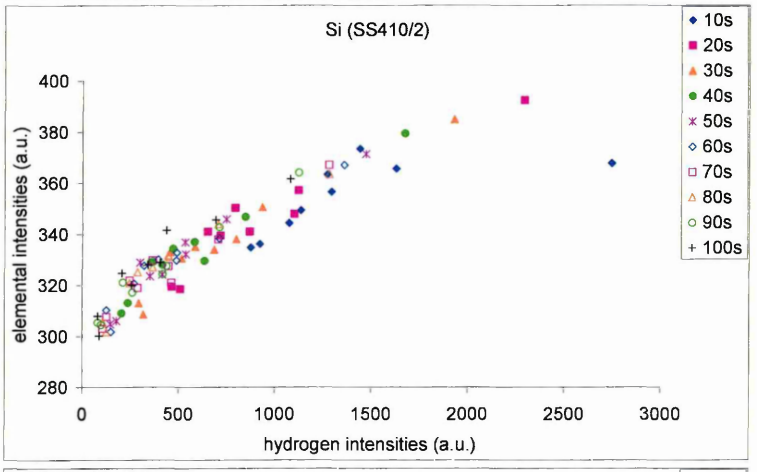
Si (SS410/2)
elemental intensities (a.u.)
hydrogen intensities (a.u.)
10s
20s
30s
40s
50s
60s
70s
80s
90s
100s

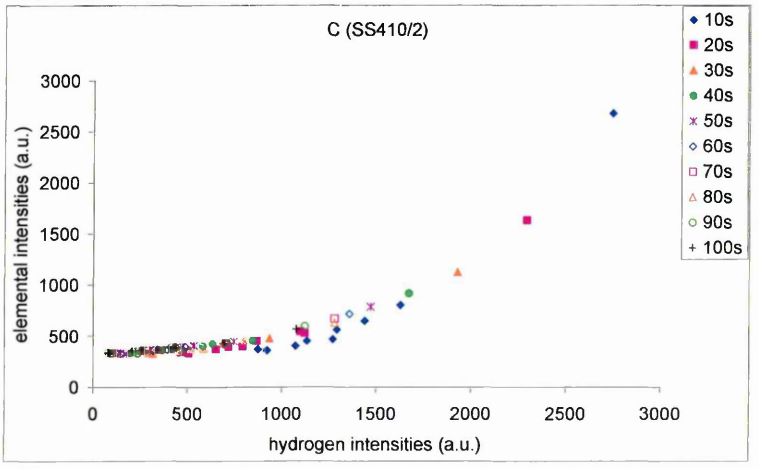
C (SS410/2)
elemental intensities (a.u.)
hydrogen intensities (a.u.)
10s
20s
30s
40s
50s
60s
70s
80s
90s
100s

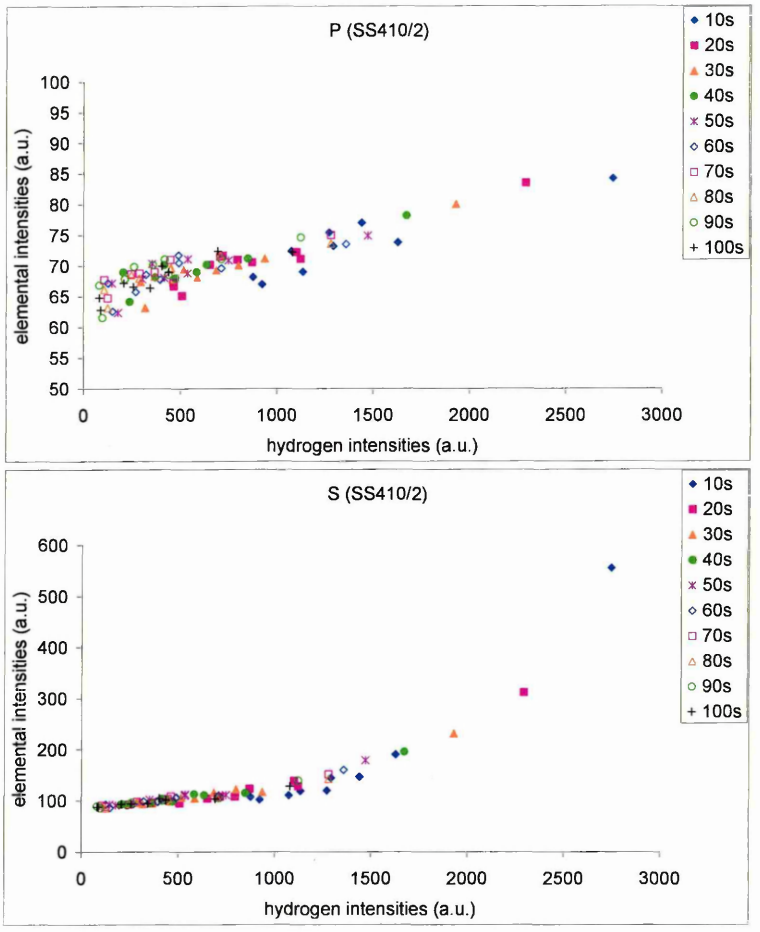

Figure 6.24. 90 data sets from the nine different burns and the different sputtering times between 10 to 100 seconds show a good correlation between the elemental intensities and the corresponding hydrogen intensities for Fe, Cr, Mn, Cu, Ni, V, Mo, Co, Si, C, P and S.
GDS: 700V/20mA/4mm anode, PMT gain of hydrogen: 10.
Sample: SS410/2.

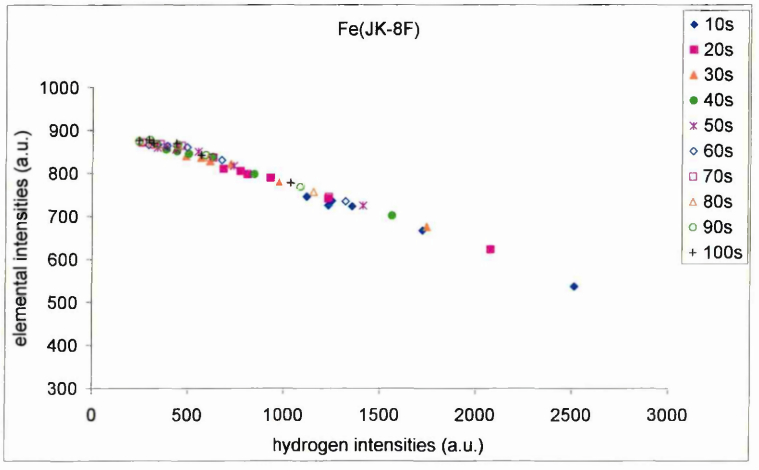

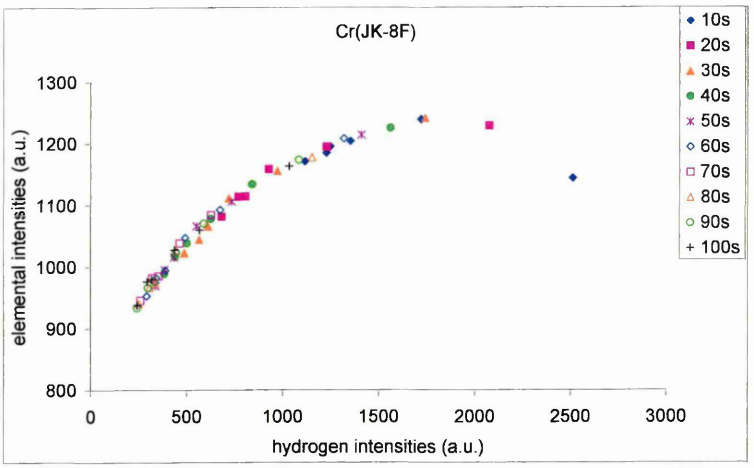
Cr(JK-8F)
elemental intensities (a.u.)
hydrogen intensities (a.u.)
10s
20s
30s
40s
50s
60s
70s
80s
90s
100s

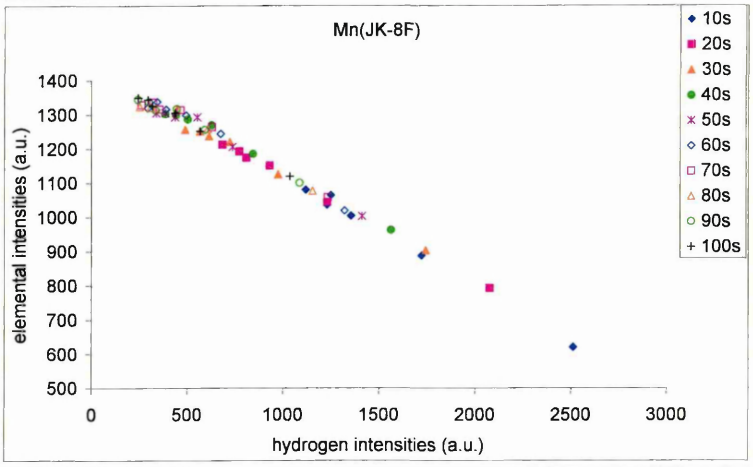
Mn(JK-8F)
elemental intensities (a.u.)
hydrogen intensities (a.u.)
10s
20s
30s
40s
50s
60s
70s
80s
90s
100s

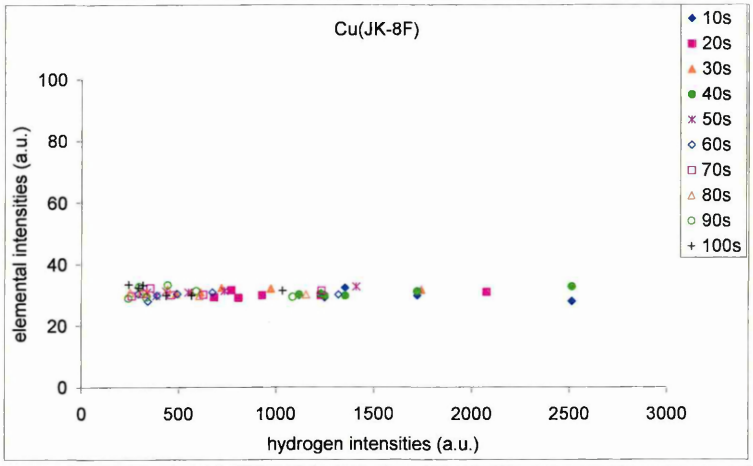
Cu(JK-8F)
elemental intensities (a.u.)
hydrogen intensities (a.u.)
10s
20s
30s
40s
50s
60s
70s
80s
90s
100s

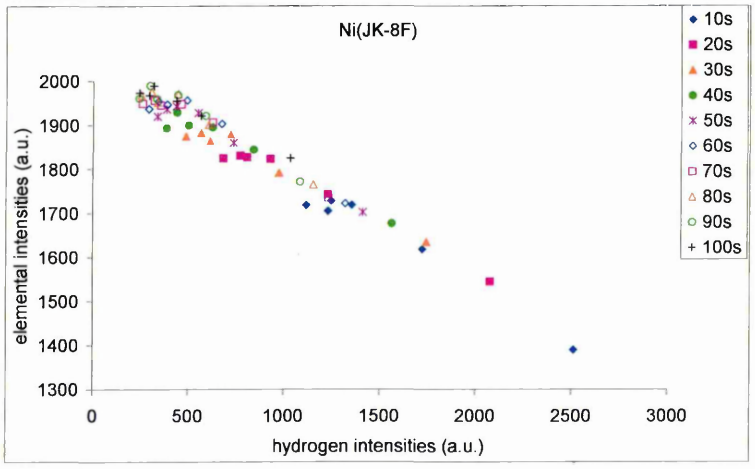
Ni(JK-8F)
elemental intensities (a.u.)
hydrogen intensities (a.u.)
10s
20s
30s
40s
50s
60s
70s
80s
90s
100s

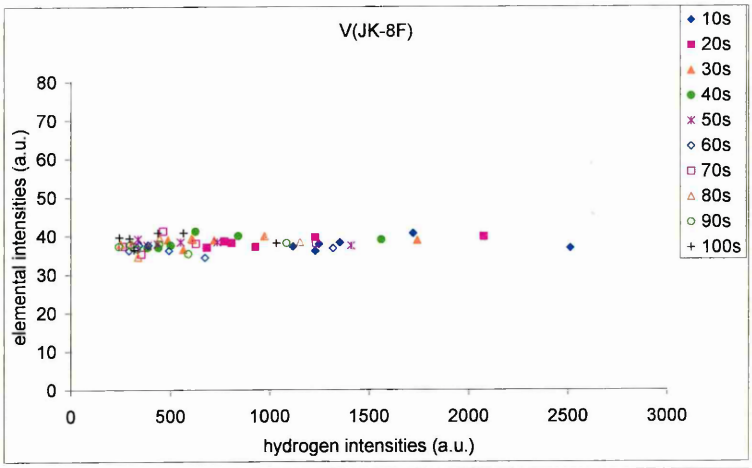
V(JK-8F)
elemental intensities (a.u.)
hydrogen intensities (a.u.)
10s
20s
30s
40s
50s
60s
70s
80s
90s
100s

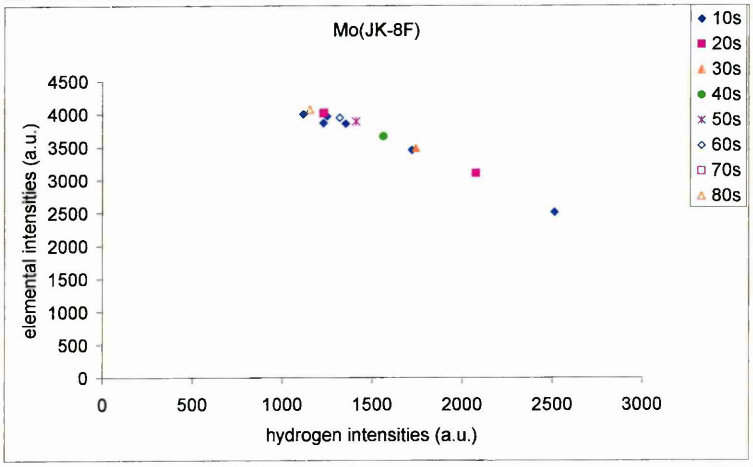
Mo(JK-8F)
elemental intensities (a.u.)
hydrogen intensities (a.u.)
10s
20s
30s
40s
50s
60s
70s
80s

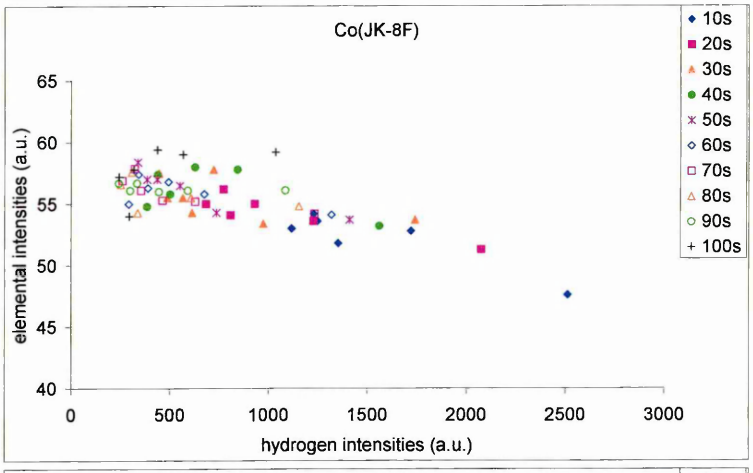
Co(JK-8F)
elemental intensities (a.u.)
hydrogen intensities (a.u.)
10s
20s
30s
40s
50s
60s
70s
80s
90s
100s

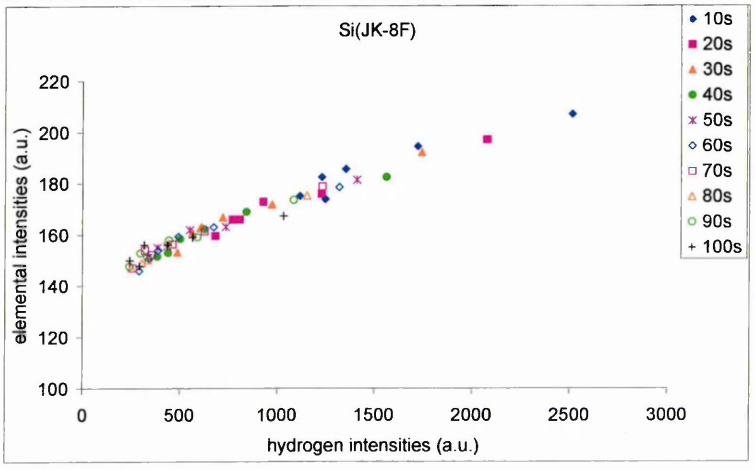
Si(JK-8F)
elemental intensities (a.u.)
hydrogen intensities (a.u.)
10s
20s
30s
40s
50s
60s
70s
80s
90s
100s

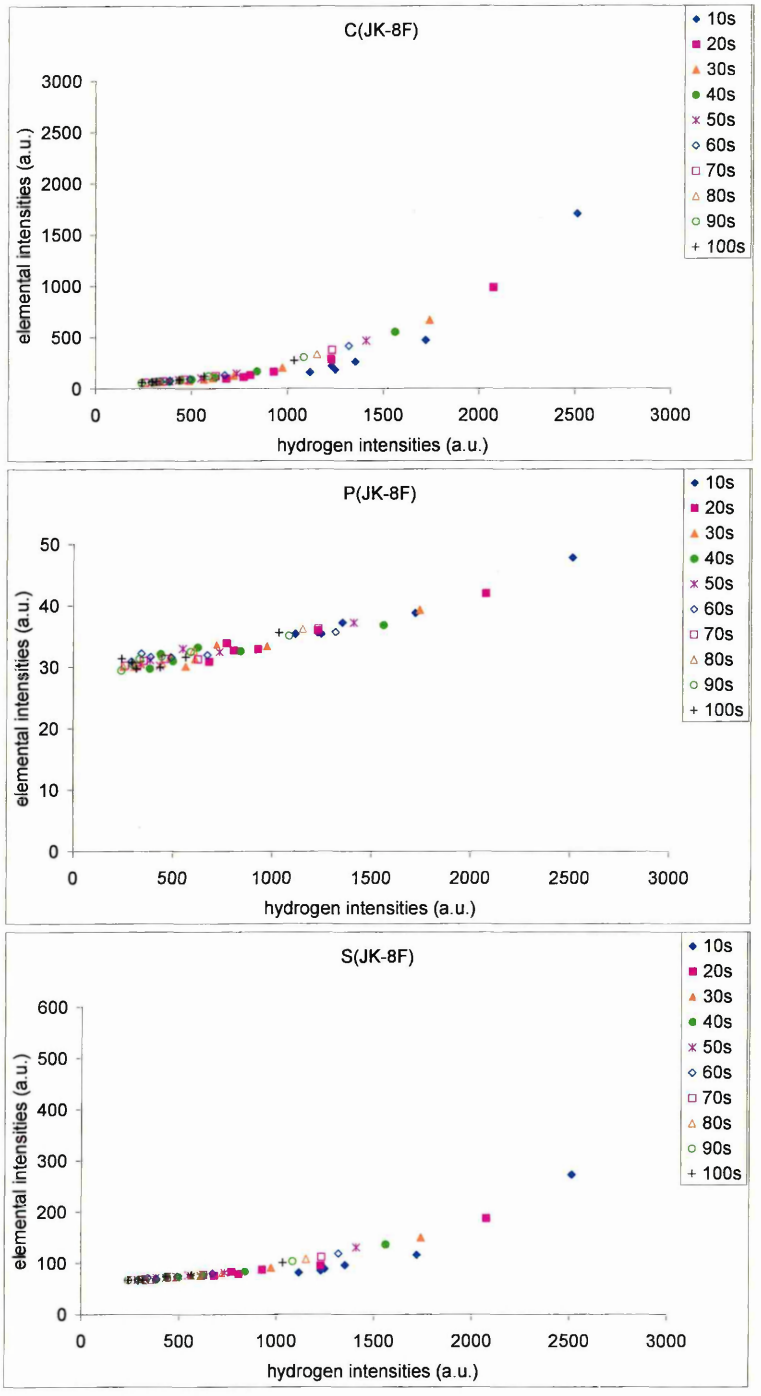

Figure 6.25. 60 data sets from the six different burns and the different sputtering times between 10 to 100 seconds show a good correlation between the elemental intensities and the corresponding hydrogen intensities for Fe, Cr, Mn, Cu, Ni, V, Mo, Co, Si, C, P and S.
GDS: 700V/20mA/4mm anode, PMT gain of hydrogen: 10.
Sample: JK-8F.

Oxygen and nitrogen may also exist in the source during the measurements. The oxygen and the nitrogen signals in the six burns of the sample JK-8F are plotted in

Figure 6.26. The oxygen and nitrogen intensities in the six burns, except for burn-01, nearly overlap and are very stable after 30 seconds of the sputtering time for oxygen and 60 seconds for nitrogen. The undulating intensities of the nitrogen signal between 20 seconds to 60 seconds are usually observed in measurements of the GDOES, which may be attributed to leaks in the vacuum system and need to be further understood. Therefore, it can be confirmed that the variations of the elemental intensities shown in Figures 6.24 and 6.25 are not caused by the existence of oxygen and nitrogen in the source.

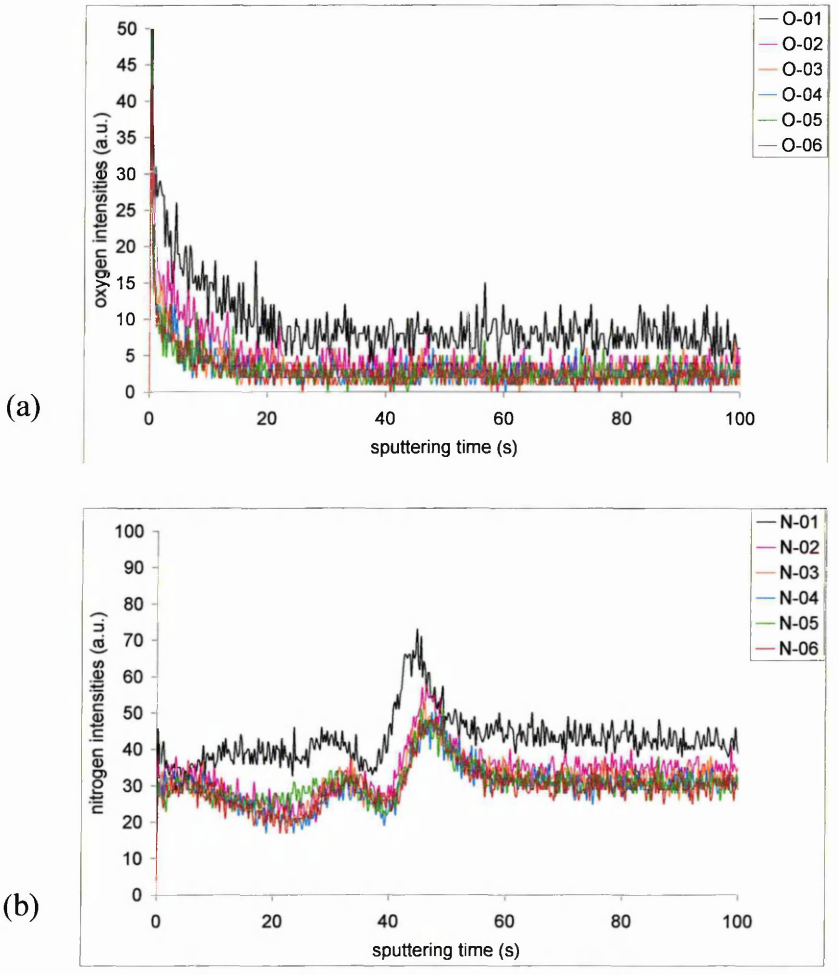

Figure 6.26. Oxygen and nitrogen signals in the GDOES measurements of the standard JK-8F in the six burns corresponding to that in Figure 6.25.
(a) Oxygen intensities.
(b) Nitrogen intensities.

6.4.2 Discussion

There remains the question of why the elemental emissions vary with the variation of hydrogen content in the source. In GDOES analysis, for a given emission line from an element *i*, the elemental emission can be expressed, if the term for background signals is eliminated (Payling, 1997a) by

$$I_i = K_i e_i q_i = K_i e_i c_i q \qquad (6.1)$$

where K_i is the instrumental detection efficiency for the element *i*. It represents a sensitivity factor of the emission detection and will vary with the gain of the PMT and wavelength for an element. For the elements with the same PMT gain in this investigation, it should be constant for each of the elements in the measurements respectively, but will vary between different elements. e_i represents the emission process of the element *i*, and q_i is the supply rate of the element *i* into the source,

$$q_i = c_i q \ , \qquad (6.2)$$

which depends on the elemental concentration c_i and the overall sputtering rate q of the measured sample. In this case, therefore, only the elemental emission process and the overall sputtering rate could have the potential to alter the intensities.

Let us first consider the overall sputtering rate. For a bulk standard, the sputtering rate can increase by a small amount during a measurement as the sputtering time increases (Section 2.4.2). If the sputtering rate is changed in a measurement, supplies of sputtered atoms into the source should change relative to the variation in the sputtering rate, but the proportion of sputtered atoms in the source should correspond to the elemental composition of the sample. This is an essential axiom employed in quantification procedures in GDOES analysis. Therefore, emissions of all the elements should change in the same direction with the change in the sputtering rate. This means that each of the elemental intensities will increase as the sputtering rate increases, and vice versa. However, the elemental intensities in Figures 6.24 and 6.25 indicate that as the hydrogen intensity increases, the intensities of the metal elements decrease, while the intensities of the non-metal and semiconductor elements increase. This contrasting

variation in the intensities implies that the variations of the elemental intensities cannot be caused by the changes in the sputtering rate.

The other term is the elemental emission process, which can be expressed as

$$e_i = S_i R_i \ , \tag{6.3}$$

where S_i is a correction for self-absorption and R_i is the emission yield of the element (defined as the number of photons emitted per sputtered atom). The self-absorption in GDOES will be close to 1 if the $c_i q$ term is small or nearly constant in GDOES measurements (Payling, 1997a). In this case, the S_i could be considered constant. The emission yield is an atomic and instrument-dependent quantity, and is independent of the sample matrix. From the concept of the emission yield, the emission intensity of an element in a spectral line is only related to the sputtered mass of that element, and should be constant as long as the excitation and the detection conditions in GDOES remain nearly constant. This is now widely accepted to be valid and is the basis of quantitative procedures in GDOES analysis (Bengtson, 1997). However, in this case, the emission intensities were no longer constant for each kind of sputtered atom ejected from the homogeneous standards. The source parameters and the detection conditions of the GDOES did not change during the measurements. A possible explanation could be that the excitation condition in the plasma had changed. The variation of hydrogen atoms in the source could alter the temperature of the energetic particles and modify the electron energy distributions function (EEDF) in the plasma (Bogaerts and Gijbels, 2000b), which could possibly affect the excitation processes of the atoms in the plasma due to the fact that atoms of different elements have different excited status and excitation cross-sections.

In order to compare the emission yield for the elements of interest, from Eqns. (6.1) to (6.3), the emission yield for element i at a given emission line can be expressed as

$$R_i = I_i /(K_i S_i c_i q) \ . \tag{6.4}$$

A relative change in the emission yield of an element i between two hydrogen levels is employed to identify the hydrogen effect on the emission yield, which is expressed as

$$\Delta R_i' = \frac{R_{iL} - R_{iH}}{R_{iL}} = \frac{I_{iL} - I_{iH}}{I_{iL}}, \qquad (6.5)$$

where $\Delta R_i'$ is the relative change of the emission yield of the element i between a high level (H) of the hydrogen intensity and a low level (L) related to that in the low hydrogen level; R_{iL} and R_{iH} are the emission yields of the element i corresponding to the low and the high levels of the hydrogen intensity. I_{iL} and I_{iH} are the intensities of element i at the low and the high levels of hydrogen, respectively. Therefore, the relative change in the emission yield of the element i can be represented by the relative change in the corresponding intensities, if the background term is ignored.

The elements Fe, Si, Cr, Mn, Ni, Mo, Cu and V in the standard SS410/2, and Fe, Si, Cr, Mn, Ni and Co in JK-8F, were picked out to compare the relative changes in the emission yields with variations in the hydrogen intensity, due to their elemental concentrations in the standards (>0.1% by mass). The low level and the high level of the hydrogen intensities of 250 and 1050 (a.u.) were selected. The difference in the hydrogen intensity of 800 (a.u.) represents a common range of variations of hydrogen intensity in practical measurements in the GDOES. The calculated relative changes in the emission yields for the elements at the two different levels of hydrogen intensities are listed in Table 6.7. The negative symbol represents the emission yield decreasing as the hydrogen intensity increases. All of the elemental intensities listed in the table were collected from linear regressive lines based on the intensity data in a range of the sputtering time from 50 to 100 seconds. 50 seconds of the sputtering time in the GDOES for the samples was responsible for a sputtered depth of 1–2 μm. Therefore, the results obtained are expected to be independent of the surface state of the samples.

Comparing the relative changes of the emission yields for the elements in both of the two standards, similar results were obtained, although there are remarkable differences in the elemental concentrations and sputtering rates between the two standards. From

the table it can be seen that the relative changes of some of the elements are significantly larger than others. For example, the relative changes of Cr are 19% and 20.4% in the SS410/2 and the JK-8F respectively, which are the largest among the elements, and Co is the smallest (−2.7%). The results in Table 6.7 reveal that hydrogen contamination does affect the elemental emission yields, and that the effects of the hydrogen on the emission yields of different elements are quite different. The order of the elements from more affected to less was Cr, Mn, Mo, Si, Fe, V, Ni, Cu and Co, based on the results in the table.

Table 6.7. *The relative changes of the emission yield between the two levels of the hydrogen intensity with the difference of 800 (a.u.) to the emission yield corresponding to the lower hydrogen intensity, based on the data in the range of the sputtering time from 50 sec. to 100 sec.*

	Elemental intensity (a.u.)				Difference of intensity $\Delta I_i = I_{i(1050)} - I_{i(250)}$		Relative change of emission yield $\Delta R_i' = (I_{iH} - I_{iL}) / I_{iL}$	
	SS410/2		JK-8F		SS410/2	JK-8F	SS410/2	JK-8F
	$I_{i(250)}$	$I_{i(1050)}$	$I_{i(250)}$	$I_{i(1050)}$	(a.u.)	(a.u.)	(%)	(%)
Fe	966.1	856.8	881.4	774.8	-109.3	-106.6	-11.3	-12.1
Si	318.2	358.5	149.8	172.3	402	22.6	12.6	15.1
Cr	79.7	94.8	964.6	1161.7	15.1	197.1	19.0	20.4
Mn	350.7	294.2	1352.1	1116.2	-56.6	-235.9	-16.1	-17.4
Ni	321.9	293.5	1981.5	1796.0	-28.4	-185.5	-8.8	-9.4
Mo	715.3	615.1			-100.2		-14.0	
Cu	192.1	178.3			-13.8		-7.2	
V	123.3	109.9			-13.44		-10.9	
Co			56.9	55.4		-1.52		-2.7

Measured elemental concentrations for each of the measurements were collected at 100 seconds of sputtering time. Averages of the measured elemental concentrations of the two standards are also listed in Table 6.6. They are very close to the identified concentrations of the standards. Elemental concentrations corresponding to the two levels of the hydrogen intensity (250 and 1050 a.u.) were also calculated based on the data in the range of 50 s to 100 s of sputtering time, using the same method as for the calculation of the intensities in Table 6.7. The relative changes in the elemental concentrations between the two hydrogen levels to those in the lower level are listed in Table 6.8. Comparing the relative changes in intensity (or emission yield) with the

concentration, some differences can be seen between Tables 6.7 and 6.8. Firstly, after the quantification procedure in the GDOES, there are some differences in the relative changes in concentration between the two samples for the elements of Fe, Si, Mn and Ni. Secondly, the order of hydrogen effect on the elements based on Table 6.8 has changed slightly from that in Table 6.7. For example, Si and Cr were more affected in terms of their concentration than in their emission intensity, while the effect for Fe, Ni and Mo was less. This could be due to the effect that in the quantification of the GDOES, the ratio of the intensity of an element to argon is employed instead of an absolute value of the element, which is believed to compensate for some variations in elemental intensity caused by variation of the discharge parameters during measurements. This seems, in this case, to reduce the hydrogen effects on some of the elements such as Fe, Ni and Mo, but to increase for Si and Cr. This is not yet fully understood at this stage and should be further investigated. In general, from the results in Tables 6.7 and 6.8, the hydrogen effects for the elements of Si, Cr and Mn should not be ignored in quantitative analysis in GDOES, if there is a big difference of hydrogen intensities of, say, a few hundred to a few thousand units at a gain of the PMT for hydrogen = 10, 700 V and 20 mA of the source parameters.

Table 6.8. *The relative changes of the measured concentration between the two levels of hydrogen intensity with the difference of 800 (a.u.) to the measured concentration corresponding to the lower level of the hydrogen intensity, based on the data in the range of the sputtering time from 50 sec. to 100 sec.*

	Concentrations (mass%)		Concentrations (mass%)		Relative change	
	SS410/2		JK-8F		SS410/2	JK-8F
H	250 (a.u.)	1050 (a.u.)	250 (a.u.)	1050 (a.u.)	(%)	(%)
Fe	93.021	91.901	68.911	64.511	-1.2	-6.4
Si	0.863	1.103	0.355	0.427	27.8	20.3
Cr	1.888	2.448	16.226	20.786	29.7	28.1
Mn	0.361	0.321	1.445	1.185	-11.1	-18.0
Ni	2.023	2.021	10.563	10.163	-0.1	-3.8
Mo	0.431	0.407			-5.6	
Cu	0.392	0.408			4.1	
V	0.341	0.325			-4.7	
Co			0.129	0.135		4.3

Figure 6.27 shows the sputtered depth of the standard SS410/2 at 100 seconds of sputtering time for the nine measurements, which were calculated by the quantification procedure in the GDOES. Hydrogen intensities for the nine measurements at 100 seconds varied in a range of 80 to 1080 (a.u.), corresponding to 0.433 μm maximum variation in depth. The relative variation in the calculated depth to the average depth of the nine measurements is 16.2%. According to the quantification procedure in the GDOES, the depth in these measurements was only affected by the emission intensities of the elements concerned. In the standards, the emission of iron dominated the variation in the calculated depth.

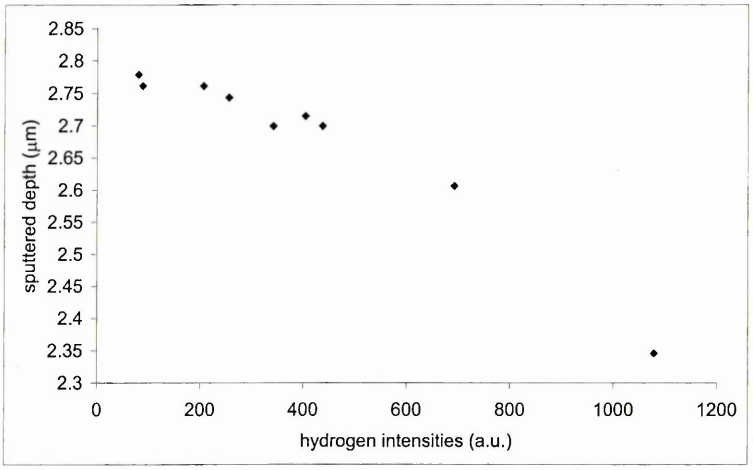

Figure 6.27. The sputtered depths of the standard SS410/2 in the nine burns corresponding to Figure 6.24 change as the hydrogen intensity increases. The depths were calculated by the quantitative procedure in the GDOES at 100 seconds of sputtering time.

In conclusion, the hydrogen effects on elemental emission, measured elemental concentration and calculated depth in GDOES have been demonstrated. The hydrogen could be from the hydrogen contamination existing in the source or the hydrogen contained in the sample. In the measurements, the hydrogen was expected to be present as contamination. Hydrogen contamination effects on elemental emissions in GDOES are significantly different for the different sputtered atoms in the plasma, which could be due to the hydrogen in the plasma modifying the energy distributions of the energetic

particles. For the elements in this experiment, the hydrogen had negative effects on most of the metal elements and positive effects on the non-metal and semiconductor elements. After the quantification procedure in the GDOES, the hydrogen effects on elemental concentrations can be partly compensated by employing the ratio of the intensity of the elements to argon for some elements, for example the elements of Fe, Ni and Mo. However, this did not work for the measured elements of Si and Cr in this experiment. In general, from the results in Tables 6.7 and 6.8, it is seen that the hydrogen effects on the elements of Si, Cr and Mn should not be ignored in quantitative analysis in GDOES. This is especially true in the analysis of a sample with a few microns' thick layer, due to the hydrogen being present as contamination (mainly from water vapour), which could be very high during the first few tens of seconds of sputtering time. As a consequence of the variation in the intensity of the matrix elements, the calculated depth by the quantification procedure of the GDOES also changed.

6.5 Conclusions

1. Hydrogen contamination in GDOES measurements was confirmed experimentally. Of the three origins of hydrogen contamination, i.e. water vapour, hydrocarbons and the hydrogen in argon gas, the water vapour deposited on surfaces of samples and the anode play a key role. The hydrogen from argon gas is the smallest among the three effects and is kept nearly stable in GDOES measurements. The hydrogen intensity due to the hydrogen contamination in the glow discharge source always decays and could be reduced to a low and stable level by proper warming-up of GDOES.
2. It is impossible to completely eliminate hydrogen contamination in a GDOES measurement. However, after a long warming-up time, say about a few thousand seconds, a hydrogen detection status can be reached. In this status, a stable hydrogen level during multiple measurements of a sample at the same

sputtering time can be obtained. Therefore, for samples with similar matrices, the hydrogen contained in the samples could be differentiated. Furthermore, the experiments showed the significance of the so-called cathode matrix effects on the intensity of the hydrogen contamination in GDOES measurements. The ejection of the γ-electron during the argon ions' impact onto the cathode surface is expected to play a crucial role in the matrix effects. On the other hand, different sputtered atoms in the glow discharge, i.e. different densities and energy levels of the ionisation and excitation of the atoms, can alter the energy distribution in the glow region and result in variation of the excitation of the hydrogen atoms in the source. In general, the matrix effects on the hydrogen intensity should be the overall result of the γ-electron, the density of sputtered atoms and the ionisation and excitation energy levels of the atoms.

3. Experimental results show that it is easy to observe differences in the hydrogen intensity between steel samples with and without hydrogen loading via the electrochemical process and with the different loading times. For the Ni/Cr plated samples, GDOES has the ability to detect hydrogen at the interface between the Ni coating and the substrate as a hydrogen hump. Comparison between sputtering rates of the samples at the interfaces and the corresponding hydrogen humps indicates that the humps are real rather than artefacts.
4. Hydrogen in the source can affect the elemental intensities in GDOES measurements and consequently the measured elemental concentrations and the sputtered depth. The hydrogen effects are believed to be due to the hydrogen in the plasma modifying the energy distributions of the energetic particles. The experimental results with two steel standards indicated that hydrogen has a negative effect on most of the metallic elements and a positive effect on the non-metal and the semiconductor elements. The results for the elements of Si, Cr and Mn have shown that the hydrogen effects on these elements should not be ignored in quantitative analysis in GDOES, especially when a thin layer of a few microns is being analysed.

Chapter 7 Conclusions and Future Work

7.1. Conclusions

1. Pure iron samples have been used to investigate the crystal orientation effects on the sputtering and the depth resolution in depth profiling analysis by the GDOES. The etched surface of the pure iron revealed different surface textures, which correspond to individual crystallites. The three main classes of surface textures are 'rough', 'concaved' and 'smooth'. Most of the areas with 'rough' texture are close to [111], the 'concaved' areas are close to [001], while the 'smooth' have higher index planes in a region between the [111] and [001] zone-axes. The fastest erosion occurred when the normal surface vector was parallel to [001]. The difference in the sputtered depth between [001] and [111] increases as the sputtering time increases from 500 s to 1000 s. At increasing sputtering times over 1000 seconds the difference in sputtered depth between [001] and [111] decreases. This is because, at this stage, the depth of the sputtered crater is above the mean crystal depth. A mixture of faster and slower crystallites has been encountered. The differences in sputtering depths of different areas, then, do not continue to increase but rather begin to decrease. The results imply that samples with small grain size will have the best possible depth resolution in GDOES.

2. When a carbon-coated silicon wafer was etched by GDOES sputtering, pits were induced on the etched silicon surface. Experimental results of the samples with Ag, Al, Si and Ge films have confirmed that a weak, low density pit-like morphology on silicon surfaces can develop after a long etching time. However, the high density, large pits were only produced on the silicon wafers with the carbon films. A large difference in sputtering rates between the film and the substrate has been shown to

play a crucial role in pit formation. For the etched surfaces of carbon-coated silicon wafers, the density of the pits decreases as the thickness of the carbon film increases. There are two possible explanations for this decrease. The first is the stochastic roughening of ion bombardment of the carbon film. A thicker carbon film needs a longer etching time to penetrate the film and to bombard the silicon wafer, which will result in a rougher surface and a lower pit-density than a thinner carbon film. The second is that some small pits have been engulfed by the development of bigger pits during the pits developing as the sputtering time increased. The sphere-like surface of the pit was confirmed by calculations of the radius of the pit surface. The radius of 42 pits from three samples with different thicknesses of carbon film were calculated based on results from AFM measurements. Developing speeds of the pit in the direction of its diameter is faster than that in its depth, which results in the pit enlarging in diameter and becoming shallower in depth as the etching time increases. The results of the AFM measurements also revealed that the thickness of the carbon film has no effect on the developing speeds of the pit in a silicon surface.

3. The EBSD patterns collected from the etched surfaces of pure iron and copper samples after GDOES sputtering have shown that the Grimm source is an excellent etching tool for removing a surface-damage layer in metal samples prior to study using EBSD. The technique could represent a very cheap and fast specimen-preparation route. GDOES has also proved a powerful tool for the study of internal oxidation, combining excellent depth resolution with good elemental sensitivity and rapid specimen-analysis. A secondary benefit of the GDOES sputtering technique is the ability to sputter to a known depth, and at the same time to measure the total concentration of various elements as a function of depth, and hence reveal the oxide morphology in a plan view. The SEM images revealed internal oxides with different morphologies on the GDOES etched surfaces of carburised carbon steels. The EDS/SEM elemental mapping and the GDOES depth profiles indicated that the

oxides with different morphologies in different layers involved the elements Cr, Mn and Si.

4. Contamination of hydrogen in GDOES measurements were confirmed experimentally. In the three sources of the hydrogen contamination, i.e. water vapour, the hydrocarbons and the hydrogen in argon gas, the water vapour deposited on the surface of the cathode sample and the anode played a key role. The hydrogen from argon gas is the smallest among the three sources and is kept nearly stable in GDOES measurements. The measured hydrogen intensity due to the contamination of hydrogen in the glow discharge source always decays and could be reduced to a low level by a proper warm-up of GDOES.

5. It was not possible to reach a steady state in the intensity of hydrogen contamination in a GDOES measurement. However, hydrogen contained in the samples with similar matrices could be differentiated in the hydrogen detection status of GDOES. Furthermore, the experiments showed significantly the so-called 'cathode matrix effect' on the intensity of hydrogen contamination in GDOES measurements. The γ-electron ejection during the argon ions' impact on the cathode surface and different sputtered atoms in the source are expected to play crucial roles in the matrix effects.

6. For hydrogen detection, GDOES has the ability to detect differences in hydrogen levels between steels without hydrogen loading and steels loaded electrochemically with different levels of hydrogen. For the plated samples, an increase in the hydrogen signal at the interfaces between Ni coating and steel substrate was detected in GDOES. Comparison between sputtering rates at the interfaces and the corresponding increase in hydrogen indicates that the increase was real rather than due to artefacts.

7. Hydrogen in the source can affect the elemental intensities in GDOES measurements, and consequently the concentrations and sputtered depth. The effects are believed to be due to the hydrogen in the plasma modifying energy distributions of the energetic particles. The experimental results with two steel standards indicated that the hydrogen has a negative effect on most of the metal elements and a positive effect on the non-metal and the semiconductor elements. The results for the elements Si, Cr and Mn show that the hydrogen effects on these elements should not be ignored in quantitative analysis in GDOES, especially in an analysis of a layer a few microns' thick.

7.2. Future Work

1. It was observed (in Chapter 3) that the crystallites close to [111] have lower sputtering rates than those close to [001] in GDOES sputtering of pure iron samples. This is in agreement with the results in the literature for ion bombardment of copper by 500 eV ion bombardment, but cannot be explained by the channelling theory, which is applied for high-energy ion sputtering. However, in low ion-energy sputtering, the surface binding energy also plays an important role. Therefore, experiments to determine the relationship between crystal orientation erosion rates and surface binding energies need to be carried out in order to develop understanding of the mechanisms of crystal orientation effects on sputtering rates at low energies.

2. The pitting phenomenon has been discussed in Chapter 4. The pits formed on silicon wafers after etching the carbon-coated film away have a potential application as random micro-lens arrays. A parallel light beam irradiating the pitted surface results in a set of luminous spots being focused by the pits at a certain distance above the surface. These form a unique luminous pattern. Due to the stochastic nature of the creation of the micro-lens, the luminous pattern created is unique and

could be used in marker technology applications. The potential application of this pitting phenomenon has been patented. However, it is still far from market application and further investigations on control of the formation of the pits need to be done.

3. Chapter 5 has demonstrated that GDOES etching is a powerful etching tool for removing a damaged layer and exposing a fresh surface that is ready for the EBSD pattern detection of crystallites. With the GDOES etch, a plan view of internal oxides of a carburised steel can also be revealed with known depth. If an SEM is combined with in-situ surface etching, it is possible to get a 3-D image of the internal oxide. For example, it should be noted that a modern environmental scanning electron microscope (ESEM) works at about the same pressure as a GDOES etch. Therefore, it would be quite technologically feasible to combine the imaging capability of ESEM with a Grimm source etch. It would then be possible to serially remove layers of specimen and capture images at each depth. The data acquired could be used to obtain a full three-dimensional image of the specimen. The plan view of internal oxides in large size also provides an opportunity to determine the crystalline structure by the EBSD pattern detection.

4. GDOES is sensitive to hydrogen, but its usefulness is complicated due to the contamination of hydrogen in the glow discharge source. However, with a long warm-up of the instrument, the intensity of the hydrogen contamination can reach a hydrogen detection status. This status can be employed to compare the hydrogen content in bulk samples. The experiments in this study have shown it is possible to indicate differences in hydrogen content between steels without hydrogen loading and steels loaded electrochemically with different levels of hydrogen. However, the sensitivity to hydrogen detection in GDOES has not yet been obtained. Quantitative hydrogen loading and detection in GDOES need to be carried out in order to test the sensitivity of GDOES detection of hydrogen in the future. One way of doing this would be to obtain a range of different steels, each with a different hydrogen

content, and to analyse the samples via both GDOES and a conventional wet chemical method. In this way, the GDOES sensitivity could be quantitatively assessed.

References

Alexandre, B., Berneron, R., Charbonnier, J.C., Namdar-Irani, R. And Nevot, L. (1981). *Mémoires Etudes Sci. Rev. Metall.* Sept., 483.

An, X., Cawley, J., Rainforth, W.M., and Chen, L. (2003). *Spectrochimica Acta* **B58**, 689-698.

Angeli, J., Haselgrübler, K., Achammer, E. M. and Burger, H. (1993). *Fresenius Journal Analytical Chemistry* **346**, 138-143.

Angeli, J. (1997). In *Glow Discharge Optical Emission Spectrometry*, R. Payling, D. Jones and A. Bengtson (eds), John Wiley & Sons, 319-328.

Batista, J.C.A., Godoy, C., Buono, V.T.L., and Matthews, A. (2002). *Materials Science and Engineering* **A336**, 39-51.

Bellini, S., Cilia, M., and Lo Piccolo, E. (2001). *Surface and Interface Analysis* **31**, 1100-1103.

Bengtson, A. (1985). *Spectrochimica Acta* **B40**, 631-639.

Bengtson, A., and Lundholm, M. (1988). *Journal of Analytical Atomic Spectrometry* **3**, 879-882.

Bengtson, A., Eklund, A., Lundholm, M., and Saric, A. (1990). *Journal of Analytical Atomic Spectrometry* **5**, 563-567.

Bengtson, A. and Eklund, A. (1992). *Comm. Eur. Communities Report EUR 14113 Prog. Anal. Chem. Iron Steel Ind.* 43-48.

Bengtson, A. (1994). *Spectrochimica Acta* **B49**, 441-429.

Bengtson, A. (1996). *Journal of Analytical Atomic Spectrometry* **11**, 829-833.

Bengtson, A., (1997a). In *Glow Discharge Optical Emission Spectrometry*, R. Payling, D. Jones and A. Bengtson (eds), John Wiley & Sons, 455-459.

Bengtson, A., (1997b). In *Glow Discharge Optical Emission Spectrometry*, R. Payling, D. Jones and A. Bengtson (eds), John Wiley & Sons, 472-482.

Bengtson, A., (1997c). In *Glow Discharge Optical Emission Spectrometry*, R. Payling, D. Jones and A. Bengtson (eds), John Wiley & Sons, 769-770.

Bengtson, A., and Hänström, S. (1998). *Journal of Analytical Atomic Spectrometry* **13**, 437-441.

Bengtson, A., Hänström, S., Piccolo, E.L., Zacchetti, N., Meilland, R., and Hocquaux, H. (1999). *Surface and Interface Analysis* **27**, 743-752.

Bengtson, A. and Hänström, S. (1999). In *Proceedings of Fifth International Conference on progress in Analytical Chemistry in the Steel and Metals Industries*, ed. R. Tomellini, European Communities, Luxembourg, 1999, 47-54.

Birks, N. and Meier, G.H. (1983). *Introduction High Temperature Oxidation of metals*, Edward Arnold Ltd.

Bishop, H. (1986). *Surface and Interface Analysis* **9**,105.

Blawert, C., Mordike, B.L., Rensch, U., Wünsch, R., Wiedemann, R., and Oettel, H. (2000). *Surface and Coatings Technology* **131**, 334-339.

Bloyce, A., Qi, P.-Y., Dong, H., and Bell, T. (1998). *Surface and Coatings Technology* **107**,125-132.

Bogaerts, A., and Gijbels, R. (1997). In *Glow Discharge Optical Emission Spectrometry*, R. Payling, D. Jones and A. Bengtson (eds), John Wiley & Sons, 176-191.

Bogaerts, A., Wagner, E., Smith, B.W., Winefordner, J.D., Pollmann, D., Harrison, W.W. and Gijbels, R. (1997a). *Spectrochimica Acta* **B52**, 205-218.

Bogaerts, A., Guenard, R.D.,Smith, B.W., Winefordner, J.D., Harrison, W.W. and Gijbels, R. (1997b). *Spectrochimica Acta* **B52**, 219-229.

Bogaerts, A., Gijbels, R. (1998). *Spectrochimica Acta* **B35**, 1-42.

Bogaerts, A., Donko, Z., Kutasi, K., Bano, G., Pinhao, N. and Pinheiro, M. (2000). *Spectrochimica Acta* **B55**, 1465-1479.

Bogaerts, A., Wilken, L., Hoffmann, V., Gijbels, R. and Wetzig, K. (2001). *Spectrochimica Acta* **B56**, 551-564.

Bogaerts, A. and Gijbels, R. (2000b). *Journal of Analytical Atomic Spectrometry*, **15**, 441-449.

Böhm, H. (1997). In *Glow Discharge Optical Emission Spectrometry*, R. Payling, D. Jones and A. Bengtson (eds), John Wiley & Sons, 676-687.

Bouchacourt, M. and Schwoehrer, F. (1997). In *Glow Discharge Optical Emission Spectrometry*, R. Payling, D. Jones and A. Bengtson (eds), John Wiley & Sons, 51-66.

Boumans, P.W.J.M. (1972). *Analytical Chemistry* **44**, 1219-1228.

Carter, G., Navinšek, B. and Whitton, J.L. (1983). In *Sputtering by Particle Bombardment II*, Edited by R. Behrisch, Springer-Verlag. 231.

Carter, G. (1995). *Vacuum* **47**, 409-420.

Carter, T.J. and Cornish, L.A. (2001). *Engineering Failure Analysis* **8**, 113-121.

Čekada, M., Panjan, P., Maček, M., and Šmíd, P. (2002). *Surface and Coatings Technology* **151-152**, 31-35.

Chapman, B. (1980). *Glow Discharge Processes —Sputtering and Plasma Etching*, John Wiley & Sons.

Changgeng, L., Yongqiang, W., Shengsheng, Y., Hui, J., and Zhihao, Z. (1995). *Vacuum* **46**, 295-297.

Clark, et al.(1978). *Nucl. Instrum. Methods* **149**, 9.

Damjantschitsch, H., Weiser, M., Heusser, G., Kalbitzer, S., and Mannsperger, H. (1983). *Nucl. Instrum. Methods* **218**, 129.

Da Silna Rocha, A., Strohaecker, T., Tomala, V., and Hirsch, T. (1999). *Surface and Coatings Technology* **115**, 24-31.

De Silva, K.T.L., Priyantha, W.A.A., Jayanetti, J.K.D.S., Chithrani, B.D., Siripala, W., and Dharmadasa, I.M. (2001). *Thin Solid films* **382**, 158-163.

Dessenne, O., Quentmeier, A. and Bubert, H. (1993). *Fresenius Journal Analytical Chemistry* **346**, 340-345.

Devanathan, M.A.V. and Stachurski, Z. (1962). *Proc.Roy. Soc.* **128**, 1668.

Dowling, W.E., Donlon, W.J., and Coupple, W.B. (1995). *Proceeding of the Second International Conference on Carburizing and Nitriding with Atmosphere*, ASM INTER, 6-8 Dec. USA.

Druger, R.A., Bombelka, R.M. and Laqua, K. (1980). *Spectrochim. Acta* **B35**, 589.

Faber, J., Hötzsch, G., and Metzner, Chr. (2002). *Vacuum* **64**, 55-63.

Fang, D. and Marcus, K. (1991). *Spectrochimica Acta* **B46**, 983-1000.

Flis, J., Mankowsky, J., and Zakroczymske, T. (2000). *Corrosion Science* **42**, 313-327.

Flis, J., Mankowsky, J., and Zakroczymske, T. (2001). *Corrosion Science* **43**, 1711-1725.

Freire Jr., F.L., Senna, L.F., Achete, C.A., and Hirsch, T. (1998). *Nuclear Instruments and Methods in Physics Research* **B136-138**, 788-792.

Fromm, E. (1989). *Aluminium* **65**, 1240-1243.

Fullenwider, Malcolm A. (1983). *Hydrogen Entry and Action in Metals*, Pergamon Press Inc., New York.

Gigandet, M.P., Faucheu, J., and Tachez, M. (1997). *Surface and Coatings Technology* **89**, 285-291.

Greene, J.E. and Whelan, J.M. (1973). *Journal of Applied Physics* **44**, 2509-2513.

Grimm, W. (1968). *Spectrochimica Acta* **B23**, 443.

Hamada, T., Wagasuma, K. and Hirokawa, K. (1995). *Surface and Interface Analysis* **23**, 213-218.

Hill, M.L. (1961). *The Behavior of Hydrogen in Iron and Steel*, In *Hydrogen Embritlement in Metal Finishing*, Edited by Harold J. Read, REINHOLD PUBLISHING CORPORATION, New York.

Hjörvarsson, B. and Rydén, J. (1990). *Nucl. Instrum. Methods* **B45**, 256.

Hodoroaba, V, Hoffmann, V., Steers, E.B.M. and Wetzig, K. (2000a). *Journal of Analytical Atomic Spectrometry* **15**, 951-958.

Hodoroaba, V, Hoffmann, V., Steers, E.B.M. and Wetzig, K. (2000b). *Journal of Analytical Atomic Spectrometry* **15**, 1075-1080.

Hoffmann, V. (1993). *Fresenius' Journal of Analytical Chemistry* **346**, 165-168.

Hofmann, S. (1997). *Applied physics* **13**, 205-207.

Hollstein, F., Wiedemann, R., and Scholz, J. (2003). *Surface and Coatings Technology* **162**, 261-268.

Howland, R. and Benator, L. (1993). *A practical Guide To Scanning Probe Microscopy*, Park Scientific Instruments.

Hunault, R. and Bailly, Y. (1990). *Selection of Internal References for Bulk Analysis of Alloys by Glow Discharge Optical Emission Spectroscopy (GD-OES)*, Luxembourg.

Ingo, G.M., Calliari, I., Dabala, M., Bultrini, G., Caro, T.De., and Chiozzini, G. (2000). *Surface and Interface Analysis* **30**, 264-268.

Ingo, G.M., Angelini, E., Bultrini, G., Calliari, I., Dabala, M., and Caro, T.De. (2002). *Surface and Interface Analysis* **34**, 337-342.

Ingo, G.M., Angelini, E., Calliari, I., Dabalà, M., and Caro, T.De. (2002). *Surface and Interface Analysis* **34**, 507-515.

Ives, M., Lewis, D.B. and Lehmberg, C. (1997). *Surface and Interface Analysis* **25**, 191-201.

Johnson, T.P., Dowson, A.L., and Ward, R.M. (1998). *Scripta Materialia* **39**, 783-789.

Jones, D.G. (1997). In *Glow Discharge Optical Emission Spectrometry*, R. Payling, D. Jones and A. Bengtson (eds), John Wiley & Sons, 160-164.

Kaminsky, M. (1965). *Atomic and Ionic Impact Phenomena on Metal Surfaces*, Springer-Verlag, Berlin.

King, V. B. (1997). In *Glow Discharge Optical Emission Spectrometry*, R. Payling, D. Jones and A. Bengtson (eds), John Wiley & Sons, 245-253, 273-286.

Kohlscheen, J., Stock, H.-R., Mayr, P. (1999). *Surface and Coatings Technology* **120-121**, 740-745.

Kozlovski, I.S., Kalinin, A.T., Novikova, A.Ya., Lebedeva, E.A., and Fefanova, A.I. (1967). *Metal Sci. Heat Treatment* **3-4**, 157-161.

Kruger, R.A., Bombelka, R.M. and Laqua, K. (1980). *Spectrochimica Acta* **B35**, 589.

Krüger, S.E., Rebello, J.M.A., and de Camargo, P.C. (1999). *NDT&E international* **32,** 275-281.

Kuhn, D., Rauch, F., and Baumann, H. (1990). *Nucl. Instrum. Methods* **B45**, 252.

Küper, A., Qiao, X., Stock, H.R., and Mayr, P. (2000). *Surface and Coatings Technology* **130**, 87-94.

Kuraica, M.M., Konjević, N. and Videnović, I.R. (1997). *Spectrochimica Acta* **B52,** 745-753.

Lanford, et al. (1976). *Appl. Phys. Lett.* **28**, 566.

Lanford, W.A. (1982). In *Advanced Techniques for Characerizing Hydrogen in Metals*, Edited by N. F.Fiore and B. J. Berkowitz, The metallurgical Society of AIME, New York, NY, 201-207.

Langberg, E. (1958). *Phys. Rev.* **111**, 91.

Leco Corporation, (1992). *Software Manual of GDS-750 QDP Glow Discharge Spectrometer*, Version 3, Leco Corporation.

Lii, D.F., Huang, J.L., and Lin, M.H. (1998). *Surface and Coatings Technology* **99**, 197-202.

Lingbergh, G., and Zhu, B. (2001). *Electrochimica Acta* **46**, 1131-1140.

Mändl, S., Günzel, R., Richter, E., and Möller, W. (1998). *Surface and Coatings Technology* **100-101**, 372-376.

Marshall, K.A. (1999). *Journal of Analytical Atomic Spectrometry* **14**, 923-928.

Marwick, A. D. (1991). In *Hydrogen in Semiconductors Vol.34*, Academic Press, Inc., 185.

Matsunami, N., Yamamura, Y., Itikawa, Y., Itoh, N., Kazumata, Y., Miyagawa, S., Morita, K. and Shimizu, R. (1980). *Radiat. Eff. Lett.* **50**, 39.

Mehs, D.M. and Niemczyk, T.M. (1981). *Spectorchimica Acta* **B36**, 965.

Michely, Th., Besocke, H.K. and Comsa, G. (1990). *Surf. Sci. Letters* **230**, L135.

Möller, W., Parascandola, S., Telbizova, T., Günzel, R., and Richter, E. (2001). *Surface and Coatings Technology* **136**, 73-79.

Natio, T., Ueda, H., and Kikuchi, M. (1984). *Metall. Trans.* **A15**, 1431-1436.

Nelis, Y. (1997). In *Glow Discharge Optical Emission Spectrometry*, R.Payling, D. Jones and A. Bengtson (eds), John Wiley & Sons, 413-417.

Mural, N., Tsumura, T. and Hasebe, M. (1997). *10^{th} international Congress of the International Federation for Heat Treatment and Surface Engineering*, Sweden, 55-70.

Olofesson, U., and Dizdar, S. (1998). *Wear* **215**, 156-164.

Oya, Y., Suzuke, T., Iinuma, K., Morita, K., Horikawa, T. and Abe, K. (2001). *Applied Surface Science* **169-170**, 246-252.

Pan, J., Leygraf, C., Jargelius-Pettersson, R.F.A., and Lindén, J. (1998). *Oxidation of Metals* **50**, 431-455.

Payling, R., and Jones, D.G. (1993). *Surface and Interface Analysis* **20**, 787-795.

Payling, R., Jones, D.G., and Gower, S.A. (1993). *Surface and Interface Analysis* **20**, 959-966.

Payling, R., Brown, N.V., and Gower, S.A. (1994). *Journal of Analytical Atomic Spectrometry* **9**, 363-368.

Payling, R., (1994a). *Surface and Interface Analysis* **21**, 785-790.

Payling, R., (1994b). *Surface and Interface Analysis* **21**, 791-799.

Payling, R., Jones, D.G., and Gower, S.A. (1995). *Surface and Interface Analysis* **23**, 1-11.

Payling, R. (1995). *Surface and Interface Analysis* **23**, 12-21.

Payling, R. (1997a). In *Glow Discharge Optical Emission Spectrometry*, R.Payling, D. Jones and A. Bengtson (eds), John Wiley & Sons, 20-47.

Payling, R. (1997b). In *Glow Discharge Optical Emission Spectrometry*, R.Payling, D. Jones and A. Bengtson (eds), John Wiley & Sons, 254-272.

Payling, R. (1997c). In *Glow Discharge Optical Emission Spectrometry*, R.Payling, D. Jones and A. Bengtson (eds), John Wiley & Sons, 287-292.

Payling, R. (1997d). In *Glow Discharge Optical Emission Spectrometry*, R.Payling, D. Jones and A. Bengtson (eds), John Wiley & Sons, 392-402.

Payling, R. (1997e). In *Glow Discharge Optical Emission Spectrometry*, R.Payling, D. Jones and A. Bengtson (eds), John Wiley & Sons, 428-439.

Payling, R. (1997f). In *Glow Discharge Optical Emission Spectrometry*, R.Payling, D. Jones and A. Bengtson (eds), John Wiley & Sons, 715-721.

Payling, R. and Jones, D.G. (1997). In *Glow Discharge Optical Emission Spectrometry*, R.Payling, D. Jones and A. Bengtson (eds), John Wiley & Sons, 460-471.

Payling, R., Aeberhard, M. and Delfosse, D. (2001). *Journal of Analytical Atomic Spectrometry* **16**, 50- 55.

Payling, R., Aeberhard, M. and Michler, J. (2002). *Surface and Interface Analysis* **33**, 472-477.

Präßler, F., Hoffmann, V., Schumann, J. and Wetzig, K. (1995). *Journal of Analytical Atomic Spectrometry* **10**, 677-680.

Pons-Corbeau, J. (1985). *Surface and Interface Analysis* **7**, 169-176.

Puomi, P., Fagerholm, H.M., Rosenholm, J.B., and Jyrkäs, K. (1999a). *Surface and Coatings Technology* **115**, 70-78.

Puomi, P., Fagerholm, H.M., Rosenholm, J.B., and Sipilä, R. (1999b). *Surface and Coatings Technology* **115**, 79-86.

Quentmeier, A. (1994). *Journal of Analytical Atomic Spectrometry* **9**, 355-361.

Quentmeier, A. (1997). In *Glow Discharge Optical Emission Spectrometry*, R.Payling, D. Jones and A. Bengtson (eds), John Wiley & Sons, 300-308.

Raymond, Louis and Associates (1987). In *Metal Handbook*, Ninth Edition, Volume **13**, Corrosio, ASM International.

Randle, V. (1993). *The Measurement of Grain Boundary Geometry (Electron Microscopy in Materials Science)*, Inst. Phys. Publishing (Bristol, UK).

Robinson, M. T. (1981). In *Sputtering by Particle Bombardment I*, R Behrisch (ed). Springer-Verlag Berlin, 73-144.

Roosendaal, H. E. (1981). In *Sputtering by Particle Bombardment I*, RBehrisch (ed). Springer-Verlag Berlin, 219-260.

Schulz, A., Stock, H.-R., Mayr, P., Staeves, J., and Schmoeckel, D. (1997). *Surface and Coatings Technology* **94-95**, 446-450.

Senna, L.F., Achete, C.A., Hirsch, T., and Freire Jr., F.L. (1997). *Surface and Coatings Technology* **94-95**, 390-397.

Shimizu, K., Einaga, Y., Ohnishi, K., Fujishima, A., Habazaki, H., Skeldon, P. And Thompson, G.E. (2002). *Surface and Interface Analysis* **33**, 35-40.

Sigmund, P. (1969). *Phys. Rev.* **184**, 383.

Sigmund, P. (1981). In *Sputtering by Particle Bombardment I*, edited by R. Behrisch, Springer-Verlag, 9-72.

Smialowski, Michael (1962). *Hydrogen in Steel*, Pergamon Press Ltd., Oxford, 64-130.

Simão, J., Aspinwall, D., El-Menshawy, F., and Meadows, K. (2002). *Journal of Materials Processing Technology* **127**, 211-216.

Smith, I.J., Gillibrand, D., Brooks, J.S., Münz, W.-D., Harvey, S., and Goodwin, R. (1997). *Surface and Coatings Technology* **90**, 164-171.

Snavely, Cloyd A. (1961). *Measurements Pertaining to Hydrogen Embrittlement*, In *Hydrogen Embritlement in Metal Finishing*, edited by Harold J. Read, REINHOLD PUBLISHING CORPORATION, New York.

SRIM (2003). *The Stopping and Rang of Ions in Matter* at URL:http://www.SRIM.org

Stott, F.H., Wood, G.C., Whittle, D.P., Bastow, B.D.,Shida, Y., and Martinez-Villafane, A. (1984). *Solid State Ionics* **12**, 365-374.

Suchaneck, G., Koehler, R., Padmini, P., Sandner, T., Frey, J., and Gerlach, G. (1999). *Surface and Coatings Technology* **116-119**, 1238-1243.

Sutton, A. P. and Balluffi, R. W. (1995). *Interfaces in Crystalline Materials*, Clarendon Press, Oxford, 12-17.

Suzuki, K., and Ohtsubo, T. (1984). *Transactions ISIJ* **24**, B-258.

Suzuki, K. (1988). *CAMP-Iron Steel Institute Japan* **1**, 1619.

Szökefalvi-Nagy, A., Weigel, J., Stojanova, L. And Fromm, E. (1994). J. *Mater. Sci. Technol.* **2**, 10-25.

Szökefalvi-Nagy, A., Stojanova, L, and Fromn, E. (1998). *Metallurgical and Materials Transactions* **B29**, 421-427.

Takadoum, J., Pivin, J.C., Pons-Corbeau, J., Berneron, R., and Charbonnier, J.C. (1984). *Surface and Interface Analysis* **6**, 174-183.

Takagi, Y., and Suzuki, K. (1999). *Applied Surface Science* **141**, 177-185.

Takimoto, K., Suzuki, D., Nishizaka, K., and Ohtsubo, T. (1987). *Nippon Steel Technical Report* **33**, 28-35.

Talbot, D.E.J., and Anyalebechi, P.N. (1988). *Mater. Sci. Technol.* **4**, 1-4.

Täschner, Ch., Ljungberg, B., Hoffmann, V., Vogt, C., and Leonhardt, A. (2001). *Surface and Coatings Technology* **142-144**, 823-828.

Thobor, A., Rousselot, C., Clement, C., Takadoum, J., Martin, N., Sanjines, R., and Levy, F. (2000). *Surface and Coatings Technology* **124**, 210-221.

Timmins, P.F. (1997). *Solutions to Hydrogen Attack in Steel*, ASM International.

Tirira, J., Serruys, Y., and Trocellier, P. (1996). In *Forward Recoil Specrometry*, Plenum Press, New York, NY.

Turley, D.M. and Samuels, L.E. (1997). *Materials Characterisation* **39**, 399-418.

Verda, R.D., Maggiore, C.J., Tesmer, J.R. Misra, A., Hhechbauer, T., Nastasi, M., and Bower, R.W. (2001). *Nuclear Instruments and Methods in physics Research* **B183**, 401-412.

Verda, R.D., Tesmer, J.R. Nastasi, M., and Bower, R.W. (2002). *Nuclear Instruments and Methods in physics Research* **B190**, 419-422.

Videnović, I.R., Konjević, N. and Kuraica, M.M. (1996). *Spectrochimica Acta* **B51,** 1707-1731.

Wäckelgård, E. (1998). *Solar Energy materials & Solar Cells* **56**, 35-44.

Wagatsuma, K. (1997). In *Glow Discharge Optical Emission Spectrometry*, R. Payling, D. Jones and A. Bengtson (eds), John Wiley & Sons, 167-175.

Wagatsuma, K. (2001). *Spectrochimica Acta* **B56**, 465-486.

Wänstrand, O., Larsson, M., and Hedenqvist, P. (1999). *Surface and Coatings Technology* **111**, 247-254.

Wänstrand, O., Fella, R., and Axén, N. (1997). *Surface and Coatings Technology* **94-95**, 469-475.

Ward, R.G., M.A, PhD. (1962). *An introduction to the physical chemistry of iron and steel making*, EDWARD ARNOLD Ltd., 184.

Watt, Ian M. (1985). *The principles and practice of electron microscopy*, Cambridge University Press, Cambridge, 243.

Weiss, Z. (1995). *Journal of Analytical Atomic Spectrometry* **10**, 891-895.

Weiss, Z. (1997). In *Glow Discharge Optical Emission Spectrometry*, R. Payling, D. Jones and A. Bengtson (eds), John Wiley & Sons, 418-427.

Weston, G. F. (1968). *Cold Cathode Glow Discharge Tube.* Iliffe Books, London.

Wielnsky, L.S., Grambole, D., Kreissig, U.,GröTzschel, R., Harding, G., and Szilágyi, E. (2002). *Nuclear Instruments and Methods in physics Research* **B190**, 693-698.

Wolpers, M., and Angeli, J. (2001). *Applied Surface Science* **179**, 281-291.

Yamamura, Y., Matsunami, N. and Itoh, N. (1983). *Radiat. Eff.* **71**, 65.

Zhu, B., Lingbergh, G., and Simonsson, D. (1999). *Corrosion Science* **41**, 1515-1528.

Zhu, B., and Lingbergh, G. (2001). *Electrochimica Acta* **46**, 2593-2604.

Ziegler, et al. (1978). *Nucl. Instrum. Methods* **149**, 19.

List of Captions of the Figures in the Thesis

silicon film, no pits can be observed even after 10 seconds etching.

Figure 4.12. SEM images of pits on a surface of carbon-coated pure iron after GDOES etching. The surface layer was still in the carbon film. Original thickness of the carbon film: ~600 nm. Etching time: 155 sec.
(a) The pits formed initially in carbon layer.
(b) The pits on the substrate where the carbon film was broken over a relatively large area.

Figure 4.13. SEM image of pits on a surface of carbon-coated pure iron after the film was completely etched out in the GDOES. The pits generated on the 'ripple' and the 'smooth' areas imply crystal structure has no effect on the pitting phenomenon. Thickness of the carbon film: ~600 nm. Etching time: 200 seconds.

Figure 4.14. SEM images of pits on etched surfaces of carbon-coated silicon wafers with different original thicknesses of the films. The surfaces were in the layers in where argon ions just penetrated through the films and silicon atoms began to be sputtered out. GDOES parameters: 600 V/25 mA/4 mm anode. Original thickness of carbon films and etched times:
(a) 50 nm/20 sec.
(b) 110 nm/39 sec.
(c) 260 nm/106 sec.

Figure 4.15. SEM images of the smallest pits on the surfaces of carbon layers. Sizes of the smallest pits in the different layers were almost same, around one micron. Original thicknesses of carbon films and etched times were:
(a) 110 nm/39 sec,
(b) 215 nm/83 sec,
(c) 260 nm/106 sec.

Figure 4.16. Densities of the pits on the surfaces of carbon layers of the samples corresponding to that in Figures 4.14 and 4.15.

Figure 4.17. Measured roughness of etched surfaces of the samples corresponding to that in Figure 4.16. The roughness increases as the sputtering time increases. A best fit straight line has been fitted to the data with R^2=0.9834.

Figure 4.18. Schematic illustration of the stochastic roughening model.
(a) With thinner original carbon film, the stochastic roughing results in a higher density of pit and leaves a thinner remaining thickness of carbon film.
(b) The thicker carbon film requires a longer sputtering time and leaves a rougher surface, which produces the pits on the silicon surface with lower density.

Figure 4.19. SEM images of pits on silicon wafers with different thicknesses of original carbon films when the films were etched out completely. Thicknesses of carbon film and etched times:
(a) 50 nm/36 sec.
(b) 110 nm/103 sec.
(c) 180 nm/163 sec.
(d) 215 nm/201 sec.
(e) 260 nm/241 sec.

Figure 4.20. Densities of the pits corresponding to the samples in Figure 4.19. A best fit

List of Captions of the Tables in the Thesis

Publications

1. Crystal orientation effects on sputtering and depth resolution in GDOES
   L. Chen, M.C. Simmonds, S. Habesch and J.M. Rodenburg
   SURFACE AND INTERFACE ANALYSIS **31** (2001) 206-211.

2. A study of internal oxidation in carburized steels by glow discharge optical emission spectroscopy and scanning electron microscopy
   X. An, J. Cawley, W.M. Rainforth, L. Chen
   SPECTROCHIMICA ACTA PART B **58** (2003) 689-698.